Metal supported carbon nanostructures for hydrogen storage

Paolo Matelloni

Thesis submitted to the University of Nottingham for the degree of

Doctor of Philosophy

March 2012

Abstract

Carbon nanocones are the fifth equilibrium structure of carbon, first synthesized in 1997. They have been selected for investigating hydrogen storage capacity, because initial temperature programmed desorption experiments found a significant amount of hydrogen was evolved at ambient temperatures. The aim of this thesis was to study the effect of impregnation conditions on metal catalyst dispersion and to investigate whether the metal loaded cones had improved hydrogen storage characteristics. Pre-treatment of carbon nanocones with hydrogen peroxide was carried out, followed by metal decoration in aqueous solution by an incipient wetness technique. Two methods of reducing the metal catalyst have been applied: in hydrogen at room temperature (RT) and in an aqueous solution of $NaBH_4$. X ray diffraction (XRD) technique confirmed the complete metal reduction and transmission electron microscope (TEM) analysis showed that the reduction technique affected the catalyst dispersion. Very fine dispersions of *ca*. 1 nm diameter metal clusters at catalyst loadings of 5 wt% were achieved and high dispersions were retained for loadings as high as 15 wt%. Hydrogen uptakes at RT were measured and an increase with metal loading was observed. In comparison the same route of pre-treatment and metal impregnation has been done over graphite nanofibres (GNF) and the hydrogen uptake showed an adsorption superior of the cumulative contribution of the substrate and metal catalyst attributing this to hydrogen spillover.

The GNF have been impregnated also with another metal catalyst Ni showing as well the phenomenon of hydrogen spillover.

The attempt to impregnate the carbon nanocones with a mixture of Pd-Ni, Pd-Cu and Pd-Ag resulted in an increase of hydrogen uptake for the first two but a decrease for the last of these.

The carbon nanocones have been also impregnated with a Mg organometallic precursor dibutyl magnesium (DBM) and then decomposed without the use of hydrogen environment synthesizing successfully MgH_2. The stoichiometry and the enthalpy of this decomposition have been studied.

Furthermore, the DBM has been mixed with another hydride $LiALH_4$ and the decomposition reaction of the complex hydride has been studied.

Acknowledgment

I'd like to thank the European Project HYCONES and the EPSRC bodies to fund my research.

I am immensely grateful to my supervisors Prof. Gavin Walker and Prof. David Grant for the patience and hard lessons they taught me making me an independent and critical mind.

I'd like to thanks a lot the personnel of Wolfson building Keith, Tom, Nigel, George, Martin and Julie that really do the hard jobs in assisting in practical things and getting my hands dirty.

Personal thanks and love to my family that supported me during the build-up of my career without a shadow of doubt.

I am also grateful to the guys in office for have shared with me good and bad mood.

A big thanks to Livia, that in the last year and half had to put up with the nervous me without losing the patience and the passion.

And also a little thank to myself, that being so "me" and stubborn, for making it through until the end and beyond.

Table of content

List of figures

List of tables

List of abbreviations

AC	activated carbon (AC)
ACF	activated carbon fibres (ACF)
ATR	attenuated total reflection (ATR)
BET	Brunauer Emmett Teller (BET)
BF	bright field (BF)
CNT	carbon nanotubes (CNT)
CVD	carbon vapour deposition (CVD)
DBM	dibutyl magnesium (DBM)
DF	dark field (DF)
DSC	differential scanning calorimetry (DSC)
FTIR	transformation infrared spectroscopy (FTIR)
FWHM	full width half maximum (FWHM)
GNF	graphite nanofibres (GNF)
IGA	intelligent gravimetric analyser (IGA)
IR	Infrared (IR)
MCT	mercury cadmium telluride (MCT)
MS	mass spectrometry (MS)
MW	molar weight (MW)
MWCNT	multi walled carbon nanotubes (MWCNT)
RT	room temperature (RT)
SAD	selected area diffraction (SAD)
SEM	secondary emission multiplier (SEM)
SWCNT	single wall carbon nanotubes (SWCNT)
TEM	transmission electron microscope (TEM)
TGA	thermogravimetric analysis (TGA)
TPD	temperature programmed desorption (TPD)
XRD	X-ray diffraction (XRD)

1. Introduction

1.1. Hydrogen as an energy carrier for automotive applications

Abating CO_2 emission from burning fossil fuels has been clearly identified as the main action to mitigate global warming and climate change. On top of this, resources of crude oil, coal and natural gas are limited requiring alternative solutions before the demand becomes not sustainable anymore. In this scenario hydrogen as an energy carrier shows great potential. Hydrogen can be produced from water electrolysis and this could make it available to rich and poor countries. It can be produced even at domestic scale and using not only water [1] but also other sources like agricultural waste [2] and other biomasses [3] (table 1.1) improving also the environmental footprints.

Table 1.1 Various methods of hydrogen production from different biomass sources [3]

Biomass species	**Main conversion process**
Bio-nut shell	Steam gasification
Olive husk	Pyrolysis
Tea waste	Pyrolysis
Crop straw	Pyrolysis
Black liquor	Steam gasification
Municipal solid waste	Supercritical water extraction
Crop grain residue	Supercritical fluid extraction
Pulp and paper waste	Microbial fermentation
Petroleum basis plastic waste	Supercritical fluid extraction
Manure slurry	Microbial fermentation

However, on a large scale, hydrogen is still produced mainly from natural gas reforming [4] (table 1.2).

Table 1.2 Source share in the industrial hydrogen production [4]

Source	**10^9 m^3 y^{-1} (STP)**	**Share (%)**
Natural gas	240	48
Oil	150	30
Coal	90	18
Electrolysis	20	4
Total	500	100

Table 1.3 reports the main chemical and physical characteristics that make hydrogen a good candidate as energy carrier. Hydrogen has a wider flammability range than the other fuels. This means an amount as small as 4 %, in oxygen environments can represent an efficient combustible mixture making the engine more efficient. This is due the very low ignition energy (0.02 MJ) compared to methane (0.29 MJ) or gasoline (0.24 MJ) The consequence of that is that hydrogen is easy to detonate when confined, however, unlike many other fuels it is very difficult to detonate if unconfined due to the high diffusivity. In fact having a high diffusivity means that it easily forms uniform mixture of fuel/air and if a hydrogen leak develops, the hydrogen disperses rapidly minimizing dangerous stagnation. Thus, unsafe conditions can either be avoided or minimized.

Table 1.3 Physical and chemical properties of three fuel options (hydrogen, methane, and gasoline) [5]

	Hydrogen	**Methane (H/C = 4)**	**Gasoline (H/C = 1.87)**
Molecular weight (g mol^{-1})	2.016	16.04	~ 110
Mass density (kg m^{-3}) at p = 1 bar , T = 0 °C	0.09	0.72	720–780 (liquid)
Mass density of liquid H_2 at 20 K (kg m^{-3})	70.9	–	–
Boiling point (K) at P = 1 bar	20.2	111.6	310–478
Higher heating value (MJ kg^{-1}) (assumes water is produced)	142	55.5	47.3
Lower heating value (MJ kg^{-1}) (assumes steam is produced)	120	50	44
Flammability limits (% volume)	4.0–75.0	5.3–15.0	1.0–7.6
Detonability limits (% volume)	18.3–59.0	6.3–13.5	1.1–3.3
Diffusion velocity in air (m s^{-1})	2	0.51	0.17
Ignition energy (MJ)			
– At stoichiometric mixture	0.02	0.29	0.24
– At lower flammability limit	10	20	n/a
Flame velocity in air (cm s^{-1})	265–325	37–45	37–43
Toxicity	Nontoxic	Nontoxic	Toxic above 50 ppm

Having a heating value three times higher than petroleum [6, 7] means that hydrogen has more calorific value per unit of mass which represents a better utilization of the resource [8]. Last but not the least, its lower normal boiling point (20K) makes hydrogen an efficient fuel at low temperature conditions which is a major drawback of conventional fuels. Such a fuel can readily and easily substitute most common types of fuel without excessive change in technology, for example in an internal combustion engine [5].

It is also the cleanest fuel in terms of products of combustion since it produces mainly water, which is also the starting material of hydrogen production, making the hydrogen a clean energy vector. Table 1.4 reports a comparison of exhaust gas

emissions from different fuels. The electricity carbon dioxide emissions are assumed to be 150 $g(CO_2)\,MJ^{-1}$ based upon the 2008 UK average electricity emissions of 540 $g(CO_2)\,kWh^{-1}$ which included 5.5 % of electricity generation from renewables. With a target for electricity to be decarbonised of 50% by 2030 this would equal 79 $g(CO_2)\ MJ^{-1}$[9]. This makes it such that electrical vehicles have a similar carbon footprint as hydrogen vehicles, but the former still have a major drawback of long recharging times and limited travelling range [10, 11]. Carbon dioxide emissions from petrol are 77.6 $g(CO_2)\ MJ^{-1}$ based upon the chemical composition of the fuel and a calorific value of 47.3 MJ kg^{-1} [12]. Hydrogen carbon dioxide emissions are assumed to be 76.9 $g(CO_2)\,MJ^{-1}$ based upon a value of 11 $kgCO_2\ kgH_2^{-1}$ for steam reforming natural gas and a calorific value of 143 MJ kgH_2^{-1} and the assumption that hydrogen will predominately be manufactured by steam reforming natural gas in 2030 [13]. Thus hydrogen competes with declining fossil fuel and emerging battery technologies in terms of carbon footprint with the advantage of not having a long charging time as with batteries. [14]

Table 1.4 Summary of CO_2 vehicle emissions for petrol, hydrogen and electricity as fuel

	Petrol	**Hydrogen**	**Electricity (2008)**
CO_2 emissions ($gCO_2\ MJ^{-1}$)	77.6	76.9	150
Fuel consumption/ (MJ $mile^{-1}$)	2.93	1.46	0.73
Emissions ($gCO_2\ mile^{-1}$)	227	112	110
Emissions ($gCO_2\ km^{-}$)[1]	142	70	68

As stated above even the electricity production is related to some sort of CO_2 production however, there are other technologies to produce electricity that are also

considered renewable like wind power or solar power which, however, to be reliable need a source of energy when these intermittent sources are not accessible [15] thus is required an energy storage medium which hydrogen can provide. This is the reason why hydrogen is an optimal energy carrier for mobile and automotive application, because it has the potential to be readily usable, to be compatible with conventional technology and be stored and transferred quickly and efficiently.

Unfortunately not being found in nature in its molecular state, it has certain refining costs, making it cost three times more than petroleum products. Another drawback is that hydrogen has low density which results in a lower volumetric energy density of the combustible mixture hydrogen/air. This leads to a reduced power output and when stored it requires a larger volume to store an equivalent energy amount than fossil fuel. In fact the real issue is the storage as this should not increase considerably the cost of a system powered by hydrogen and has to be very compact.

In table 1.5 are the latest reported (2011 Interim Update) DOE requirements [16] for optimum storage hydrogen in light duty vehicles: a high H-storage capacity of 1.5 kWh kg^{-1} system (4.5 wt% hydrogen) and 0.9 kWh l^{-1} (0.040 kg hydrogen l^{-1}) in 2010 increasing in 2017 to 1.8 kWh kg^{-1} system (5.5 wt% hydrogen) and 1.3 kWh l^{-1} (0.040 kg hydrogen l^{-1}). Obviously, the gravimetric and volumetric capacities of the material alone must be higher than the system-level targets.

Table 1.5 System requirements for a competitive and efficient hydrogen system of automotive applications (DOE 2011)

Storage Parameter	Units	2010	2017
Gravimetric Capacity	$kW\dot{h}\ kg^{-1}$ (wt% hydrogen)	1.5 (4.5%)	1.8 (5.5%)
Volumetric Capacity	$kW\dot{h}\ l^{-1}$ ($kg\ (H_2)\ l^{-1}$)	0.9 (0.028)	1.3 (0.040)
Fuel cost	$ per gallon gasoline equivalent at pump	3-7	3-4
Operating ambient temperature	°C	-30/50 (sun)	-40/60 (sun)
Cycle life (1/4 tank to full)	Cycles	1000	1500
Onboard efficiency "Well" to powerplant efficiency	% %	90 60	90 60
System fill in time (5kg)	min	4.2	3.3

Optimization of a material performance to meet these criteria can be made by engineering the storage materials in their structure and components. Figure 1.1 shows a schematic of the tunable parameters for improving the desired performances of hydrogen storage systems.

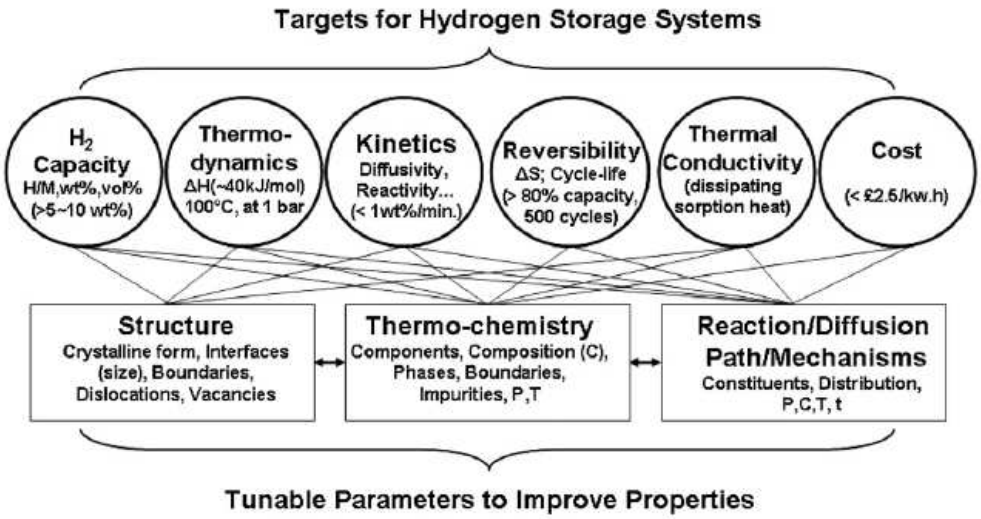

Figure 1.1 Optimization strategies in relation to the hydrogen system application [17]

The following sections will describe several methods for hydrogen storage: compression, liquefaction, physisorption, metal hydrides, and complex hydrides.

1.2. Status of current solutions

In this session will be discussed hydrogen storage canonical techniques in their technical details and their limitations.

1.2.1. Compression

Compression is the simplest way to store hydrogen in a cylinder at pressures up to 700 bar, but due to the energy density of 1.3 kWh l^{-1} would require a storage volume too big to satisfy the fuel demand of 350 miles range (or 5.6 kg of H_2 on board) [18]. The issues with gas tanks revolve around high pressure, weight, volume, conformability and cost. The latter is mainly represented by the cost of the carbon

fibres that must be used for light-weight structural reinforcement and the energy cost of pressurising to 700 bar. At the same time, such materials must still be capable of meeting tank thickness constraints in order to help meet the volumetric capacity targets. Thus, lowering cost without compromising weight and volume is a key challenge.

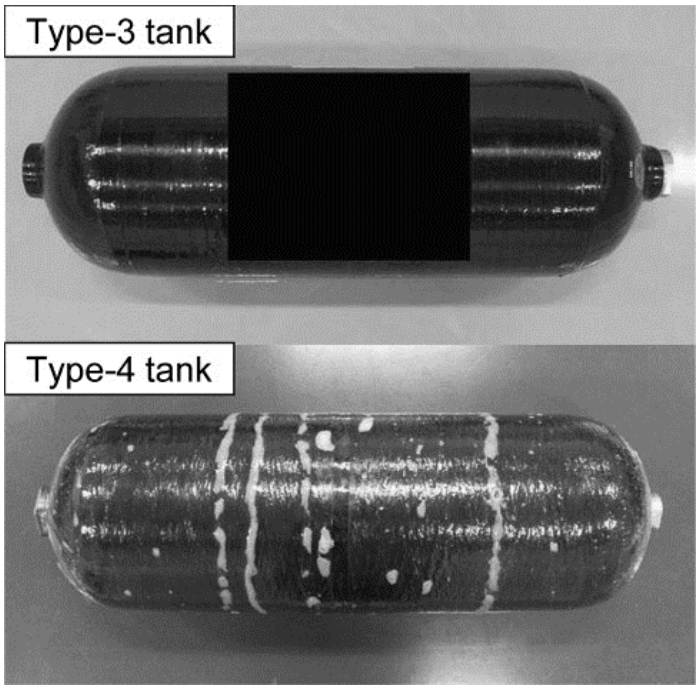

Figure 1.2 Type 3 (Al liner and carbon fibre reinforced shell, volume 34 l and diameter × length 280 mm × 830 mm) and type 4 (polyamide liner and carbon fibre reinforced shell, volume 40 l and diameter × length 287 mm × 884 mm) tanks for compressed gas hydrogen storage [19]

In order to increase the gravimetric and volumetric storage capacities, new cryo-compressed tanks have been developed. This is based on the fact that, at fixed pressure and volume, the gas tank volumetric capacity increases as the tank temperature decreases. However, the system size increases due to the thicker tank walls required to retain the low temperatures, hence the effective increase of capacity is negated.

1.2.2. Liquefaction

Cryogenic liquid hydrogen tanks are smaller than compressed hydrogen gas cylinders because of the high density of liquid hydrogen at low pressures which is 70.8 g l^{-1} for saturated liquid at 1 bar. Such tanks can be refuelled quite rapidly (in 3 min) with relatively limited evaporative losses [20]. However, despite existing insulated cryogenic tanks with extremely low heat transfer from ambient (1–3 W), evaporative losses are still a problem. In fact hydrogen has to be vented after 3–5 days of inactivity, and it can happen after long periods of inactivity that hydrogen in the vehicle may be depleted completely from the tank [21]. The structure of a liquid hydrogen tank and its components is represented in figure 1.3. Because liquid hydrogen expands considerably as it warms between 20 K and its critical point (33 K), the tanks are filled to only 85–95 % capacity to prevent spills, leaving 5–15 % of empty space called ullage [22].

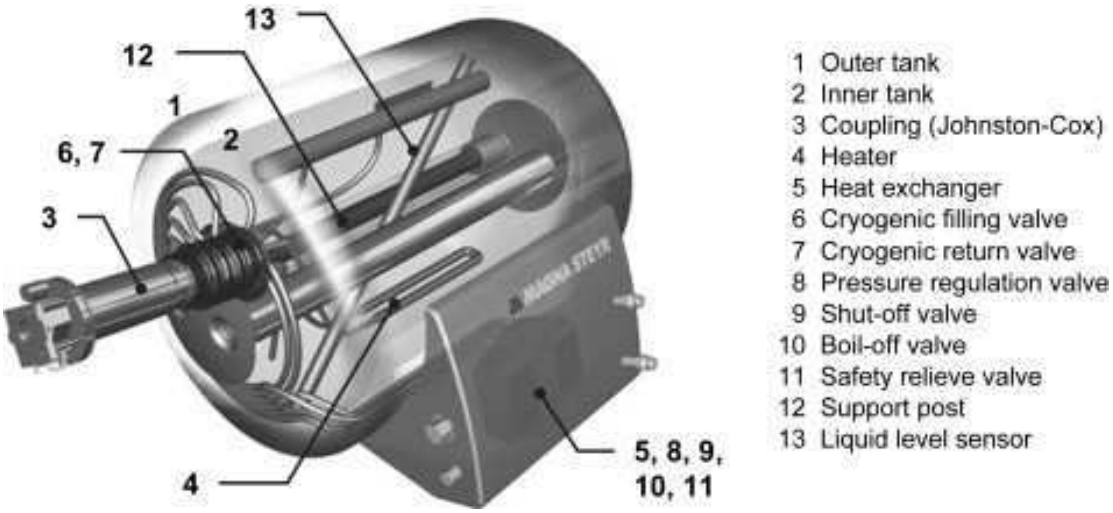

Figure 1.3 Liquid hydrogen tank system capable of store 8 litres of liquid hydrogen [23]

Having a pressurizing liquid hydrogen tank that can withstand pressure (cryo-compressed H_2 storage option or cCH_2) could overcome some of these problems. In fact the period of inactivity, called dormancy, is greatly extended if the pressure inside the vessel is allowed to increase [22]. A vehicle with an insulated pressure vessel will not be completely stranded due to evaporative losses because venting stops when the tank reaches ambient temperature, but will still have hydrogen gas at pressure >240 bar, at which point the hydrogen density is still 30% of the initial liquid density, leaving some driving autonomy. A diagram of the pressure control system is shown in figure 1.4. A way to reduce or eliminate ullage space is exploiting the fact that hydrogen becomes a supercritical fluid at a pressure above 13 bar before there is a need to vent. The storage density may be higher in insulated pressure vessels since liquid hydrogen is slightly compressible: at 21 K and 240 bar the liquid density is 87 g L^{-1} compared to 70 g L^{-1} at 21 K and 1 bar [22].

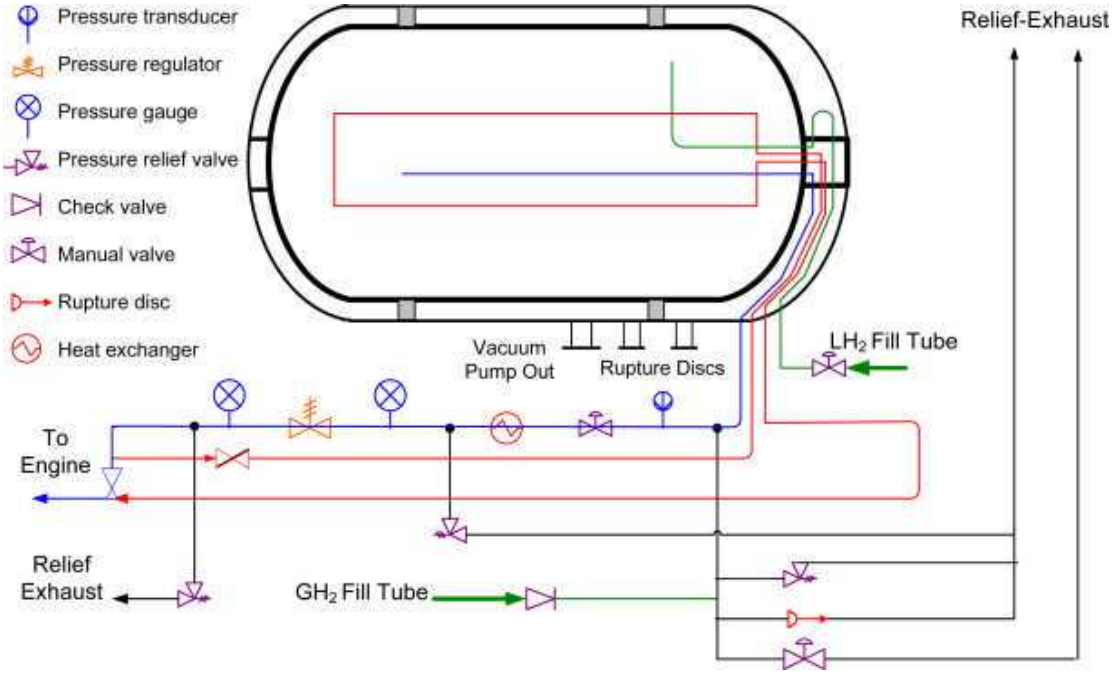

Figure 1.4 Design schematic of the Gen-3 cryo-compressed H_2 storage tank system [24]

Nevertheless this method has two major flaws: the efficiency of the liquefaction process and the boil-off of the liquid. The latter is the evaporation of liquid hydrogen inside the cryogenic (21.2 K) vessel, which means there is a constant loss of hydrogen from the store. The critical temperature of hydrogen is very low (33 K), above which the liquid state cannot exist. Therefore, liquid hydrogen can only be stored in an open system where the temperature is maintained constant otherwise the pressure in a closed system can reach pressures as high as 10000 bar if the storage vessel warms up to room temperature. However, with new generation of vessels the tolerable pressure is of 350 bar before venting extending the dormancy seven times longer than a conventional liquid hydrogen storage tank [25]. Still the energy requirement for hydrogen liquefaction is high; typically, 30 % of the heating value of hydrogen is required for liquefaction [26] whereas compressing H_2 to 250–1000 bar requires 1.5–2.0 kWh kg^{-1} which is nearly half the theoretical energy needed to liquefy H_2 by

cooling to 20 K (3.25 kWh kg^{-1}) [25]. The large amount of energy necessary for liquefaction and the boil-off of the liquid limits the use of this storage system to applications where the cost of hydrogen is not an important issue and the hydrogen is consumed in a rather short time, e.g. aerospace applications.

1.2.3. Physisorption in porous materials

The International Union of Pure and Applied Chemistry (IUPAC) definition of physisorption [27] is the adsorption occurring in any solid/fluid system in which the forces involved are similar, such as van der Waals forces, as those involved between a real gas and the condensation of vapours. These intermolecular forces will not affect significantly the electronic orbital patterns of the species involved hence the chemical nature of the fluid is not altered during adsorption and subsequent desorption. The consequence of that is that the physical adsorption from a gas phase does not involve an activation energy. The extent of physical adsorption increases with increase in gas pressure and usually decreases with increasing temperature. The formation of this monolayer allows the calculation of the surface area. Under appropriate conditions of pressure and temperature, the material can adsorb more molecules than those in direct contact with the surface, called a monolayer, forming another layer above them, called a multilayer, or they can even fill micropores. The pore sizes can be calculated at this stage. Pore filling involves the process in which molecules are adsorbed in the whole accessible space within the micropores. When in porous solids adsorption multilayers reaches the point at which pore spaces are filled with liquid separated from the gas phase by menisci that is called capillary condensation. At this point is

possible to calculate the total pore volume. A schematic of these concepts is offered in figure 1.5.

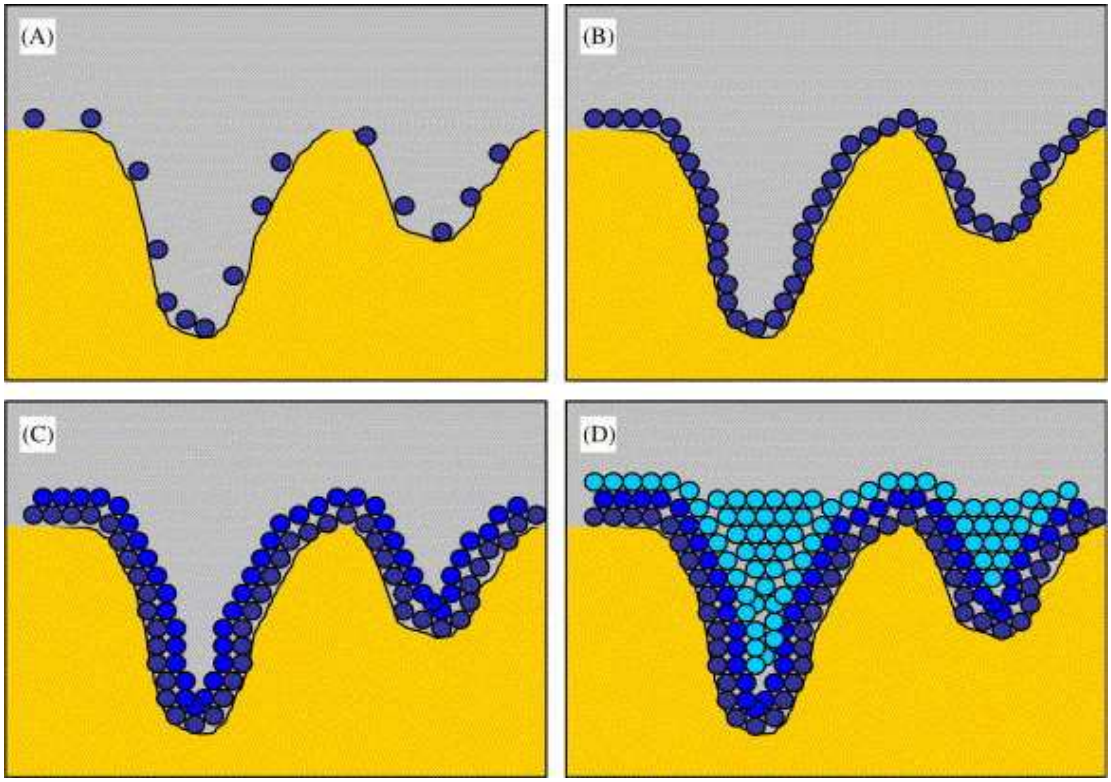

Figure 1.5 Gas molecules are attracted to the pore surfaces (A) forming a complete coverage of the surface, the monolayer (B) if the adsorption continues multilayer filling occurs (C) till the pores volume it totally filled (D) [28].

As suggested by Benard and Chahine [29] the development of the materials using the physisorption for hydrogen storage goes towards the optimization of three parameters: the characteristic binding energy of the hydrogen molecule with the material, the available surface for the adsorption to occur and the bulk density of the gas adsorbed. The combination of these last two features is the average surface available per unit volume of the adsorbent. The binding energy determines the operating temperature of a hydrogen storage system based on the solid.

Carbon nanostructures show good potential for solid state storage of hydrogen. Porous carbons with high surface areas have been shown to have high excess adsorption of hydrogen, 6-7 wt%, at 77 K and 20 bar pressure [30]. However, there is a desire to have equally high uptakes but at temperatures closer to RT. Due to the weak physisorption interactions of hydrogen on carbon materials, *ca*. 6-9 kJ mol^{-1}, and with high surface area carbon materials the capacity at room temperature (RT) and 100 bar is < 0.5 wt% [31]. Therefore, to use carbon nanostructures as RT hydrogen storage media, an activation mechanism, like coupling with metal catalyst, is needed to enhance the hydrogen interaction with the substrate and ultimately the capacity.

1.2.4. Chemisorption in metal hydrides

Chemisorption involves the endothermic dissociation of the hydrogen molecules into two hydrogen atoms that are chemically bonded with the medium surface. It is characterized by an initial activation energy for the reaction to occur at the surface monolayer and an enthalpy change for the creation of the products from the reagents.

The easiest way to distinguish between physisorption and chemisorption are enthalpy measurements, as chemisorption typically has much larger enthalpic changes compared to physisorption. Moreover, in the kinetics of hydrogen loading and release, physisorption shows a much smaller or negligible activation energies. The difference is represented in figure 1.6 where is depicted that physisorption does not have an activation energy whereas chemisorption requires an activation energy and the

resulting structure is electronically different, generating a difference in the energetic status. Such a difference is called enthalpy of reaction.

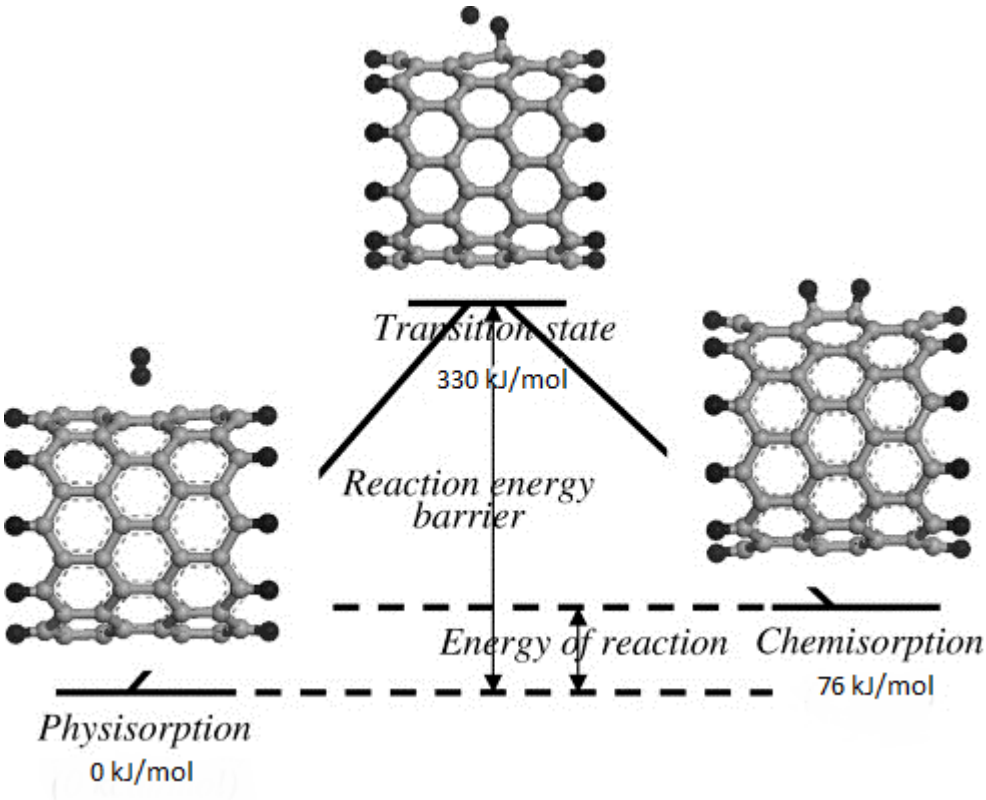

Figure 1.6 Schematic of theoretical pathway of the reaction from physisorption of hydrogen to chemisorption at 0 K carbon surface [32]

Metal hydrides are composed of metal atoms that constitute a host metal lattice and hydrogen atoms. In simple systems, metal and hydrogen usually form two different kinds of solid solutions, a phase with low ratio M/H called the α-phase and the metal hydride called the β-phase. Metals differ in the ability to dissociate hydrogen, depending on surface structure, morphology and purity. An optimum hydrogen-storage material is required to have the following properties: high hydrogen capacity per unit mass and unit volume, low dissociation temperature, moderate

dissociation pressure, low heat of formation in order to minimize the energy necessary for hydrogen release, low heat dissipation during the exothermic hydride formation, reversibility, limited energy loss during cyclic charge and discharge of hydrogen, fast kinetics, high stability against O_2 and moisture for long cycle life, low cost of recycling and charging infrastructures and high safety [33].

Light metals such as Li, Be, Na, Mg, B and Al, form a large variety of metal–hydrogen compounds. They are especially interesting due to their light weight and the number of hydrogen atoms that can be bond to the metal atom, which is in many cases is two or more.

The Mg-based hydrides possess some good functional properties such as reversibility and cyclability. On the other hand the main disadvantages of MgH_2 as a hydrogen storage is the high temperature of hydrogen discharge, slow desorption kinetics and a high reactivity toward air and oxygen. Investigations into the thermodynamic properties of magnesium hydride shows a high operating temperature which is too high for practical on-board applications [34] corresponding to a dehydrogenation temperature of 300 °C at 1 bar H_2 [35]

Another critical factor for hydrogen adsorption by metals is the metal surface where, through dissociating the hydrogen molecules, hydrogen atoms are diffused into the bulk. Diffusion is not the limiting step initially because no material has been reacted and there are sufficient active sites available, but the hydride formation rate is the slowest step for pure Mg at this point [36]. But as the reaction progresses, hydrogen diffusion becomes more important as the hydride layer grows, and the diffusion through this hydride layer becomes the rate-limiting step in the hydride formation process [36].

In addition to the formation of a hydride layer, reaction with any oxygen impurities will also lower the absorption rate due to the formation of a highly stable oxide layer [35]. A study by Andreasen *et al*. [37] demonstrated that the increase of apparent activation energies correlates with the presence of MgO on surface layer inhibiting diffusion of hydrogen. To improve the sluggish kinetics ball-milling offers an energy intensive but relatively simple way to create fresh surfaces during processing [38]. The main effects of ball-milling are increased surface area, formation of micro/nanostructures and creation of defects on the surface and in the interior of the material. Depending on the ball-milling conditions, the shift of the onset of dehydrogenation temperature can be as large as 100 °C for MgH_2 [35].

Catalysis is critical in improving the hydrogenation kinetics in metal hydride system. Effective catalysts, even added in small amounts, enhance the formation of the hydride to a reasonable extent. The rate of absorption is controlled by the following factors: the rate of hydrogen dissociation at the surface, the capability of hydrogen to penetrate from the metal surface which is typically covered by an oxide layer into the bulk metal, the rate of hydrogen diffusion into the bulk metal and through the hydride already formed. The poor kinetics of MgH_2 can also be improved by addition of different oxide catalysts, such as V_2O_5 [39] and Cr_2O_3 [40] activating the hydriding properties at lower temperature. The oxide particles may operate also as a milling aid during high-energy ball-milling that creates many defects in the Mg powder, providing hydrogen with an easier path into the Mg.

Furthermore, it has been found that the hydrogenation/dehydrogenation temperature and hydrogenation rate can also be improved by forming composite structures. Zhu *et al*. [41] reported that a possible reason is that those components combined with Mg in the composite can catalyse the hydrogenation reaction of Mg

improving of the hydrogenation properties. Results of their experiments show that the improvement in properties is closely related to the type of component combined with Mg, the size of them and their distribution. The best results were obtained with a Mg/Mm–Ni (where Mm = mish-metal) multi-layer film having temperature of hydrogenation/dehydrogenation of 150 °C and 200 °C, respectively.

Wang *et al*. [42] combined both the catalytic and milling effects in a system of fine $ZrFe_{1.4}Cr_{0.6}$ particles covering Mg particles. Other combinations of MgH_2 and metals like Ti, V, Mn, Fe and Ni, have been investigated extensively [43, 44] finding that composites containing Mg–Ti and Mg–V exhibit rapid hydrogenation kinetics such as 2–5 min for magnesium hydride at 200 °C. The drawback in all these cases is a decrease in capacity.

Cyclic stability is one of the major criteria for applicability of metal/metal hydride systems for reversible hydrogen storage.

The results from Tien *et al.* [45] have demonstrated that the hydrogen capacity of Mg powder is influenced drastically by the nucleation rate of the hydride. For example, at low hydrogenation temperatures, owing to a fast nucleation rate the capacity will be low. At high nucleation rate the hydride grain surface is covered with MgH_2 in a short time during the hydrogenation. After this point, further hydrogen absorption takes place by diffusion of hydrogen through the MgH_2 layer. MgH_2 having low diffusion rate [46] hinders the other Mg to react with hydrogen resulting in a low capacity.

On the other hand, increasing the hydrogenation temperature will enhance the growth rate but will decrease the nucleation rate, hence reducing hydrogenation rate. In fact as temperature increases, the rate of diffusion increases; molecules are able to get to the site of nucleation at a fast enough rate to promote growth of the nucleus.

However, as temperature increases, molecular fluctuations increase and molecules tend to escape from the nucleus, causing a decreased rate of nucleation. Due to these fluctuations it will take more time for the hydride nucleus to form and hence the rate of hydrogenation, i.e. hydride formation, is reduced. Therefore, there is an optimum hydrogenation temperature, where a good capacity is reached in a relatively fast manner. Depending on the nature of the additives, cycling temperatures and starting microstructures, various structures and intermediate phases can be obtained.

The resistance of metal hydrides to poisoning with impurities like N_2, O_2, CO_2 and CO is another critical issue for on-board applications in order to maintain performance over the lifetime of a store material [47]. Both O_2 and N_2 slowed the rate of hydrogenation, while CO and CO_2 entirely prevented the uptake of hydrogen [48].

The incorporation of hydrides into a thin film form is discussed by Jain *et al* [49] as remedy to prevent interaction between hydrides and impurities. The main advantages of thin film metal hydrides are that these provide large surface area with fast charging discharging rate for hydrogen, pulverization is slower, both critical pressure and critical temperature are significantly lower, better heat transfer arrangements, protective surface coating could be used to stop poisoning by oxygen and activation of thin film hydrides is possible by coating with a layer of catalytic material.

To conclude it is not possible to say that there is a perfect choice of hydrogen store material to meet the set US DOE goals for transport applications. Although some results are encouraging, such as improved kinetics and lower decomposition temperatures for metal hydrides, further research is needed to develop materials satisfying the needs for technical applications. In the light of the achievements, there is a good potential skill in developing better hydride materials with high reversible

hydrogen capacity at ambient temperatures by combining physisorption and chemisorption.

1.3. Aims and scopes of the research

On the basis of the above depicted background in research on carbon nanostructures for hydrogen storage, the thrust of the research was to look into the interaction of hydrogen with metal doped carbon nanostructures covering these key points of interest. The aims of the research were:

1. To characterize a novel carbon nanostructure, such as carbon nanocones, a particular graphitic carbon nanostructure present in a shape of cone with difference angle from 0 ° to 60 ° that has received interest within the scientific community but whose application into the field of hydrogen storage has not been fully exploited. Such structure will be treated in details in the following chapter on section 2.2. Surface area measurement, morphology observation through transmission electron microscope (TEM), powder X-ray diffraction (XRD) and hydrogen uptake at 77 K and room temperature through intelligent gravimetric analyser (IGA) will be used with the aim of characterize the material.

2. Improving such structures towards an innovative material for hydrogen storage, ideally requiring milder conditions of de/hydrogenation in conformance with the engineering requirements for automotive applications [50]; the approach of an oxidative pre-treatment aims to improve the compatibility with a metal catalyst. Results of this procedure will be monitored by XRD in order to verify any chemical modification, by surface area analysis and transmission electron microscopy to verify if such treatment created some structural modifications and the hydrogen

uptake at 77 K will be measured and compared with the results of the pristine material.

3. To explore the synergistic contribution of a metal catalyst doping the surface to improve the hydrogenation at room temperature. Candidates in the literature are many: Pt [51], Pd [52], Ni [53], Co [54] with the Pd being the most largely used in literature and will be attempted other possible substitutes including a cheaper metal (Ni). The metal catalyst will impregnated over the carbon surface and then activated. The activation will be verified by XRD. The resulting dispersion will be observed by TEM in order to measure the cluster size. The surface area will be characterized and compared with that for the pristine material with aim to verify the influence of the presence of the metal on the surface. Furthermore, the hydrogen uptake will be measured and compared with that for the corresponding unloaded material to determine the contribution of the catalyst.

4. To verify the existence of a mechanism called hydrogen spillover for enhancing hydrogen storage capacity at ambient temperatures.

5. To combine reversible storage contribution from carbon nanostructure with a material with higher hydrogen capacity like MgH_2 and complex hydrides. It will be attempted to form magnesium hydride from an organometallic precursor such as dibutyl magnesium (DBM) and through thermogravimetric analysis (TGA), differential scanning calorimetry (DSC) mass spectrometry (MS) and Fourier transformation infrared spectroscopy (FTIR) will be attempted to quantify the stoichiometry and thermodynamics of formation. Dispersion of the metal hydride on the carbon nanostructure will be monitored with TEM to measure the cluster size. The reaction of dehydrogenation will be analysed by TGA and DSC in order to measure the hydrogen capacity as well as the enthalpy of reaction and the

dehydrogenation temperature in an attempt to link any changes on the thermodynamics of the dehydrogenation reaction with the effect of the mixture with the carbon nanostructure. Furthermore, the magnesium hydride formed in such fashion will be mixed with another hydride such as $LiAlH_4$ and the sequence of reactions during thermal decomposition and will be followed by DSC, TGA and FTIR with the aim of characterize the sequence of decomposition and verify if any improvement of the performances in terms of decrease of temperature of decomposition/dehydrogenation would occur.

1.4. Overview of the thesis

Chapter 2 will introduce more in depth the background literature relating to carbon nanostructures, showing the differences in terms of structure and introducing on carbon nanocones. From here the hydrogen storage published literature is reviewed with a final focus on the spillover mechanism and its applicability to hydrogen storage purposes. Futhermore, the published findings related to combination between carbon nanostructures and metal hydrides will be discussed.

Chapter 3 will provide an overview of the experimental methods used in this work, with a mention on the basis of each technique. In addition the methods of preparing carbon nanostructures, their initial treatment and finally their combination with metal catalysts are described. The characterization methods that were used to monitor the materials quality and their performances in hydrogen adsorption will also be explained in this chapter.

Chapter 4 reports the results for the characterization of the carbon nanostructure as synthesized, after an initial oxidizing pre-treatment and after impregnation with

various metal catalysts. The hydrogen uptake performance of the materials with different metal catalysts, both at 77 K and room temperature will be shown. Results are also presented of a novel attempt to mix carbon nanostructures with a high capacity metal hydride such as magnesium hydride and the characterization of the decomposition of the magnesium based complex hydride $LiAlH_4$:MgH_2.

Chapter 5 will discuss the performance improvements introduced by the different preparations of the materials under analysis. The results of hydrogen adsorption measurements of these materials will be explained in connection with the physical and chemical characteristics and such performances will be compared with other literature findings.

Finally the novel formation of magnesium hydride from the organometallic precursor DBM will be discussed and its enthalpy of reaction will calculated. Moreover, the route of decomposition of the complex hydride $LiAlH_4$:MgH_2 will be analysed and explained through combination of several analysis techniques such as TGA, DSC, FTIR and XRD.

The thesis will finish with conclusions and future work of the presented research.

2. Literature review

2.1. Scope

This literature review is concerned with the suitability of certain carbon nanostructures, like carbon nanocones, as hydrogen storage materials and the characterization of hydrogen adsorption performance in combination with various metal catalysts, specifically reviewing the literature on hydrogen spillover. Finally there is a short review of work which investigates combining carbon nanostructures with high hydrogen capacity metal hydrides to improve the kinetics and or thermodynamics for the system.

2.2. Types of carbon nanostructures of interest to hydrogen storage

The research for this PhD is focused on two main structures, graphite nanofibres and carbon nanocones, from a wide range of carbon nanostructured materials [55], e.g. activated carbon, multi-walled and single-walled carbon nanotubes, carbon nanofibres, carbon nanohorns and carbon nanocones. These structures have two dimensional conformations that range in the nanometer scale.

Activated carbon (AC) is a general term for carbon materials obtained by several methods such as carbonization [56], oxidation [57] or oxidation followed by steam or alkali-metal-assisted invigoration [58] of carbon containing materials. In general this material shows mix of mesoporous (pore diameter between 20 and 500 Å) and microporous structure (pore diameter <20 Å) and they are often used as

adsorbents for various substrates, for example toxic substances such as trihalomethane like in city water management.

Activated carbon (AC) is a general term for carbon materials obtained by several methods such as carbonization [56], oxidation [57] or oxidation followed by steam or alkali-metal-assisted activation [58] of carbon containing materials. In general this material shows a mix of microporous structure (pore diameter <20 Å) and mesoporous structure (pore diameter between 20 and 500 Å) (Figure 2.1) and they are often used as adsorbents for various substrates, for example removal of toxic substances such as trihalomethane in city water management.

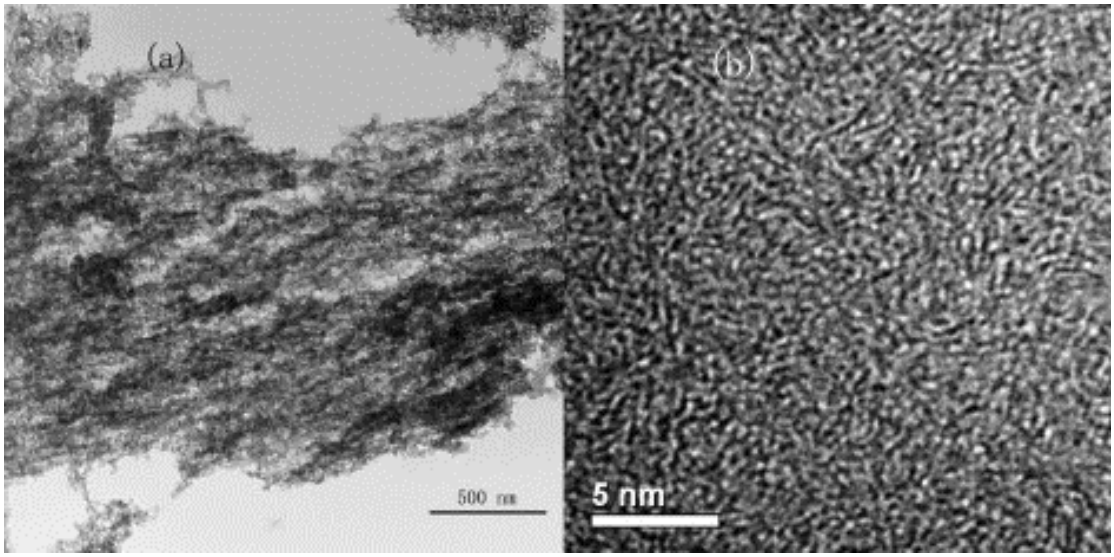

Figure 2.1 a) TEM and (b) HRTEM images of activated carbon prepared by activation with 50 wt% H_3PO_4 impregnation ratio of 5:1 and a carbonization process at 500 °C for 0.5 h [59]

The high surface area and chemical inertness of activated carbons have made these materials attractive as catalyst supports, each dedicated to a specific application,

such as CuO for adsorption of SO_2 [60], Mg, Ba, Pb, Cu and Fe and their binary mixtures with V for conversion of CO_2 to CO [61], Pd and Ni which can be used either in hydrodeclorination of wastewaters [62, 63] and hydrogen storage [64, 65].

Amorphous carbon nanotubes (CNTs) can be produced by DC arc discharge in an atmosphere of hydrogen gas at temperatures above 300 °C [66]. These nanotubes are hollow structures with an external diameter ranging from 10 nm to 15 nm. When there are number of concentric cylinders of graphene sheets they are called multi walled carbon nanotubes (MWCNT) (Figure 2.2). The number of concentric cylinders can vary from two to several tens, with external diameters up to 100 nm. The walls are spaced by 0.34 nm similar distance to that for the intergraphene distance as evidenced in [67]

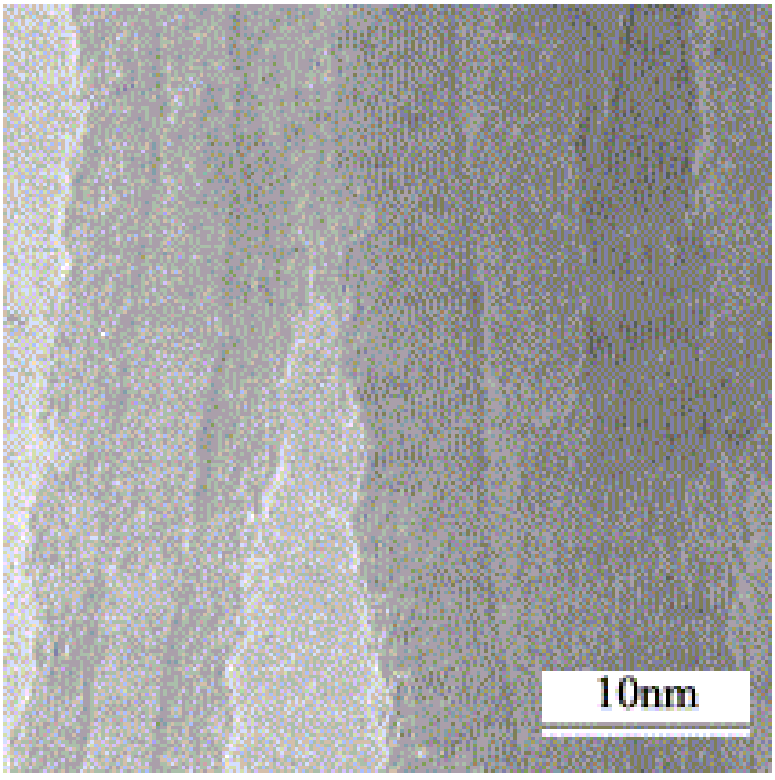

Figure 2.2 TEM image of multi walled carbon nanotubes [68]

The first evidence that these nanofilaments were carbon nanotubes is reported in 1959 in the work of Hillert and Lange [69] using transmission electron microscopy (TEM).

Single-wall carbon nanotubes are made of a single graphene sheet. Such a sheet is considered a mono-atomic layer made of a hexagonal network with sp^2 hybridized carbon atoms, rolled up into a cylinder and closed at the extremities by hemispherical fullerenes [70] (Figure 2.3). The internal diameter of these structures can vary between 0.4 and 2.5 nm and the length ranges from a few microns to several millimetres.

Pores in MWCNT can be mainly divided into inner cavities of small diameter distributed between 3 and 6 nm and voids resulted from the aggregation of single fibres which have a distribution between 20 and 40 nm [71, 72]. The latter according to Yang [68] contribute as well to the nitrogen adsorption at the surface area analysis. Experimentally, the specific surface area of SWCNT is often larger than that of MWCNT the former having a between 400 and 900 $m^2 g^{-1}$ (micropore volume, 0.15–0.3 $cm^3 g^{-1}$) whereas, for MWCNT the total surface area ranges between 200 and 400 $m^2 g^{-1}$ [68] being the diameter of the tubes is the main factors that influence the BET value [68].

Electronic properties are mainly governed by the tube diameter and the helicity, which is the way in which the graphene layer is rolled up [73] which are called: armchair, zigzag or chiral (Figure 2.3).

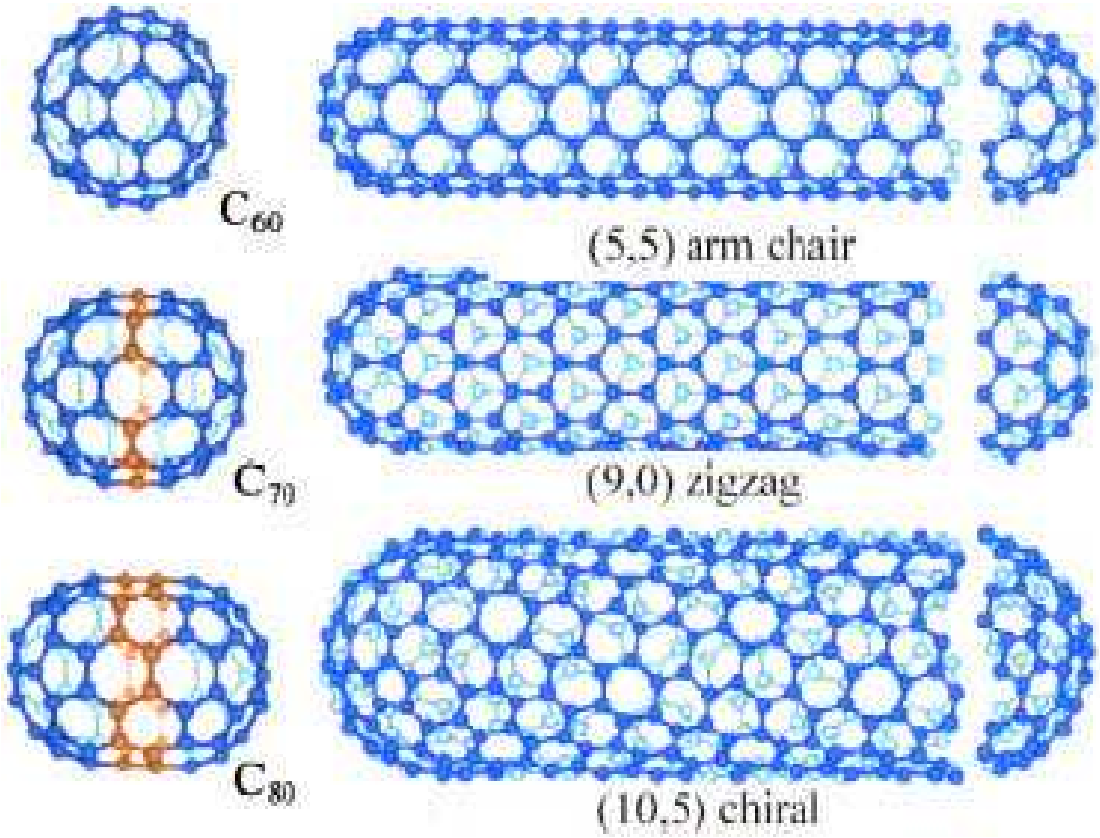

Figure 2.3 Nanotube geometries: armchair (top), zigzag (middle), chiral (bottom) [74]

For example armchair and chiral SWCNT has metallic-like behaviour whereas the zigzag displays a semi-conductor behaviour because the curvature of the sheet modifies the electronic behaviour, opening energy gaps.

A geometrical model of how those conformations are generated has been extrapolated starting from a plane graphene sheet [75]. The geometrical parameter deciding the conformation is called the rolling up vector (C)

$$C=na_1+ma_2=(n,m) \qquad \text{(eq. 1.1)}$$

where a_1 and a_2 are the primitive lattice vectors of the graphene and n and m are integer numbers (Figure 2.4.).

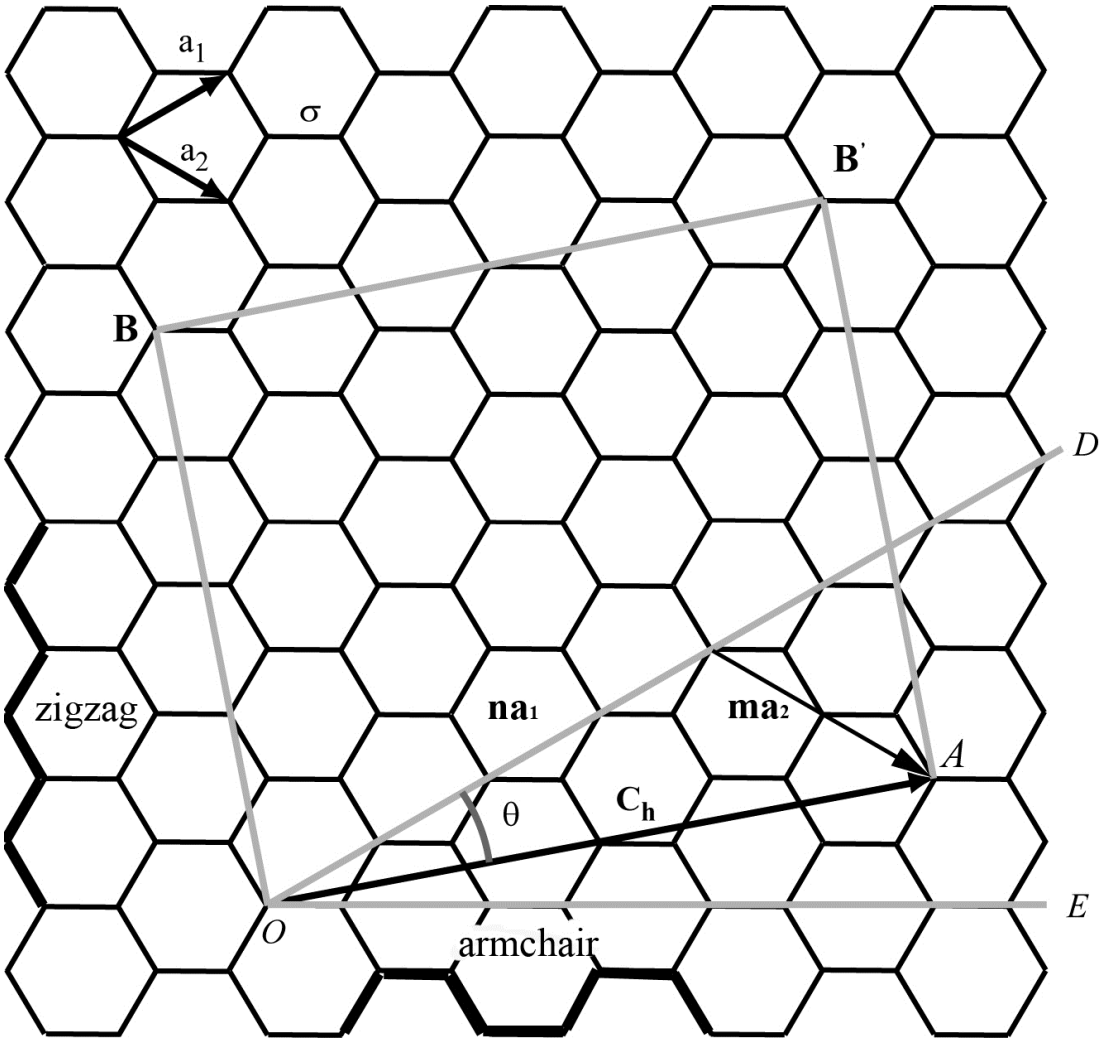

Figure 2.4 Schematics of the generation of a carbon nanotube by folding a section of graphene sheet [75]

SWNTs will be armchair for the pair (n,n), zigzag for (n,0), and chiral for (n,m) with $n \neq m$. SWNTs are metals when $\frac{(n-m)}{3}$ is an integer, otherwise they are semiconductors [76].

It has been theoretically predicted that electronic properties can be also modified by the presence of vacancies, impurities or defects of the hexagonal network that in the rearrangement would form pentagons and heptagons [77]. It has been demonstrated that the binding sites of transition metal atoms with CNT change

depending on the structure of the support: the curvature affects the values of magnetic moments on the metal atoms on the nanotube wall and the charge transfer direction between metal and carbon can be inverted [78].

CNT can be chemically modified and functionalised in order to improve their characteristics. For examples friction reduction and anti-wear ability of MWNTs are improved by functionalization with fatty acid when MWCNTs are used as lubricant additive [79]; or the emission current density increasing (J) from 2.5 mA cm^{-2} for the pristine CNT to 7 mA cm^{-2} at 5 V μm^{-1} for the oxygen plasma treated and the threshold electric field are improved when opening the tips of the tubes and introducing defects thanks to a combination of oxygen plasma, nitric acid, and hydrofluoric acid treatment [80]; or the synthesis catalyst is removed and the internal surface of the tube is exposed by shortening the length and opening the ending by immerging the CNTs in diluted HNO_3 solution with ultrasonic then milling by ball at a high velocity [81]. Coupling such structure with catalyst is also quite popular especially in field of wastewater purification using Ru [82], oxidation of carbon species such as CO and methanol is performed using Pt [83] or Pt-Ru [84], dehydrogenation is accomplished with Fe_2O_3 [85] or hydrogen generation with Co [86].

Graphite nanofibres (GNF) are a graphite structure obtained for the first time in 1990 by Murayama [87]. They were prepared by the catalysed decomposition of carbon-containing gases over selected metal and alloy surfaces at temperatures in the range 450−750 °C. The catalysts used to grow the graphite nanofibres are usually bimetallic, e.g. Ni–Cu or Fe–Cu, with Ni-base being a more active base than Fe-base [88].

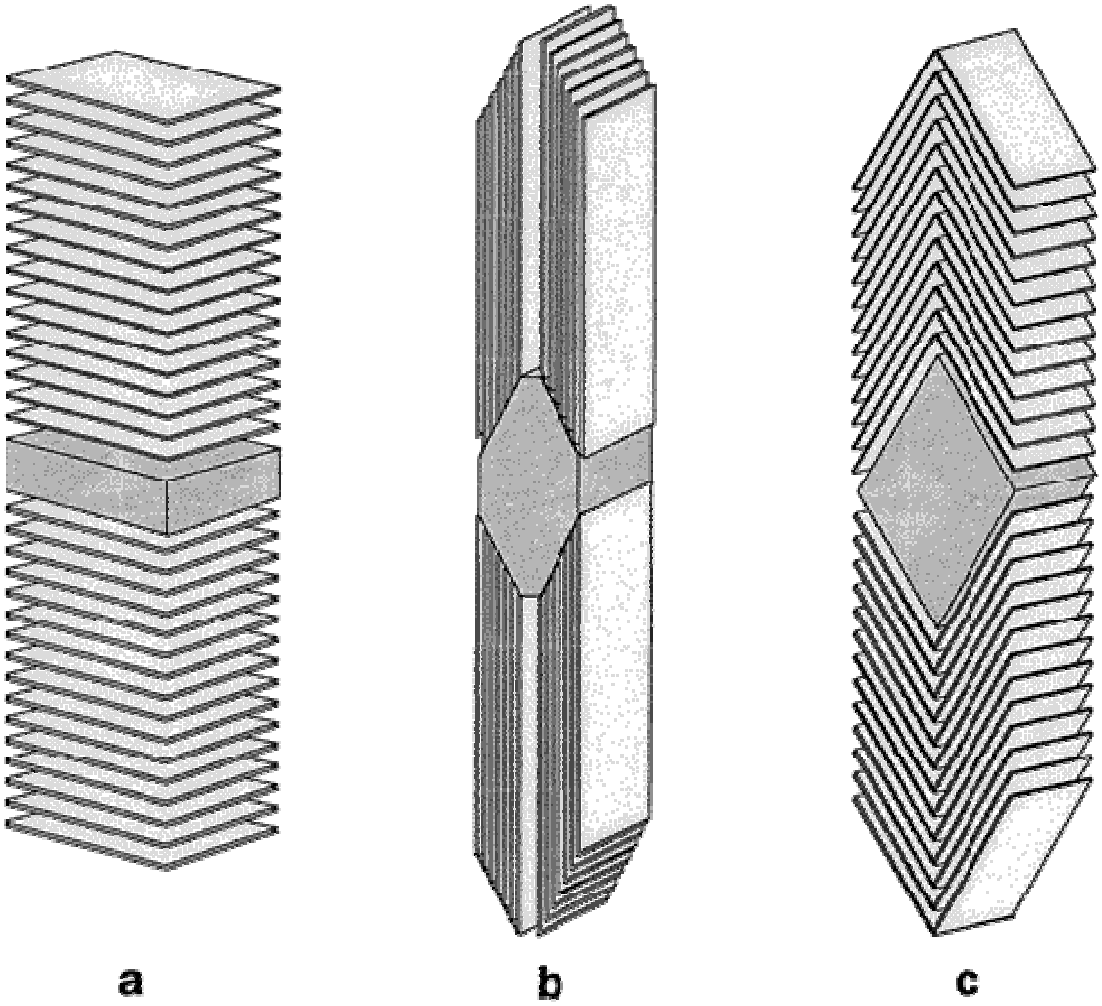

Figure 2.5 Representative TEM images of the different type of GNFs: (a) platelet, (b) ribbon, (c) herringbone [89]

GNF can be synthesized into three types: platelet graphite nanofibres where graphene layers are perpendicular to the fibre axis [67] (figure 2.5 a); ribbon graphite nanofibres where graphene possesses a structure in which the graphene sheets are oriented in a direction parallel to the growth axis [90] (figure 2.5 b); herringbone (or cup-stacked) graphite nanofibres where the graphene layers are tilt and truncated conically along the fibre length [91, 92] (figure 2.5 c and figure 2.6).

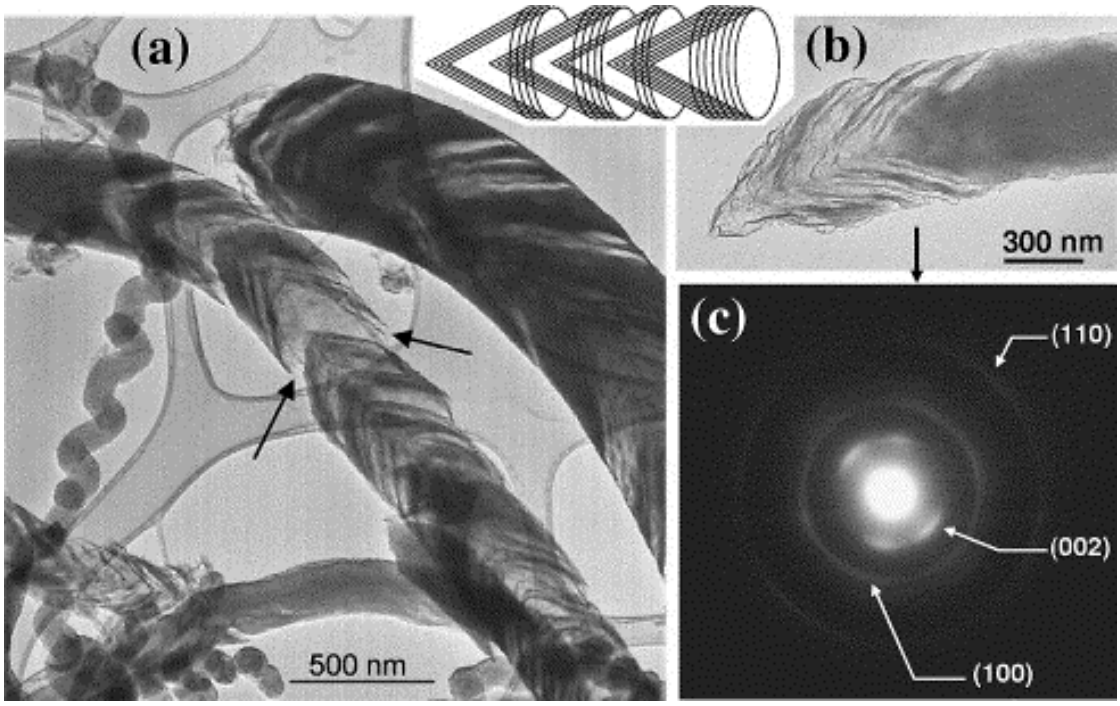

Figure 2.6 TEM images of herringbone GNF after exfoliation (a and b). (c) shows the selected area diffraction pattern of the nanofibre in (b) [91]

The diameter, length, and graphene layer arrangement can be controlled by synthesis conditions using various hydrocarbons, metal catalysts [93], and temperatures [94].

The diameters of GNF are generally larger than those of nanotubes and can reach 500 nm and a cross-sectional area that varies from 0.3 to 5.0 nm^2 (30 to 500 $Å^2$) [67]. GNFs have good elastic properties (Young's modulus: 150–600 GPa, maximum tensile strength: 1–3 GPa) [95] and high electrical conductivity (specific resistivity: 10^{-3} – 10^{-2} Ω cm^{-1} [96]). The mechanical properties are exploited in the field of composite materials where impact strengths are improved considerably by the inclusion in the composites of just 1–5 wt% GNFs in the glassy polymer poly(methyl methacrylate) (PMMA); it also lowered thermal shrinkage compared with the pristine

polymer and increased the thermal decomposition temperatures of composites [97]. Furthermore, the high density of edge plane defect sites on the graphite nanofibres makes such conformation much more favourable for electron-transfer reactions than the basal plane sites enhancing the electrochemical activities. This implies a promising application in paste electrode for high sensitivity amperometric detection of hydrogen peroxide and NADH with wide linear ranges and low detection limits [98].

Carbon nanohorns can be produced by the CO_2 laser ablation of carbon at room temperature without a metal catalyst [99]. They belong to the same family of materials as single-walled carbon nanotubes [99] and individual nanohorns are a single-layer graphene sheet wrapped into an tube with a diameter of between 2 and 5 nm and a length of 30–50 nm [100-102] but the tips are cone-shaped with an average angle of ca. 20° [100, 101] (figure 2.7 b).

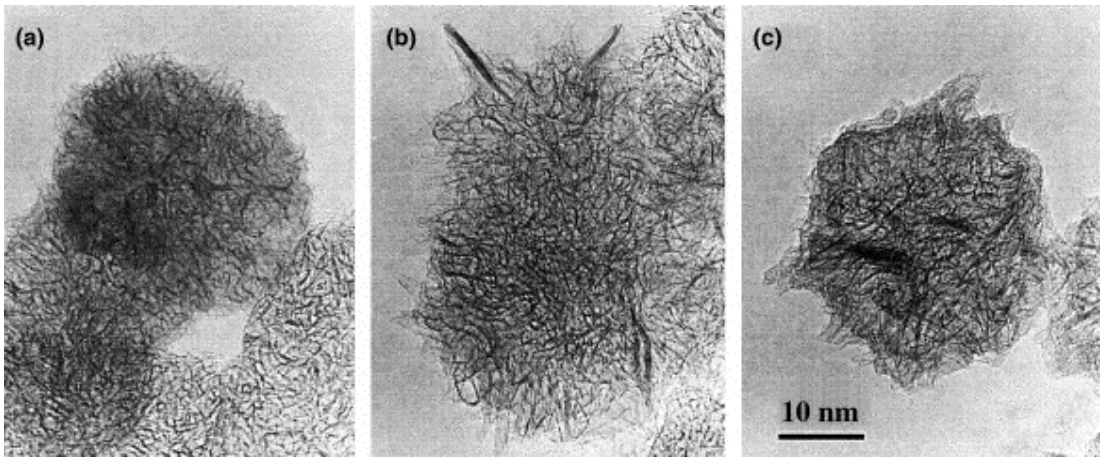

Figure 2.7 Electron micrographs of SWNHs generated from carbon rods pre-heated at: (a) RT; (b) 1000 and (c) 1400 °C [99]

Carbon nanohorns do not pack into ropes like nanotubes, but they from spherical aggregates that have diameters of around 50–100 nm [100-103] (figure 2.7). Different types of nanohorns aggregates can result depending on the conditions present during

their production (i.e. the type of inert gas used, its pressure, the effective temperature of production, etc.) [104]. Dahlia-like aggregates where the tips are clearly visible at the surface of the spheres [104] or bud-like aggregates where there are no horns on the surface and the tubular structures are shorter [104].

The main trend in research in carbon nanohorn is toward use of this material for practical applications, for example in gas storage like in the work of Yang [105] where the adsorption of methane can reach from 2 wt% to 11wt% after a HNO_3 treatment of H_2O_2/H_2SO_4. Another field of exploitation is the development of more effective substrates for nanoparticle catalyst supports as described by Murata [106] where EuPt has been dispersed homogenously with a particle size of 1.7 nm.

Nanocones belong to the family of nanohorns and have an interesting novel structure which has raised interests due to its unusual electronic properties such as unusual effective magnetic and electric-field configurations. In fact by orienting a magnetic field perpendicular to a cone's axis an effective field can be produced which changes sign from one side of the apex to the other [107]. Carbon nanocones are produced in an industrial process that decomposes hydrocarbons into carbon and hydrogen with a plasma torch having a plasma temperature above 2000 °C [108]. Another interesting features are the improved field emission properties like field emission current density (J) of 173 mA cm^{-2} at 10 V μm^{-1} [109] compared with the above mentioned CNT which was 2.5 mA cm^{-2} for the pristine CNT at 5 V μm^{-1}. The cone angle is determined by the number of pentagons at the tip, yielding five discrete cone angles (19.2 °- 5 pentagons, 38.9 ° - 4 pentagons, 60 ° - 3 pentagons, 83.6 ° - 2 pentagons, and 112.9 °- 1 pentagon) [50, 108] (figure 2.8).

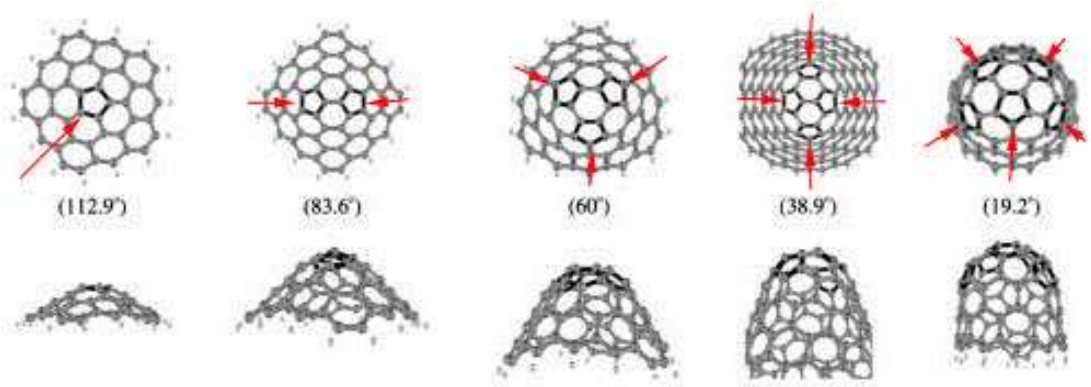

Figure 2.8 Top and side views of the predicted topologies on the conic tips of carbon nanocones [110].

The length of the nanocones varies between 300 and 800 nm with a maximum base diameter between 1 and 2 μm. The wall thickness is in the range 20–50 nm. Carbon discs are typically 0.8–3 μm diameter and of 20–50 nm thickness [111]. Some nanocones are similar in shape to nanohorns, which have long cone-shaped tips with cone angles of about 20° and diameters of about 2–4 nm. Open and closed ends of the carbon nanocones are predicted to have a difference in their electronic structure [112] and these materials may offer more favourable sorption sites. In the study on hydrogen adsorption of Yu [113] the mixture of disc-cones rich in discs showed at the temperature programmed desorption (TPD) analysis a maximum dehydrogenation peak at 250 K. Such desorption is shown to change with the increase of hydrogen volume the sample has been exposed to. This desorption peak is attributed to hydrogen physisorption. Hydrogen chemisorption has be excluded since the desorption temperature of chemisorbed hydrogen is expected to be much higher (>400 K) [114]. Yu measured the work function relative to the Fermi level with the change of the hydrogen volume the material was exposed to. After larger exposures of molecular hydrogen, the value of the work function changes less. At this stage nearly

all available positions on the carbon cones have been occupied by molecular hydrogen and the adsorption of hydrogen on the carbon cone sample has nearly reached saturation. The observed changes in the work function with adsorption of hydrogen indicate chemisorption-like bonding where surface dipoles are formed. In fact the physisorption of hydrogen is not expected to result in a change in the work function due to the absence of a surface dipole However, from Yu TPD results, the adsorption on carbon nanocones is argued to form relatively weak bonds. The author postulates that there might be a relatively weak interaction between molecular hydrogen and carbon cone substrate, which is similar to that of chemical C–H bonding.

Carbon nanomaterials have been widely studied in the attempt to improve their adsorption via modification of their physical and chemical characteristics. The modifications of textural properties can have a profound effect on surface area (table 2.1).

Table 2.1 Examples of different activation processes to improve textural properties of carbon samples.

Activation Technique	**Physical characteristic improved**	**Changes in physical characteristic**	**Ref**
Oxidation with N_2O	Specific surface area	Specific surface area +72%	[115]
Heat treatment by steam or methane and stream at 1000 °C	Micropore and mesopore volumes	Micropore volume (+50–70%), mesopore volume (+65-90%)	[116]
Heat treatment with CO_2 flow	Specific surface area	+ 1000% (from 130 m^2g^{-1} to 1341 m^2g^{-1})	[117]

AC surfaces can display acidic, basic and/or neutral characteristics depending on the presence of surface functional groups [118]. Surface functional groups on the surface of AC are defined as bridging links in the defective hexagonal carbon layer

planes (typically 5 nm wide) of the AC twisted network [119]. Heteroatoms can be incorporated into the network and also to the periphery of the planes. The existence of surface functional groups on the carbon matrix can be manipulated by thermal or chemical treatments (table 2.2).

Table 2.2 Examples of studies to chemically modify ACs

Researchers	**Type(s) of surface functional group created**	**Technique used**	**Metal species removed**	**Effect on adsorption capacity**
Gomez-Serrano *et al*. [120]	Sulfur-based (C–S, S–S, C═S and S═O)	Heat treatment in H_2S	Mercury (as $HgCl_2$)	Increased by 140% (approximation)
Park and Jang [121]	Weakly acidic	Treatment using hydrochloric acid	Cr(VI)	Increased by 170%
Vladimir and Malik [122]	Weakly acidic (carboxylic, lactonic, phenolic and carbonic)	Oxidization using nitric acid	Cu^{2+}, Mn^{2+}, $Ni^{2+}$and Zn^{2+}	Increased by up to 400%(for Cu^{2+})
Yantasee *et al*. [123]	Amine ($–NH_2$)	Electrophilic aromatic substitution of nitro groups onto AC followed by reduction of $–NO_2$ to $–NH_2$	Cu^{2+}, Pb^{2+}, Cu^{2+} and Ni^{2+}	Distribution coefficient, K_d was increased by up to 140% (for Cu^{2+}) and 400% (for Pb^{2+})

Treatments to improve the chemical characteristics of AC may also negatively affect its physical characteristics as illustrated in (table 2.3).

Table 2.3 Technical advantages and disadvantages of modification techniques [124]

Modification	Activation Treatment	Advantages	Disadvantages
Chemical characteristics	Acid	-Increases acidic functional groups on AC surface. - Enhances chelation ability with metal species	- May decrease BET surface area and pore volume - Has adverse effect on uptake of organics - May give off undesired SO_2 (treatment with H_2SO_4) or NO_2 (treatment with HNO_3) gases
	Basic	Enhances uptake of organics	May, in some cases, decrease the uptake of metal ions
	Impregnation of foreign material	Enhances in-built catalytic oxidation capability	May decrease BET surface area and pore volume
Physical characteristics	Heat in CO_2 flow	Increases BET surface area and pore volume	Decreases oxygen surface functional groups

2.3. Hydrogen physisorption

Carbon-based nanoporous materials have promising potential as adsorbents for hydrogen. They may be optimized for hydrogen storage through various physical and chemical treatments.

The three parameters to optimize are: the binding energy of the hydrogen molecule with the material, the available surface for adsorption processes and the bulk density of the adsorbate [125]. Research has been concentrated on increasing the available surface area modulating the texture of the material.

Microporous materials typically have pore sizes in the range of 1–10 nm. Hydrogen molecules can enter these pores and interact with the material via van der

Waals forces. The strength of the interaction between hydrogen and the adsorbent is expressed by the isosteric heat of adsorption. Due to this being a very low interaction strength for hydrogen on carbon surfaces of 4-6 kJ mol^{-1} [126], at low molecule concentration, hence at low pressures, only those molecules very close to the surface of the pores can efficiently interact by van der Waals forces, eventually forming a monolayer of hydrogen molecules when there is a high enough pressure. Therefore the adsorption capacity of a microporous material is proportional to its surface area, which will increase with increasing porosity. Most adsorbents have pores significantly larger than 0.6 nm (twice the kinetic diameter of a hydrogen molecule) and the remaining pore space can be filled with hydrogen gas at appropriate pressure and temperature. Furthermore, adsorption materials are mostly available in powder form that will have additional interparticle void space, which can also contain hydrogen gas. Therefore the total capacity of an adsorbent is the sum of the adsorbed hydrogen and the hydrogen gas contained in the pores and the interparticle voids. If the interparticle void space is known, then the total hydrogen in the system is simply the sum of the excess gas plus the gas that would normally occupy that volume at that temperature and pressure.

The typical absolute supercritical hydrogen adsorption isotherm is characterized by a steep increase in hydrogen uptake at low pressure while at higher pressure the capacity reaches a plateau and further increase of pressure will not lead to an increase of capacity. This is called type I or Langmuir isotherm [127]. No multilayer is formed because the interaction strength between single layers is too weak at temperature higher than the critical temperature of hydrogen [128].

On the other hand the excess isotherm, measured experimentally as the weight gain in the gravimetric analysis, does not have a plateau but a maximum at a certain

pressure. It then decreases with further increases of pressure. That is when the gas adsorbed in the pores saturates while the gas density increases. For this reason the excess adsorption can be zero or even negative at very high pressure or low temperature. An example of the excess uptake and absolute uptake is shown in figure 2.9.

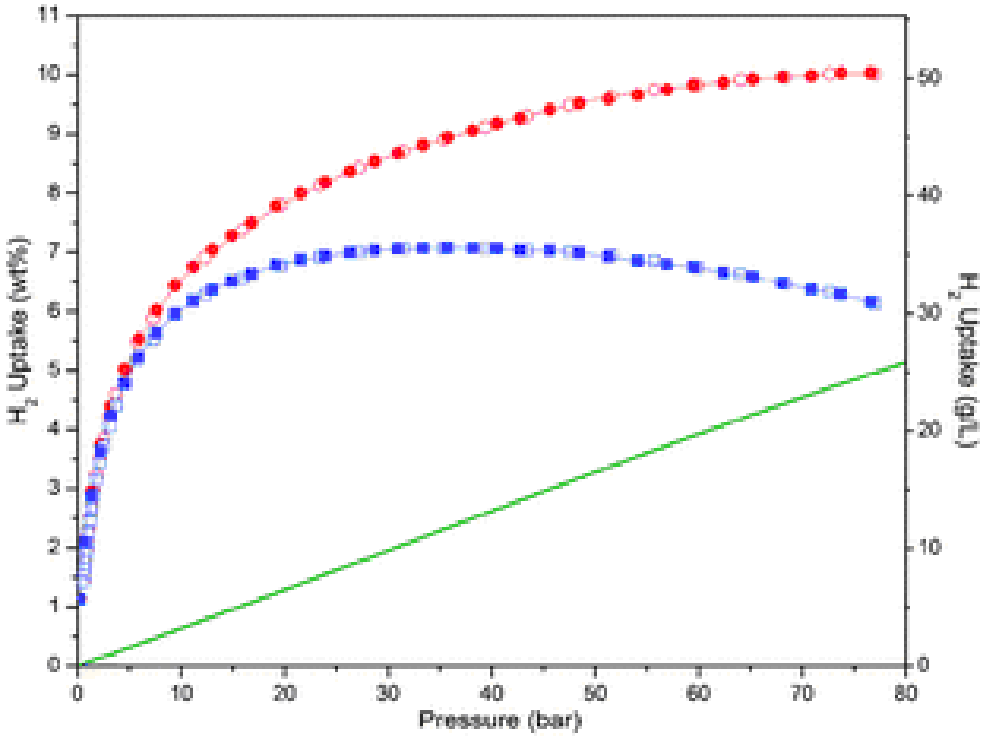

Figure 2.9 High pressure excess hydrogen adsorption isotherms at 77 K (by volumetric method) are shown as red circles (total uptake) and blue squares (excess uptake). The solid olive line indicates the density of H_2 gas at different pressures (right-hand scale). Filled symbols indicate adsorption and open symbols indicate desorption. [129]

Theoretically, the excess uptake would become zero, if the bulk hydrogen gas is compressed to the same density as the adsorbed layer. With such assumption for the

density of the adsorbed layer its volume can be calculated and the hydrogen uptake can be corrected. This gives the so called absolute uptake value.

The correlation between the hydrogen uptake and the specific surface area has been established in the studies of several research groups [29, 130-132]. In the study by Schimmel [131] compared the interaction of hydrogen with several carbon nanostructures such as: activated charcoal, carbon nanofibres, single walled carbon nanotubes (SWNT), and electron beam 'opened' SWNT. The storage capacity below 77 K of these materials correlates with the surface area of the material with the activated charcoal having the largest. The interaction potential, extrapolated from the pressure–temperature curves was found to be <4.8 kJ mol^{-1} in all samples, leading to significant adsorption below 50 K. The author concluded that the morphology of the adsorption sites at more than one carbon bond distance has less importance stating thus, that different forms of carbon interact in the same way with hydrogen molecules as long as they possess the characteristic aromatic carbon rings. The amount of hydrogen storage is governed by the number of accessible aromatic carbon bonds in the sample, which is related to the surface area. In his work Texier-Mandoki [130] compared the hydrogen adsorption of different carbon nanostructures and the CO_2 adsorption at 273 K. They found a linear relation between the hydrogen adsorption capacity and the CO_2 micropore volume. This means that microporosity is a way of increasing the amount of surface area, that is there is still a linear correlation between surface and uptake.

2.4. Spillover mechanism

2.4.1. Reported results

Very promising publications reporting high hydrogen storage capacities in carbon nanotubes [133, 134] resulted in an enormous research activity summarised in figure 2.10. In particular Dillon *et al*. [135] developed an opening and cutting procedure for the nanotubes and measured a storage capacity of about 7 wt% for purified SWNTs after loading at 0.7 bar and at room temperature after heating to 900 K in a high vacuum. However, the temperature of hydrogen release was now significantly higher (two maximum peaks measured at 450 and 600 K) compared to their former investigations (single maximum at 300 K). The opening and cutting method developed was a high-power sonication in HNO_3, leading to the contamination of the sample with metal particles from the sonicator probe [136] composed of 90 wt% Ti, 6 wt% Al, and 4 wt% V. The authors suggested that introducing the Ti alloy particles stimulated hydrogen adsorption on the SWNTs. Subsequently Hirscher's research team tried to reproduce the experiments of Dillon *et al*., but obtained contrasting results [137]. Those carbon materials treated by the Ti alloy sonicator horn indeed showed adsorption but no hydrogen desorption (below 0.005 wt%) was observed if the SWNTs sonicated in contact with stainless steel balls. The maximum storage capacity reported by Hirscher was 1.5 wt% in purified SWNTs sonicated with a Ti alloy horn for 24h. Assuming that all hydrogen is stored in the Ti alloy particles, the hypothetical hydrogen content of the metal particles lies in the range 0.4–3.3 wt%, which is comparable to the storage capacity of the Ti alloy of 3.4 wt%. In a later report [138] Dillon applied an unknown cutting method, which

would avoid contamination by metal particles, and reported a hydrogen content below 1 wt% and 340 K.

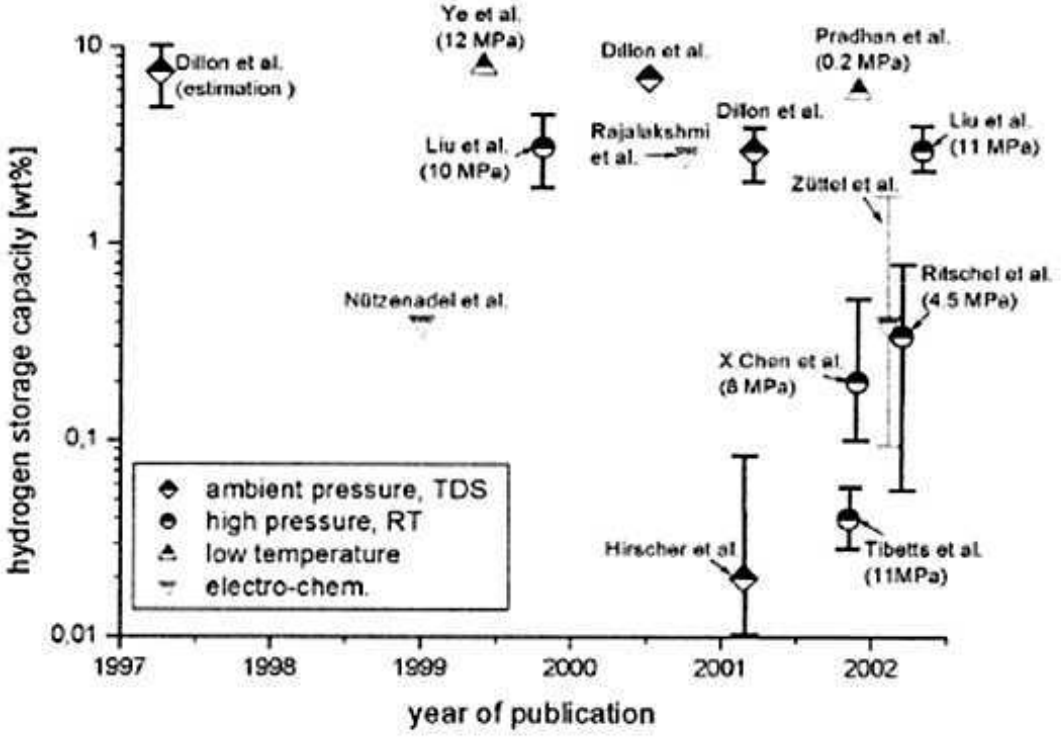

Figure 2.10 Summary of the scatter in the hydrogen storage capacity of carbon nanostructure reported in literature [137]

There are a number of reports of surprisingly high uptakes of 10 wt% at RT and 120 bar for graphitic nanofibres [139] and 4.2 wt% for single walled carbon nanotubes at RT and 1000 bar [140]. On the other hand, there are other reports where the hydrogen uptake reaches close to the theoretical contribution from the metal hydrogenation plus hydrogen physisorption onto the carbon surface, e.g. graphite nanofibres decorated with 10 wt% palladium stored 0.12 wt% of hydrogen at 650 bar [141] where the hydrogen adsorption of the bare carbon substrate was 0.01 wt% and the theoretical contribution of the palladium catalyst was 0.072 wt%.

In fact this hydrogen spillover variation illustrated in figure 2.10 has led to debate because of their non-reproducibility, such as in the case of Hirscher attempt to replicate Dillon experimental results. The potential for cumulative errors in measurement shows experimenters must be careful. Common problems are presence of gas impurities like moisture [142] especially in conjunction with utilization of heterogeneous carbonaceous materials (metal doping, substitution, intercalation), small sample size, compressibility of hydrogen according to the real gas law and attempting to measure small margins of improvement which are within the errors of measurement.

Gas impurities have been revealed as source of erroneous hydrogen adsorption measurement. Yang *et al*. in their work [142] underline how a drying pre-treatment is necessary when the material is composed by elements sensitive to oxygen which would lead to anomalous weight increase that could be mistaken for hydrogen adsorption. Yang re-evaluated the work of Chen *et al.* [143] reducing the hydrogen capacity from 14% down to 2% for a Li doped carbon nanotubes.

An example of how the magnitude of spillover capacity reported from one research group has reduced with time is given in figure 2.11 showing the work of R.T. Yang and the hydrogen uptake results through the years (also summarised in Table 2.4). It is possible to see the claim of 3.7 wt% hydrogen uptake in 2004 has reduced to only 1.1 wt% in 2009.

Table 2.4 Summary of Yang *et al* [142] results for hydrogen spillover uptakes reported through the years.

Year	Uptake (wt%)	Material	Temperature (K)	Pressure (bar)	Ref
2004	3.7	MWCNT + NiMgO	298	69	[144]
2005	1.8	AX-21/carbon bridge + 5wt% Pd	298	100	[145]
2007	1.2	SuperAC + 5.6 wt % Pt	298	100	[146]
2008	0.83	Norit activated carbon (NAC), 3 wt% Pt	298	100	[147]
2008	1.35	Pt 6% on templated carbon	298	100	[148]
2009	1.1	Superactivated Carbon doping with 6 wt % Pt and 2 wt % $TiCl_3$	298	100	[149]

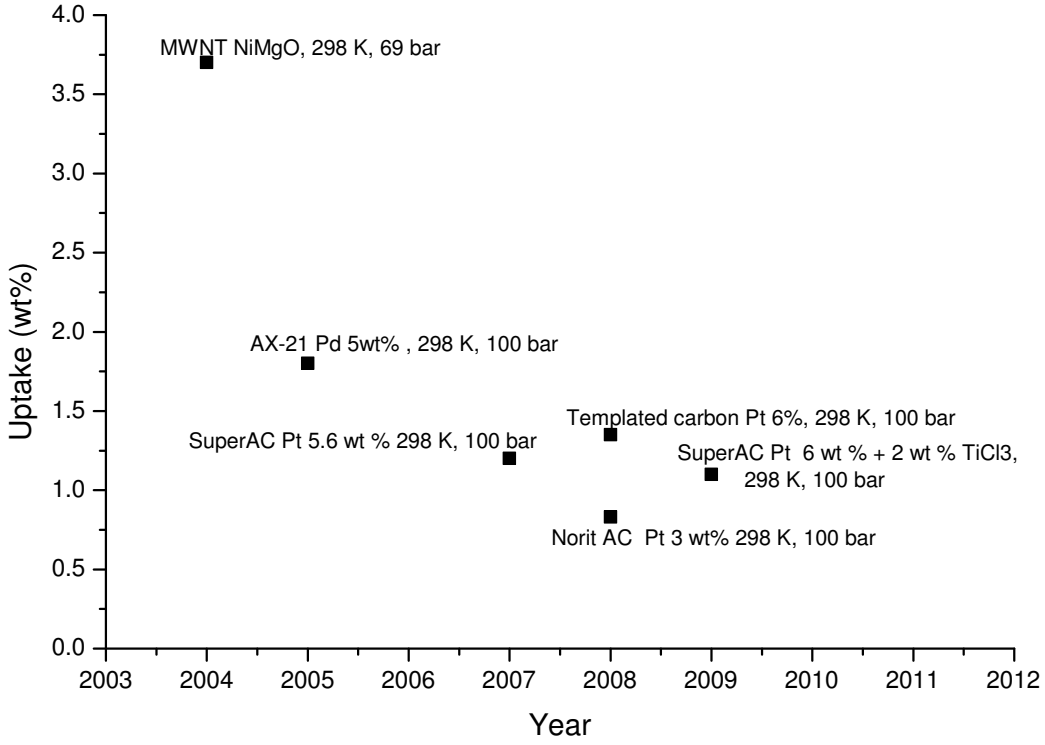

Figure 2.11 Trend of results in works of R.T. Yang *et al*. [142]

Ultimately the scepticism is not towards the existence of hydrogen spillover but towards how a mechanism known in the field of heterogeneous catalysis could really contribute as synergetic effect to hydrogen storage. In order to clarify certain

objections, it is wise to focus on the two fundamental features of hydrogen spillover: the contribution of the metal catalyst and the theoretical model of hydrogen migration.

Having an insight of the latter will help to verify if it is feasible that a stable species of atomic hydrogen can stay bonded to the surface without recombination, on the surface, into a hydrogen molecule that then would desorb. This concept is the core difference between hydrogen spillover in a catalytic assisted reactions where the generated atomic hydrogen is desired to react with another reagent to form a new product (hence is only a transitory species) and hydrogen spillover for hydrogen storage where the atomic hydrogen is not desired to recombine with anything.

2.4.2. Different types of metal/carbon system

The strategy here has been to decorate the surface with metal species that either add more binding sites, improve the adsorption capacity of the surface through electronic interactions, or both. Computational studies suggest that transition metal atoms, especially low atomic transition metals in low oxidation states, can bind to fullerene like surfaces via the Kubas interaction, to form stable media for hydrogen storage [150].

There has been a lot of interest in these catalysts on carbon materials to dissociatively adsorb dihydrogen leading to a spillover of hydrogen atoms onto the support. The catalysts mostly used for hydrogen storage are those belonging to the platinum group in the periodic table and especially palladium. The equilibrium pressure of palladium hydride phase at room temperature is below 0.01 bar much below the 10–100 bar range (where the H uptake by carbon nanostructure is of interest) [151]. Once a carbon nanostructure is coupled with palladium metal the hydrogen storage capacities can be 30 % greater than the original samples for carbon

nanotubes due to the formation of palladium hydride[152] and in general palladium can bring consistent enhancements in the hydrogen uptake [153-156].

It is reported by Park *et al.* that the presence of platinum group metal catalysts on carbon materials can enhance the hydrogen storage capacity by the hydrogen spillover contribution [157]. Platinum [158], vanadium [152] and palladium [159] can increase the hydrogen storage as much as twice the performance registered with the initial material increasing the hydrogen uptake from 1.48 wt% to 3.72 wt% in the case of the latter.

Some examples of studies of coupling carbon nanostructures with Pd, Ni and Cu are summarized in table 2.5.

Table 2.5 Examples of hydrogen uptake results using Pd and non-Pd group metal as catalysts

Material	Uptake (wt%)	Conditions (298K, bar)	Reference
Pd			
multi-walled nanotubes with a Pd 13 wt%	0.18 wt%.	16 bar	[160]
Pd 2.5 wt% doped-multi-wall carbon nanotubes	0.66 wt%	20 bar	[152]
Ni			
graphite nanofibres with Ni 5.1 wt%	2 wt%	100 bar	[161]
activated carbon 1wt% nickel	0.53 wt%	30 bar	[162]
carbon nanospheres with 5 wt% Ni	0.42 w%	90 bar	[163]
Cu			
Activated carbon and Cu	0.69 wt%	100 bar	[164]

The graphite phase interacts strongly with transition metal atoms and this interaction has strong variations of the hybridization strength between carbon p_z and the transition metal *d* orbitals [165, 166]. For example it was found [160] that multi-walled nanotubes with a Pd 13 wt% loading achieved at 298 K and 16 bar a hydrogen

uptake of 0.18 wt%. Another work [152] shows an increase in hydrogen storage capacity of 0.13 wt% from 0.53 wt% for the pristine material to 0.66 wt% for 2.5 wt% Pd doping.

Similarly, nickel nanoparticles on carbon nanotubes can also enhance the hydrogen storage capacity [161, 167]. Transition metals with similar electronic configuration as nickel can interact with hydrogen molecules at the metal surfaces inducing a partial polarization of the hydrogen molecules, then the molecules are accelerated and dissociate to form energetic bonds at metal–carbon interfaces. In the study of Kim *et al.* [161] it was found that increasing the nickel content also increased the amount of hydrogen stored by 2.2 wt% on a sample of graphite nanofibres with nickel metal content around 5.1 wt%. The results reported by Zielinski [162] claim that hydrogen adsorption can happen at room temperature with nickel catalysts provided the pressure used is high enough and that this hydrogen can be reversibly adsorbed and desorbed under room temperature and atmospheric pressure. However, their results showed that there is no correlation between the metal surface area and the hydrogen storage capability of the catalyst.

Another study by Zubizarreta [163] reported that the presence of Ni produces an increase in hydrogen storage capacity at moderate temperatures. At room temperature the maximum hydrogen storage capacity of 0.42 wt% was reached when 5 wt% of Ni was deposited onto the carbon nanospheres compared with the hydrogen uptake of about 0.20 wt% of the carbon substrate alone. It was observed that for higher Ni content (10 and 15 wt% of Ni) the gain in hydrogen storage capacity decreases. Samples doped with 10 and 15 wt% gave two endotherms one at 75 °C and the second one at 280 °C - 370°C depending on the metal content. The first reported peak corresponds to hydrogen adsorbed on the Nickel but not interacting

with the carbon support [168]. The second peak was attributed to hydrogen that was more tightly adsorbed, which was assigned to the spillover mechanism. The author also explains that this interaction with the support is promoted by the presence of oxygen surface groups introduced by air oxidation. However, the author seems to neglect that the ultimate receptor of atomic hydrogen spread on the surface are those basic sites with low point zero charge so the amount of extra capacity is due to them rather than the strong or weak interaction between nickel and the substrate. Furthermore, the decrease of hydrogen uptake with higher metal content is not due to the deactivation of the catalyst but due to the higher surface coverage by the catalyst that means fewer oxidized sites on the support to bond with the atomic hydrogen.

Other transition metals like copper are potential candidates to improve hydrogen storage. In the work of Park *et al.* [164] the activated carbon fibres sample electroplated with Cu for 30 s obtaining a Cu particle dispersion of 200-300 nm was found to store 84.7 cm^3g^{-1} (equivalent to a hydrogen uptake of 0.69 wt%) of hydrogen at 100 bar and room temperature. Their results shows that the adsorption and desorption isotherms are the same with almost all the hydrogen desorbed at 298K. The author based the mechanism of spillover on the work of Li and Yang [169] stating that there is formation of metal hydrogen bond. However, the author neglect to consider that in the work of Yang the catalyst used was a mix of platinum and copper and that the platinum can easily form a hydride enhancing then the hydrogen uptake. Furthermore, Park does not consider that the activity of copper in hydrogen spillover that he reported is referred to an experiment where copper is in pair with silicon oxide such as in study of Burch [170]. Furthermore, the spreading of atomic hydrogen on the surface would be unlikely going beyond one step. In fact Park, following the logic in the mechanism of Li and Yang, states that the electron acceptor metal would make

the carbon in the vicinity positively charged and be more prone to form hydrogen bond. Even if true, despite the lack of supporting evidence, Park does not explain how the spreading would occur after this first step where there is not in the vicinity a metal particle to charge positively the carbon.

2.4.3. Theoretical model

Hydrogen spillover is thought to be the hydrogen atom migration from a metal (being able to dissociate the hydrogen molecules) towards an acceptor phase of the support which is in physical and/or chemical contact [171]. This metal modifies the chemical nature of the support but activates the support material that was previously were inactive [172]. Factors influencing the hydrogen spillover are the chemical bridges formed whether they might be carbon bridges [173] or proton acceptors [174]. However, there is a dispute in literature regarding the species actively involved in the spillover, and how reactive those species are and their migration processes [175, 176].

A study of a mixture of a catalyst supported activated carbon [162] shows that the hydrogen uptake increases with the dilution to a maximum then decreases. Hence the hydrogen migration process is controlled by a distance factor. Dilution increase the number of H species stabilized by the active carbon by increasing the available surface area and lowering the recombination rate of these species in molecular hydrogen. Moreover, oxygen groups are generally thought to act as receptors for spillover hydrogen [177] as well as increasing physisorption [178].

Lachawiec [145] attempted to determine the ratio of atomic hydrogen (H) to surface metal atoms (M_S) ($H:M_S$) exposed to the adsorbate. If the ratio exceeded unity it would indicate that hydrogen is spilling over onto the support. The limitations of this method arise when an attempt was made to determine the monolayer coverage of

hydrogen from a low-pressure chemisoption isotherm, which may asymptotically approach a larger adsorbed amount or continue to rise as pressure is increased due to the spillover.

However, spillover can be still quantified in systems containing metals that form solid solutions with hydrogen, as ($H:M_T$) which is the ratio of total adsorbed hydrogen (including that adsorbed by the metal) to total metal atoms (M_T) exceeding the stoichiometric ratio of the hydride. A schematic of this process is depicted in figure 2.11.

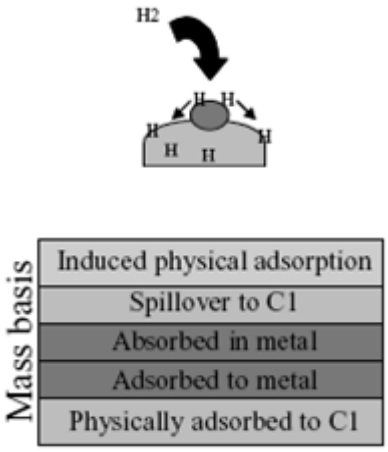

Figure 2.12 Steps of spillover reaction [144]

The amount of metal on the surface, M_S, is estimated by the Benson and Boudart [179] method where the hydrogen isotherm from low pressures (0.07–0.3 bar) is extrapolated to zero pressure:

$$Q_M = \lim_{P \to 0} Q_T \qquad (2.1)$$

where Q_M is the uptake by the metal and can include adsorption and/or absorption, Q_T is the total hydrogen uptake of the material, including both the metal and carbon (primary and/or secondary). This value was then used to calculate the atoms of metal

on the surface per gram of material, assuming that each surface metal atom interacted with one hydrogen atom (i.e. $H/M_S=1$). The hydrogen monolayer coverage was calculated by extrapolating to zero pressure the uptake of the metal Q_M.

The enhancement factor, η compares the degree of hydrogen spillover between carbons:

$$\eta = \frac{Q_C}{Q_C^{'}} \qquad (2.2)$$

where Q_C is the uptake of the carbon when mixed with a supported catalyst and Q_C' is the uptake of the carbon measured with no catalyst. Q_C, is the sum of contributions of each component to hydrogen uptake assuming they are independent of the presence of other components:

$$Q_C = Q_T - Q_{M+C1} \qquad (2.3)$$

where Q_T is the total hydrogen uptake of the composite material, Q_{M+C1} is the hydrogen uptake of the primary supported catalyst, and Q_C is the uptake attributed to the secondary carbon. Summarizing what those equations express, it is possible to say that increasing hydrogen spillover does not necessarily lead to the best overall hydrogen uptake. Hence work has to be done also in optimizing the physisorption but still relying also on chemisorption by doping the material.

A H_2-TPD study showed that residual hydrogen desorbs at high temperatures (750–780 K) from an activated carbon sample decorated with Nickel [162]. Hence this hydrogen has to be tightly bonded to the carbon support or at the metal-support interface. In a study of Ho [180] it was estimated that the hydrogen desorption higher temperature represents 5 % of the whole uptake. A possible mechanism of hydrogen storage and desorption could be written as:

$$H_2(g) \overset{M}{\Leftrightarrow} 2H_M \overset{AC}{\Leftrightarrow} 2H_C \Leftrightarrow H_2(g) \qquad (2.4)$$

where M and AC are metal and carbon sites respectively and H_M and H_C the hydrogen atoms adsorbed on a metal or a carbon site, respectively.

Roland [181] speculated that the spillover species may modify the electronic properties of the support and create new sites for the adsorption of hydrogen molecules from the gas phase. Accordingly the corresponding mechanism of hydrogen storage and desorption would be written as follows:

$$H_2(g) \overset{M}{\Longleftrightarrow} 2H_M \overset{AC}{\Longleftrightarrow} 2S_C \Leftrightarrow H_2(g) \qquad (2.5)$$

where S_C are carbon sites created by the hydrogen spillover species.

Doping to enhance chemisorption is a common approach for many nanotube–metal composites functionalized with transition metals, such as Ti ($[Ar]3d^24s^2$), V($[Ar]3d^34s^2$), Pd and Pt [182], [166], [183], [152], [184] and [185]. The enhanced hydrogen storage capacity of metal atoms with less than half-filled d-shells, such as titanium, is attributed to the adsorption of up to four hydrogen molecules via hybridization between titanium-*d*, hydrogen σ^* antibonding, and CNT C-*p*-orbitals [166] and [183]. The hydrogen adsorption of transition metal atoms with nearly completely-filled d-shells, such as Platinum ($[Ar]4f^{14}5d^94s^1$) and Palladium ($[Ar]4d^{10}$) or Nickel ($[Ar]3d^84s^2$) and Cobalt ($[Ar]3d^74s^2$), on the other hand, involves site-dependent dissociative chemisorption of up to two hydrogen molecules [184]. It has been reported in a theoretical work [184] that in these composite materials, each metal atom, additionally, adsorbs a third hydrogen molecule via long-range van der Waals type of interaction. This bond has a very low binding energy of typically ~ 1.8 kJ mol^{-1} hence these van der Waals bonded hydrogen molecules can desorb from the metal atom at ambient temperature [184].

The oxidative addition of hydrogen to metals has been treated by Kubas [186], who concluded that the hydrogen acts in the same time as a σ donor using its bonding

electrons and as acceptor of metal electron back into the σ * orbital. Such interactions lead to the disruption of the H-H bond and the formation of two new M-H bonds. These interactions can also lead to the formation of a complex where the hydrogen is a π-acid ligand in the same fashion as ethylene acts as ligand [150]. Dihydrogen can be thought of as a σ-bonded species and thus can be used as a model for the interaction of a metal with other fairly non-polar σ bonds. Because hydrogen does not have the steric constraints as many other oxidatively adding molecules have, hydrogen becomes uniquely reactive.

Dag *et al*. [184] concluded that the interaction of a hydrogen molecule with the surface platinum atoms dispersed on a single-walled carbon nanotube initially resulted in the dissociative chemisorption to form PtH_2. The estimated average binding energy of chemisorbed hydrogen is ~ 96 kJ mol^{-1} [184]. Each of the PtH_2, additionally, can bind two more hydrogen molecules via long-range van der Waals type of interaction, and are characterized by comparatively lower binding energy of 1.8 kJ mol^{-1} [184]. This renders a platinum hydride composition of PtH_2+$2H_2$. An alternate scheme of platinum hydride formation forecast by Dag *et al*. [184], involves the chemisorption of two hydrogen molecules on each surface platinum atom followed by the physisorption of a single hydrogen molecule via a long-range van der Waals interaction [184]. This leads to the hydride composition of PtH_4 + H_2. Very similar to this, Sachse *et al*. [187] suggested that the chemisorption and the complete electrical passivation of platinum by hydrogen require the binding of at least four hydrogen atoms. Based on these binding energy considerations of physisorbed and chemisorbed hydrogen species, it can be assumed that in an event of ambient temperature spillover, only the van der Waals bonded hydrogen molecules undergo diffusion on to carbon nanotube surface [152] and [188].

Experimental evidence however, might differ from theoretical studies because traditional computational models only assume that all metal atoms in the clusters are involved in the hydride formation overestimating the hydrogen storage capacity. Instead, it would be better to consider the interfacial diffusion of hydrogen from metal nanoparticles to the carbon surface [184] and [188].

In fact bulk-platinum can form non-stoichiometric hydrides thanks to 'un-hydrided' or 'partially-hydrided' platinum atoms in the bulk of the nanoparticles as reported in [189]. So for more precise estimation of the hydrogen storage capacity of platinum islands it has to be considered the hydrogen storage capacity only of surface and immediate sub-surface platinum atoms.

Cheng *et al.* [190] in their ab initio molecular dynamic simulations of hydrogen on single-walled nanotubes, showed rapid exchange of partially chemisorbed hydrogen between the interior wall and the exterior wall. For desorption of molecular hydrogen that requires desorption activation energy below 40-60 kJ mol^{-1}, desorption can take place readily at room temperature.[191]. A few hydrogen atoms on the interior sites of the SWCNT desorbed first. The binding energies on these few interior sites are lower than 40-60 kJ mol^{-1}. Since adsorbed hydrogen atoms are mobile and interior-exterior exchange is possible, these interior sites continue to be replenished and, from them, hydrogen is desorbed as molecular hydrogen. Since the large number of such patches of desorption sites, a broad desorption peak would be possible during temperature programmed desorption as observed by Dillon *et al*. [192] When coupled with a metal catalyst the bond energy of hydrogen on metal can be comparable with the one above, e.g., 76 kJ mol^{-1} for H_2 on Pt.. Through such desorption paths, reversibility of the hydrogen adsorption and desorption isotherm is expected and is observed [145].

2.4.4. Experimental evidences for hydrogen spillover

Lueking *et al.* [144] found a hydrogen uptake for the Pd-doped SWCNTs was about 0.1 %wt at 1 bar and 300 K as experimental evidence of hydrogen uptake measurements involving hydrogen spillover..

In the study of Zacharia *et al.* [156] the maximum hydrogen storage capacity of carbon nanotube samples measured at 298 K and at an equilibrium pressure of 16.7 bar was found to be 0.075 wt%. Whereas hydrogen storage capacity of platinum-doped CNTs reproduced over several experimental runs was found to be 2.9 ± 0.3 wt%, and nearly 95% of the equilibrium hydrogen storage was completed in less than 10 s. Zacharia estimated the expected spillover contribution and the hydrogen spillover capacity of pristine carbon nanotubes of 2.9 ± 0.3 wt% and 0.075 wt% respectively. From the calculation it was observed that the spillover contribution is larger than the physisorption contribution only when in all metal nanoparticles, platinum atoms of up to 15 shells from the surface are involved in the spillover of hydrogen on to the carbon nanotube surfaces. It also implies that the platinum atoms of shells deeper than 15 shells behave like bulk-platinum giving little or no spillover contribution.

In the study of Yang and Lachawiec [193] the presence of a hysteresis loop in the adsorption/desorption cycles was interpreted as that spillover of hydrogen, in the form of atoms, had accessed higher energy sites compared to those present in the pure SWCNTs and hence requiring lower pressure before they could recombine to molecular hydrogen and then desorb. This hydrogen is not readily desorbed at 1 bar and 298 K while the hydrogen that occupies the lower energy sites is reversibly desorbed. To fully desorb the hydrogen at 298 K, the sample was placed a vacuum

(10^{-5} bar) for at least 12 h or heated to at least 423 K. This behaviour is consistent with a bond energy of the order of 41.8 kJ mol^{-1}[194].

Chien-Hung Chen *et al.* [195] observed hydrogen spillover on Co loaded as-prepared CNTs was less significant than (0.71 wt%) that on the Co loaded-activated CNTs (4.47 wt%). This difference has been attributed by the authors to the dissociation of hydrogen and subsequently the migration of the dissociated hydrogen only from Co metal to the external surface of the CNTs occurring in the former sample. Whereas in the latter hydrogen atoms easily diffused and migrated from external surface into inner graphene layers through the defect sites on the surface of the activated CNTs, causing hydrogen spillover enhancement, as illustrated in figure 2.12.

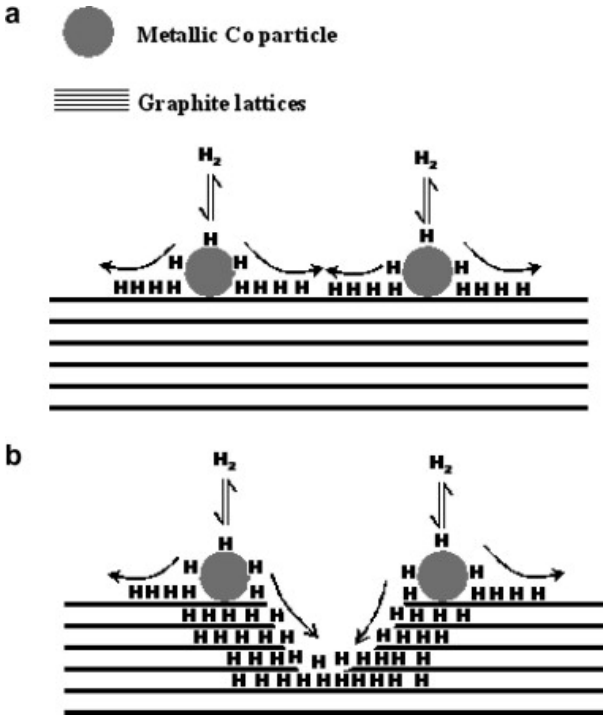

Figure 2.12. Hydrogen spillover on plain (a) and on defective (b) carbon surface[196]

The atom ratio of H/Co for the Co loaded as-prepared CNTs was effectively independent of the amount of Co loaded. It was also found that the H/Co atom ratio ranged from 9 to 37 for the Co loaded-activated CNT, and reduced with increasing amount of Co loaded onto the CNTs. That was a sign that hydrogen spillover took place over the Co loaded CNTs, since the value of atom ratio was larger than one.

In this study of Chien-Hung Chen, the enhancement factor (η) expressing the ratio between the uptake of the sample mounting a catalyst and the sample without catalyst, was calculated for the as-prepared and the activated CNT samples with different amount of Co loaded. The value of enhancement factor increased with increasing the amount of Co loaded onto the CNT samples. For high Co loaded content (>5 wt%), the enhancement factor of the activated CNTs was even larger than 3.

Another analysis approach to the characterization of hydrogen spillover is offered by Kim *et al*. [167] who suggested that spillover hydrogen atoms from a nickel catalyst would be chemical bonded with the surfaces of MWCNTs under 40 bar at 300K, and the C–H_n stretching vibration in the range of 2850–3300 cm^{-1} to confirm the theory was observed by FTIR studies of nickel dispersed MWCNTs after hydrogenation.

2.5. Hydride nanoconfinement in porous substrates

Another interesting group of metals that could enhance the hydrogen adsorption is the group of alkaline and alkaline earth metals which form high hydrogen capacity hydrides. Wu *et al.* [197] prepared various Mg/carbon and Mg/noncarbon composites by mechanical milling (figure 2.13) and investigated their hydrogen storage

behaviours. It was found that all the carbon composite additions had an advantage over the non-carbon additives in improving the hydrogen capacity and dehydriding/hydriding kinetics of Mg. The hydrogen capacities of all Mg/C composites at 573 K reached more than 6.2 wt% within 10 min, about 1.5 wt% higher than that of pure MgH_2 at the identical operation conditions and the rate of Mg/C system reaches up to about 1.5 wt% min^{-1} while for the pure MgH_2 the desorption rate is only about 0.1 wt% min^{-1}.

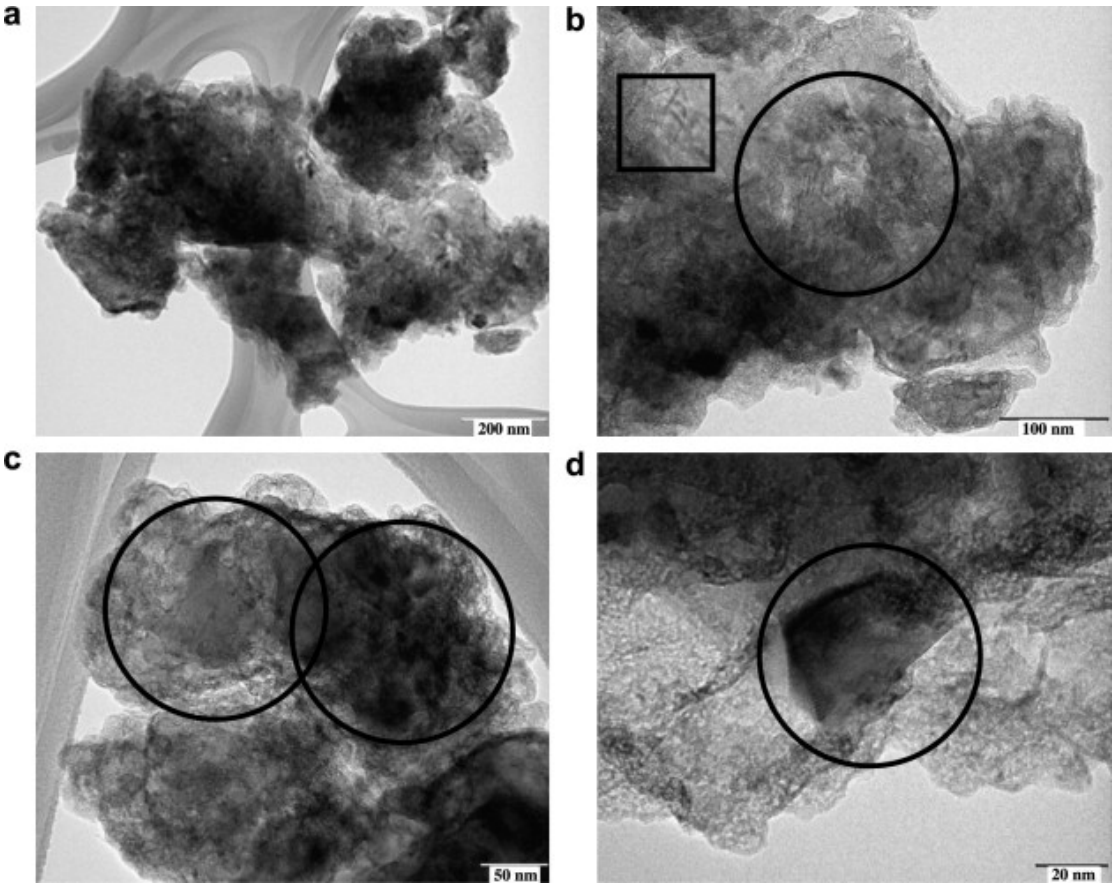

Figure 2.13 TEM images of MgH2 + 5 wt.% MWCNT as milled (squares delimit carbon and circles delimit crystalline areas of Mg). a, b, c and d correspond to different images of the sample [198]

The author speculates that most likely the effect of carbon additives on the hydrogen storage of Mg is that the incorporation of carbon leads to an increased phase boundary and hydrogen diffusion driving force. This is coupled with a sensible decrease of hydride particle size during the milling making this mechanical treatment an essential contribution rather than a specific interaction hydride/carbon.

Another hydride composite material is the addition of $LiAlH_4$ with carbon nanostructures. In a paper published by Hima Kumar [199] the dehydrogenation characteristics of $LiAlH_4$ mixed with CNFs and activated carbon (Vulcan XC72R) were studied and compared with that of pure lithium aluminium hydride. Here the author theorized that the possible mechanism for the dehydriding of $LiAlH_4$ upon addition of carbon materials was the reduction of particle and crystallite size of $LiAlH_4$ during mechanical milling. Because this leads to short diffusion paths for the hydrogen and combined with a reduction of crystallite size then the combined effect is the enhanced dehydrogenation kinetics thanks to the high density of grain boundaries that also act as nucleation centres for new phases as well as diffusion pathways.

A process that differentiates from the mechanical mixing to produce small particle sizes but is related to having a small particle size is nanoconfinement.

Such nanoscale dispersion of the hydride is obtained by melting the hydride into the carbon support. An example of this was achieved by Vajo *et al.* [200] by melting $NaAlH_4$ at 180 °C and decreasing the dehydrogenation temperatures by up to ~100°C, increasing the isothermal dehydrogenation rates by more than 50 folds when hydrides are confined to dimensions smaller of 25nm.

Such impressive results unfortunately cannot be achieved with MgH_2. In fact due to its higher melting point (~ 600 °C) the direct intercalation into the substrate pores of the liquid hydride has not been possible. A further issue is the poor

wettability of carbon by the Mg. An attempt to solve such problem has been done in a work of Gross *et al.* [201] by depositing a wetting metal layer of Ni or Cu and then proceed to the melting of Mg in and hydrogenating it to MgH_2 as depicted in figure 2.14. All samples demonstrated a 20 times faster hydrogen exchange kinetics compared to MgH_2 mechanically milled with graphite, however, no thermodynamic changes were observed. Such claims do not take into account the alloying potentials of Mg and Ni or Mg and Cu [202]. Inevitably during the magnesium thermal deposition at 700°C the Mg forms an alloy with Ni that can hydride such as Mg_2NiH_4 [203] independently from the nanoconfinement.

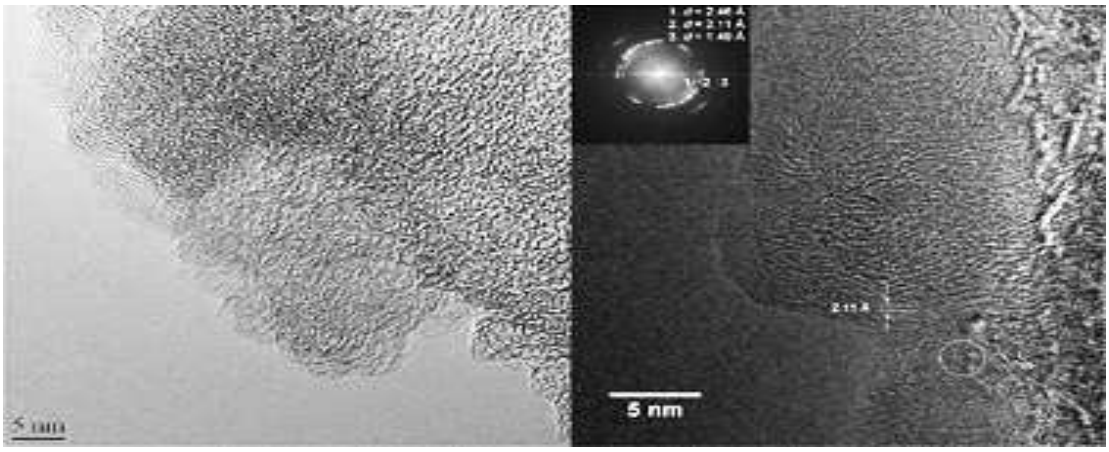

Figure 2.14 Left: HR-TEM image of the activated carbon fibres (ACF); right: HR-TEM image of oxidized MgH_2/ACF composite and the electron diffraction fringe of MgO in the ACF matrix [204]

A different approach to disperse MgH_2 at nanoscopic level is to start from a Mg precursor and decompose it till obtaining the hydride. So far only a few researchers have explored the alternative route [204-206] of dibutyl magnesium (DBM) as hydride precursor. Such a compound has been decomposed at the experimental conditions of 170 °C of temperature and pressure of 55 bar of hydrogen for 24 hours.

Results from the work of Zhang [205] show that 75 % of such hydride is reversible over ten cycles. Incorporated MgH_2 had more than 5 times faster dehydrogenation kinetics than ball-milled activated MgH_2 proving to be a better way than direct milling of carbon and magnesium hydride. Such reversibility has been confirmed by the work of Nielsen [206].

Zhao-Karger *et al.* [204] showed from experimental studies that MgH_2 particles with a smaller particle size (<3 nm) exhibit significant reductions of ΔH and ΔS of 11 kJ mol^{-1} and 19 J K^{-1} mol^{-1}, respectively.

However, the overall decrease of the thermodynamic desorption temperature was only 11 °C at 1 bar of hydrogen compared to bulk MgH_2 [207]. Fichtner [208], from the same research team of Zhao-Karger [204], has theorized the mathematical correlation between particle radius and the molar free energy of formation of the hydride. The author linked such destabilization to some unsatisfied bonds of surface atoms may be lowered by species which have a binding interaction with these surface atoms leading to a partial saturation of the bonds. In the case of metal/hydride particles the saturation may be caused by hydrogen gas molecules. Moreover, also suggested the wall of a carbon pore may strongly interact with the metal surface, too, and contribute to the total energy to a considerable extent due to chemical interactions or to elastic constraints.

In the same paper [208], an investigation of the equilibrium pressures with complex hydride $NaAlH_4$ infiltrated in various microporous scaffolds showed in each case a broad distribution of equilibrium states. Hence, there seems to be a great variation of states and stabilities in the sample. Possible reasons are the pore diameters distribution and ultimately the particle sizes as well as the fact that the structure at the surface or interface of a hydride nanoparticle may be strongly

disordered and less stable while the interior resembles more the bulk structure and properties. Hence both destabilization and stabilization were found, depending on the system.

2.6. Summary

The understanding behind the use of existing carbon nanostructures as hydrogen storage materials is well developed but some new structures, such as carbon nanocones, require investigation due to their unique electron configuration at the tips. In general carbon nanostructures have a physical interaction with hydrogen, called physisorption, which does not provide sufficient hydrogen uptake at room temperature to comply with the latest requirements of the DOE. For that reason more recent research has coupled a metal catalyst that would bond the hydrogen chemically, via chemisorption, in an attempt to increase the hydrogen storage capacity at RT.

In an attempt to increase the hydrogen storage capacity at RT, the research behind this thesis aims to improve the interaction between those two heterogeneous materials, chemically treating the carbon support to enhance their compatibility, and optimizing the metal dispersion towards smaller and smaller particles.

Furthermore, in order to reduce the production costs, expensive catalyst such as Pd, are attempted to be replaced by cheaper metals, like Ni, Cu and Ag and evaluate the resulting hydrogen adsorption performances.

In the literature it is reported that metal catalysts are capable of breaking the hydrogen molecules in atomic hydrogen and spreading those atoms on the supporting surface. This spillover has created much controversy in the area due to it being

difficult to replicate and to prove its implication in some outstanding results in matter of hydrogen storage. For this reason it is worth investigating the potential of a spillover mechanism for a carbon material which has a unique electronic structure such as that exhibited by the nanocones.

Another trend of development is to improve the capacity of the material combining carbon structures with light metal hydrides, well renowned for their large capacity, and confining them in nanoscale spaces such as the micropores of the carbonaceous structure. Such composite materials so far have been synthesized by direct mixing, via ball milling or via melting, of the two components with improvements limited to only the kinetics and not the thermodynamics and with drawback of being limited to those hydrides with lower melting point. Only recently a few studies have attempted to overcome such limitation by synthesizing the composite material using precursor compounds of the metal hydride with some encouraging results. This offers the opportunity to explore such routes for other types of carbon nanostructures.

3. Experimental Methods

3.1. Preparation of carbon nanocones and GNF

The carbon nanocones material was supplied by n-Tec, a Norwegian company, made by the Kvaerner Carbon Black & Hydrogen Process, see Section 2.2.

GNFs were synthesized using NiO powder as the catalyst precursor. The catalyst was prepared adding an aqueous solution of Ni-nitrate [$Ni(NO_3)_2 \cdot 6H_2O$] (99.9% Sigma Aldrich) to 2 M ammonia solution (from solution at 35 % Sigma-Aldrich), and the precipitate was calcined for 4 h at 400 °C. The GNF were prepared by carbon vapour deposition (CVD). The catalyst precursor was placed in a tube furnace in an alumina crucible. A feedstock gas H_2/C_2H_4 at 20:80 cm^3 min^{-1} was flowed for 1 h at 600 °C temperature using mass flow controllers (MKS Ltd).

Samples were pre-treated under reflux with 12 M H_2O_2 solution (Sigma-Aldrich, 35 %) for 3 h to enhance the dispersion of the carbon in aqueous solutions as well as to create structural defects to improve the nucleation of the catalyst precursor precipitates.

3.2. Impregnation with metal catalyst

Catalyst impregnation was made via the incipient wetness technique [153] using an aqueous solution of palladium (II) nitrate hexahydrate (Sigma-Aldrich, 99.9 %). Two different reduction reactions of the palladium deposits were performed: a reduction into 1:9 H_2:Ar atmosphere, with a total gas flow of 100 cm^3 min^{-1} at room

temperature (RT) for 3 h; or reduction with $NaBH_4$ (Sigma-Aldrich, ~98 %) [209] added in excess to the Pd-containing aqueous solution at RT, stirred for 3 h, then filtering the solution and washing with water.

Two different kinds of reduction of the metal deposited on the surface were performed: a standard reduction in H_2 atmosphere at high temperature in a furnace and a reduction with $NaBH_4$ [209, 210] at ambient temperature. While well dispersed Pd particles on carbon cones can be obtained via 300 ^oC reduction in hydrogen, it results in an increased particle size. Hence a reduction at room temperature was successfully adopted avoiding any significant increase of particle size. Whereas reduction of Ni and Co has been possible only via 300 ^oC reduction in hydrogen due to their higher reduction potentials according to the Ellingham diagram.

Impregnation with Mg was made by transferring the carbon nanocones into a round bottom flask attached to a vacuum/gas manifold (Schlenk line) and left under vacuum overnight to dry. Subsequently, n-dibutyl magnesium (1.0 M solution in heptane, Aldrich Chemicals) was added under Ar flow in an amount to target 10 wt% Mg. The mix was stirred and gently heated under vacuum to evaporate the heptane solvent. The material was then thermally decomposed under flowing Ar of 100 cm^3 min^{-1} and heated for 4 h at 170°C.

3.3. Materials characterization techniques

3.3.1. Powder X-ray diffraction (XRD)

Composition analysis of the synthesised samples, as well as of the *ex-situ* samples from the thermal analysis was carried out. XRD offers a quick way to

characterize the crystalline structure of the material. The technique is based on the theory of Bragg law [211]

$$n\lambda = 2d\sin\theta \qquad (3.1)$$

where n is the order of diffraction, λ is the X-ray wavelength, d is the inter-planar spacing and θ the angle of incidence of the beam.

XRD patterns were collected on a Bruker D8 Advanced equipped with Cu-Kα source, λ = 1.5418 Å, over a 2θ range of 5° to 70°, a step size of 0.02°, an interval of 5 s and a slit size of 0.6 mm. For small and/or air sensitive samples a single crystal silicon wafer was used. Furthermore, samples were loaded in an Ar glove-box and protected by amorphous polymer tape to minimize the contact with oxygen or moisture. Identification of the crystalline phases was done through comparison of experimental XRD patterns and reference patterns stored in databases such as ICSD (Fluck 1996) and JCPDS-ICDD (Jcpds-Icdd 1996).

It is possible also to calculate the particle size of the material using the Scherrer formulae [211]:

$$\tau = \frac{k\lambda}{\beta\cos\theta} \qquad (3.2)$$

where k is the atomic factor of 0.89 for the cubic structure, τ is the mean size of the ordered crystalline domain, λ is the X-ray wavelength, β is the broadening at full width half maximum (FWHM) of the peak and θ is the incident angle.

3.3.2. Transmission electron microscopy (TEM)

Transmission electron microscopy (TEM) was performed on a JEOL JEM-2000FX II. Particle size analysis from the microscope images was conducted using ImageJ software [212]. For the sample preparation the fine particles of the materials were dispersed in a volatile liquid (water, buffered solution, alcohol or hydrocarbon solution) according to the material specific requirements. Stirring or sonicating separates the agglomerated particles and ensures a homogenous suspension. A dilution step was sometimes required to obtain very low concentrations of the material, so that the particles on the support film remain isolated. A droplet of the suspension was placed on the coated grid. The specimen is ready for observation after complete evaporation or drying.

Electron transparent samples (~ 0.1 μm thick) can be examined by TEM at a very high resolution, ultimately limited by the wavelength of the incident electron beam, although the real resolution achieved will depend on the aberrations associated with the electron optics. Figure 3.1 is a schematic for a TEM microscope [213]. Electrons are produced by the electron gun made of a W or LaB_6 filament, and are accelerated towards the anode at a high energy, in our case 200 kV. An apparatus composed of several condenser lenses focuses the electron beam. Starting from the top the condenser aperture filters the electrons that are far from the optic axis and regulate the number of incident electrons. Then the objective aperture, located in the back focal plane of the objective lens, blocks any transmitted electrons with a large scattering angle, thereby enhancing the contrast of the projected image. The sample generally inserted on a plane perpendicular to the optic axis and situated close to the focal plane of the objective lens is passed through by the electron beam and the image is projected onto an electron sensitive florescent screen by the projector lens.

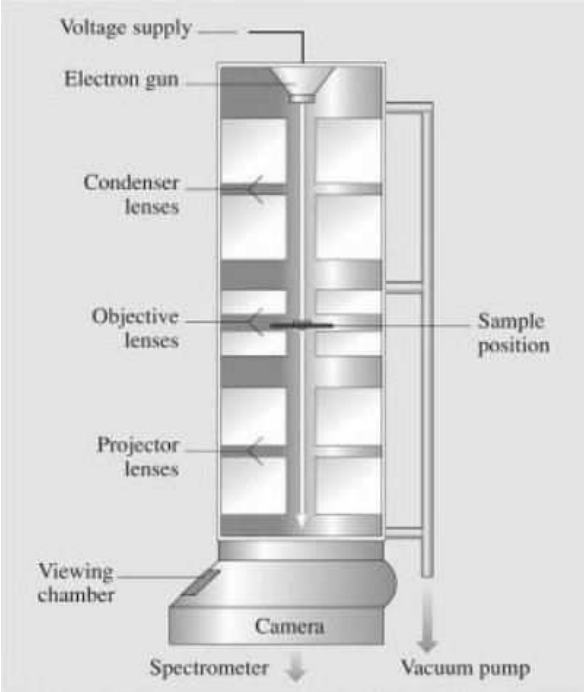

Figure 3.1 Schematic of a TEM apparatus [213]

Details of the beam deflection path are given in figure 3.2.

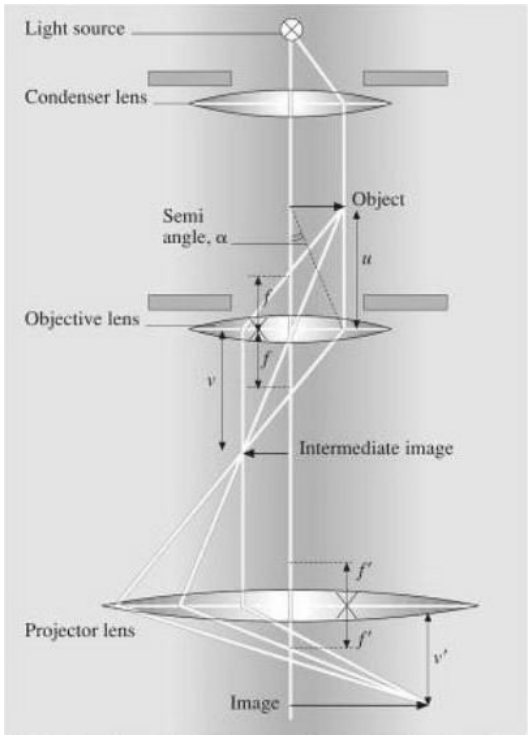

Figure 3.2 Details of the electron beam path for a transmission projection microscope [213]

To obtain an electron diffraction pattern, the objective aperture must be removed and a selected area aperture is inserted into the intermediate image plane so that the projector optics focuses on the back focal plane of the objective lens. In this way only a small area of the specimen is selected to represent the electron diffraction pattern. The changes in the optics setup in order to form the electron diffraction patterns are show in figure 3.3.

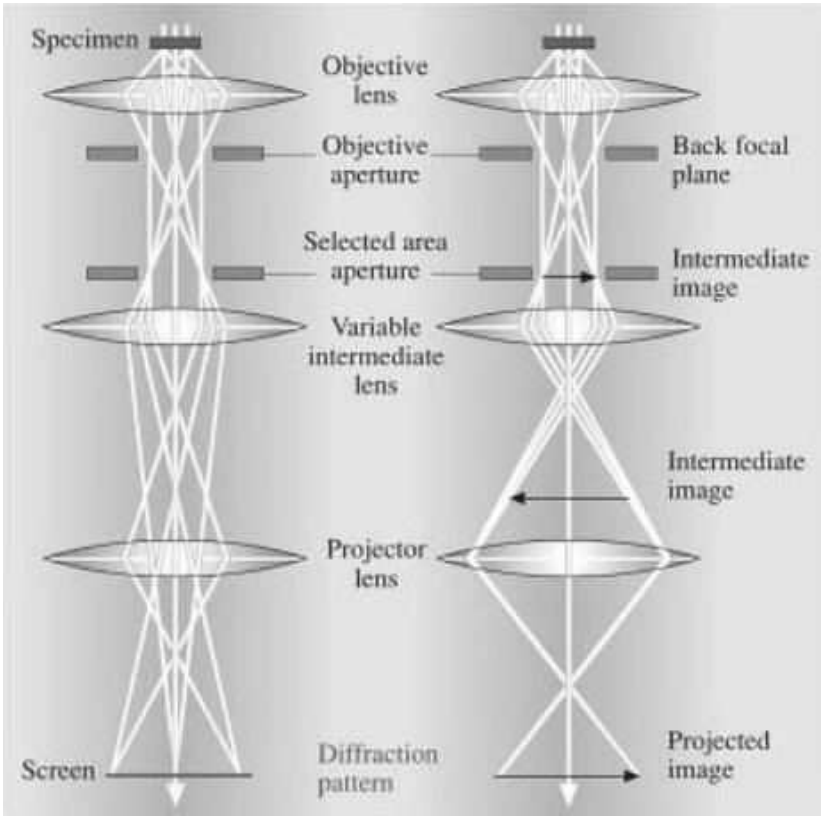

Figure 3.3 Schematic representation of the projection of the diffraction pattern (left) and the normal image onto the display screen (right) [213]

The diffraction pattern can give information on the crystallography and crystal orientation. The angle of diffraction (θ) is very small because of the very small wavelength of high energy electrons (as compared with the wavelength of X-rays) resulting in small distances between the transmitted electron beam and diffracted spots, R_{hkl}, which is the measured spacing [214] as shown in figure 3.4. This allows one to achieve good resolution images at high magnification.

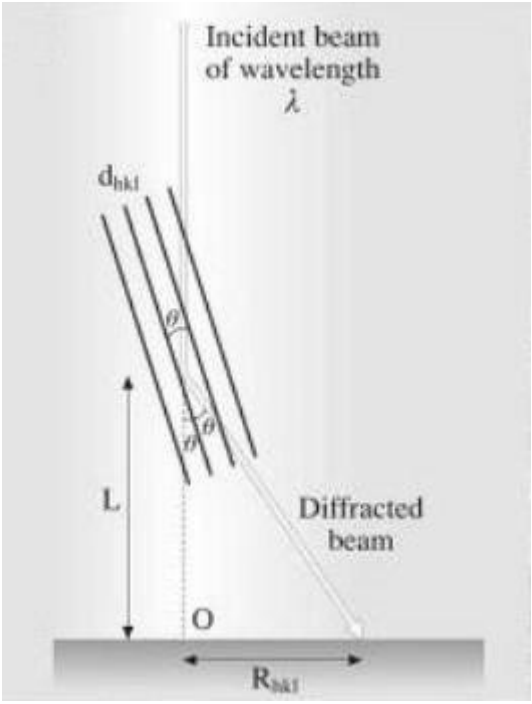

Figure 3.4 Illustration of the concept of the camera constant [213]

The camera length is the effective distance or magnification between the specimen and the detector plane and is a calculated value rather than a physical distance. For this calculation the Bragg equation can be simplified since $\sin\theta \approx \theta$ for small θ (in radians):

$$\lambda = 2d_{hkl}\theta \tag{3.3}$$

where λ is the electron wavelength, d_{hkl} the lattice d spacing and θ the angle of diffraction. From figure above, the following equation is obtained:

$$\tan 2\theta = \frac{R_{hkl}}{L} \approx 2\theta = \frac{R_{hkl}}{L} \tag{3.4}$$

where L is the camera length, the effective distance between the specimen and the recording plane. Combining these two equations we can obtain:

$$\lambda L = R_{hkl} d_{hkl} \tag{3.5}$$

The term λL is known as the camera constant and can be obtained using a reference sample of known lattice parameter under the same electron-optic conditions. By using this equation, crystal plane spacings, d_{hkl}, of an unknown material can be calculated and associated diffraction spots indexed.

Images in TEM can be formed either using directly transmitted or scattered electrons. The electrons are filtered by an aperture into the back focal plane of the objective lens, thus blocking out most of the diffraction pattern. If the central spot is chosen, a bright field image is formed using directly transmitted electrons, as shown in figure 3.6. There are three different mechanisms which lead to contrast in the TEM image. In amorphous samples, thicker regions of the sample and areas with a higher atomic number appear darker, due to mass-thickness contrast. Low index crystalline orientations of crystalline samples that satisfy Bragg diffraction also appear darker, termed diffraction contrast.

In all cases, regions imaged with the transmitted beam are termed bright field (BF). Alternatively, by aligning a diffracted beam down the optic axis of the microscope, a dark field (DF) image may be formed, as shown in figure 3.5 and in Figure 3.6 by a real example.

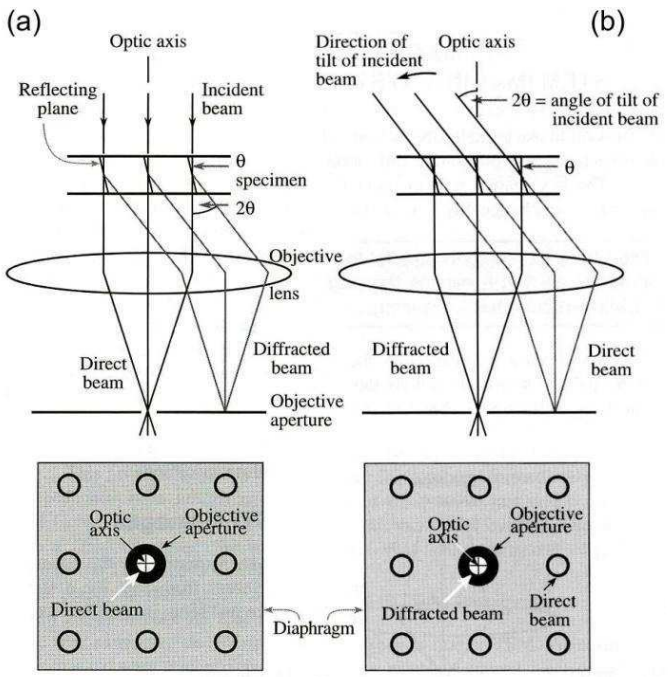

Figure 3.5 Schematic diagram showing the formation of (a) a bright field diffraction contrast image using the direct transmitted beam and a (b) a centred dark field diffraction contrast image, with the incident beam tilted so that the scattered beam remains on the optic axis [215].

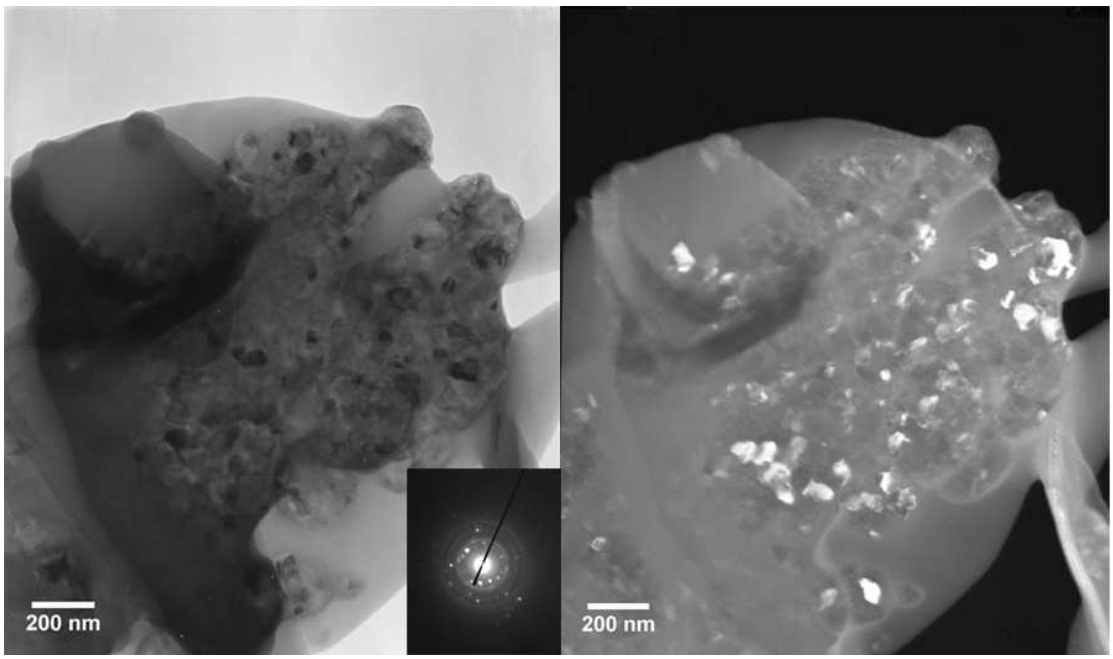

Figure 3.6 Example of bright field on the left, and dark field image on the right

Analysis was performed using bright field, dark field and selected area diffraction pattern modes of operation.]

Image analysis using the image analysis tool of ImageJ software [212] consisted first of all in the scale of the image. A reference image containing a feature of known exact size, in the case of this thesis it was graphitised carbon having layer distance of 3.42 Å, was used to link the pixel per nm ratio. Subsequently it was enhanced the grey scale contrast between the dark features (metal particles) and the bright features (carbon substrate). The software then transforms all the dark features in black pixel and the bright features in white pixels.

The particle analysis tool then considers as particles all the features with adjacent black pixel having an area larger than 1 nm^2. This is done to avoid considering as particles small cluster of pixels deriving from image noises or imperfections. Once done that, the software report for each particle the area and the average diameter of every single particle. The average particle size of the particles distribution is then calculated along with the standard error.

3.3.3. Fourier transform infrared spectroscopy

Infrared (IR) spectra were recorded at room temperature using a Bruker Tensor 27 FTIR spectrometer, attenuated total reflection (ATR) apparatus, employing a mercury cadmium telluride (MCT, HgCdTe) detector, MIR (HeNe laser) source and analysed using *OPUS* software. A beam of infrared light is passed through the ATR diamond crystal being then reflected at least once off the internal surface in contact with the sample. From this reflection is formed an evanescent wave which penetrates between 0.5 and 2 μm into the sample. The beam is then collected by a detector as it

exits the crystal. The crystal is made of diamond because it is a material with a higher refractive index than the sample being studied.

Samples under study were solids and thanks to the use of ATR accessory there was no need for further sample preparation. The sample simply was clamped into direct contact with the crystal to improve with a more intimate contact so that trapped air is not the medium through which the evanescent wave travels, as that would distort the results.

Infrared radiation is passed through a sample and absorbed by covalently bonded molecules at their resonant frequency of vibration. A molecule has many vibrational modes that are only considered "IR active" if they result in an associated change in permanent dipole. These vibration modes can be symmetrical, asymmetrical or scissoring. The number of observed absorptions may be increased by additive and subtractive interactions leading to combination tones and overtones of the fundamental vibrations, in much the same way that sound vibrations from a musical instrument interact. In FTIR, the IR radiation is collected by an interferometer, which measures all IR frequencies to produce an ‘interferogram’. The data-processing technique of Fourier transformation converts the interferogram into a spectrum, a plot of wavenumber (wavelength) against absorbance or transmittance, signatures of which are characteristic to the covalent bonding present in the sample [216].

3.3.4. Hydrogen sorption characterization: Intelligent Gravimetric Analysis (IGA)

Gravimetric analysis was used to characterize the equilibrium sorption isotherm by measuring the mass of the hydrogen adsorbed. Such an isotherm measures the reversibility of the adsorption and desorption of hydrogen by the sample. Gravimetric

determination of hydrogen uptake capacity was performed using an Intelligent Gravimetric Analyzer (IGA-003, Hiden), which incorporates a microbalance with an error of ±1 μg. The mass of the samples was of the order of 100 mg. Hydrogen uptake was determined at -196 °C as well as at RT (25 °C) over the pressure range 0-20 bar (pressure transducer had an error of 50 mbar corresponding to 0.05% of full scale) of high purity hydrogen (Air Products, purity N6.0). Further purification was done by passing the gas through a zeolite molecular sieve. The samples were outgassed (10^{-10} bar) at 250 °C overnight before the measurement was started. Further, an isotherm was collected with a long equilibration time (up to 20 h) for pressures below 5 bar and shorter equilibration times (3 h) per point for pressures up to 20 bar.

Since the pressure changes the mass buoyancy of the sample must be corrected according to the Archimedes's principle. The upward force due to the buoyancy, C_b for a solid with a density ρ_s and mass m_s surrounded by a gas of density ρ_g is expressed by the formula:

$$C_b = m_s \cdot \frac{\rho_g}{\rho_s} \qquad (3.6)$$

The excess adsorbed density ρ_{ex} is expressed as the difference between the number of adsorbate molecules N_a in the voids volume V_{void} of the adsorbent minus the number of molecules N_g what would occupy the voids volume if there were no adsorbate-adsorbent interaction [217]. N_g can be easily calculated from the density of the bulk gas ρ_g occupying the voids volume.

$$N_g = -\rho_g V_{void} \qquad (3.7)$$

The voids volume V_{void} is the sum of the volume of all the pores V_{pores} plus the volume not occupied by the adsorbent V_{empty}.

$$V_{void} = V_{empty} + V_{pores} \qquad (3.8)$$

So the excess number of molecules adsorbed is defined as:

$$N_{ex} = N_a - N_g = N_a - \rho_g V_{void} \quad (3.9)$$

and the density of such molecules is:

$$\rho_{ex} = \frac{N_{ex}}{M} \quad (3.10)$$

where M is the mass of the adsorbent.

Note that the excess density is above defined as the ratio between the excess number of molecules adsorbed and the adsorbent mass. However, it is not possible to state the same for the density of the adsorbed gas ρ_a. The density of the adsorbed gas does not correspond to the ratio between the number of adsorbate molecules (N_a) in the voids volume and the adsorbent mass because such density includes also the density of the molecules in the empty volume V_{empty}. Hence these two densities differ of the a member corresponding to the density of the molecules in the pores, i.e.:

$$\rho_{ex} = \rho_a - \frac{\rho_g V_{pores}}{M} \quad (3.11)$$

Such equation is important because the excess density is the quantity obtained through the volumetric method of adsorption measurement. Combining equations 3.9, 3.10 and 3.11 we obtain that the absolute adsorbed density as:

$$\rho_a = \frac{N_a - \rho_g V_{empty}}{M} \quad (3.12)$$

The excess hydrogen uptake capacity is expressed by the percentage of the mass adsorbed m_{H_2} over the sum of the masses of both the adsorbate and the adsorbent m_s:

$$wt.\%(T,p) = \frac{m_{H_2}}{m_{H_2} + m_s} \quad (3.13)$$

3.3.5. Textural analysis: Brunauer Emmett Teller (BET) and Barret Joyner Helenda (BJH) methods

The measurement of the surface area was carried out using an Autosorb-1 (Quantachrome, instrument error 5 %) instrument using N_2 (BOC, 99.998% minimum) as the adsorbate at a temperature of 77 K. A precisely weighed sample (± 0.0001 g - the scale precision) was degassed at 300 °C for at least 5 h under vacuum pressure. The dried sample mass was weighed before loading on the testing station. The pressure steps were of 0.03 of relative pressure and the equilibrium time out was 10 min per point. The most common technique to calculate the surface area is based on the Brunauer Emmett Teller equation [218]:

$$\frac{1}{W \cdot \left(\frac{p}{p_0} - 1 \right)} = \frac{1}{W_m \cdot C} + \frac{C-1}{W_m \cdot C} \cdot \frac{p}{p_0} \quad (3.14)$$

where W is the weight of the gas adsorbed at a relative pressure and W_m is the weight of a monolayer of the adsorbate. The relative pressure is defined as the ratio between the absolute pressure p and the saturation pressure p_o which is the vapour pressure of the pure liquid adsorbate, C is the BET constant and is connected to the energy of adsorption for the first monolayer.

The experiment consists in measuring the adsorption and desorption isotherm for an inert gas (e.g. N_2) at low temperature and express the amount of gas adsorbed

as function of the relative pressure $\frac{p}{p_0}$. The equation 3.14 is solved by graphical means, by plotting $\frac{1}{(V[\frac{p_0}{p}]-1)}$ versus $\frac{p}{p_0}$. Such relationship between these two parameters shows a linear trend only at low values of relative pressure, typically between 0 and 0.35 [219]. Often, BET theory is also applied to obtain the specific surface area of microporous materials, although from a scientific point of view the assumptions made in the BET theory do not take into account micropore filling [220]. For such samples the linear BET range is found usually at relative pressures < 0.1, in contrast to the classical BET range, which extends over relative pressures between 0.05 – 0.35. Ignoring the interaction of the quadrupole moment of nitrogen molecule with the surface and assuming the cross sectional area of nitrogen being 16.2 $Å^2$ the BET surface area is overestimated [221]. However, despite the inability to accurately measure the true surface area of microporous materials, the BET method is widely accepted. The slope *s* of this trend line is found graphically and is expressed by:

$$s = \frac{C-1}{W_m \cdot C} \tag{3.15}$$

and the intercept is:

$$i = \frac{1}{W_m \cdot C} \tag{3.16}$$

Rearranging these two formulas we can find the weight of the monolayer adsorbed W_m as:

$$W_m = \frac{1}{s+i} \tag{3.17}$$

and hence the total surface area (S_t)can be written as:

$$S_t = \frac{W_m \cdot N_A \cdot A_{CS}}{M} \tag{3.18}$$

where A_{CS} is the cross sectional area of the adsorbing species (16.2 Å^2 for N_2), N_A is the Avogadro number (6.02214129 × 10^{23} mol^{-1}) and M is the molar mass of the absorbate. The interesting parameter is the specific surface area of the sample, S which is the total surface area per mass unit of the sample W_s:

$$S = \frac{S_t}{W_s} \tag{3.19}$$

The Barrett-Joyner-Halenda (BJH) method was proposed in 1951 and was originally developed for coarse porous materials with a wide range of pore sizes [222]. However, such method is applicable to almost all types of porous materials. The analysis is based on the assumption that the pores are cylindrical in shape and that the radius of the capillary is equal to the sum of the Kelvin radius and the thickness of the adsorbed film on the pore walls. For determining the thickness of the adsorbed layer, t, as a function of $\frac{P}{P_0}$, the researchers used a t-curve provided by C. Schull, 1948 [223]. They also assumed that the thickness of the adsorbed layer inside the pores is the same as the thickness of the adsorbed layer on a flat surface and that all pores are filled at a relative pressure of 1.0. They divided the pore sizes into groups, and for simplicity they assumed that all pores in each group of capillaries have an average radius r_c with the average pore radius increasing by 0.5 nm from one pore size group to the other up to a pore radius of about 6 nm, and increases by l mn

above 6 nm. The analysis is achieved using the data of the desorption branch of the experimental isotherm. Computations start at a relative pressure of 0.967 down, through a series of pressure steps, to a relative pressure of approximately 0.4; in this way, pores with a radius greater than 30 nm are ignored. Despite large pores could contain up to 10% of the total volume of condensate their number is generally small compared to the number of smaller pores; hence their contribution is negligible. The amount of adsorbate removed during each pressure lowering step is divided between inner pore emptying from liquid adsorbate and film thinning processes. Once details of the isotherm curve are accurately expressed as a series of pressure vs. quantity adsorbed data pairs the pore volume calculation can be summarized in the following formula [224]

$$v_{ads}(x_k) = \sum_{i=1}^{k} \Delta V_i (r_i \le r_c(x_k)) + \sum_{j=k+1}^{n} \Delta S_i t_i (r_i > r_c(x_k)) \qquad (3.20)$$

Where $v_{ads}(x_k)$ is the volume of adsorbate $cm^3\ g^{-1}$ at relative pressure x_k; which was calculated from the value of adsorption, V is pore volume ($cm^3\ g^{-1}$), S is surface area ($m^2\ g^{-1}$), and t is the tickness of adsorbed layer (nm).

This formula shows that the adsorbed amount at the k^{th} point of adsorption isotherm may be divided into two distinct parts: first is a volume in condensate in all pores smaller than some characteristic size depending on current relative pressure, $r_c.(x_k)$. The second part is a volume of adsorbed film on all larger pores calculated by a sum of the terms: Σ (pore surface) (thickness of film in pore).

For the adsorption isotherm branches the calculation scheme is the same. It always starts from the point where all pores are filled-up i.e. the last point of adsorption branch $x_{ads,k}$ where the adsorbed amount is the same as on the desorption

branch $x_{des,L}$ and the pore system is oversaturated then it goes along decreasing pressure, i.e. counting isotherm point counter downwards ($x_{ads,I}$ i = K, K- 1, K-2) for the adsorption and upwards for desorption ($x_{des,i}$ i = L, L+1, L+2 ...).

The thickness t is in general function of relative pressure x_k and possible to estimate by using the following Halsey equation [225] when x_k, is larger than 0.5.

$$t = 0.43\left[\frac{5}{2.303\log x_k}\right]^{\frac{1}{3}} \tag{3.21}$$

When the relative pressure is lowered from $\left(\frac{P}{P_0}\right)_1$ to $\left(\frac{P}{P_0}\right)_2$, the largest pores empty of their capillary condensate and a reduction in thickness of the adsorbed layer occurs by the amount Δt. Further reduction of pressure will not only result in evaporation and thinning of the adsorbed film in the second group of pore sizes, but also from a second thinning of the physically adsorbed layer from the first group of pore sizes. Halsey even though assumed cylindrical pores for their analysis such method is suitable also when slit-shaped pores are assumed.

3.3.6. Differential scanning calorimetry (DSC)

The instrument used for such analysis was Netzsch 204 HP Phoenix and usually (unless specified) the sample underwent a temperature ramp from room temperature to 585 °C at 10 °C min^{-1}. Measurements took place under an inert gas (Ar, BOC purity N6.0) at 100 cm^3 min^{-1} at 1 bar of absolute pressure. Where stated samples were

analyzed under flowing hydrogen (Air Products, purity N6.0 supplied through liquid nitrogen trap) at 1 bar absolute pressure at 100 cm^3 min^{-1}.

The specimens were prepared in a glove-box by placing them in an Al_2O_3 crucible and sealed into Al pans. The sample was quickly transferred from the glove-box to the DSC instrument. The Al lid was pierced prior the measurement to allow the gas flowing into the sample. Once the sample was inserted, the chamber was filled with Ar and flushed repeatedly to avoid any trace of oxygen or moisture.

The test sample (S) and a reference material (R) (an empty sample pan + lid) were enclosed in the same furnace on top of a metallic surface with high thermal conductivity that ensures a good heat-flow path between the two. The enthalpy or heat capacity changes in the sample (S) lead to temperature differences relative to (R). This, results in a difference in heat-flow between (S) and (R). The temperature difference ΔT between (S) and (R) is recorded and further related to the enthalpy change in the specimen using calibration experiments. To measure ΔT a chromel disc and connecting wire are attached to the underside of each platform and the resulting chromel-constantan thermocouples are used to determine the differential temperatures of interest. Alumel wires are also attached to the chromel discs to provide chromel-alumel junctions which measure the sample and reference temperatures separately. Another thermocouple is embedded in the Ag block and serves as temperature controller for the programmed heating/cooling cycle (figure 3.7.).

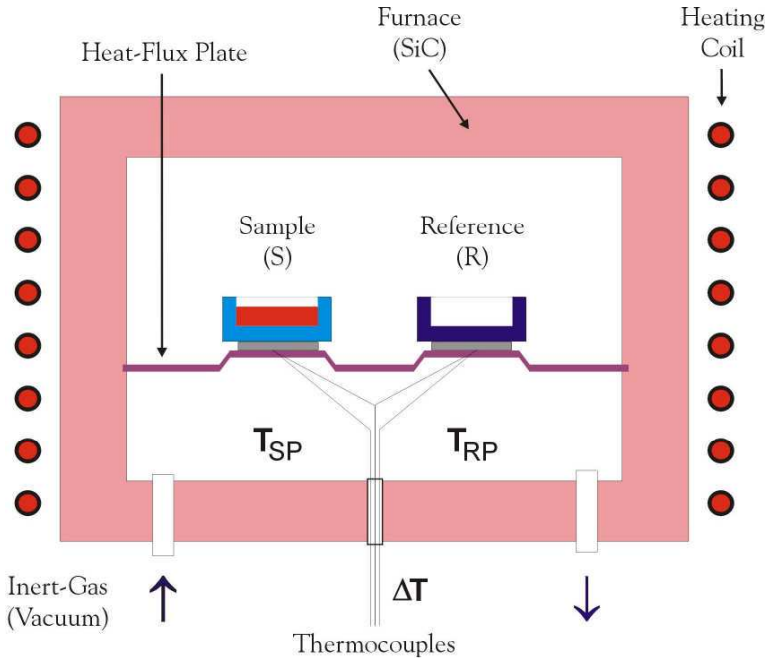

Figure 3.7 Main components of a typical heat-flux DSC cell [226].

3.3.7. Thermogravimetry (TG)

Analysis was performed using a Netzch 209 F1 Iris thermogravimetric analyser. A buoyancy calibration run on an empty pan was undertaken immediately prior to running the sample. This was involved an initial evacuation followed by 1 h isotherm at room temperature under Ar flow at 100 cm^3 min^{-1} to allow the balance to settle and heated from room temperature to 585°C at 10°C min^{-1}. The sample run also followed this procedure.

Thermogravimetry (TG) is a technique by which the weight of a substance, in an environment with heated or a cooled controlled rate is recorded as a function of time or temperature [227]. The equipment consists of a precision balance, a temperature programmable furnace, a reaction chamber and a data recording system capable of continuously registering any weight changes in the test sample during the heating process. The apparatus is a null point balance. Here any movement of the balance

beam caused by weight changes is counteracted by a restoring force to bring the beam back to its original position; this force is then taken to be proportional to the weight change concerned. Such setup makes the instrument adaptable to operation in a vacuum. The thermocouple is placed in direct contact with the sample (figure 3.8.).

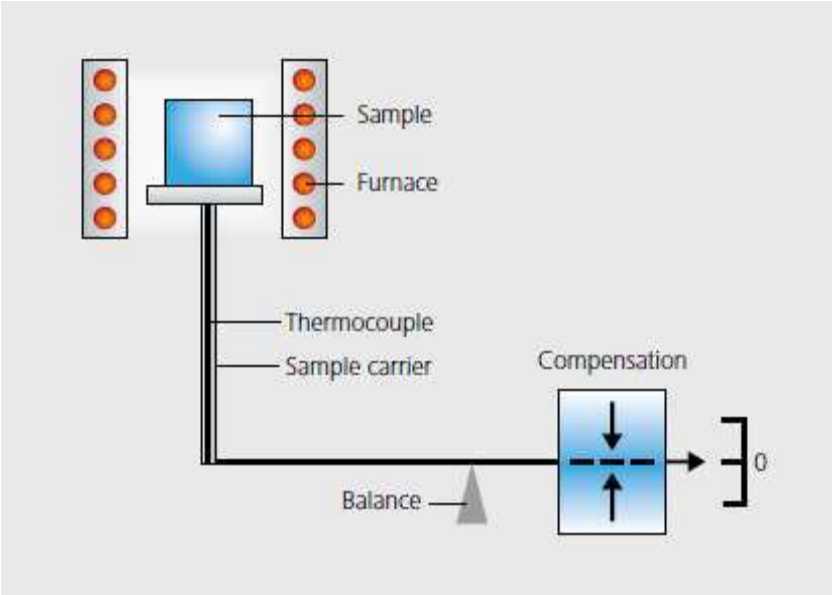

Figure 3.8 Schematic of the null point balance in the TGA instrument [228]

TG is a quantitative and dynamic technique, and a number of factors can affect the shape of the TG curve [229]. TG gives absolute changes in sample weight so the calculated extent of reaction is not affected by the heating rate used, although the start and finish temperatures are a function of heating rate because of kinetic barriers. Since factors like temperature gradients, air buoyancy and convection currents within the furnace tube contribute to the buoyancy effect and ultimately to the weight recorded, an inert empty crucible is placed in the furnace and changes with temperature are recorded. This generates a correction curve to compensate for these effects, making certain that at the same gas flow and temperature conditions the changes in the actual experiment are due to the properties on the material under test.

The main applications of TG include the measurement of thermal stability, ageing characteristics, decomposition, reactivity and the structures of compounds.

3.3.8. Mass spectrometry (MS)

Analysis of the gases coming from the decomposition of DBM has been made with a mass spectrometer HPR20 from Hiden Isochema. The instrument has an electron impact ionisation type source, a quadrupole filter and a Faraday detector. The upper mass limit was 200 m/z.

There are in fact three main components of a mass spectrometer: an ionization source, a mass analyser and a detector (figure 3.9).

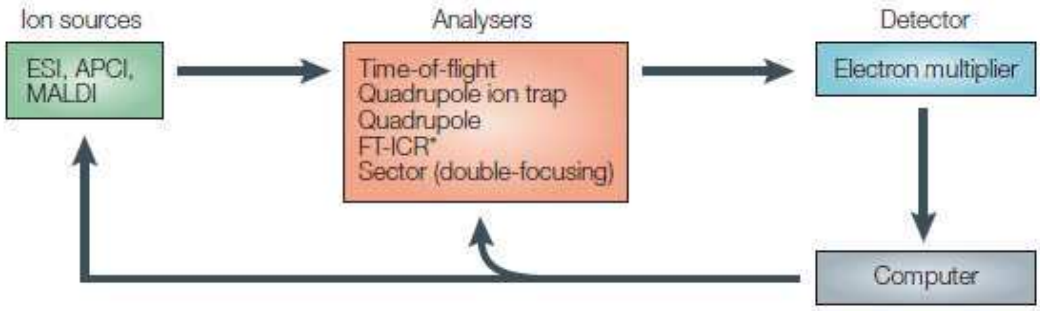

Figure 3.9 Basic components of a typical mass spectrometer used in drug discovery [230]

Despite the molecular mass is the know parameter of a compound, what is actually measured in a mass spectrometer are individual ions, and the true units of the measurement are kilograms per Coulomb. The transformation of molecules into ions is done in the ion source.

In an electron impact ionisation source electrons are produced through thermionic emission by heating a wire filament that has electric current running through it. The electrons are the accelerated to 70 eV before entering to the ion source block and then concentrated into a beam by being attracted to the trap electrode. Then the neutral molecules of the sample are introduced to the ion source in a perpendicular direction to the electron beam. The passage of energetic electrons causes large fluctuations in the electric field around the neutral molecules inducing ionization and fragmentation. The positive ions (cations) are then diverted towards the mass analyzer by repeller electrodes called quadrupoles.

Mass separation in a quadrupole is achieved thanks to the ion motion in a dynamic radio frequency electric field and is dependent directly on the ratio mass to charge (m/z) of the ion (figure 3.10). The mass resolution is a function of the ratio of the radio frequency and dc voltages and is often varied such that unit resolution is obtained over the whole mass range. Practically the mass analysis is achieved by making ion trajectories unstable in a mass-selective manner. Depending on the physical parameters of the quadrupole, the upper m/z limit can vary from 200 to 4000; the mass accuracy is generally in the hundreds of ppm.

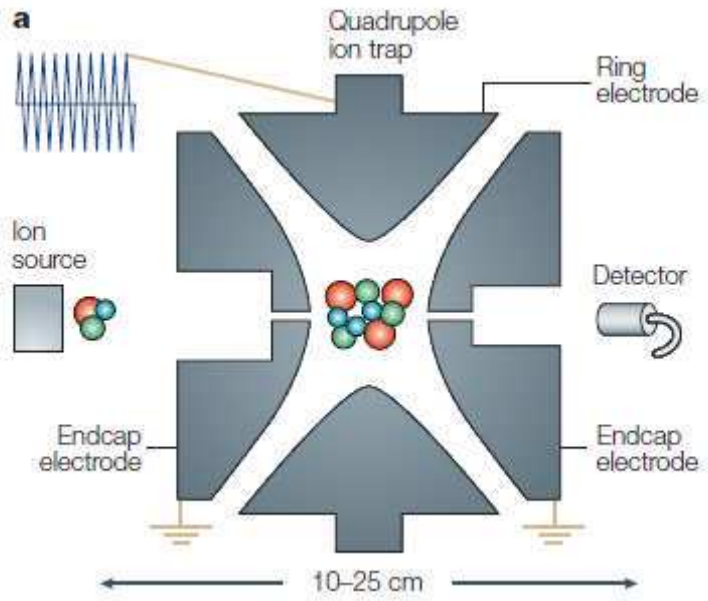

Figure 3.10 Ions in a quadrupole ion trap maintain stable trajectories inside the device as a result of the application of a radio frequency voltage to the ring electrode. [230]

Incident ions may have a wide range of energies, with 500–1500 eV being typical for mass spectrometry applications. At these energies, the incident ions have more than one collision with the walls of the Faraday cup detector. The trapping process for this detector is to drop the ion momentum and kinetic energy each time that the incident ion scatter off of the cup walls and ultimately becoming physisorbed onto the inner conducting surface of the cup, to which its carried charge is added (figure 3.11).

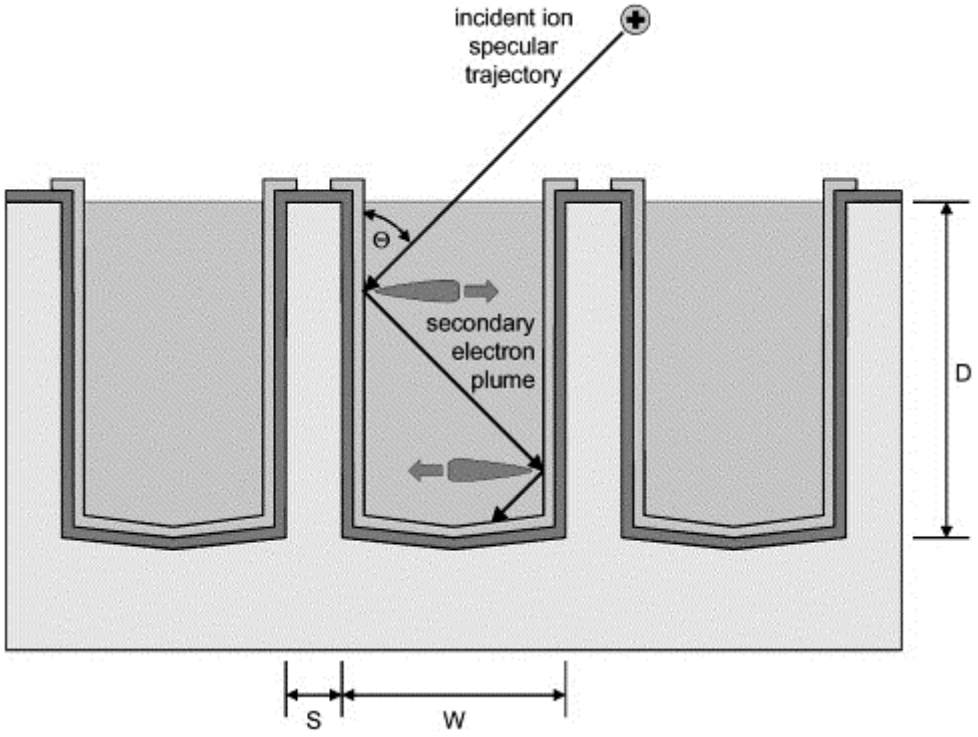

Figure 3.11 Ion capture processes within a Faraday cup [231]

This then draws electrons up to the Faraday bucket and these are measured with a sensitive amplifier within the radio frequency head. The secondary emission multiplier (SEM) detector is an off axis detector. By applying a large negative voltage to the front end, ions are pulled into it. They then hit the surface and start a cascade of electrons. The SEM voltage is tuned to give the same signal as the Faraday and this then gives the SEM a 1000 times gain in signal.

Main applications of MS analysis are: reaction monitoring and optimization, assessment of library compound quality and structural analysis of library products.

4. Results

4.1. Introduction

The results are presented in this chapter in the following sections: section 4.2 shows in detail the characterisation of the pristine carbon nanostructures and the nanostructures after various oxidative treatments with H_2O_2 and after single metal (Pd) impregnation and subsequent metal reduction with either H_2 or $NaBH_4$. Section 4.3 gives results of a different metal impregnation (Ni) onto GNF and section 4.4 shows the results for mixed metal impregnations Pd-Ni Pd-Cu and Pd-Ag onto the carbon nanocones. The results of the hydrogen adsorption studies at 77 K and room temperature are presented in section 4.5 with post characterisation of these structures. The analysis of the processing route of the decomposition of the organimetallic precursor dibutyl magnesium (DBM) to form a metal hydride is given in section 4.6.1. Section 4.6.2 details the results for the coupling of carbon nanostructure with metal hydrides and complex hydrides. The final section 4.7 shows such synthesized hydride in mixture with another hydride.

4.2. Metal loaded and unloaded carbon nanostructures

Table 4.1 reports a list of the samples under analysis in this thesis specifying which treatments they have undergone. Nanocones are labelled as (NC) the H_2O_2 oxidative treatment is identifying with code “OX” and then the metal and its weight percentage is reported followed by the type of reduction used (H is for the H_2 hydrogen reduction and B is for $NaBH_4$ reduction). GNF has been already introduced as for graphite nanofibres, as well as DBM stands for dibutyl Magnesium and for $LiAlH_4$ obviously has been used the chemical

formulae. So for example the sample NCOXPD10NI10H is the carbon nanocones sample initially oxidized with H_2O_2 which has been impregnated with 10 wt% Pd and 10 wt% of Ni and then the metal has been reduced with hydrogen.

Table 4.1 List of sample and their sequence of treatments

Sample Name	**H_2O_2 oxidation**	**Metal impregnation**	**H_2 reduction**	**$NaBH_4$ reduction**	**Ar thermal decomposition**
NC					
NCOX	x				
NCOXPD5H	x	Pd 5 wt%	x		
NCOXPD10H	x	Pd 10 wt%	x		
NCOXPD15H	x	Pd 15 wt%	x		
NCOXPD5B	x	Pd 5 wt%		x	
NCOXPD10B	x	Pd 10 wt%		x	
NCOXPD15B	x	Pd 15 wt%		x	
NCOXPD10NI10H	x	Pd 10 wt% Ni 10 wt%	x		
NCOXPD10CU10B	x	Pd 10 wt% Cu 10 wt%		x	
NCOXPD28AG10B	x	Pd 28.5 wt% Ag 10 wt%		x	
GNF					
GNFOX	x				
GNFOXPD5H	x	Pd 5 wt%	x		
GNFOXPD10H	x	Pd 10 wt%	x		
GNFOXPD15H	x	Pd 15 wt%	x		
GNFOXPD5B	x	Pd 5 wt%		x	
GNFOXPD10B	x	Pd 10 wt%		x	
GNFOXPD15B	x	Pd 15 wt%		x	
GNFOXNI10H	x	Ni 10 wt%	x		
NCDBM					x
DBM					x
LIALH4DBM					x
x = treatment applied					

The nanocone sample NC as received was a mixture of soot (figure 4.1. b), nanodiscs (figure 4.1 a) and nanocones (figure 4.1 b) in a distribution of 81 % discs (size 1-3 μm) 14 % soot (size below 0.5 μm) and 5 % cones (size 0.8-2.5 μm) respectively.

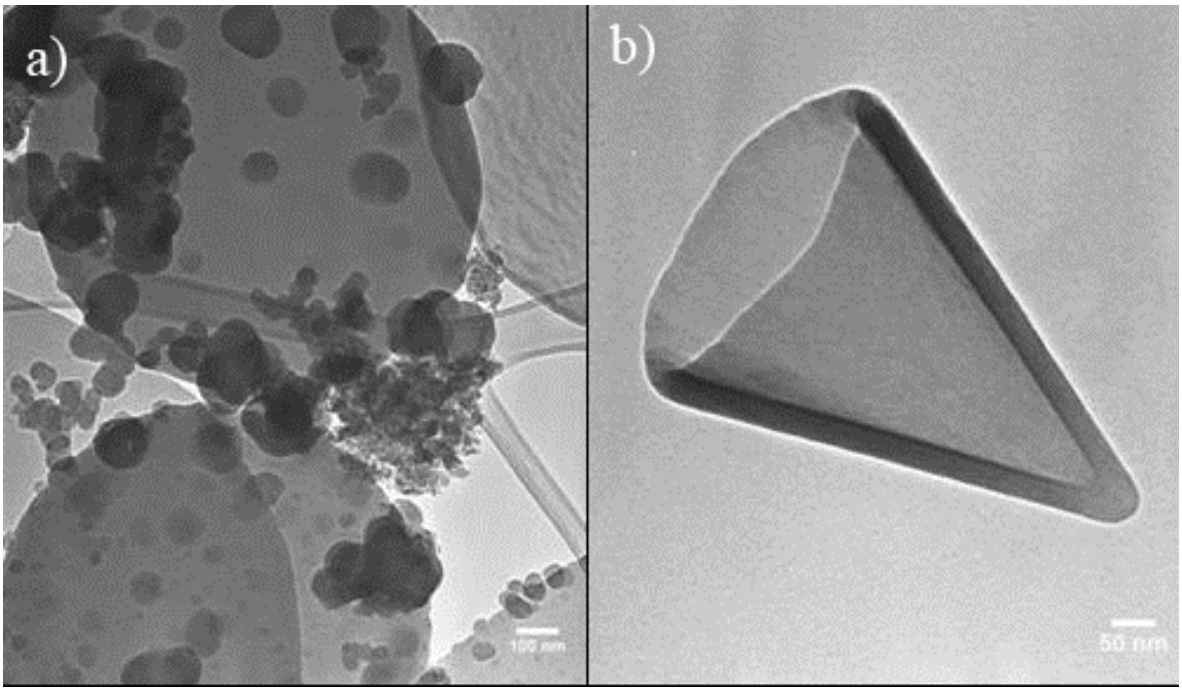

Figure 4.1 TEM images of as received nanocones (NC) sample being a mixture of (a) carbon nanodisc and (b) carbon nanocones

TEM revealed that the carbon nanostructures had been etched by the oxidative treatment and sometimes the nanostructure was cracked and broken apart, as illustrated in figure 4.2.

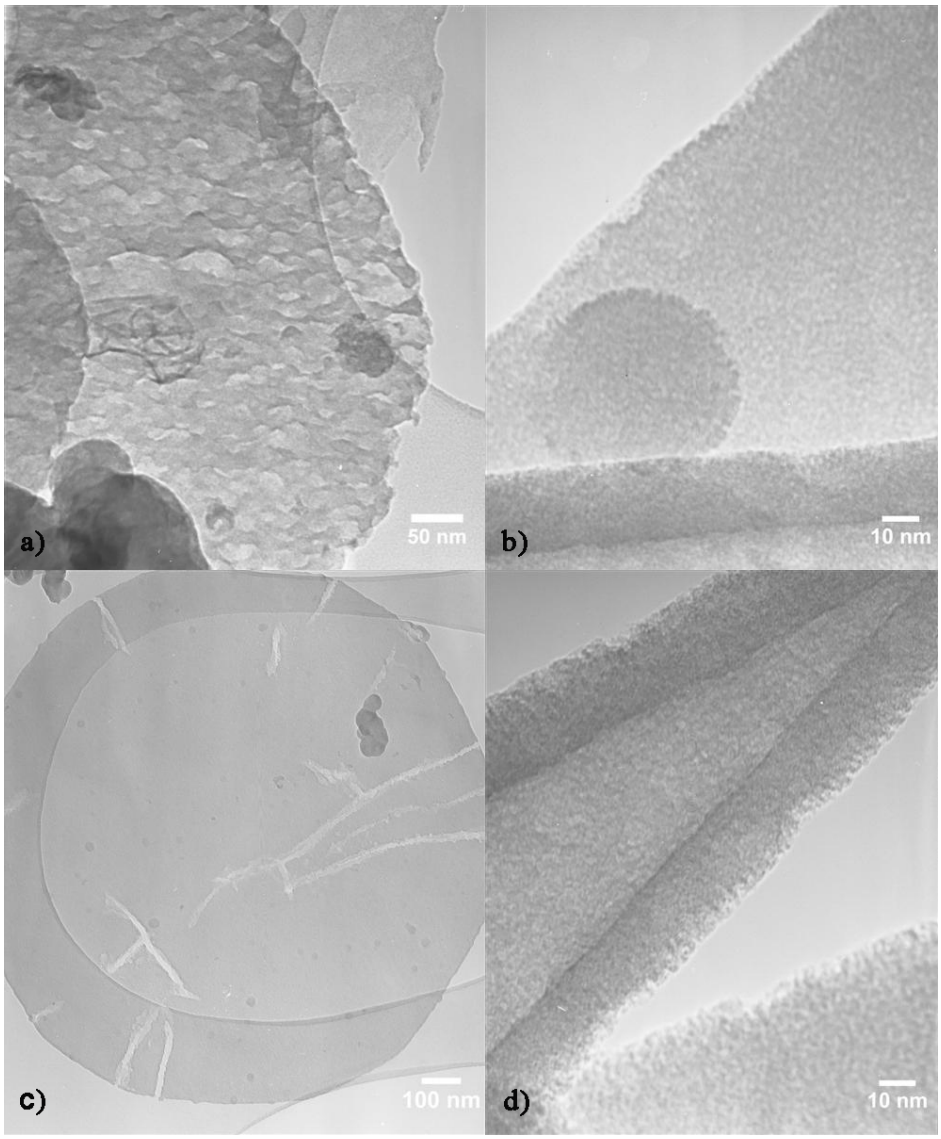

Figure 4.2 TEM images of a nanocone sample after H_2O_2 oxidative treatment (NCOX) a) surface pitting of a nanodisc; b) etching of a nanodisc and nanocone; c) cracks in a nanodisc; c) surface etching of a nanocone

The impregnation procedure by incipient wetness led to an average particle size of metal oxide of 2.5 nm for 5 wt% metal content (figure 4.3 a, the dark spots represent the particles). Reducing with H_2 at 300 °C achieved an average particle size of 3.3±0.2 nm on a sample of 430 particles. Since the considerable increase of particle size the Pd metal has been reduced with H_2 at RT led to an average particle size of (2.3 ±0.1) nm for Pd 5 wt% (NCOXPD5H), and (3.1 ±0.09) nm and (4.5 ±0.2) nm for Pd 10 wt% (NCOXPD10H) and Pd

15 wt% (NCOXPD15H) respectively (figures 4.3 b, c and d). $NaBH_4$ reduction achieved a smaller grain size of (1.2 ±0.03) nm (3.6 ±0.07) nm and (4.3 ±0.5) nm for samples impregnated with Pd 5 wt% (NCOXPD5B), Pd 10 wt% (NCOXPD10B) and Pd 15 wt% (NCOXPD15B), respectively (figures 4.3 e, f and g). The results are listed in table 4.2.

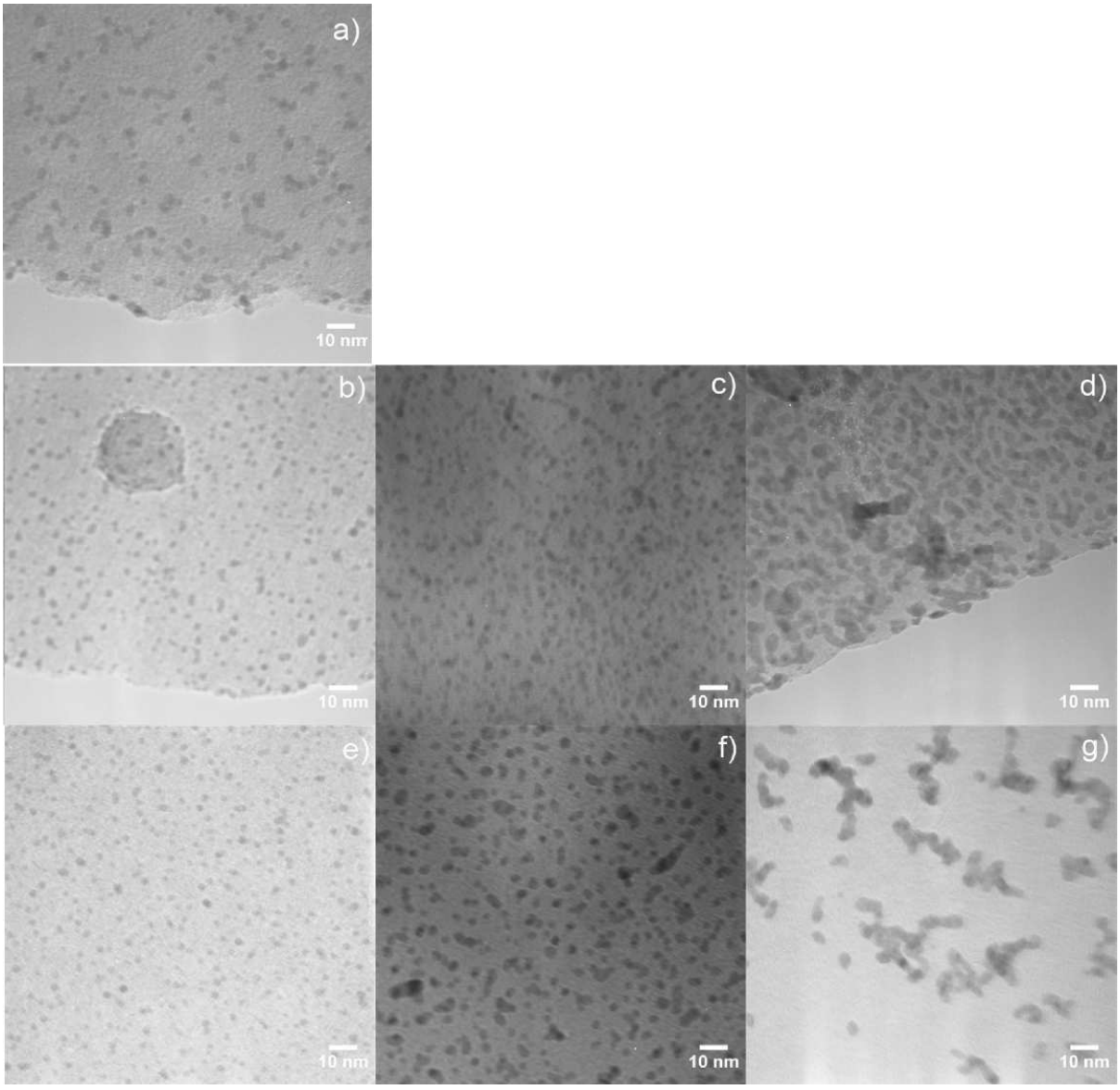

Figure 4.3 TEM images of Pd loaded nanocone samples a) after incipient wetness impregnation with Pd 5 wt% but before H_2 reduction and b) after subsequent reduction by either H_2 at RT for the sample impregnated with Pd 5 wt% (NCOXPD5H), c) with Pd 10 wt% (NCOXPD10H) and d) with Pd 15 wt% (NCOXPD15H), or e) after reduction with

$NaBH_4$ at RT for the sample impregnated with Pd 5 wt% (NCOXPD5B), f) with Pd 10 wt% (NCOXPD10B) and g) with Pd 15 wt% (NCOXPD15B)

Table 4.2 Results of particle size image analysis of the Pd loaded nanocones at 5 wt%, 10wt% and 15wt% reduced with H_2 and with $NaBH_4$

Sample	**Particle size (nm) (± standard error)**	**Number of particles**
NC	-	
NCOXPD5 (impregnated non oxidated)	2.5±0.1	265
NCOXPD5H	2.3±0.1	463
NCOXPD10H	3.10±0.09	346
NCOXPD15H	4.5±0.2	290
NCOXPD5B	1.20±0.03	433
NCOXPD10B	3.60±0.07	464
NCOXPD15B	4.3±0.5	130

Graphite nanofibre samples (GNF) were prepared by a carbon vapour deposition (CVD) technique over a NiO catalyst precursor. The GNFs made had a diameter ranging between 50 nm and 250 nm, figure 4.4, and that the GNFs formed were of the platelet and herringbone type.

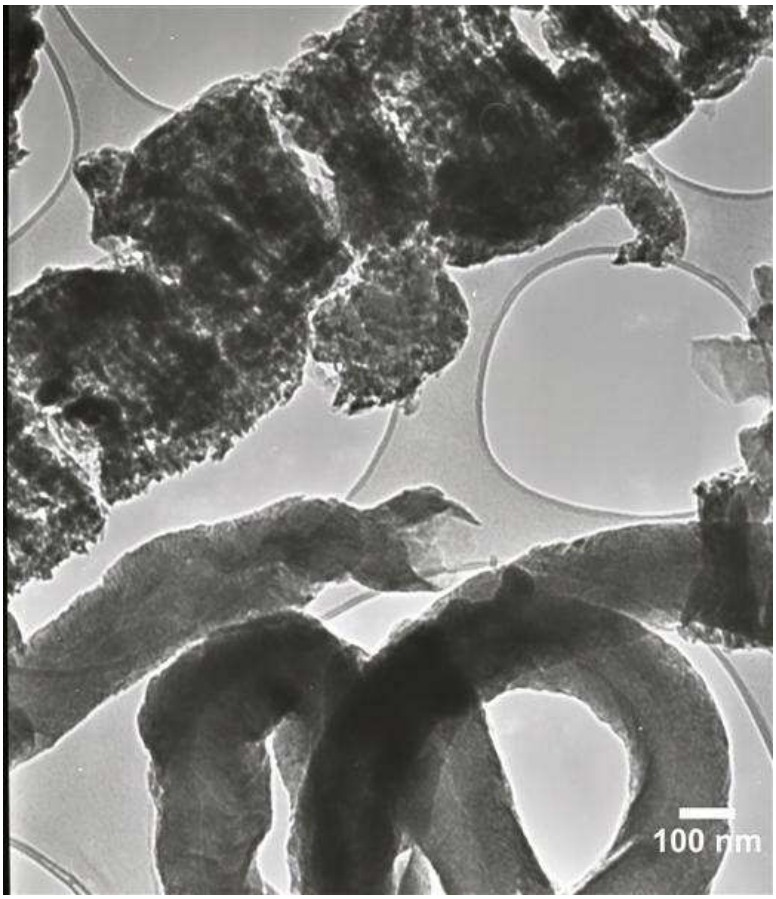

Figure 4.4 TEM image of as prepared GNF sample

After the oxidative treatment the GNF sample, the TEM images showed that the material had changed in morphology for example the platelet fibres had become dislodged and misaligned between each other, as shown in figure 4.5.

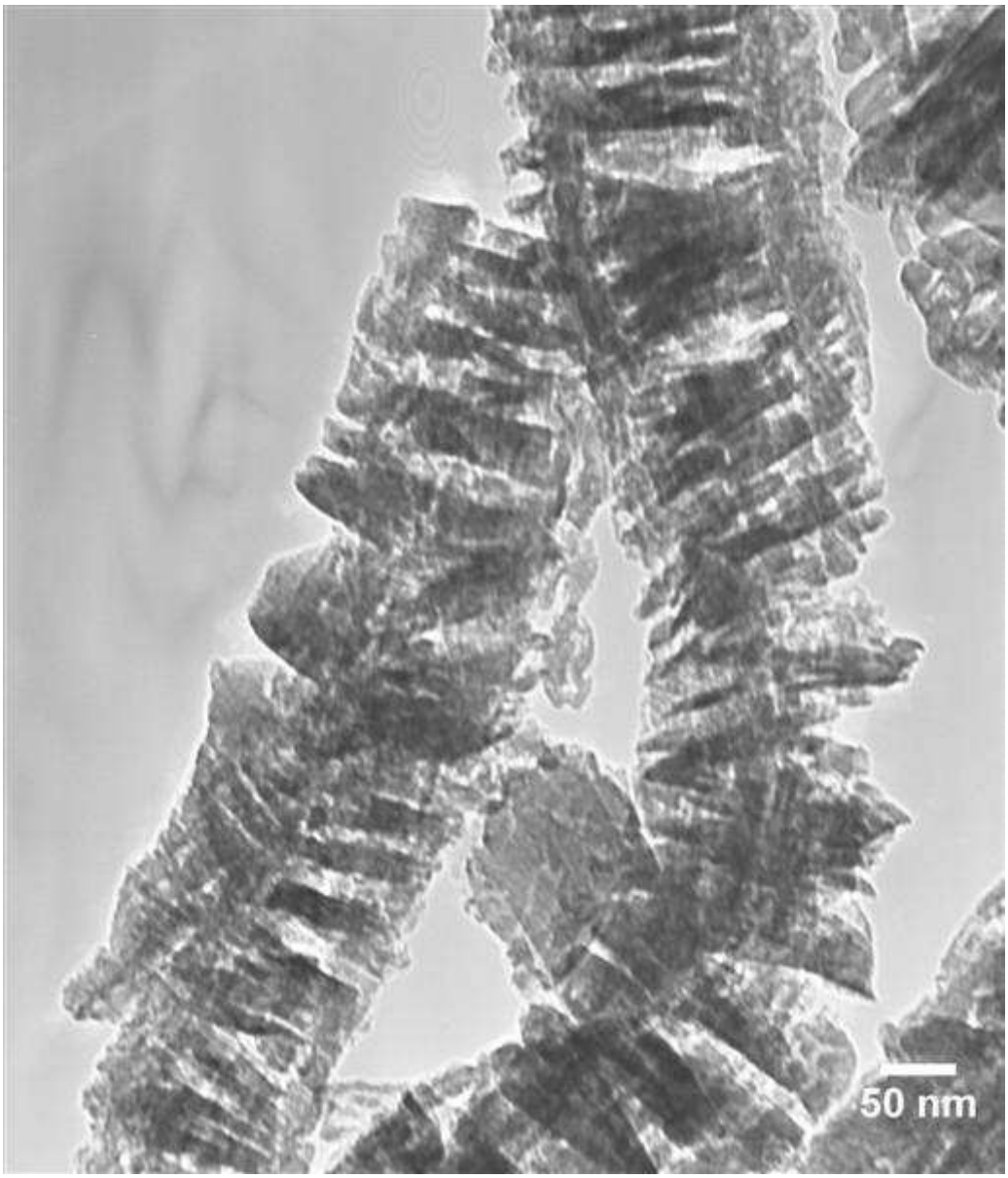

Figure 4.5 TEM image showing an example of structural modification of a platelet type of GNFOX graphite nanofibre after oxidative treatment with H_2O_2

The particle dispersion for the Pd loaded GNF samples was found to have, after reduction with H_2 at RT, an average particle size of (3.34±0.18) nm for Pd 5 wt% (GNFOXPD5H), and (4.24±0.24) nm and (3.84 ±0.11) nm for Pd 10 wt% (GNFOXPD10H) and Pd 15 wt% (GNFOXPD15H) respectively (figures 4.6 a, b and c). After a $NaBH_4$ reduction the grain size was found to be (4.6 ±0.24) nm (3.7 ±0.09) nm and (4.17±0.09) nm

for samples impregnated with Pd 5 wt% (GNFOXPD5B), Pd 10 wt% (GNFOXPD10B) and Pd 15 wt% (GNFOXPD25B) (Figures 4.6 d, e and f). Table 4.3 summarizes these results.

Table 4.3 Results of particle size image analysis of the Pd loaded GNF at 5wt%, 10wt% and 15wt% reduced with H_2 and with $NaBH_4$

Sample	**Particle size (nm) (± standard error)**	**Number of particles**
GNFOXPD5H	3.3±0.2	321
GNFOXPD10H	4.2±0.2	235
GNFOXPD15H	3.8 ±0.1	189
GNFOXPD5B	4.6 ±0.2	112
GNFOXPD10B	3.7 ±0.1	394
GNFOXPD15B	4.2±0.1	283

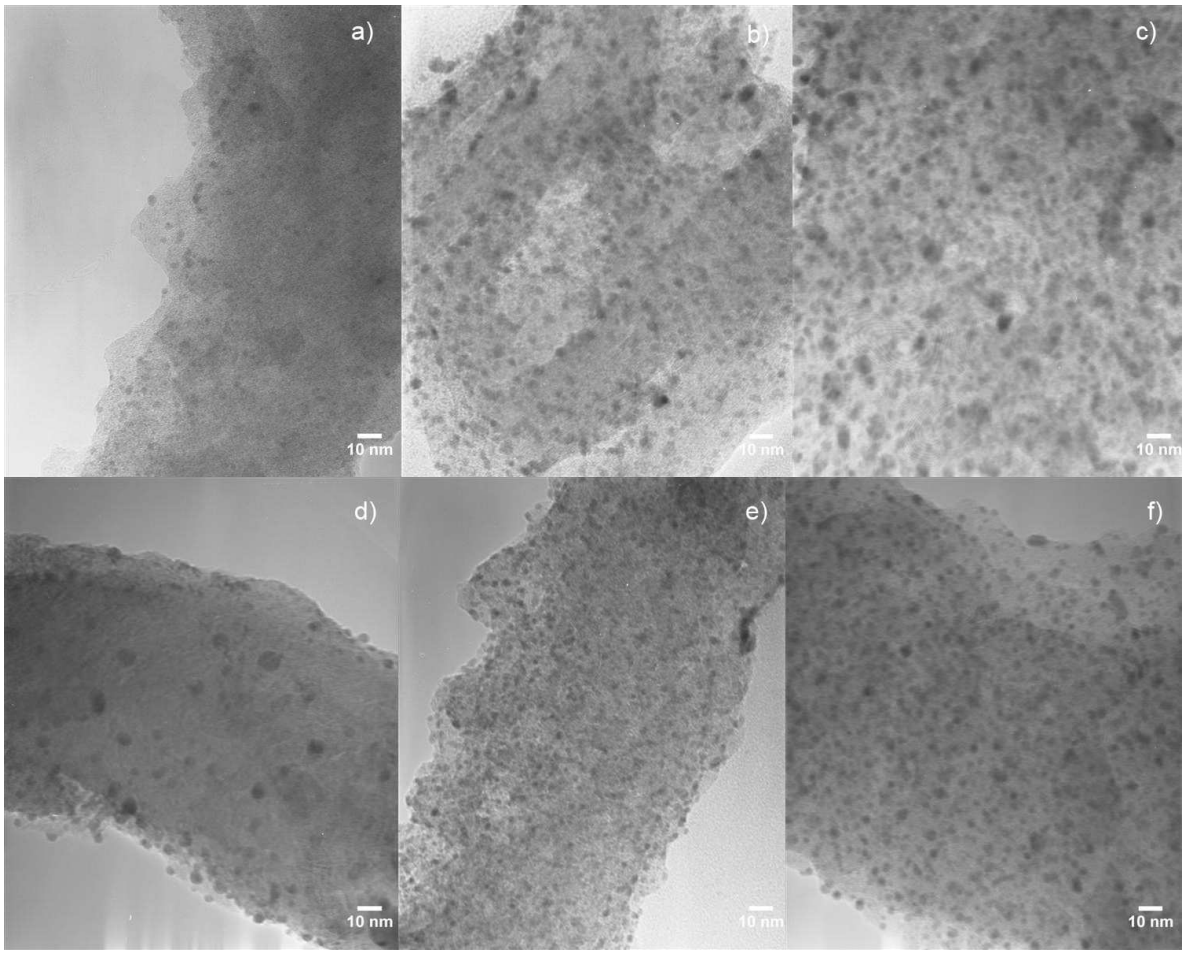

Figure 4.6 TEM images of GNF samples after incipient wetness impregnation and reduced with H_2 at RT, a) impregnated with Pd 5 wt% (GNFOXPD5H), b) with Pd 10 wt%

(GNFOXPD10H) and c) Pd with 15 wt% (GNFOXPD15H) and samples reduced with $NaBH_4$ at RT and impregnated with d) Pd 5 wt% (GNFOXPD5B), e) with Pd 10 wt% (GNFOXPD10B) and f) with Pd 15 wt% (GNFOXPD15B).

The BET surface area measured for the as received carbon nanocones NC was 22 $m^2 g^{-1}$. The surface area for the oxidized sample NCOX was 27 $m^2 g^{-1}$, signifying that there was a small increase in surface area considering an experimental error or 5%

For the GNF sample was 148 $m^2 g^{-1}$ and after the oxidation the surface area was found to have increased to 181 $m^2 g^{-1}$ (sample GNFOX).

The surface area and the pore volume for the nanocones and GNF impregnated with Pd at different impregnation, as well as those for carbon nanocones and GNF both as received and oxidized, are summarized in table 4.4.

Table 4.4 Surface area and pore volume data for carbon nanocones and GNF at different metal loadings

Sample	Surface area ($m^2 g^{-1}$)	Pore volume ($cm^3 g^{-1}$)
NC	22.5±1.1	0.088±0.004
NCOX	27.3±1.4	0.173±0.009
GNF	148.1±7.4	0.277±0.014
GNFOX	181.4±9.1	0.297±0.015
NCOXPD5B	26.8±1.3	0.074±0.004
NCOXPD10B	27.1±1.4	0.12±0.006
NCOXPD15B	20.44±1.02	0.117±0.006
GNFOXPD5B	234.3±11.7	0.49±0.024
GNFOXPD10B	99.18±4.96	0.347±0.017
GNFOXPD15B	101.32±5.05	0.141±0.007

Figure 4.7 illustrates a typical XRD pattern of the as received nanocone material and after the oxidative treatment and subsequent metal loading. The as received material had an intense broad peak at 2θ of 25.82 ° (d_{002} = 3.43 Å) and a second graphite reflection at a 2θ of

43.14 ° (d_{100} = 2.11 Å). The XRD pattern for the oxidised carbon nanocone sample (treated with H_2O_2) was similar to the as received material.

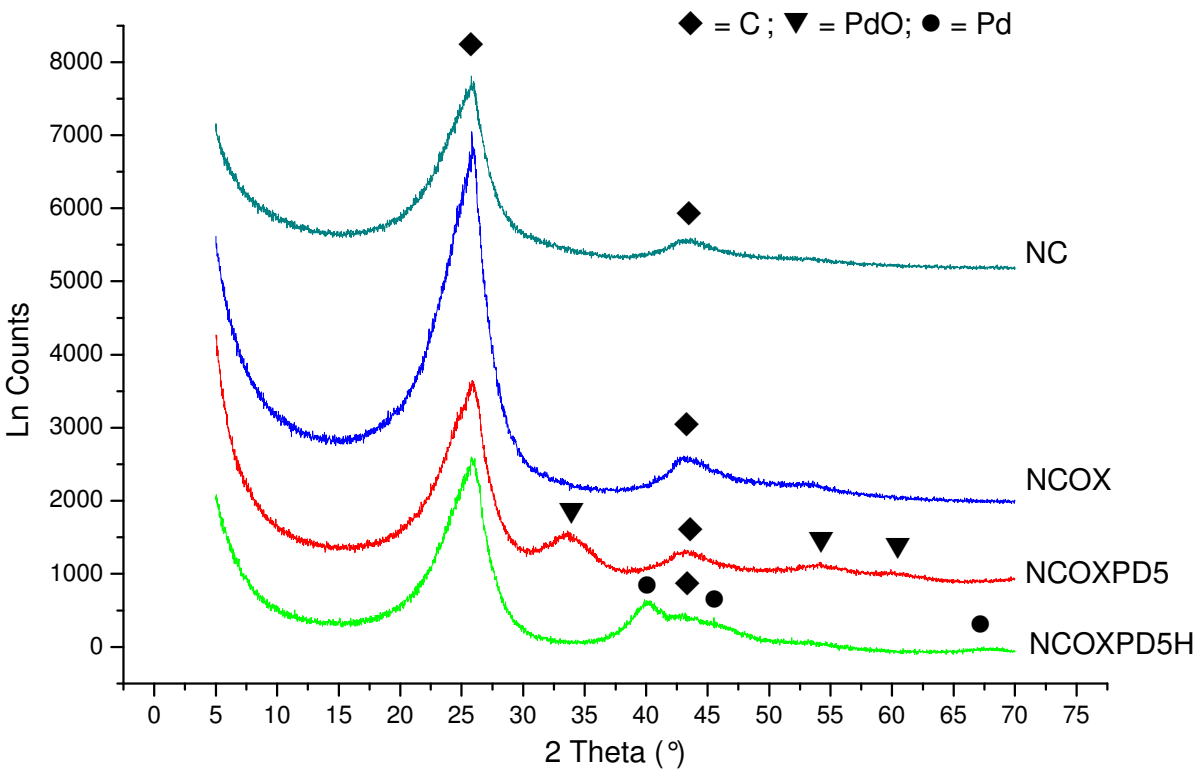

Figure 4.7 XRD pattern for an as received carbon nanocone sample and after the material has been oxidized with H_2O_2, impregnated with Pd before the reduction and after the metal reduction with either H_2 or $NaBH_4$

No significant change was identified by XRD between the as received nanocones sample and the oxidized nanocones sample. In the XRD pattern corresponding to the nanocones sample decorated with Pd, but before reduction, there was a PdO characteristic peak at a 2θ of 33.62 ° (d_{101} = 2.66 Å), a 2θ of 54.62 ° (d_{112} = 1.66 Å) and a 2θ of 60.17 ° (d_{103} = 1.53 Å) observed. Once reduced with H_2, only peaks corresponding to Pd metal were

found at 2θ values of 40.11 ° (d_{111} = 2.24 Å), 46.65 ° (d_{200} = 1.94 Å) and 68.28 ° (d_{220} = 1.37 Å). For the reduction using $NaBH_4$ the same characteristic pattern for Pd metal was present and no oxide.

The XRD pattern of the GNF as synthesized (figure 4.8.) shows a peak at 2θ of 26.04 ° (d_{002} = 3.43 Å) a second graphite reflection at a 2θ of 43.04 ° (d_{100} = 2.11 Å) and a third reflection at a 2θ of 53.4 ° (d_{101} = 2.02 Å).

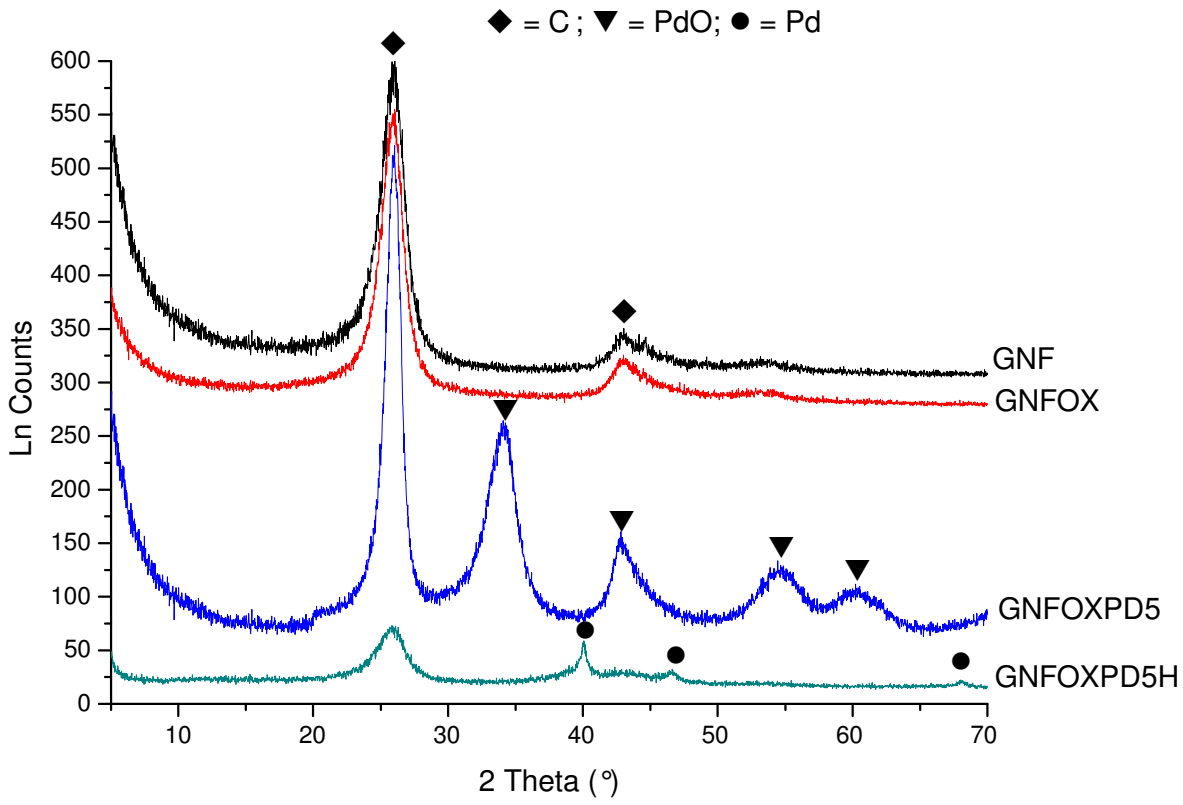

Figure 4.8 XRD pattern of graphite nanofibres as prepared

The oxidized GNFs had similar XRD peaks as before, figure 4.10., at 2θ of 26.04 ° (d_{002} = 3.43 Å), a second graphite reflection at a 2θ of 43.04 ° (d_{100} = 2.11 Å) and a third reflection at a 2θ of 53.4 ° (d_{101} = 2.02 Å).

The GNF decorated with Pd showed also a PdO phase present with characteristic peaks at a 2θ of 33.62 ° (d_{101} = 2.66 Å), at a 2θ of 54.62 ° (d_{112} = 1.66 Å) and at a 2θ of 60.17

° (d_{103} = 1.53 Å). After reduction either by H_2 or by $NaBH_4$ the PdO phase was no longer present and for Pd there was only the metal phase resulting in reflections at 2θ values of 40.11 ° (d_{111} = 2.24 Å), 46.65 ° (d_{200} = 1.94 Å) and 68.28 ° (d_{220} = 1.37 Å).

4.3. Impregnation with other metal catalysts

The impregnation with Ni metal has been done with incipient wetness technique starting from an aqueous solution of Ni salt obtaining a dispersion of NiO over the carbon nanostructure. The reduction to Ni metal was performed in an H_2 atmosphere at 300°C for 3 h. Figure 4.9 is a typical TEM image of a GNF sample impregnated with the Ni salt and with Ni metal after the reduction with hydrogen at high temperature. The average particle size measured from 31 particles was found to be 11.8 ±2.1 nm

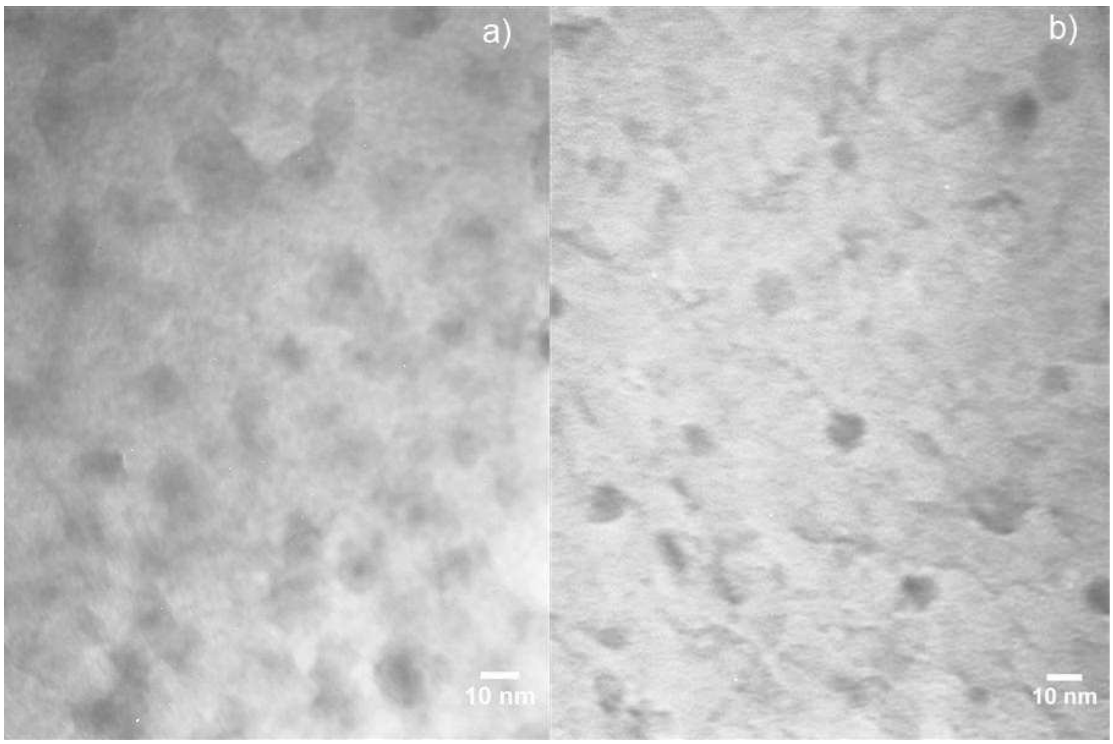

Figure 4.9 TEM image of carbon nanocones impregnated with Ni salt a) before reduction and b) after the reduction with H_2.

Figure 4.10 shows the XRD pattern of a GNF sample impregnated with Ni salt by the method described in section 3.2. The XRD pattern corresponds to a NiO phase at a 2θ of 37.25° (d_{111} = 2.41 Å), a 2θ of 43.28 ° (d_{200} = 2.08 Å) and a 2θ of 62.87 ° (d_{103} = 1.47 Å). The oxide phase was no longer present after the reduction process and the sample only had X-ray reflections for Ni metal phase, i.e. peaks at a 2θ of 44.49° (d_{111} = 2.03 Å) and a 2θ of 51.82 ° (d_{200} = 1.76 Å).

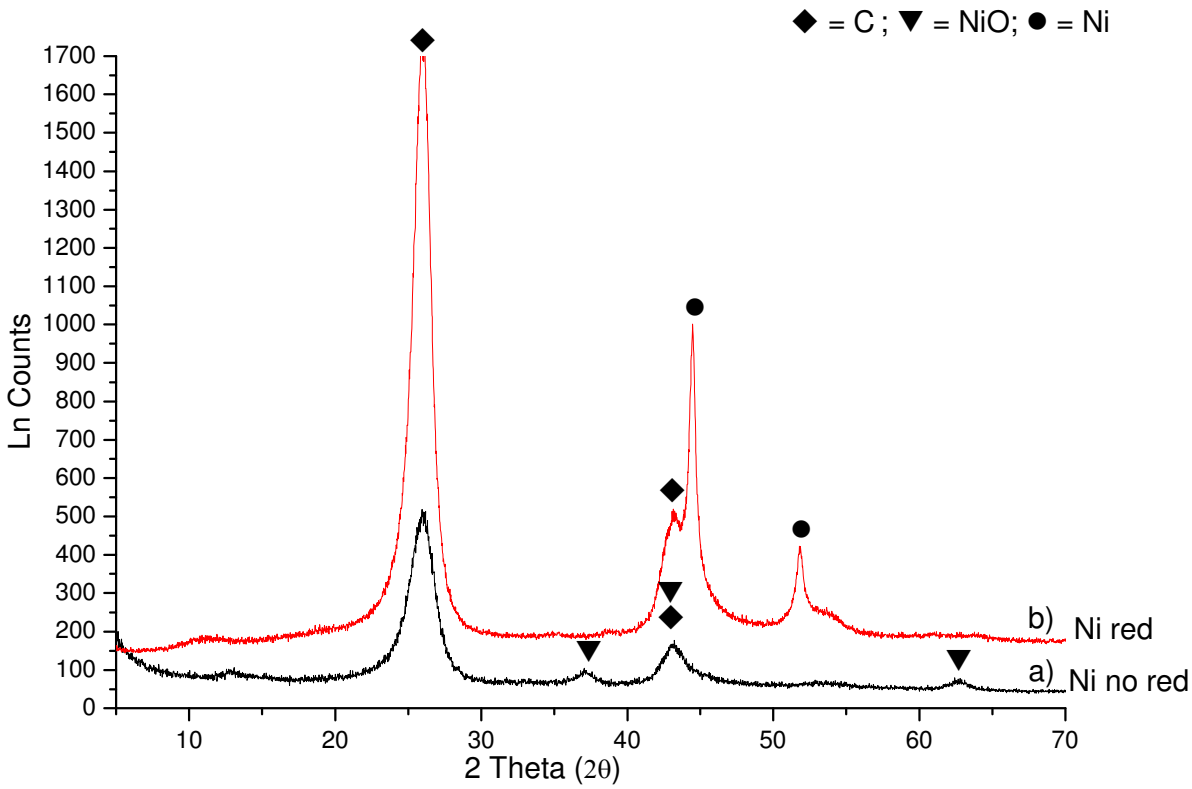

Figure 4.10 Typical XRD patterns of GNF impregnated with Ni salt a) before the reduction and b) after reduction with H_2.

4.4. Mix impregnation with binary alloys

This sub-section presents the results of attempts to develop a mixed metal impregnation route for carbon nanocones with Pd, and light transition metals, such as Ni, Cu and Ag. All the impregnations were done with incipient wetness technique using the aqueous solution of the metal salt. Figure 4.11 a) shows the particle distribution of carbon nanocones impregnated with Pd 10wt% and Ni 10wt% reduced in H_2 atmosphere at 300°C for 3 h (NCOXPD10NI10H). The particle size obtained was 4.4 ±0.2 nm out of 344 particles. For sample with the mixed impregnation of Pd-Cu (NCOXPD10CU10B), the metals could be reduced with $NaBH_4$ in aqueous solution at RT. The particle size obtained was 5.6 ±0.3 nm from a sample of 79 particles (figure 4.11 b). The sample with impregnation of Pd-Ag (NCOXPD28AG10B) was also reduced by $NaBH_4$ in aqueous solution at RT. The particle size obtained from a sample of 120 particles was 6.6±0.3 nm (figure 4.11 c).

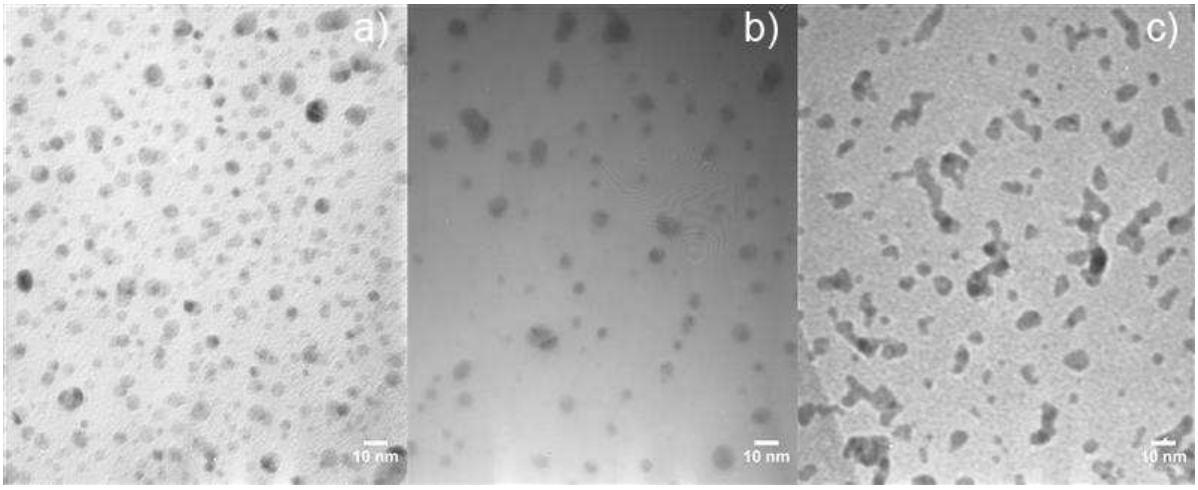

Figure 4.11 TEM images for a carbon nanocone sample impregnated with a) Pd 10wt% and Ni 10wt% (NCOXPD10NI10H), b) Pd 10wt% and Cu 10wt% (NCOXPD10CU10B), c) Pd 28.5 wt% Ag 10wt% (NCOXPD28AG10B) (corresponding to Pd 76 at%-Ag 24 at%).

Figure 4.12 is an XRD pattern of carbon nanocones impregnated with Pd 10wt% and Ni 10wt% reduced in H_2 atmosphere at 300°C for 3 h. Peaks observed were at a 2θ of 41.09 ° (d = 2.18 Å) , attributed to Pd (Pd, d_{111} = 2.24 Å), as well as the one at 2θ of 48.23 ° (d = 1.88 Å) (Pd, d_{200} = 1.94 Å) and 69.58 ° (d_{220} = 1.34 Å). For the sample impregnated with Pd and Cu the corresponding XRD pattern shows a broad peak at a 2θ of 41.53 ° (d = 2.17 Å) which is attributed to Pd (Pd, d_{111} = 2.24 Å), as well as the one at 2θ of 47.91 ° (d = 1.89 Å) (Pd, d_{200} = 1.94 Å) and 69.28 ° (d_{220} = 1.35 Å). The XRD pattern corresponding to the sample impregnated with Pd and Ag shows a broad peak at a 2θ of 38.79 ° (d= 2.32 Å) which is attributed to Pd (Pd, d_{111} = 2.24 Å), as well as the one at 2θ of 45.84 ° (d = 1.97 Å) (Pd, d_{200} = 1.94 Å) and 65.59 ° (d = 1.42 Å) (d_{220} = 1.35 Å). As possible to notice from figure 4.12 and from the values given in table 4.5 the Pd peaks are shifted at different d spacing when alloyed with Ni, Cu and Ag. Table 4.5 summarize the Pd peak positions in each of these three samples.

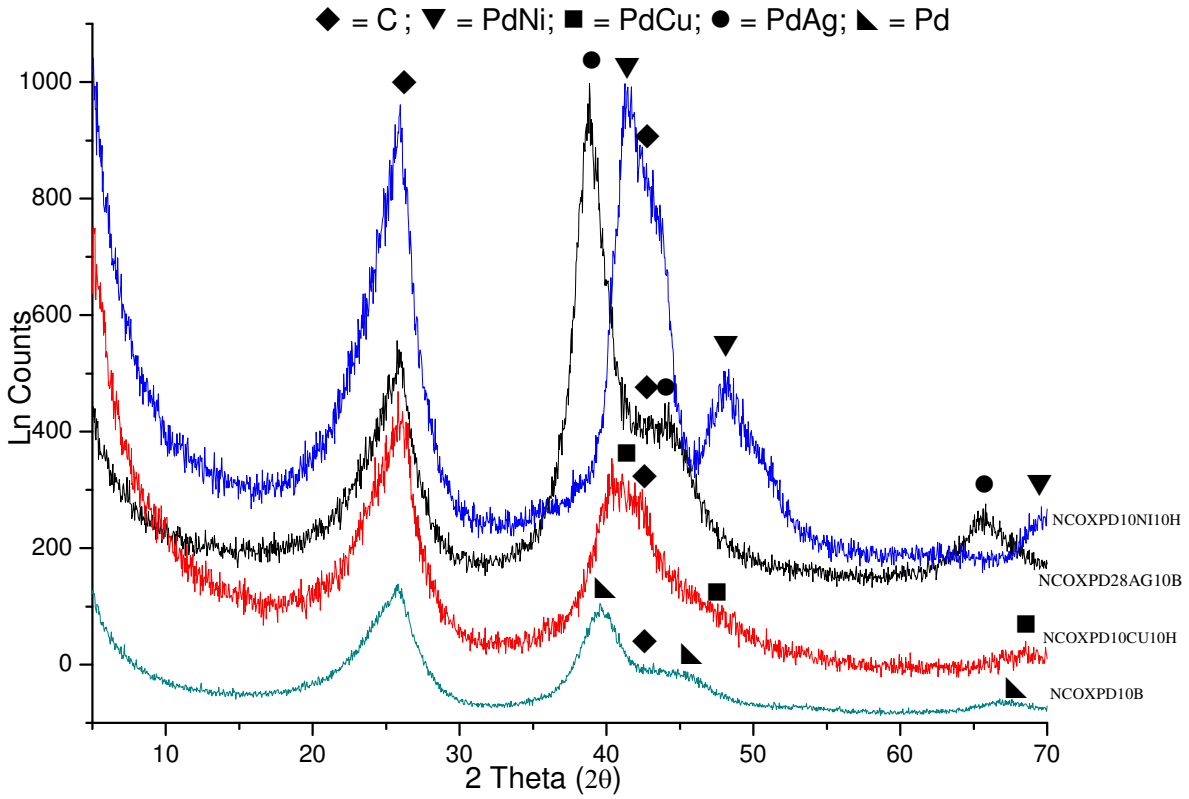

Figure 4.12 XRD pattern for the carbon nanocones samples impregnated with binary alloys PdNi (NCOXPD10NI10H), PdCu (NCOXPD10CU10B) and PdAg (NCOXPD28AG10B), showing the Pd peaks for the alloy sample being shifted in reference with the sample decorated with only Pd.

Table 4.5 Peaks position for Pd peaks in carbon nanocones samples impregnated with Pd and Pd-M binary alloys (M= Ni, Cu, Ag)

Sample	Main Pd peak (2θ)
Pd	40.11 ° (d_{111} = 2.24 Å)
PdNi	41.09 ° (d_{111} = 2.18 Å)
PdCu	41.53 ° (d_{111} = 2.17 Å)
PdAg	38.79 ° (d_{111} = 2.32 Å)

4.5. Hydrogen uptakes

Table 4.6. and figure 4.13 and figure 4.14 summarise the excess hydrogen uptake results at 77 K and RT for the carbon nanocone and GNF samples from the starting material through the oxidizing process and at various metal loads.

For the nanocones samples the hydrogen uptake at 77 K there is a decrease from 0.119 wt% of the as received nanocones sample to 0.105 wt% for the sample decorated with Pd 5 wt%, 0.084 and 0.51 for the samples decorated with Pd 10 wt% and with Pd 15 wt% respectively. For GNF samples at temperature of 77 K seems that there is not an evident trend with the GNF as synthesized having a hydrogen uptake of 0.502 wt%, and an uptake of 0.718 wt%, 0.444 wt% and 0.700 wt% for the samples decorated with Pd 5 wt%, Pd 10 wt% and Pd 15 wt% respectively.

For the measurement at RT the nanocones samples and the GNF decorated with Pd an increase of the uptake of hydrogen is observed with the increase of Pd content. For the as received nanocones sample starting with an uptake of 0.019 wt% and uptakes of 0.065 wt%, 0.076 wt% and 0.113 wt% for the nanocones samples impregnated with Pd 5 wt%, Pd 10 wt% and Pd 15 wt% respectively. For the as synthesized GNF an uptake of 0.016 wt% and increasingly 0.131 wt%, 0.169 wt% and 0.229 wt% for the GNF samples impregnated with Pd 5 wt%, Pd 10 wt% and Pd 15 wt% respectively. For the GNF sample impregnated with Ni 10 wt% the hydrogen uptake measured was 0.072 wt%. For the nanocones samples impregnated with mixed catalysts the hydrogen uptake was 0.080 wt%, 0.097 wt% and 0.154 wt% for the samples impregnated with Pd 10 wt% and Ni 10 wt%, Pd 10 wt% and Cu 10 wt% and Pd 28.5 wt% and Ag 10 wt% respectively.

Table 4.6 Hydrogen uptake results at 77 K and at RT for various samples of carbon nanocones and GNF

Sample	**H_2 uptake at 77 K (wt%)**
NC	0.119±0.001
NCOXPD5B	0.105±0.001
NCOXPD10B	0.084±0.001
NCOXPD15B	0.051±0.001
GNF	0.502±0.002
GNFOXPD5B	0.718±0.004
GNFOXPD10B	0.444±0.002
GNFOXPD15B	0.700±0.003
Sample	**H_2 uptake at RT (wt%)**
NC	0.0193±0.0001
NCOXPD5B	0.0650±0.0003
NCOXPD10B	0.0763±0.0004
NCOXPD15B	0.1139±0.0006
GNF	0.0161±0.0001
GNFOXPD5B	0.1314±0.0006
GNFOXPD10B	0.1695±0.0008
GNFOXPD15B	0.229±0.001
GNFOXNI10H	0.0725±0.0004
NCOXPD10NI10H	0.0798±0.0004
NCOXPD10CU10B	0.0967±0.0005
NCOXPD28AG10H	0.1541±0.0008

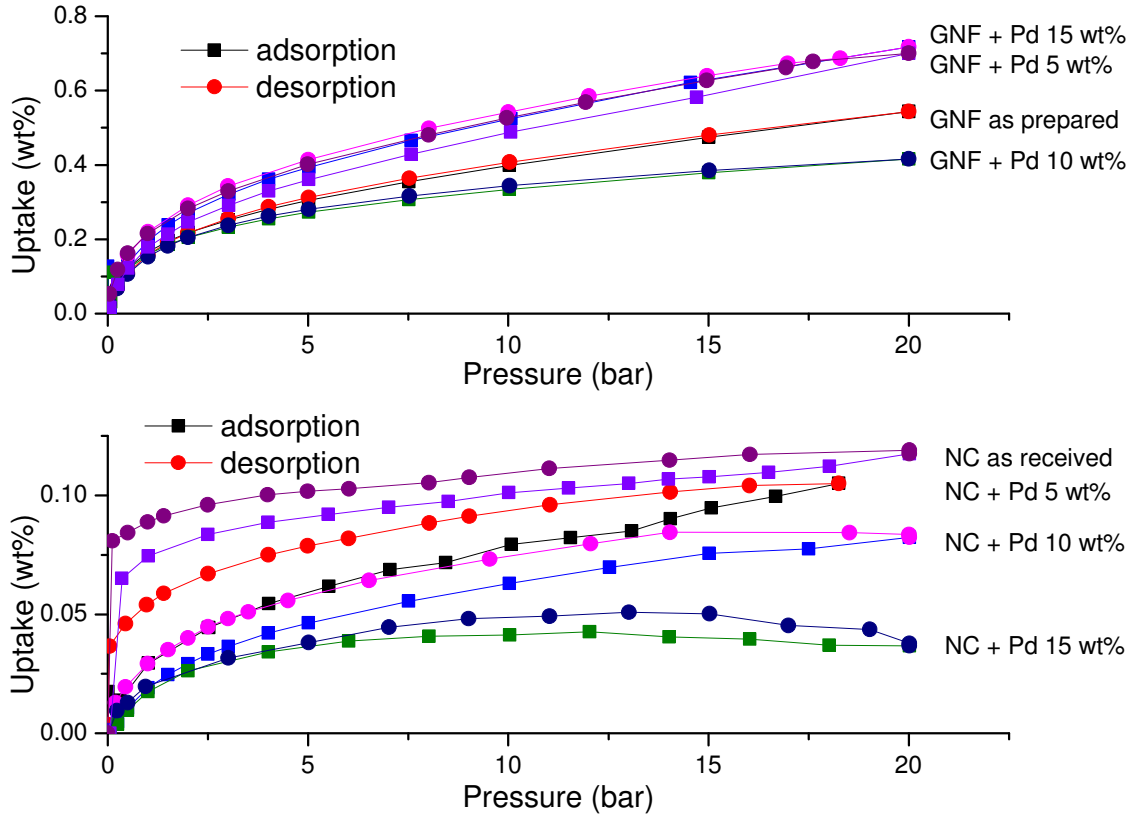

Figure 4.13 Hydrogen adsorption isotherms at 77 K for the GNF samples impregnated with Pd 5 wt%, Pd 10 wt% and Pd 15 wt% as well as for the nanocones samples samples impregnated with Pd 5 wt%, Pd 10 wt% and Pd 15 wt% respectively

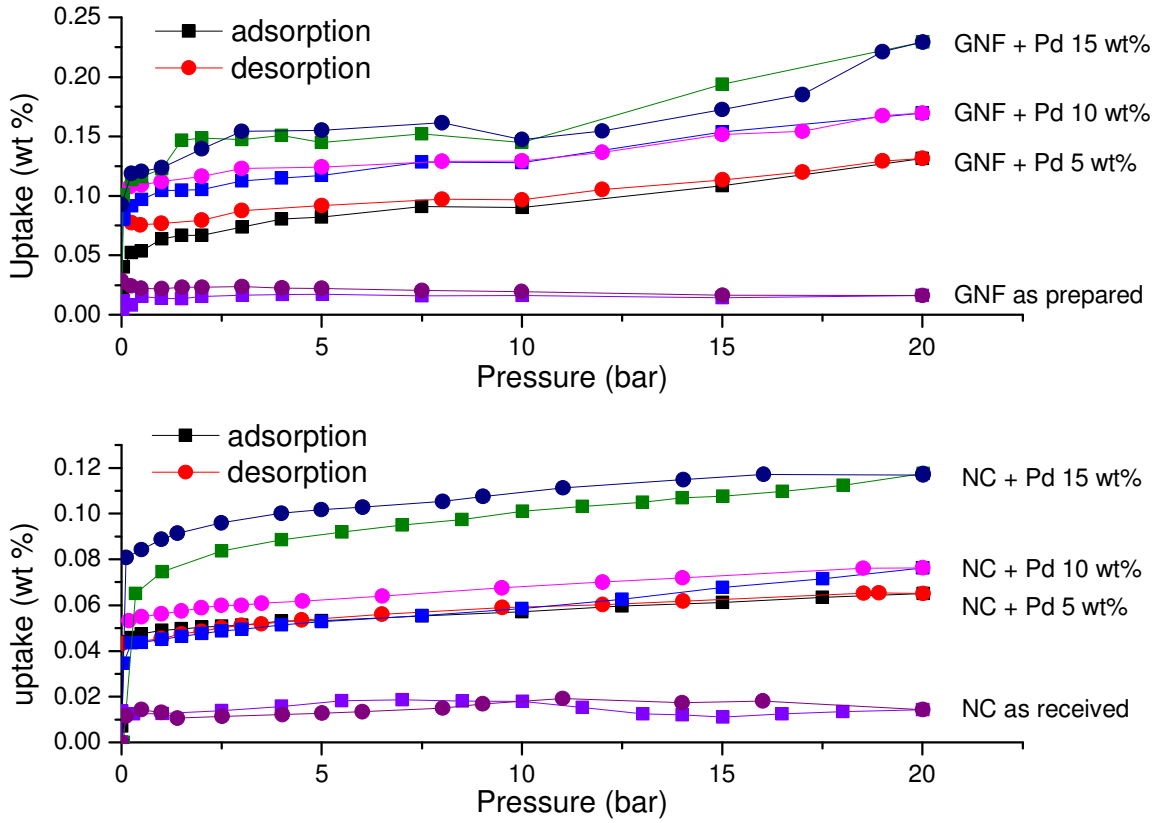

Figure 4.14 Hydrogen adsorption isotherms at RT for the GNF samples impregnated with Pd 5 wt%, Pd 10 wt% and Pd 15 wt% as well as for the nanocones samples samples impregnated with Pd 5 wt%, Pd 10 wt% and Pd 15 wt% respectively

4.6. Carbon nanostructure – hydride composites

In order to combine carbon nanocones with MgH_2 and /or $LiAlH_4$, the MgH_2 phase has been synthesized by the thermal decomposition in the thermogravimetric instrument of an organic precursor, dibutyl magnesium. Hence in sub-section 4.6.1 the pure compound DBM have been studied and the reactions occurring during the thermal decomposition. In addition to characterising the end hydrogen storage materials the process of decomposition of DBM has also been investigated in section 4.6.2.

4.6.1. Decomposition of DBM to form MgH_2

This section investigates the formation of magnesium hydride from DBM. The DBM is purchase in heptane solution and after evaporating off the solvent the starting material DBM has been analyzed at the XRD (figure 4.15). The pattern shows peaks at 2θ of 9.06° (d = 9.79 Å),12.79° (d = 6.93 Å), 18.90° (d = 4.68 Å), 20.27° (d = 4.37 Å), 21.02° (d = 4.22 Å), and 26.38° (d = 3.38 Å),.

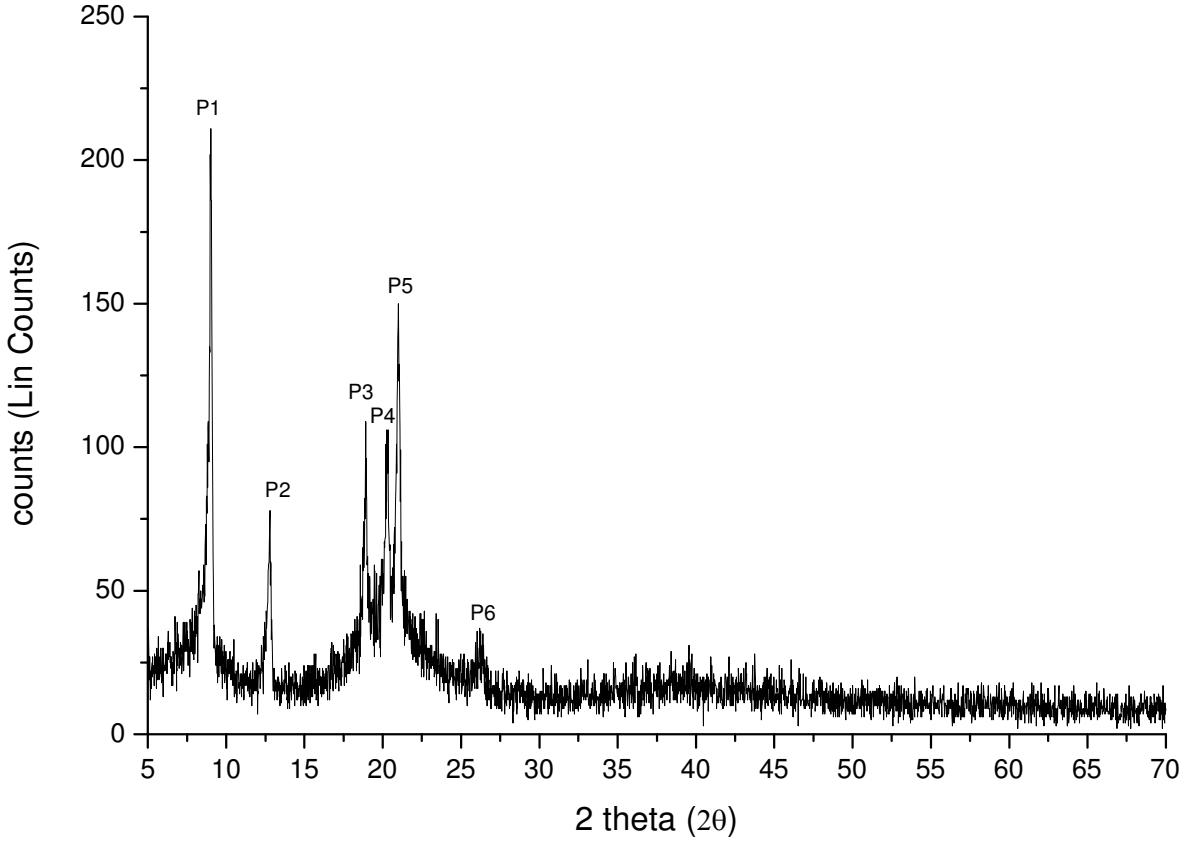

Figure 4.15 XRD pattern for crystallised DBM

The DSC analysis of the decomposition of DBM was performed with a heating ramp of 10 °C min^{-1} under 1 bar of Argon with a flow rate of 100 mL min^{-1} till a maximum temperature of 585 °C. The DSC curve for pure DBM shows two main peaks at 255 °C and 375 °C (figure 4.16). The heat content of the first event was 317 J g^{-1} and the second peak was 241 J g^{-1}. corresponding to a weight loss of 68% and 80% respectively.

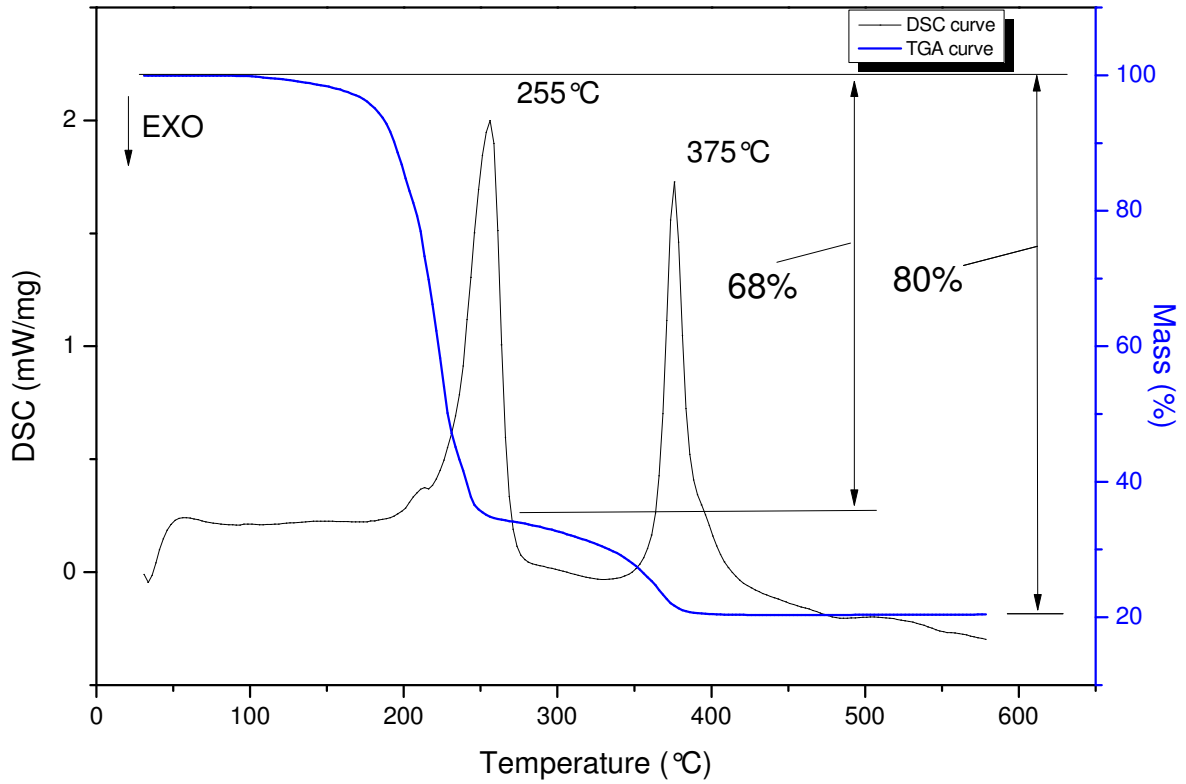

Figure 4.16 DSC-TGA data for crystallised DBM decomposed under Ar

In order to compare with experiments undertaken for the DBM-nanocone composites presented in the following section, the decomposition at 175 °C, 250 °C and 585 °C was repeated and the products analyzed by XRD and TGA analysis, figure 4.28. For the decomposition at 175 °C the XRD shows a very weak pattern for the formation of MgH_2 but peaks at 2θ of 18 ° and 21 ° still remain confirming the presence of DBM (figure 4.17). The decomposition of DBM at 175 °C had a corresponding weight loss of 36 %.

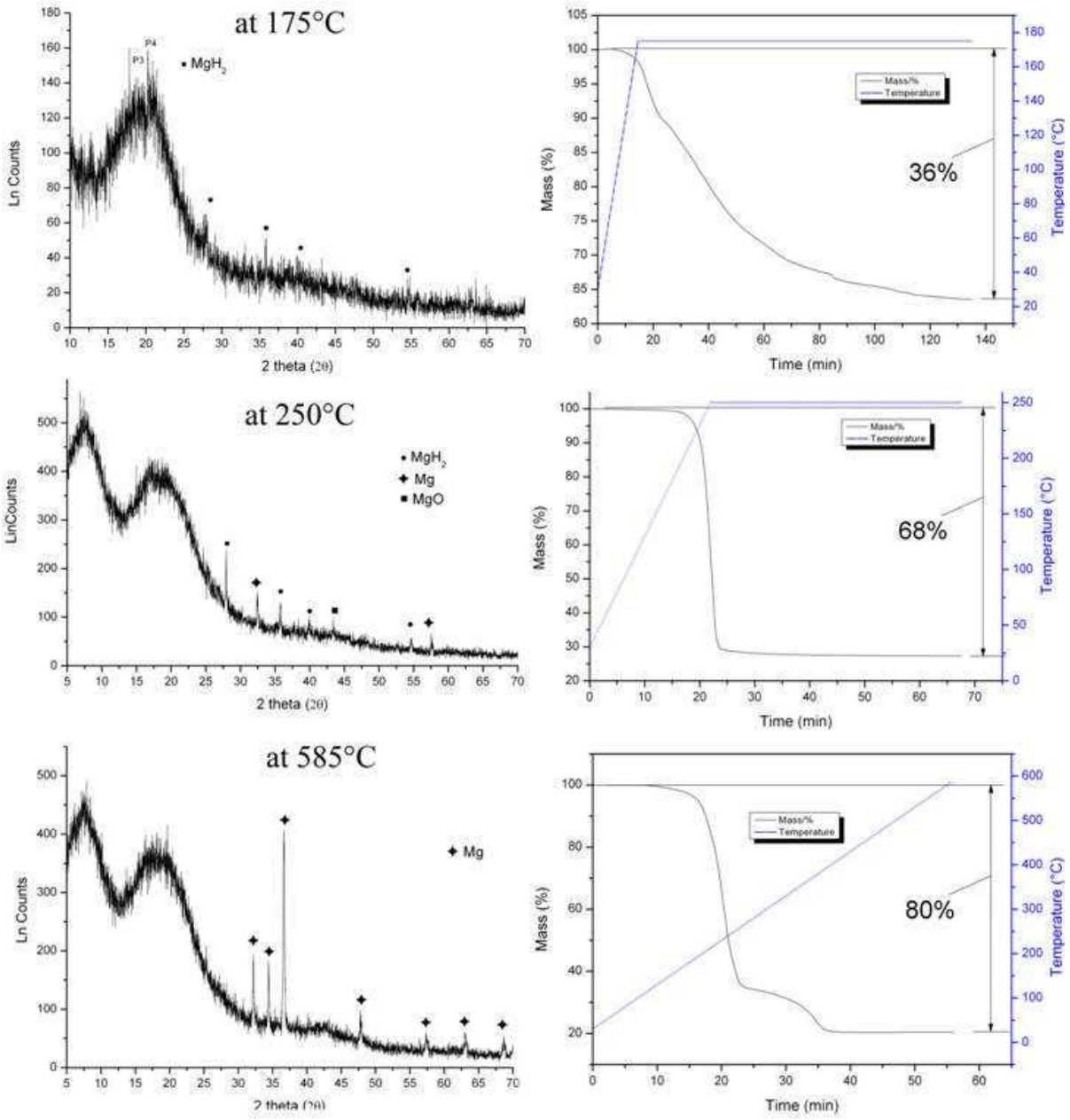

Figure 4.17 XRD and TGA patterns of pure DBM decomposition at 175 °C, 250 °C and 585 °C

The XRD pattern for the decomposition carried out at 250 °C (figure 4.15) showed the presence of MgH_2 (peaks at 2θ of 27.91 °, 35.73 °, 39.88 ° and 54.61°), and at 2θ of 32.44 ° and 57.16 ° identified as Mg metal. The corresponding weight loss for this sample was 68 %. There was an oxide contamination but this was attributed to contamination when transferring the sample to the XRD as there was no oxide formed for any of the other DBM

decomposition samples, ruling out contamination during the DSC-TGA. For the decomposition at 585 °C, XRD confirms the only presence of Mg with peaks at 2θ of 32.08° (d_{100} = 2.78 Å), 34.26° (d_{002} = 2.78 Å), 36.48° (d_{101} = 2.46 Å), 47.63° (d_{102} = 1.90 Å), 57.17° (d_{110} = 1.61 Å), 62.81° (d_{103} = 1.47 Å) and 67.07° (d_{200} = 1.39 Å). The corresponding weight loss was 80%.

Analysis of the TGA exhaust gases by MS showed the formation of butene (molar mass = 56 g mol^{-1}) as a by-product of the reaction. The following plot (figure 4.18) shows butene characteristic fragments peaks at m/z of 27, 28, 39, 41 and 56 when the temperature is held at 250 °C for 45 minutes and hydrogen (m/z = 2) peak at a temperature of about 370 °C. It is also plotted the pattern for fragment at m/z 43 which is the most intense peak for butane to demonstrate that no butane was formed.

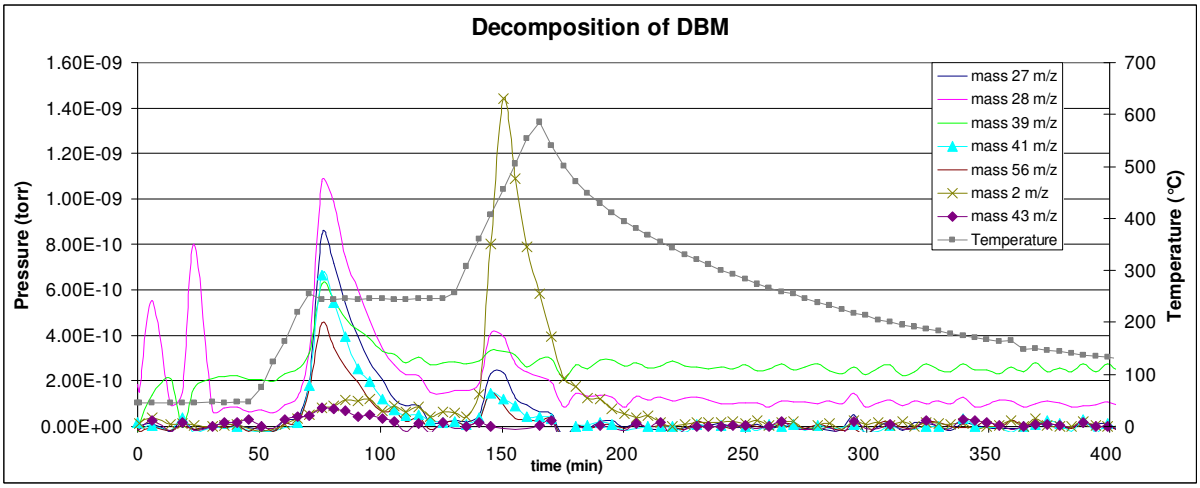

Figure 4.18 MS analysis of crystallised DBM during decomposition on the TGA showing the peaks in pattern of m/z of 2 (cross), 27, 28, 39, 41 (triangle), 43 (diamond) and 56 as well as the temperature profile (square)

FTIR analysis with ATR apparatus was used to characterize the DBM starting material as well as the ex situ products of the decomposition at 250 °C at different times. The

spectrum of the starting material DBM (figure 4.19 - top spectrum) shows a peak at 2955, 2922 and 2869 cm^{-1} falling into the range of overtone of C-H stretching of CH_3 and the peak at 1461, 1376 and 1061 cm^{-1} falling into the range of the C-H stretching of CH_2 .

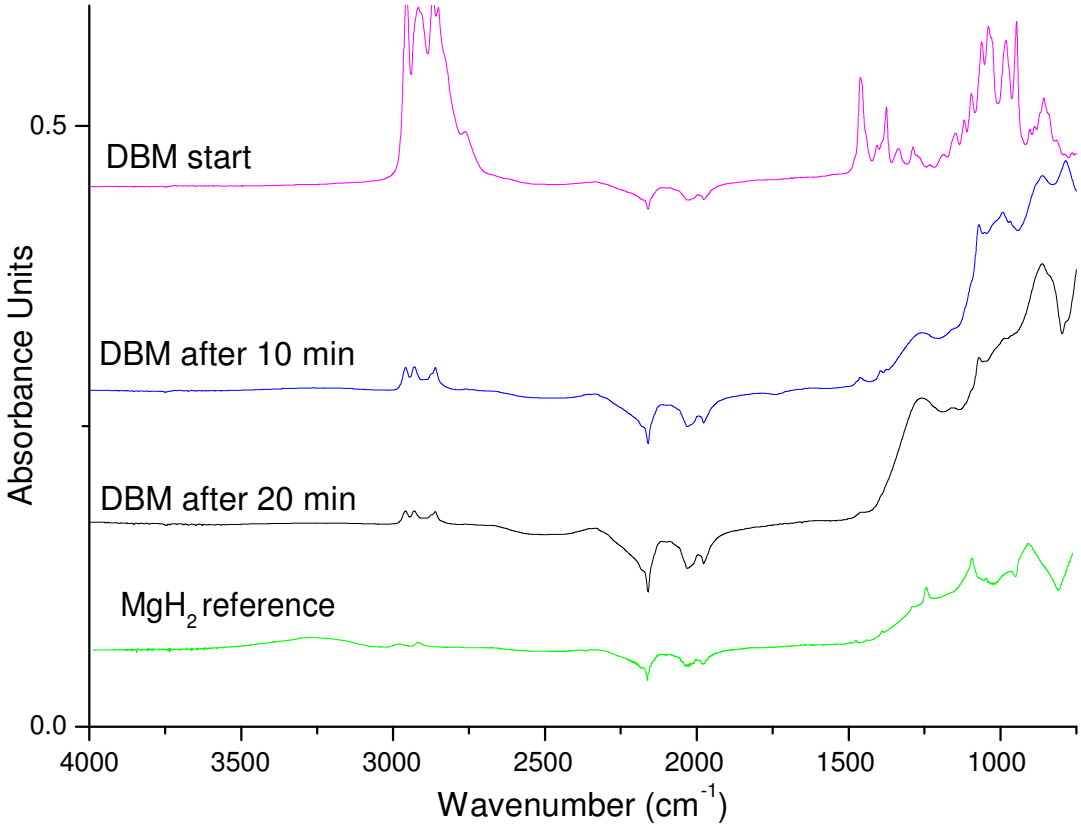

Figure 4.19 FTIR spectra under ATR mode of the products at different time points of the DBM decomposition at 250 °C in the TGA instrument compared with the spectrum of reference MgH_2

The intensities of the two groups of peaks characteristic of DBM, at 2955, 2922 and 2869 cm^{-1} and at 1461 and 1376 and 1061cm^{-1}, decrease through the course of the decomposition as shown in figure 4.17 pattern after 10 minutes and pattern after 20 minutes. The latter was compared with a spectrum for MgH_2 powder as purchased (Aldrich Chemicals

99 % pure) for comparison. The C-H stretching bands remaining at 2869 cm^{-1} were from grease on the mirrors.

4.6.2. Composites with MgH_2

The DSC analysis of the decomposition of nanocones impregnated with DBM was performed with a heating ramp of 10 °C min^{-1} under 1 bar of Argon with a flow rate of 100 mL min^{-1} up to a maximum temperature of 585 °C. The DSC curve for the decomposition of DBM impregnated onto the carbon nanocones had four endothermic reactions at 250 °C, 320 °C, 377 °C and 525 °C (figure 4.20). The weight loss for the complete decomposition was 29 %.

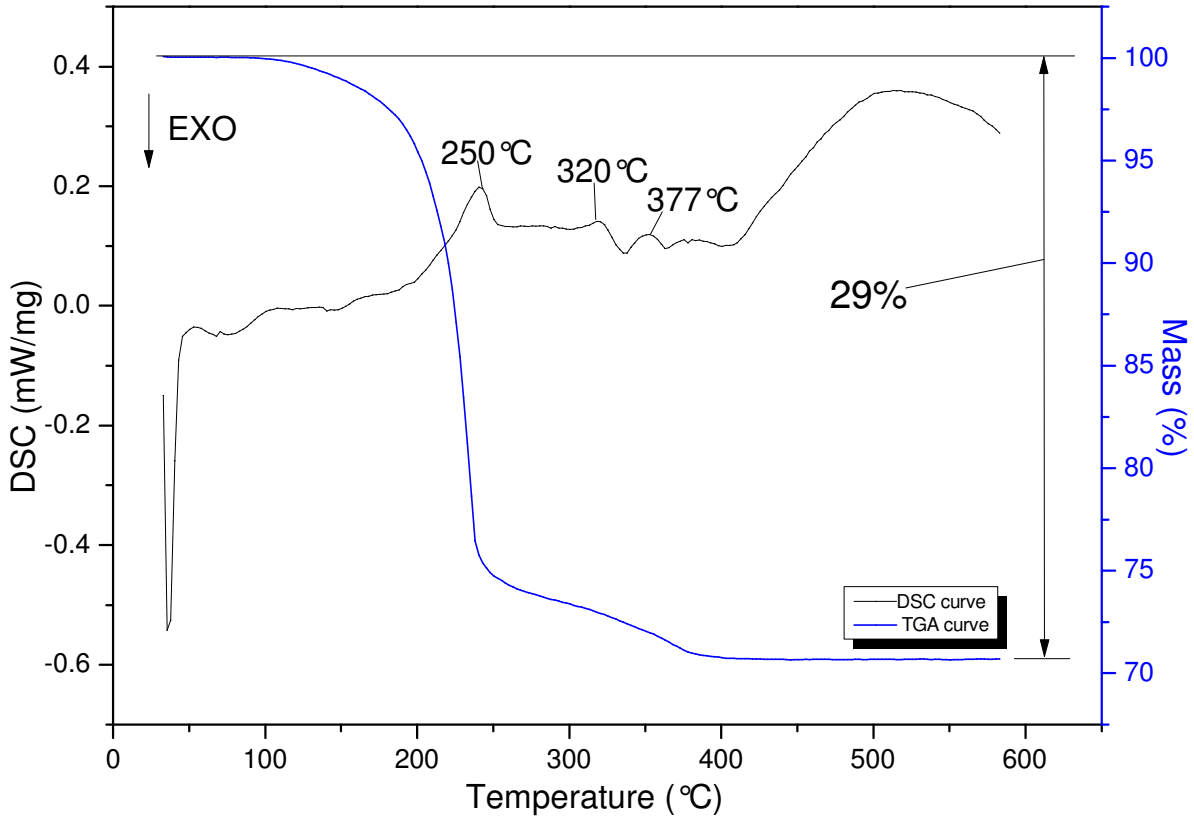

Figure 4.20 DSC-TGA data for the decomposition of DBM impregnated on carbon nanocones (NCDBM)

The XRD pattern for carbon nanocones impregnated with DBM, in comparison with the pattern of pure DBM and the pattern of pure carbon nanocones are shown in figure 4.21. The pattern for the sample carbon nanocones mixed with DBM shows the DBM characteristic diffraction peaks at 2θ of 9.06° 12.79° 18.90° 20.27° 21.02° and 26.38° (marked previously as P1, P2, P3, P4, P5 and P6). The peaks at 2θ of 25.82 ° (d_{002} = 3.43 Å) and at 2θ of 43.14 ° (d_{100} = 2.11 Å) belong to the carbon. The two wide peaks centred at 7° and 18° correspond to the diffraction of amorphous tape covering the sample to protect the sample from air.

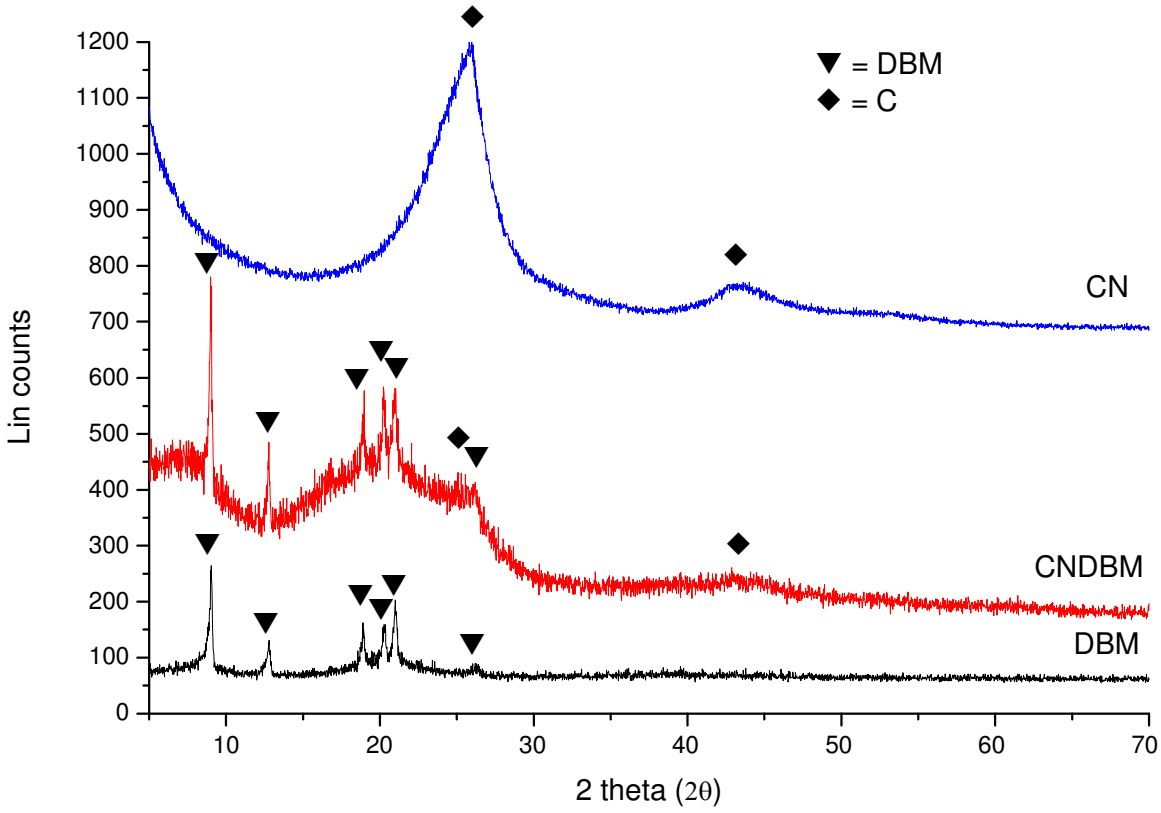

Figure 4.21 XRD patterns of cones impregnated with DBM (NCDBM)

Experiments to study the decomposition of DBM impregnated into nanocones under an Ar atmosphere were conducted at the following temperatures: 175 °C, 250 °C and 585 °C and the resulting products analysed by XRD, figure 4.22.

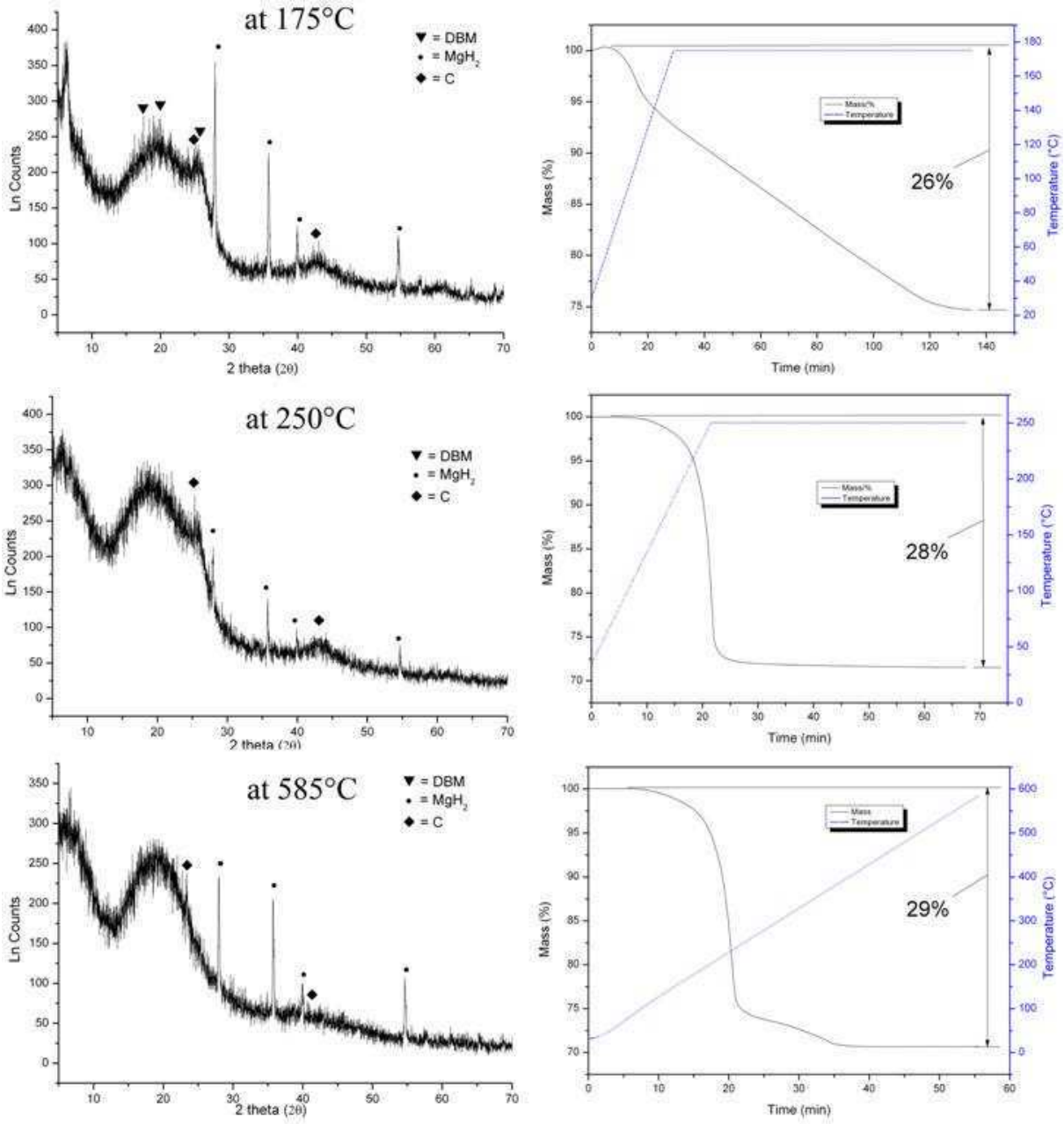

Figure 4.22 XRD patterns and TGA curves for the decomposition of DBM impregnated on carbon nanocones at 175 °C, 250 °C and 585 °C.

After a reduction at 175 °C for 2 h the XRD pattern of the resulting product (figure 4.20) shows the formation of MgH_2 with sharp peaks at 2θ of 27.91° (d_{110} = 3.19 Å), 35.73° (d_{101} = 2.51 Å), 39.88° (d_{200} = 2.25 Å) and 54.61° (d_{211} = 1.67 Å). The DBM is still present

with the peaks at 2θ of 18.90°, 21.02° and 26.38°. The peaks at 2θ of 25.82 ° (d_{002} = 3.43 Å) and at 2θ of 43.14° (d_{100} = 2.11 Å) corresponding to the carbon are unchanged. The TGA weight loss profile shows a slow and steady loss of 26%. For the decomposition at 250 °C a MgH_2 phase was identified by XRD with sharp peaks at 2θ of 27.91° (d_{110} = 3.19 Å), 35.73° (d_{101} = 2.51 Å), 39.88° (d_{200} = 2.25 Å) and 54.61° (d_{211} = 1.67 Å) but with a rapid weight loss of 28%. The grain size calculated from the Scherrer equation [232] gives an average particle size of 47 nm. For the decomposition at 585°C the XRD shows the same peaks corresponding to MgH_2 (2θ of 27.91°, 35.73°, 39.88° and 54.61°) despite the temperature is higher than the dehydrogenation of MgH_2. The weight loss was 29 %.

The bright field image (figure 4.23 a) shows the surface of a carbon nanodiscs decorated with quite large clusters agglomerated very close to each other. The dark field image (figure 4.23 b) shows more clearly the crystals. From the TEM dark field image of the DBM-nanocones sample decomposed at 250 °C, the crystallite size was found to be 29.9 ±3.8 nm (figure 4.23). The selected area diffraction (SAD) pattern exhibits the experimental lattice spacing of 3.21 Å belonging to MgH_2 (d_{110} = 3.19 Å) and a lattice spacing of 2.62 Å corresponding to MgH_2 (d_{101} = 2.51 Å) and the C (d_{101}) lattice spacing of 2.07 Å is the carbon (d_{100} = 2.11 Å).

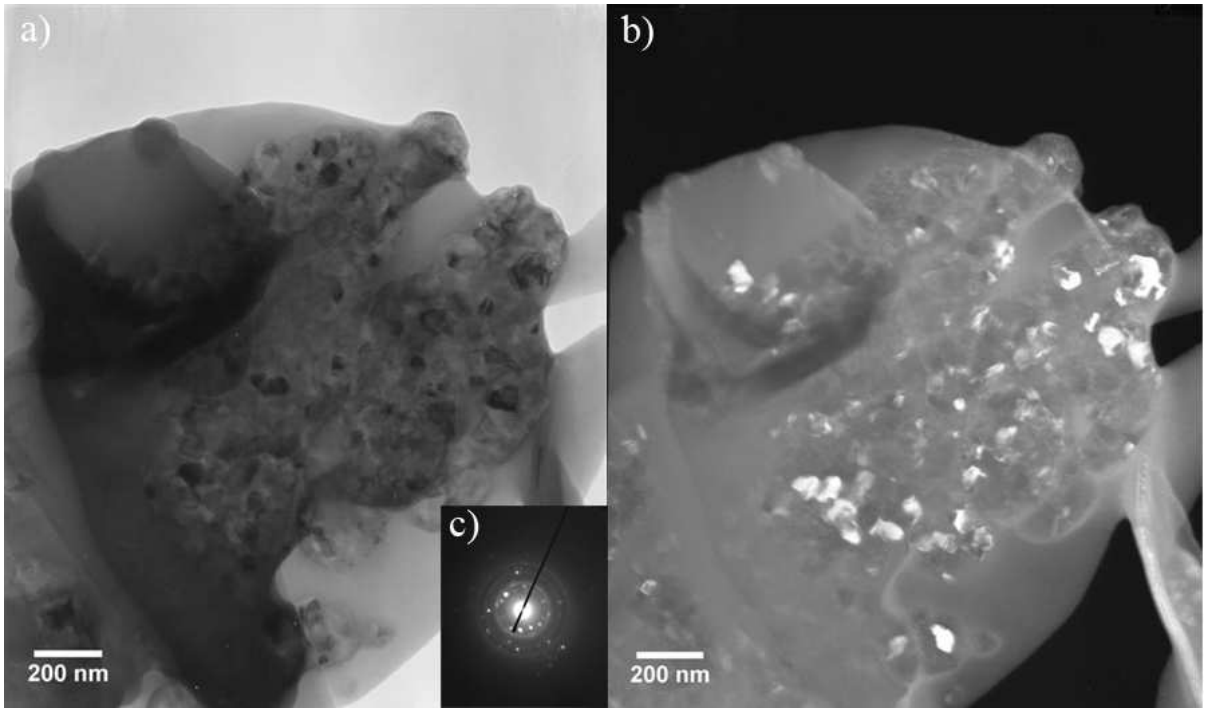

Figure 4.23 TEM images of the nanocones samples impregnated with DBM and then reduced to MgH_2 showing a) the bright field with SAD inserted and b) the corresponding dark field image of MgH_2 nanoclusters and c) the SAD pattern of a MgH_2 particle

4.7. Mixed hydrides

In an attempt to destabilize the MgH_2 system, a $LiAlH_4$ – DBM complex hydride was prepared by mixing with a magnetic stirrer the $LiAlH_4$ powder with the heptane solution of DBM in the molecular ratio of 4 molecules of $LiAlH_4$ to 1 molecule of DBM. The solvent in which the DBM was dissolvent has been evaporated.

For the reference sample of pure $LiAlH_4$ the DSC curve shows peaks at 156 °C, 171 °C, 185 °C, 248 °C and 490 °C. The TGA analysis revealed a total weight loss of 10 % (figure 4.24). Such weight loss is constituted of three steps: the first with a mass loss of 5 % until 203 °C in correspondence of the first two peaks of the DSC pattern (the endothermic peak at 171 °C and the exothermic peak at 185 °C), a second loss of 3% between 203 °C and 352 °C

corresponding to the peak at 248 °C and the third step with a weight loss of 2 % for the remaining peak between 352 °C and 490 °C

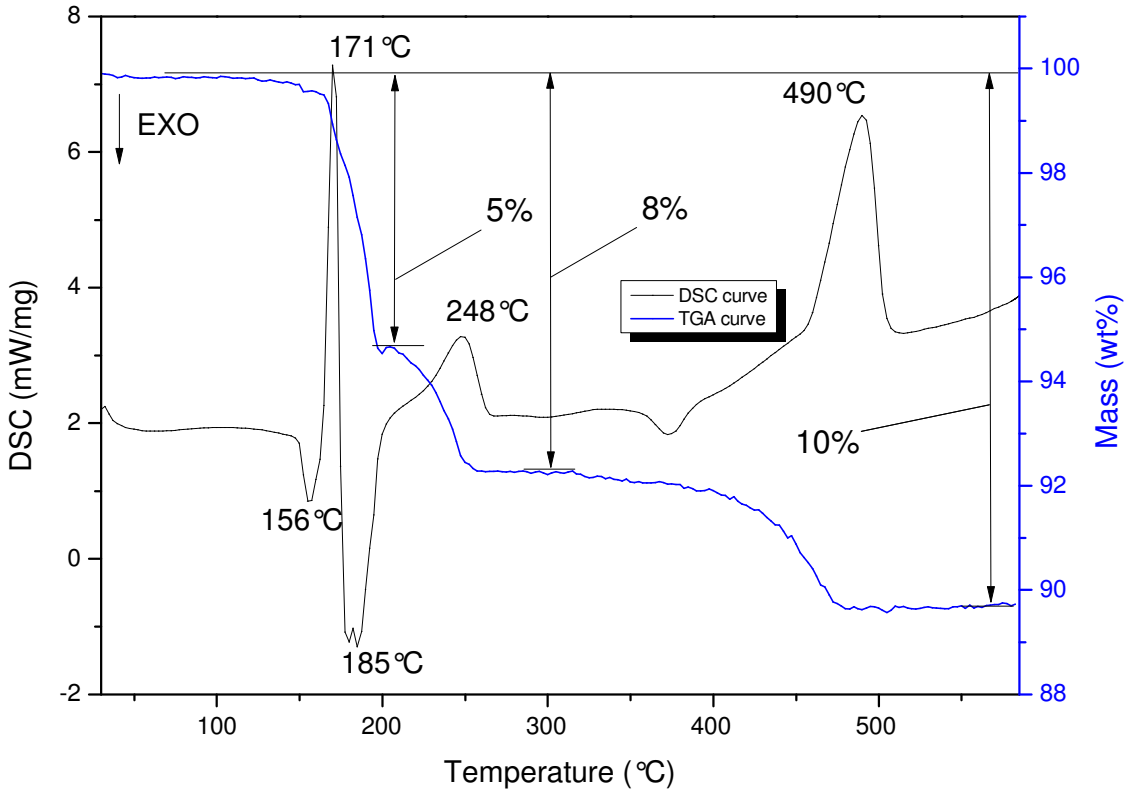

Figure 4.24 DSC and TGA curves for the decomposition of as received $LiAlH_4$

The DSC pattern for the $LiAlH_4$DBM (4:1) sample (figure 4.25) decomposition until the temperature of 585 °C shows several peaks at 170 °C, 195 °C, 220 °C, 350 °C, 470 °C and 535 °C out of which only a peak at 195 °C is exothermic and the total weight loss in TGA analysis was 42 %. This occurs in two steps: the first with a mass loss of 5 % until 210 °C in correspondence of the first two peaks of the DSC pattern (the endothermic peak at 170 °C and the exothermic peak at 194 °C) and the other of 37% accounting for the remaining DSC peaks between 210 °C and 475 °C.

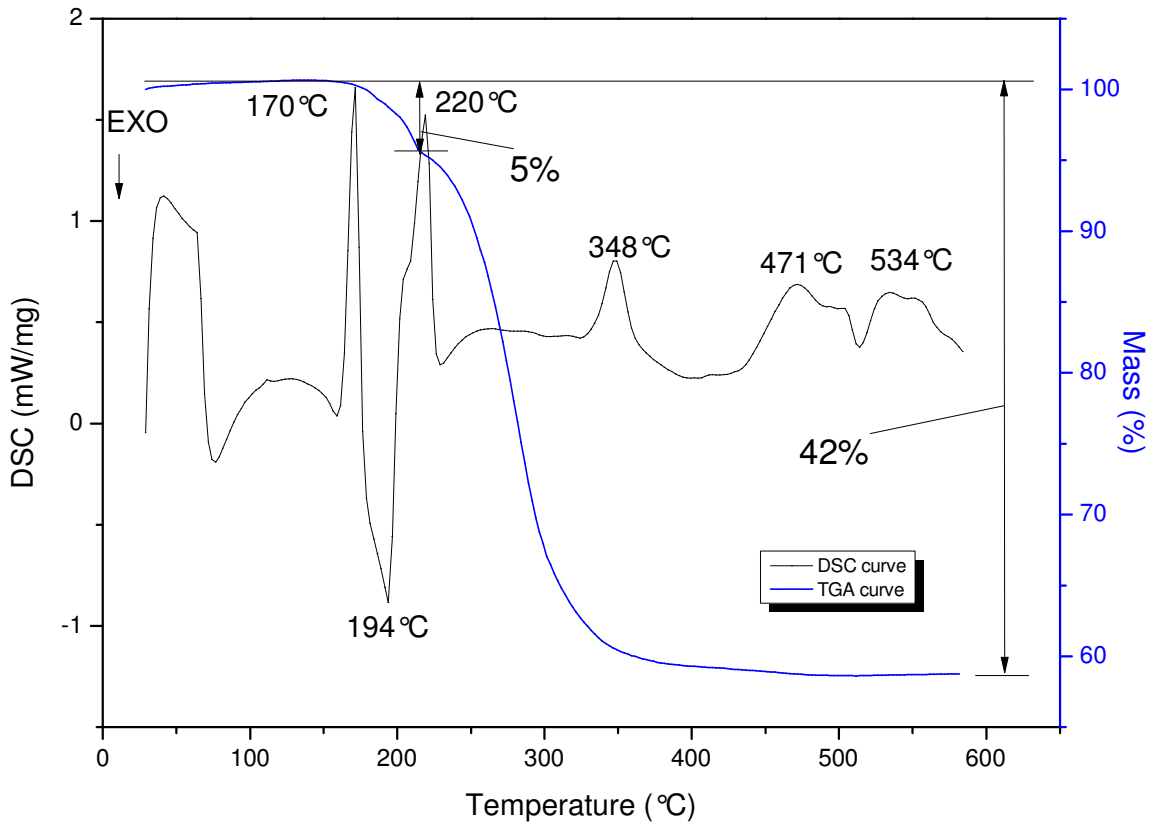

Figure 4.25 DSC and TGA curves for the decomposition of $LiAlH_4$DBM (4:1)

Figure 4.26 shows the comparison between XRD pattern for the as received $LiAlH_4$, the pure DBM and the sample $LiAlH_4$DBM (4:1).

The XRD pattern of a mixture $LiAlH_4$ and DBM in the molecular ratio of 4 to 1 shows only the reflections for $LiAlH_4$ and the reflections of DBM are absent.

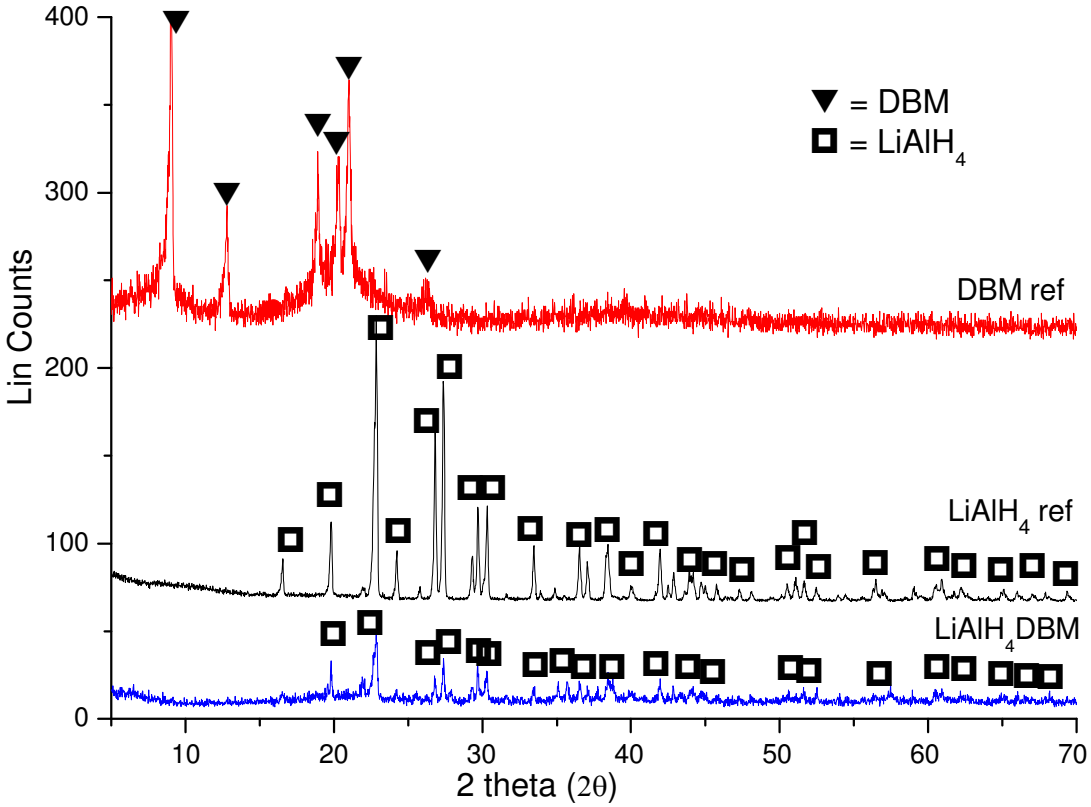

Figure 4.26 Comparison between XRD pattern for as received $LiAlH_4$, the pure DBM and for $LiAlH_4$ DBM (4:1)

In order to identify the reaction occurring at each of the peak in the DSC curve for the sample of LiAlH4DBM (4:1) a XRD analysis of an in situ thermal degradation has been carried out at the temperatures of each peak (30 °C, 170 °C, 195 °C, 250 °C, 350 °C, 475 °C, 535 °C and then cooled down to 30 °C) (figure 2.27).

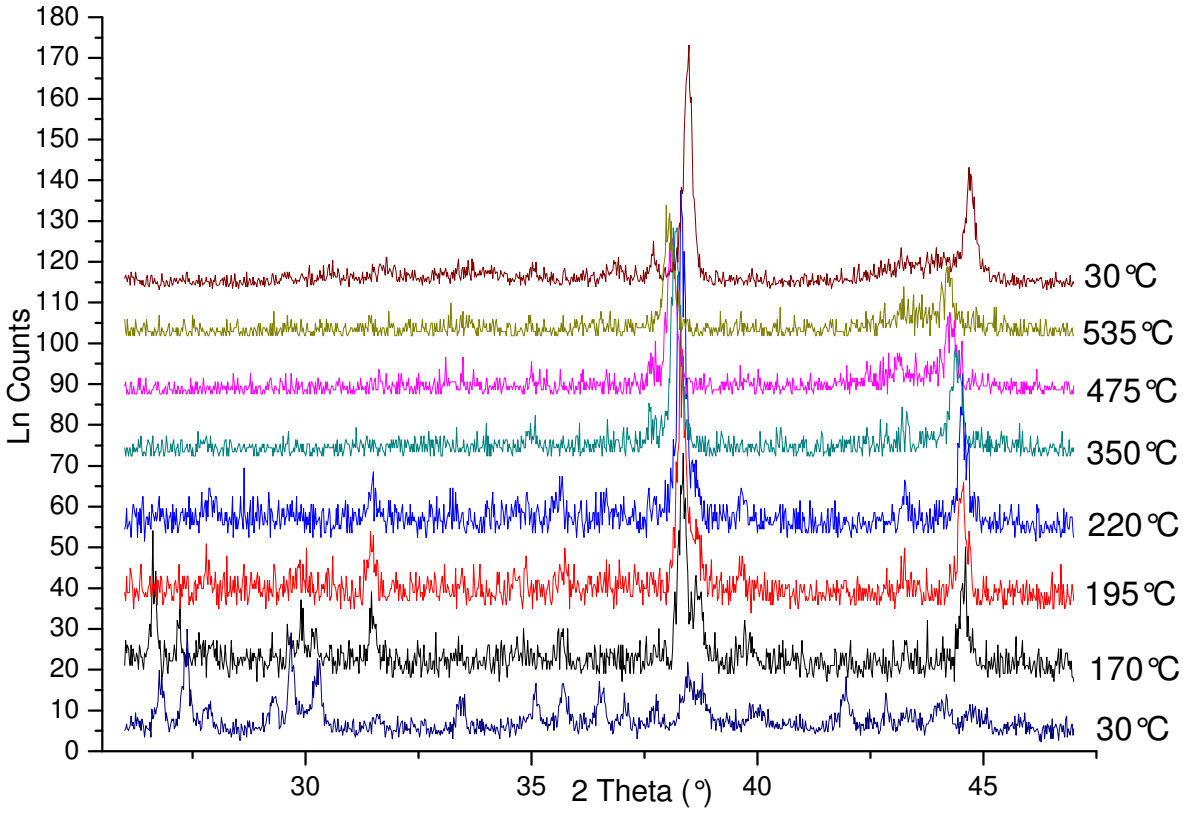

Figure 4.27 In situ XRD decomposition of the of $LiAlH_4$DBM (4:1) sample heated to 30 °C, 170 °C, 195 °C, 250 °C, 350 °C, 475 °C, 535 °C and then cooled down to 30 °C.

Figure 4.27 shows the full experiment but hasn't been indexed because in order to index the patterns more clearly the set of data of the same experiment has been divided between two figures. Figure 2.28 reports the first four temperature steps up to a temperature of 350 °C, whereas figure 2.29 show the following temperature steps until the cooling down pattern at 30 °C.

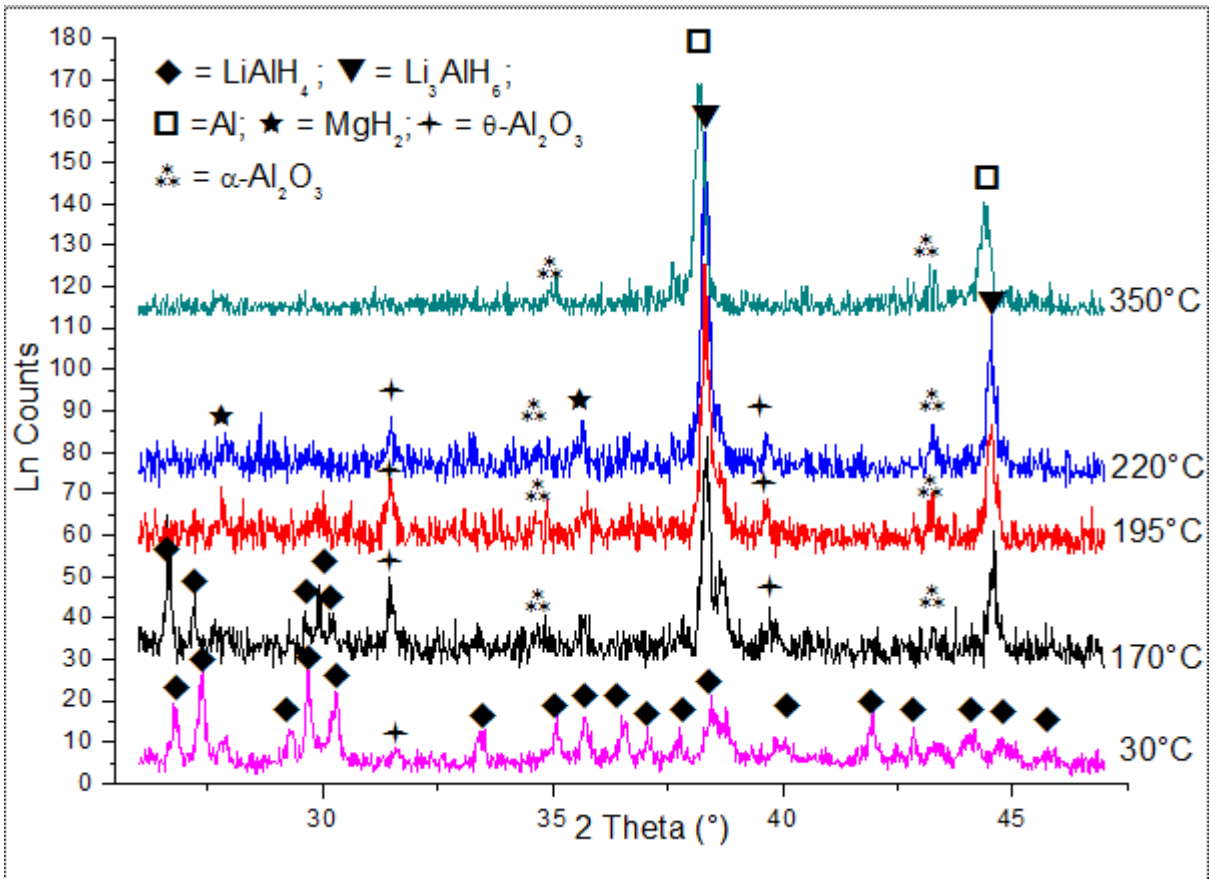

Figure 4.28 In situ XRD decomposition of the of $LiAlH_4$DBM (4:1) sample heated to 30 °C, 170 °C, 195 °C, 250 °C, 350 °C

From figure 4.28 it is possible to see that at 170 °C the initial product still has a pattern corresponding to $LiAlH_4$ keeping some of its characteristic peaks (at 2θ of 26.61° and 27.20°) but also had other peaks at 2θ of 38.34° (d_{113} = 2.34 Å) and 2θ of 44.58° (d_{004} = 2.03 Å) corresponding Li_3AlH_6. At 195 °C the peaks corresponding to $LiAlH_4$ had completely disappeared and only the peaks of Li_3AlH_6 were left. The peaks at 2θ of 31.47° (d_{-401} = 2.84 Å) and 39.74° (d_{202} = 2.66 Å) correspond to θ-Al_2O_3 and those at 2θ of 35.15° (d_{104} = 2.55 Å) and 43.35 (d_{113} = 2.08 Å) correspond to at α-Al_2O_3 (belonging to the sample holder). At temperature of 220 °C it can be noticed the appearance of MgH_2 peaks at 2θ of 27.91° (d_{110} = 3.19 Å), 35.73° (d_{101} = 2.51 Å) along with the peaks of Li_3AlH_6. At 350 °C the two main peaks shift at higher displacing till 2θ of 38.16° (d_{111} = 2.35 Å) and at 2θ of 44.38° (d_{200} =

2.04 Å) are attributed to LiH. At 475 °C (figure 4.29) there is a further shift of the peaks till 2θ of 38.11° (d_{111} = 2.35 Å) and at 2θ of 44.25° (d_{200} = 2.04 Å) are attributed to Al. At 535 °C another shift of the peaks till 2θ of 38.04° (d_{111} = 2.35 Å) and at 2θ of 44.19° (d_{200} = 2.04 Å) are attributed to Al.

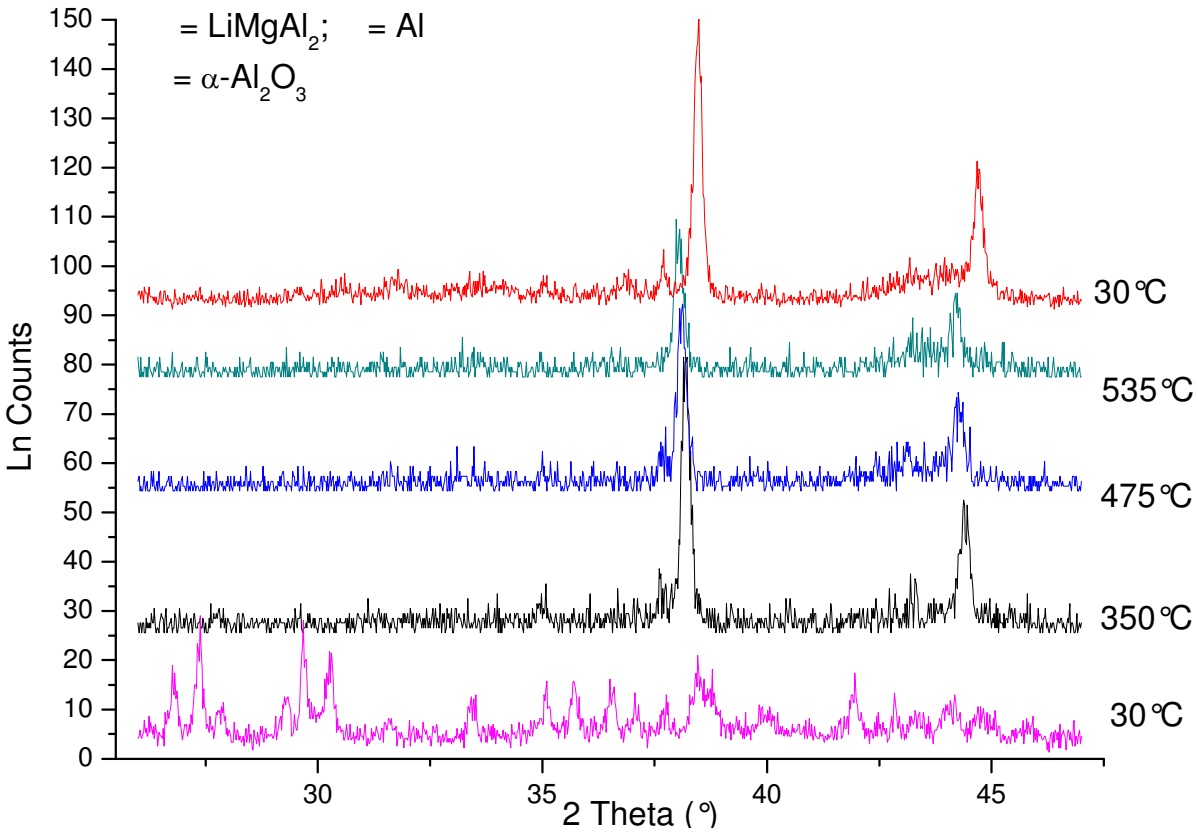

Figure 4.29 XRD in situ decomposition at 30 °C,475 °C,535 °C and the again at 30 °C

The XRD scan at 30°C after the in situ decomposition (figure 4.29 top pattern) shows peaks at 2θ of 38.47° (d_{111} = 2.33 Å), of 44.71° (d_{200} = 2.02 Å) and of 65.07° (d_{220} = 1.43 Å) attributed to Al and peaks at 2θ of 21.38° (d_{422} = 4.15 Å), of 22.97° (d_{511} = 3.86 Å), of 31.72° (d_{711} = 2.81 Å), of 34.06° (d_{731} = 2.62 Å), of 36.88° (d_{820} = 2.38 Å), of 37.69° (d_{660} = 2.38 Å) and of 42.86° (d_{931} = 2.10 Å) attributed to the alloy $LiMgAl_2$.

During the in situ experiment reported in figure 4.27 the peak corresponding to Al has been shift to larger d spacing. Such a shift has been compared with shift of Al peak in pure Al

sample to verify that such expansion is just a thermal effect and not a formation of a different compound. Table 4.7 summarize the d spacing values at different temperatures for Al peak in $LiAlH_4$ DBM (4:1) sample and pure Al sample

Table 4.7 d-spacing values of the Al peak at various temperatures in the $LiAlH_4$DBM (Al-Mg 4÷1) sample and pure Al sample used as standard reference

$LiAlH_4$ DBM (4:1)			**Al reference**		
Angle	d value	temperature	Angle	d value	temperature
2-Theta °	Angstrom	°C	2-Theta °	Angstrom	°C
38.469	2.34	30	38.472	2.34	30
38.351	2.34	170	38.375	2.34	170
38.324	2.35	195	38.344	2.34	195
38.317	2.35	220	38.313	2.35	220
38.191	2.35	350	38.199	2.35	350
38.115	2.36	475	38.096	2.36	475
38.027	2.36	535	38.025	2.36	535

The TGA has been done at temperatures of 300 °C, 400 °C and 585 °C between the temperatures corresponding to the DSC peaks in order to measure the eventual weight loss deriving from the reaction at those steps. The TGA analysis at temperature of 300 °C showed a mass loss of 36 %. The TGA analysis showed for a temperature of 400 °C mass loss of 41% the same weight loss seen also in figure 4.24 for the TGA analysis until the temperature of 585 °C.

FTIR analysis was also used to characterize the thermal decomposition of $LiAlH_4$ DBM sample. It has been also analysed the reference $LiAlH_4$. (figure 4.30 first spectrum from the bottom). It shows the stretching modes at 1760 and 1610 cm^{-1}.

The spectrum of the starting material $LiAlH_4$ DBM (figure 4.30 – second spectrum from the bottom) shows peaks at 2954, 2919 and 2867 cm^{-1} and at 1461 and 1376 cm^{-1}, characteristic of the DBM as seen before but no stretching modes at 1760 and 1610 cm^{-1} that would be typical of $LiAlH_4$ (bottom spectrum) were not observed. The spectrum for the

sample heated at 170 °C shows a broad band starting around 1450 cm^{-1} and having a maximum at 1374 cm^{-1}. At 195°C there appears two peaks at 1457 cm^{-1} and 1374 cm^{-1} attributed to stretching mode ν_3(F1) and a peak at 1043 cm^{-1} attributed to bending mode ν_4(F1)of Li_3AlH_6. The same pattern is found in the spectrum for the sample heated at 220 °C. At 300°C the characteristic peaks of DBM disappear showing a broad peak at 3254 cm^{-1} attributed to MgH_2 and another broad peak at 1250 cm^{-1} attributed to LiH. At 400°C such peaks disappear and no significant peaks are left.

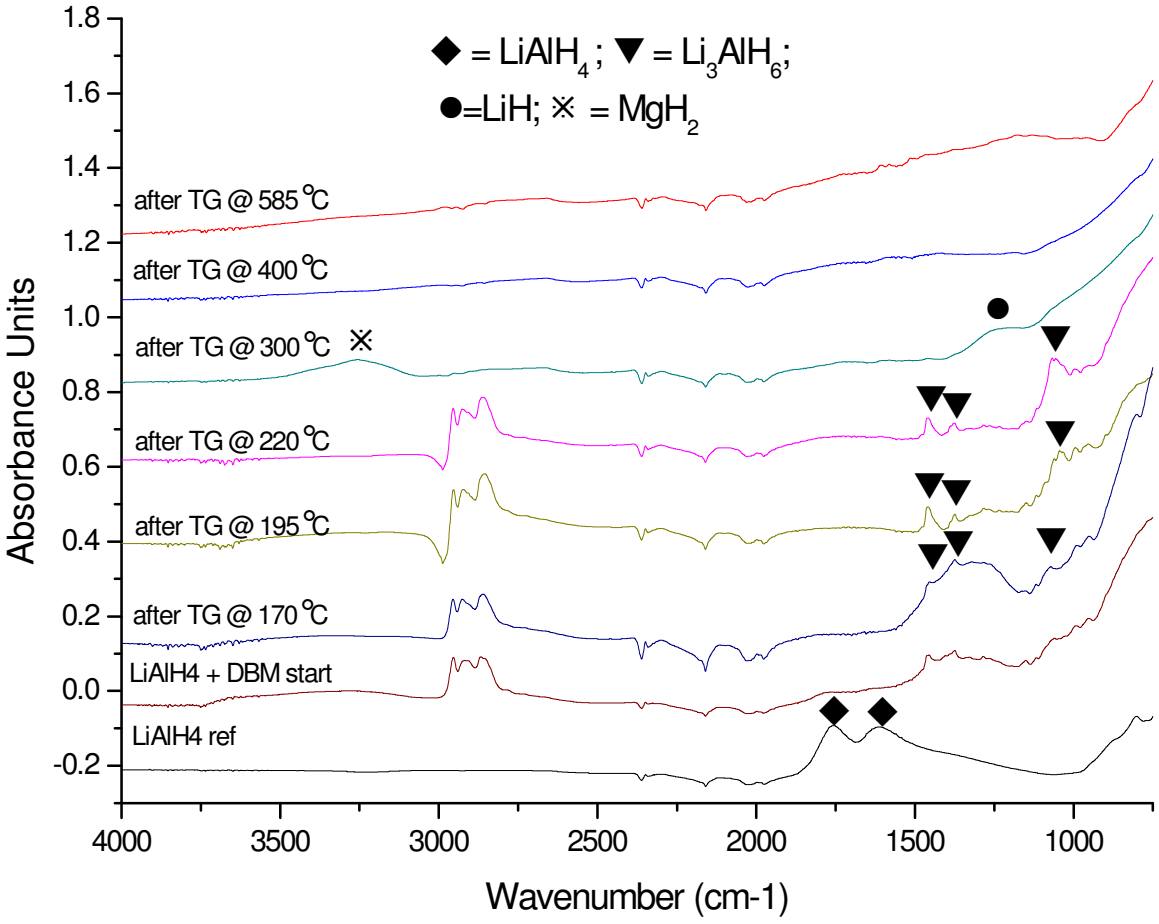

Figure 4.30 IR spectra comparison or products derived from decomposition of $LiAlH_4$ + DBM (4:1) at 170 °C,195 °C,250 °C,300 °C,400 °C,585 °C

5. Discussion

5.1. Optimization of metal catalyst dispersion

The optimization of the metal catalyst dispersion on carbon nanostructures has been performed by improving the compatibility of carbon surface with the inorganic metal catalyst and then improving the metal activation through the choice of catalyst and chemically dispersing it at the nano level.

The treatment of the nanocones with 12 M H_2O_2 solution under reflux for 3 h changed the chemical behaviour of the carbon surface, making it dispersible in water, and also etched the surface of the carbons as typified in figure 4.2. The procedure described here differs from those used by other groups in that a 3 h experiment was performed rather than 24 h, as used by Hernadi [233] and under reflux conditions rather than by sonicating at 60 °C as done by Feng [234]. From the XRD results in figure 4.7 there was no significant difference in peak position or in peak shape between the carbon support in the as-received state (NC) and the oxidised one (NCOX) unlike that observed in the work of Chiang [235] who noted a sharper C_{002} peak at a 2θ of 26.1° which indicated that the graphite structure was oxidized and hence structurally modified. The author states that a decrease in the order of crystallinity in carbon materials makes the XRD peaks broader [236]. The Chiang results show that the order of crystallinity was primarily damaged even in the early oxidation period which was not the case in the present study.

Comparing the TEM images of figure 4.1 with figure 4.2 or the images of figure 4.4 with figure 4.5, it can be seen that the oxidized carbon surface is more granular and shows evidence of etching which would be expected to increase the surface area.

This observation is supported by the BET measurements. The oxidative treatment with H_2O_2 increased the surface area of GNF from 148 to 181 $m^2 g^{-1}$ for GNFOX and structural modification was observed as a loss of the ordered and straight structure of the platelet fibre. An example of this is shown in figure 4.4 where the platelets of the GNF fibres that were nicely stacked in GNFOX are dislodged and inclined at an angle to each other, figure 4.5. These results are consistent with the work utilising an oxidising treatment to increase the surface area of a GNF as reported by Bououdina [237] where a sample with around 67 $m^2 g^{-1}$ surface area achieves, after an oxidative treatment, a surface area of about 132 $m^2 g^{-1}$.

After this initial oxidative pre-treatment, metal impregnation by incipient wetness was performed, as described in section 3.2, followed by the reduction of the catalyst to its metal element. A key parameter to be controlled in these subsequent experiments was the optimization of the metal particle size.

The process of reduction of the metal catalyst from metal oxide to elemental metal was initially carried out at 300°C following examples in the literature by Toebes *et al.* [151, 238]. Toebes [238] noted the effect of thermal reduction was detrimental for the metal particle size, and this effect is found also in the work of this thesis with an evident increase of size from 2.5±0.1 nm to 3.3±0.2 nm. Della Negra [239] in his study proved that such phenomenon is related to a clustering phenomenon due to the diffusion of Pd over the surface at temperatures as low as 400 °C and in times as short as 30 min. Confirmation of such diffusion rates has been performed by Beszeda [240] who measured that at ca. 310 °C (583 K) the diffusion coefficient for Pd on alumina and silica is about 2.69 $x10^{-16}$ $m^2 s^{-1}$ which would result in a linear diffusion distance of 1.5 μm for a time of 3h at 300 °C (573 K). The nearest neighbour distance has been calculated for the particle size distributions showed in

this thesis (figure 4.3. and figure 4.6) showing an average distance to the nearest neighbouring particle of 4 nm, 3 nm and 2.5 nm for the nanocones sample mounting Pd 5wt%, 10 wt% and 15 wt% respectively. Such a calculation is explained in the work of Stockholm *et al*. [241]. The calculated diffusion distance is clearly bigger than the distance among the particles making the encounter and the clustering inevitable. In the work of Beszeda the mass transfer surface self-diffusion coefficient is expressed by the following equation [240]

$$D_s = 1.1\times10^{-7} e\left[\frac{-97\pm13\frac{kJ}{mol}}{RT}\right] \tag{5.1}$$

In order to have a migration distance of 4 nm in a time of 3 h (10800s) the surface diffusion coefficient should be 1.48 x10^{-21} m^2 s^{-1} resulting in a minimum temperature of 92 °C (365 K) to have a migration distance comparable to the average distance among the particles. This means that having particles packed at 4 nm distance the maximum temperature of reduction to avoid clustering would be 92 °C. Furthermore, Beszeda work showed that the diffusion coefficient is substrate independent, making this value applicable to the work presented here in the case of Pd on carbon surface.

In order to avoid this increase in particle size it was decided to attempt the metal reduction at room temperature. It is possible to reduce PdO at room temperature accordingly to the thermodynamic data [242]. At RT the standard free energy of formation (-ΔG°) for the oxidation of Pd is lower than the one for the oxidation of hydrogen which means that Pd can be reduced at the cost of reaction of hydrogen with oxygen in PdO. The reductions with hydrogen at RT are presented in figure 4.3,

showing the benefit of a reduced temperature approach as there was no significant increase in average size of the particles.

The other reduction method explored in this work was that of $NaBH_4$. $NaBH_4$ is a known reducing agent mainly exploited in the organic field [243, 244] but it also has some indirect applications with those metals that form insoluble hydroxides (e.g. Co) for the purpose of precipitation and separation [245]. Whereas in the work of this thesis, $NaBH_4$ is used to reduce the metal. The advantage of its use is that the $NaBH_4$ is introduced directly in the aqueous solution of the metal salt in which the impregnation process of the metal onto the carbon nanostructure is undertaken. This avoids the intermediate step of evaporating off the solution to obtain a dry specimen to be reduced under hydrogen. The drying step can generate loss of sample or clustering due to the long time and temperature above RT needed for evaporating the aqueous solution whereas the procedure that use $NaBH_4$ is carried out at room temperature. The $NaBH_4$ method developed in this work achieved the highest particle dispersion in comparison with the hydrogen flow method. A higher degree of dispersion was correlated with production of smaller metal particles.

The particle size distribution has been measured through digitalisation of images taken at the TEM microscope as detailed in chapter 3 subsection 3.3.2. The method of reduction with hydrogen in the work presented here was optimized at a temperature of 25 °C and the particle size obtained was: 2.3 nm for nanocones impregnated with Pd 5 wt%, and 3.1 nm and 4.5 nm for Pd 10 wt% and Pd 15 wt% respectively. Hence an increase in particle size with increasing of metal loading.

Overall the results from the approaches adopted here are very promising if compared with the literature. For example Qian Jian [246] dispersed Pd 10 wt% on activated carbon (AC), on Vulcan XC-72 and also on multiwalled carbon nanotubes

(MWCNT) by a $PdCl_2$ incipient wetness method, reducing with $NaBH_4$. They reported metal cluster sizes for the Pd/AC of around 5 nm but with significant agglomeration and for Pd/Vulcan sizes of 2–3 nm with better dispersion than the Pd/AC. Suttisawat [141] deposited 10 wt% Pd on MWCNTs with a broad particle size range from 3 to 25 nm, with an average particle size of 5.8 nm. They also observed agglomeration of the Pd particles. Furthermore, Zhi-Peng Sun [247] dispersed ca. 12 wt% Pd over MWCNT and reduced with $NaBH_4$ with a mean particle size of 5.3 nm. The dispersions achieved in this work either with the hydrogen reduction method or reducing with $NaBH_4$ gave smaller Pd clusters, the latter process producing the smallest clusters of 1.2 nm. Hence, this method has the advantage of yielding smaller particle sizes and is a much simpler procedure requiring fewer stages. Such small catalyst dispersions can be of use in the field of other catalytic applications such as in the Heck reaction [248]. It is well known that the activity of palladium-supported catalysts depends on the metal dispersion and its particle size, due to correlation between the exposed catalyst surface area and the turnover number. However, to achieve the reactions of C-C bond coupling, the requirement of a small Pd particle size are more critical than for oxidation or hydrogenation reactions. In fact, through a complex process of nucleation [249], the catalyst gets deactivated hence the size of the particle has to be very small (< 5nm [250]) to avoid collisions and thus clustering, which usually requires stabilisation with surfactants [251]. The approach here offers a useful alternative.

In the case of GNFs, there appeared to be no correlation between particle size and the metal loading. For the $NaBH_4$ reduction route, a particle size of (4.6 ±0.2) nm (3.7 ± 0.1) nm and (4.2 ± 0.1) nm were observed for samples impregnated with Pd 5 wt%, Pd 10 wt% and Pd 15 wt% respectively (figures 4.6. d, e and f). At low metal

loadings these are not such finely dispersed particles compared with carbon nanocones, 1.2 nm against 4.6 nm. This cannot be explained by the morphology of the fibres. In fact GNFs have a much larger surface area than the carbon nanocones, 181 $m^2 g^{-1}$ against 27 $m^2 g^{-1}$, and thus they could have more room to accommodate more metal particles avoiding agglomeration and particle growth. The GNF curved surface is an obvious structural difference between the GNF and the carbon nanocones mixture rich in flat discs and the bigger average particles size on the GNF seems to suggest that the curvature maybe be the factor that prevent to have a high particle dispersion. The carbon nanocones are between 300 and 800 nm long with a maximum base diameter between 1 and 2 μm [50, 108] and carbon discs are typically 0.8–3.0 μm diameter and of 20–50 nm thickness [111]. However, it is important to note that cones represent only a small fraction of the system with the carbon nanodiscs representing more than 80% of the material [252].

Nevertheless, the particle size obtained for the nanocones sample is very competitive with what is in the literature for GNF. For example Amorim [253] found the average particle size is 37 nm with a GNF with a metal load of ~9 wt% and Park *et al*. [254] where using the same substrate of GNF and a load of Pd 10 wt% the particles were found to be in the range of 6 – 17 nm. Table 5.1 summarizes the particle size results achieved in this work compared with those reported in literature

Table 5.1 comparison of the average particle size of Pd obtained in this work with the literature findings

Sample	Particle size (nm)
NCOXPD5B	1.20±0.03
NCOXPD10B	3.60±0.07
NCOXPD15B	4.3±0.5
GNFOXPD5B	4.6 ±0.2
GNFOXPD10B	3.7 ±0.1
GNFOXPD15B	4.2±0.1
Pd 10 wt% on activated carbon (AC) (Yang [246])	5
Pd 10 wt% on Vulcan XC-72 (Yang [246])	2-3
10 wt% Pd on MWCNTs (Suttisawat [141])	5.8
12 wt% Pd over MWCNT (Sun [247])	5.3
Pd/GNF 9 wt% (Amorim [253])	37
GNF Pd 10wt% (Park [254])	6-17

5.2. Effect of oxidative pre-treatment and catalyst impregnation on hydrogen adsorption at 77 K

Hydrogen uptake at liquid nitrogen temperatures is demonstrated to be connected to the surface area [55, 130, 255-259]. Such a correlation indicates the hydrogen adsorption depends only on the physical characteristics of the material and for this reason is referred as physisorption. In agreement with this mechanism, results obtained in this work gave values expected for physisorption interactions alone for carbon nanocones characterized by low surface area. In fact with the increase of metal load and subsequent covering of surface we can see a decrease of hydrogen adsorption, indicative of physisorption (figure 5.1).

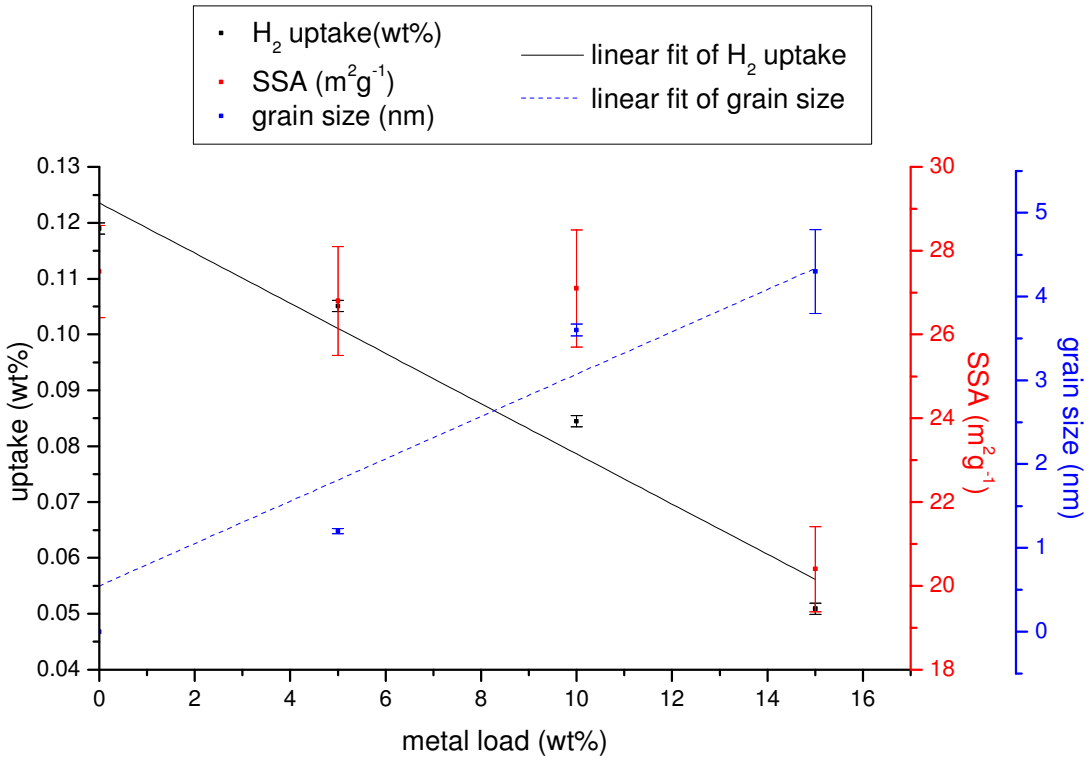

Figure 5.1 Hydrogen uptake trend at 77K for carbon nanocones samples (NCOXPD5B, NCOXPD10B and NCOXPD15B) at different metal loads versus the particle size trends

As stated above, the increase of Pd content reflects the increase of size of the particles covering the carbon nanocones surface, from 1.2 nm for Pd 5 wt% to 4.3 nm for Pd 15 wt%, which will decrease the surface available for physisorption, from 27 m^2g^{-1} for Pd 5 wt% to 20 $m^2 g^{-1}$ for Pd 15 wt%, and ultimately the hydrogen uptake at 77 K, which is decreasing at a faster rate for each addition of Pd, -12% -20% and -40% reduction for Pd 5 wt%, Pd 10 wt% and Pd 15 wt% respectively. It corresponds to an average loss of 0.003 wt% per $m^2 g^{-1}$.

The correlation between hydrogen uptake of various carbon nanostructures at 77 K and their specific surface area is also reported by Zuttel *et al*. [260] stating that the theoretical value of potential hydrogen adsorbed was 0.00228 wt% uptake for each

square meter of surface area for the adsorption of a monolayer of hydrogen at the surface which indicates that the nanostructures investigated here follow this theoretical relationship between uptake and surface area.

In the case of GNF the uptake values are 0.72 wt%, 0.44 wt% and 0.70 wt% for GNF with Pd 5 wt%, Pd 10 wt% and Pd 15 wt% (figure 4.13) respectively and the surface area is 234, 165 and 101 $m^2 g^{-1}$ for samples impregnated with Pd 5 wt%, Pd 10 wt% and Pd 15 wt% respectively. In this case, unlike the carbon nanocones, there is no significant trend of hydrogen uptake for the GNFs with metal loading. The particle size results of (4.6 ±0.2) nm (3.7 ±0.1) nm and (4.2±0.1) nm for samples impregnated with Pd 5 wt%, Pd 10 wt% and Pd 15 wt% respectively also shows a lack of variation with the increase of metal load. This means that GNFs can be exploited for applications which require a considerable amount of catalyst without changing the particles size, as seen in case of the Heck reaction where particle size and catalytic efficiency are correlated [251]. Such system can be exploited when it is necessary not to lose hydrogen capacity with an increase in metal catalyst loading.

There is not a direct correlation between the surface area and the hydrogen uptake in the case of GNF.

Such deviation from the relation between the hydrogen uptake and the surface area have been observed in the literature in several other studies [261-263]. These studies by Lueking and Browning illustrate that the surface areas accessible to nitrogen in BET measurements (kinetic diameter is 3.64 Å) may not necessarily be accessible to the hydrogen molecule (kinetic diameter is 2.89 Å). Thus hydrogen uptake does not always correlate to BET surface area, particularly for nanocarbons [261, 262].

Panella *et al*. [55] postulated that the hydrogen storage capacity of carbon materials is proportional to their volume of micropores. To verify their postulate using the work of this thesis the volumes of hydrogen adsorbed at 1 bar for the GNF samples were compared with the pore volume measured at 1 bar by nitrogen adsorption and the results are show in table 5.2. The table indicates that the difference between the volume of gas adsorbed by the as prepared material and that of the Pd loaded samples and their pore volumes is in quite good accordance between the pore volume and the hydrogen adsorbed. However, the difference between the volume of hydrogen adsorbed and the pore volume of the exfoliated samples is much lower, almost three fold. This confirms what was stated by Lueking and Browning [261, 262] that nitrogen can access areas where hydrogen cannot access.

Table 5.2 Comparison between volumes of hydrogen adsorbed at 77 K and total pore volume for GNF samples

Sample	**H_2 uptake at 1 bar (wt%) at 77 K**	**H_2 volume ($cm^3\ g^{-1}$)**	**Pore volume ($cm^3\ g^{-1}$)**	**Surface area ($m^2\ g^{-1}$)**
GNF	0.101±0.002	0.255	0.277±0.014	148.1±7.4
GNFOXPD5B	0.197±0.004	0.286	0.49±0.024	234.3±11.7
GNFOXPD10B	0.159±0.002	0.265	0.347±0.017	99.18±4.96
GNFOXPD15B	0.179±0.003	0.161	0.141±0.007	101.32±5.05

To summarize, the hydrogen physisorption results show correlation to the surface area when considering the oxidative treatment and the metal covering the surface in the case of carbon nanocones. However, in the case of GNFs, where the hydrogen adsorption does not follow the trend of surface area, the hydrogen physisorption is related to the pore volume suggesting the intercalation of hydrogen within the graphene layers.

5.3. Catalytic effect of metal impregnation on hydrogen uptake at room temperature: evidence of hydrogen spillover

Among the nanocone samples that had been impregnated with catalyst the hydrogen uptake measurements showed that the sample decorated with Pd 15 wt% and reduced with $NaBH_4$ gave the most hydrogen uptake at 0.113 wt% whereas the hydrogen uptake for the unloaded carbon sample was 0.019 wt%. To establish if there has been any hydrogen uptake beyond what would be expected for the physisorption contribution of the carbon substrate and the chemisorption contribution of the metal catalyst the sum of the former, achieved experimentally, and the latter calculated from thermodynamic data available in literature was compared. Any additional uptake would be considered as evidence of hydrogen spillover mechanism discussed in chapter 3. The experimental maximum uptake for pure Pd is 0.72 wt% [264] hence for the Pd 15 wt% sample the theoretical uptake for solely Pd should be 0.108 wt%. Summing this chemisorption datum with our experimental physisorption datum for the unloaded carbon substrate we obtain 0.124 wt% indicating that the experimental data matched the sum of the theoretical Pd capacity plus carbon support contributions. Repeating this calculation for the hydrogen uptake results for the other metal loadings (table 5.3.), then the uptake can be explained easily based on surface area physisorption and metal hydride chemisorption. In other words there is no experimental evidence of hydrogen spillover on the nanocone samples. This can be explained by the predominance of the flat discs in the mixture of the material since it is known that hydrogen atoms generally adsorb more strongly at the edge sites than the inner sites of flat carbon surfaces [265].

Table 5.3 Experimental hydrogen uptake VS calculated for Pd loaded carbon nanocones.

Sample	Experimental H_2 uptake at RT (wt%)	Theoretical $PdH_{0.67}$ contribution	Sum ($PdH_{0.67}$+ cones) contribution
NC	0.019	-	0.019
NCOXPD5B	0.065	0.035	0.054
NCOXPD10B	0.076	0.072	0.091
NCOXPD15B	0.113	0.105	0.124

The highest result in table 5.3 is comparable with that in the literature [160] where multi-walled nanotubes with a Pd 13 wt% loading achieved at 298 K and 16 bar a hydrogen uptake of 0.18 wt%. The higher storage capacity can be accounted for by the fact that these nanotubes used had a much higher surface area (116 $m^2 g^{-1}$) than the nanocones and with a higher experimental hydrogen adsorption of 0.075 wt%. Considering the contribution of Pd 13 wt% in forming the hydride would be 0.0936 wt% the cumulative adsorption is 0.17 wt% in accordance with the experimental result and again confirming that hydrogen adsorption is simply the cumulative sum of support and catalyst adsorption. Other results [152] show an increment of 0.13 wt% in hydrogen storage capacity before and after metal impregnation, which is similar to the increment reported for the nanocone samples. Therefore as stated above, from the samples researched in this thesis there is no evidence of higher than expected hydrogen uptakes as reported in the literature that can be attributed to a spillover-type mechanism for the nanocone samples.

The same calculations were performed for the GNF and the hydrogen uptake results are plotted in figure 5.2 and presented in table 5.4.

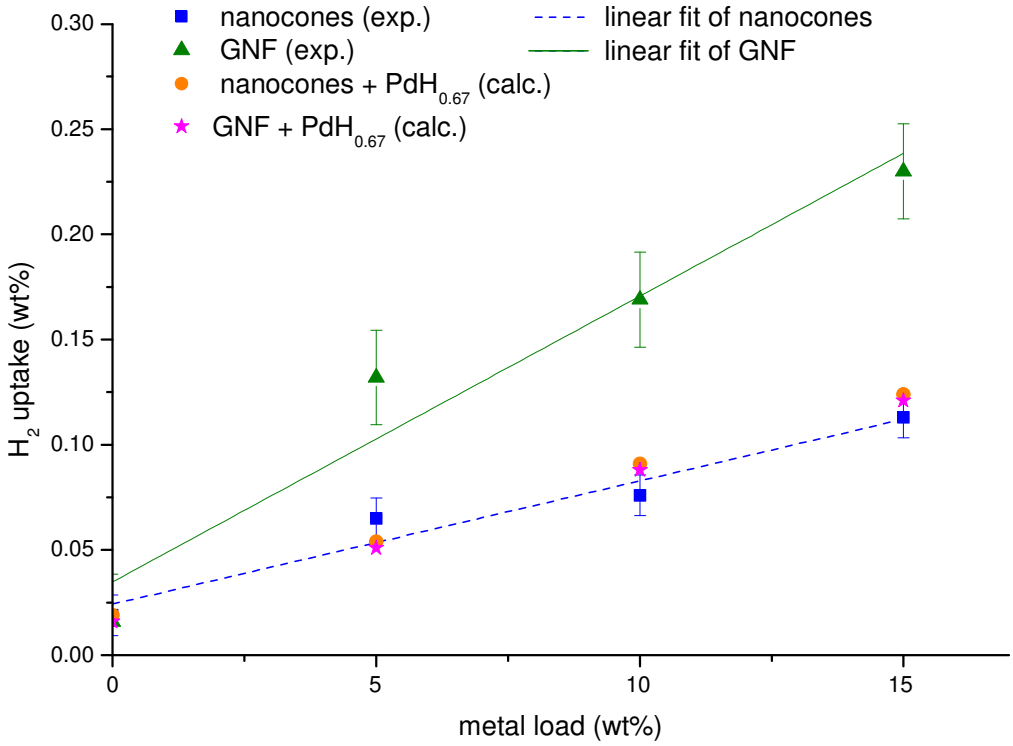

Figure 5.2 Results of hydrogen uptake at RT for carbon nanocones (squares) and GNF (upward triangle) compared with the calculated cumulative contribution physisorption plus chemisorption.

Table 5.4 Experimental hydrogen uptake VS calculated for Pd loaded GNF

Sample	**Experimental H_2 uptake at RT (wt%)**	**Theoretical $PdH_{0.67}$ contribution**	**Sum ($PdH_{0.67}$+ GNF) contribution**
GNF	0.016	-	0.016
GNFOXPD5B	0.131	0.035	0.051
GNFOXPD10B	0.169	0.072	0.088
GNFOXPD15B	0.230	0.105	0.121

Table 5.5 offers a side to side comparison of hydrogen uptake at RT for the samples carbon nanocones and GNF at each metal load. Comparing table 5.5 and figure 5.2 it is clear that the hydrogen uptakes of the unloaded carbon nanocones and GNF samples are very similar in spite of the difference in surface area of 148 m^2g^{-1}

for the GNF against 22 m^2g^{-1} for the carbon nanocones. This would suggest that the morphology of the carbon substrate without metal impregnation is not giving a substantial contribution in the hydrogen uptake at RT.

Table 5.5 Comparison of the hydrogen adsorption data for the carbon nanocones and GNF at each metal load contents

Sample	Experimental H_2 uptake at RT (wt%)	Theoretical $PdH_{0.67}$ contribution	Sum ($PdH_{0.67}$+ cones) contribution	Surface area (m^2/g)
NC	0.019	-	0.019	22
GNF	0.016	-	0.016	148
NCOXPD5B	0.065	0.035	0.054	27
GNFOXPD5B	0.131	0.035	0.051	234
NCOXPD10B	0.076	0.072	0.091	27
GNFOXPD10B	0.169	0.072	0.088	164
NCOXPD15B.	0.113	0.105	0.124	20
GNFOXPD15B	0.230	0.105	0.121	101

However, following the hydrogen uptake trend for the GNF through the different metal loadings versus the calculated expected trend in table 5.4 (or table 5.5) then there is evidence of consistent differences, as the experimental values are approximately double the calculated values. An attempt to explain these differences can be done considering the trend in metal particle size. In case of the GNF there is not an increase of particle size of (4.6 ±0.2) nm (3.7 ±0.1) nm and (4.2±0.1) nm for samples impregnated with Pd 5 wt%, Pd 10 wt% and Pd 15 wt% (Figures 4.6. d, e and f). This similar particle size is due to the higher surface area that can accommodate more metal particles which overall means higher catalyst surface area. If each catalyst particle interacts with the corrugated and curved surface on the GNFs to enable the

diffusion of chemisorbed hydrogen from the metal particles toward the surface of the GNF then this would explain the increase with catalyst and the additional amount than predicted is due to a spillover mechanism. In support of this hypothesis, work from Kostov [266] showed how the interactions C-H are dependent on curvature and site dependent (exohedral preferred over endohedral) and the postulate is that this result is important for carbons with a large circumferential curvature where conventional force fields (force fields such as: bonding interactions contributed by forces due to deformations of bond distances, bond angles and torsion angles, out-of-plane interactions, couplings between deformations of internal coordinates and nonbonding interactions describing van der Waals forces and electrostatic interactions) are inadequate. Kostov's work suggests that the effect of carbon curvature becomes more pronounced as the nanotube diameters get smaller. The modelling simulation proposed in his work give a strong preference for H_2 adsorption on the exohedral surface of SWNTs. Other evidence towards the importance of the structure is provided in a study by Chen [267] in which different types of carbon structures, from planar graphene to nanotubes with different diameters, were compared. The results confirm that the calculated hydrogen chemisorption strength was found to be curvature-dependent with higher adsorption energies associated with the carbon atoms of nanotubes with more pronounced curvature. Therefore, a large curvature enhances the adsorption strength and reduces the mobility of H on the surface.

The amount of spillover uptake increases with the increase of metal catalyst and reaches a maximum in the case of GNF with Pd 15 wt% where the increase is 0.117 wt%. This provides evidence for spillover and this may be a consequence of the curvature of the substrate, but the amount is relatively small considering the relevant

metal content of 15 wt% and does not support the larger claims of 3.5 wt% [144] or 2 wt% [145] with only 5 wt% Pd.

To summarize, the hydrogen adsorption results for GNFs support a hydrogen spillover mechanism [185, 196] onto carbon fibre/tube-like structures where the curvature is high (average diameter is 20 nm). On the other hand the reason why such a phenomenon was not observed in the nanocones samples is due to the mixture of three structures (discs, cones, soot) where the presence of discs with flat graphene—like surface, above 80% of the population, dominates the structure.

5.4. Effect of loading different metals on hydrogen uptake

A different metal catalyst such as Ni 10 wt% impregnated on GNF shows a lower hydrogen uptake at RT (0.072 wt%) compared with the GNF sample loaded with Pd 10 wt% (0.170 wt%). However, Nickel hydride formation is not feasible under these conditions [268, 269], and the solubility of hydrogen in Ni is also negligible being in the range 5×10^{-4}–10^{-5} atom fraction of H into Ni [270-272]. Therefore, the hydrogen storage increase from 0.016 wt% to 0.072 wt% is due to a hydrogen spillover mechanism. This effect with Ni has been reported for other systems. For example Wang *et al.* [273] doped 6 wt% Ni onto a AX-21 activated carbon which originally had a hydrogen storage capacity of 0.6 wt % at 298 K and 100 bar but after doping the hydrogen uptake was enhanced to 1.12 wt %. An uptake of 0.53 wt% at RT and 30 bar has been achieved by Zielinski *et al.* [53] loading with 1 wt% Ni onto activated carbon that initially had a 0.1 wt% hydrogen uptake. In the work presented here the initial GNF has a hydrogen uptake 0.016 wt% and the 10 wt% Ni loaded 0.072 wt% for a gain of 0.056 wt%. This gain provided by the

addition of Ni onto carbon is lower than those reported by Wang or Zielinski, however, it is worth considering the work of Lin *et al*. [274]. Lin *et al*. showed an improvement upon decorating carbon nanotubes but noted how small changes of metal loading can severely compromise the hydrogen uptake either due to lack of dissociation centres or excessive surface coverage. According to their results the uptake depends on the metal particle size with the most efficient particle size achieved being 5 nm for a 9.2 wt% metal loading. Whereas, when particle size reaches 10 nm for an 18.5 wt% metal load then the metal contribution starts to be detrimental. This observation agrees with the work presented here since despite a similar metal loading of 10 wt% the particle size was of 11.8 nm (similar particle size to Lin *et al*.) where particle growth and undesirable aggregation degraded the reaction activity of Ni and blocked the hydrogen adsorption sites.

Another way to reduce the costs of the material by reducing the Pd content is to alloy Pd with Ni, Cu and Ag and then verify hydrogen diffusion into these alloys. At silver contents below 0.25 atomic ratio, it is postulated that the silver atoms block the energetically favoured diffusion paths in the Pd matrix leading to a complex diffusion pathway [275]. At silver concentrations above 0.6 atomic ratio, Pd atoms act as traps for hydrogen in a silver matrix which is principally due to the difference in the enthalpies of hydrogen solution of the two pure metals. If Ag is substituted by Ni in the alloy with Pd an analogous behaviour is observed. Regarding the substitution with Cu in the Pd alloy the same can be said only for the face centre cubic (f.c.c.) phase region of PdCu phase diagram. However, the atomic ratio PdCu 1:1 used in this thesis work s predominantly face centre cubic [276]. In addition, two studies by McLellan *et al*. [277, 278] show that the addition of Ni or Cu to Pd causes a lattice contraction compared to pure Pd impeding hydrogen diffusion whereas the addition of Ag to Pd

causes a lattice expansion. The purpose in this work was to use the lattice contraction as a trap for hydrogen atoms. Such lattice contraction serves to explain the peak identification in the XRD patterns for figure 4.12 where the peak corresponding to Pd is shifted at higher 2θ, or smaller lattice distances, for Ni (from 40.11 ° to 41.09 ° or from d_{111} = 2.24 Å to d = 2.18 Å) and Cu (from 40.11 ° to 41.53 ° or from d_{111} = 2.24 Å to d = 2.17 Å) but is shifted and higher lattice distance in case of Ag (from 40.11 ° to 38.79 ° or from d_{111} = 2.24 Å to d= 2.32 Å).

In the experiments presented here coupling the Pd catalyst with other metals has improved the hydrogen adsorption. In case of carbon nanocones impregnated with Pd 10 wt% and Cu 10 wt% the hydrogen uptake is 0.097 wt% compared with the uptake of 0.076 wt% for the Pd only 10 wt% sample. This is a good synergic improvement considering that at such temperatures (RT) and pressures (20 bar) Cu does not form a hydride [268]. In a study by Opalka *et al* [279] the H solubility into Cu exhibits a maximum ratio of 0.033 H/metal (3.2 at.%) for a $Pd_{0.48}Cu_{0.52}$ composition (Pd 61 wt% and Cu 39 wt%) at 43.8 bar and 673 K. The corresponding H solubility contribution at the conditions applied in this work is estimated about 0.1 at%. This estimation assumes a ratio Pd-Cu in a 50-50 wt% and experiment conditions of 20 bar and 298K rather than 43.8 bar and 673K. The hydrogen uptake of 0.097 wt% corresponds to a 0.0135 at% hydrogen content showing that the solubility in the sample analyzed here is lower than that reported in the literature.

The addition of 10wt% Ni to Pd resulted in an uptake as high as 0.079 wt%. Such a result is higher if compared with Campesi *et al*., [280] where mesoporous carbon of 850 m^2g^{-1} was impregnated with Pd 10 wt% and Ni 6 wt% and at 5 bar and (RT) and the hydrogen uptake increased from 0.01 to 0.027 wt% whereas in this study

a material with much lower surface area such as the carbon nanocones (27 m^2g^{-1}) achieved at 5 bar a hydrogen adsorption increase from 0.014 of 0.051 wt%.

The uptake decreased in case of Ag additions to prove that the lattice expansion of PdAg alloy (from d_{111} = 2.24 Å to d= 2.32 Å) revealed to be a detrimental factor for hydrogen storage purposes. For a Pd metal loading of 28.5 wt% the cumulative uptake should be of 0.207 wt% rather than 0.154 wt% measured for sample with Pd 28.5wt% and Ag 10wt%. This particular ratio of Pd was chosen based on previous work [281, 282] where it was reported that the addition of Ag greatly increases the Pd α phase hydrogen sorption capacity and diminishes the Pd α- and β-phase transition due to the dilation of the lattice constant. It was postulated that since the α phase has already a high capacity of hydrogen adsorption then the phase transition would be the rate limiting step in the hydrogen absorption process hence the kinetics could therefore be increased with the addition of Ag. More specifically Makrides [282] reasoned that the main effects of silver are a decrease of the hydrogen pressure corresponding to the α- and β transition (with the lowest pressure for Pd – Ag 76/24 atomic ratio) and a decrease of the solubility at 1 bar. The first effect is described by the author as an attractive interaction between silver and hydrogen, which is similar to that between dissolved hydrogen atoms. The second can be attributed to a decrease in the unoccupied electron states in the *d*-band of the alloy resulting from the random substitution of silver for palladium. Hence in this work the postulate was thanks to a faster kinetics combined with a lower plateau pressure a better performance would be achieved for hydrogen storage despite the diminished hydrogen solubility Pd to Ag, thus an atomic ratio of 76/24 was chosen. Unfortunately the experimental values showed that the solubility contribution has a dominant effect.

5.5. Combination of carbon nanostructure with hydrides

The objective of this work was to combine synergistically the reversible effect of hydrogen adsorption on carbon nanostructure with a material with high capacity such as magnesium hydride. Moreover, having seen the encouraging results in obtaining a fine catalyst dispersion onto the surface, it was decided to start from a precursor of the metal to be dispersed on the surface. The precursor chosen was n-dibutyl Magnesium (DBM), and it was attempted to develop a novel method of synthesis for the magnesium hydride starting from this precursor.

The compound n-dibutyl magnesium (DBM) was characterized by XRD, DSC, FTIR and MS. The XRD results (figure 4.15) showed its characteristic diffraction peaks at 2θ of 9.06° 12.79° 18.90° 20.27° 21.02° and 26.38° (marked as P1, P2, P3, P4, P5 and P6). From the DSC analysis (figure 4.16) a strong endothermic phenomenon occurred at 250 °C and XRD analysis of the sample after a DSC analysis at the temperature of 250 °C (figure 4.17) confirmed the formation of MgH_2. Comparing with the literature Zhang *et al*. and Nielsen *et al*. [205, 206] who proposed an experimental condition of 170°C and a pressure of 55 bar of hydrogen for 24 hours. The work presented here demonstrates that there is no need of hydrogen atmosphere or such high pressure conditions since the DSC was under flowing Ar

The FTIR spectrum (figure 4.19 top spectrum) of DBM shows two main peaks at 2958 cm^{-1} and 1384 cm^{-1} corresponding to the overtone of C-H stretching of CH_3 and CH_2 respectively. Since this organometallic compound has a butyl function, its spectrum was compared to the n-butane spectrum [283 2010, 2010, 2010] having peaks at 2950, 1470, 1400 and 960 cm^{-1}. The good agreement experimentally confirmed that the function butyl is present in the compound.

In addition the MS spectrum (figure 4.18) of the DBM decomposition under Ar flow showed that the resulting gas species is mainly 1-butene (C_4H_8). Such conclusion is drawn by analysing the intensity of the pattern corresponding to the fragment ion with 41 m/z which is the highest in the 1-butene MS spectrum [284] with the intensity pattern of the fragment ion with 43 m/z which is the highest in the butane MS spectrum[285]. The latter is not present at all while the former shows to have two peaks at 250 °C and 370 °C. Other relevant fragment ions belonging to 1-butene are at at m/z of 27, 28, 39 and 56 m/z. Among those the fragment ions the one resulting having the highest intensity is the one at 28 m/z. Unfortunately this fragment ion has the same amu of the fragment ion for nitrogen [286] and in fact is possible to see in the first 30 minutes of the experiment two peaks for the pattern of fragment ion with 28 m/z belonging to nitrogen present in the tubes that then disappear once the Ar flow has evacuated the tubes from the nitrogen. The results of such MS analysis indicate that during the decomposition the alkyl chain remains intact and there is a loss of one hydrogen atom per chain which explains the formation of MgH_2. The organic function is itself the supplier of the hydrogen. Equation 5.2 shows the reaction equation:

$$MgBu_2 \xrightarrow{\substack{1bar\_Ar,\\ 250^oC,4h}} MgH_2 + 2Butene \qquad (5.2)$$

From the DSC analysis (figure 4.16) the other main endothermic peak is at 370 °C which is attributed to the dehydrogenation of MgH_2. This is confirmed by the XRD pattern of the decomposition at 585 °C (figure 4.19), where the only species present was Mg.

The MS data reveal that only 81.5 % of DBM is transformed into MgH_2 in the reaction occurring at the first DSC peak hence the decomposition of DBM has two stages, postulated as:

$$MgBu_2 \xrightarrow{\substack{1bar\_Ar,\\ 250^oC,4h}} \frac{4}{5}MgH_2 + \frac{1}{5}MgBu_2 + \frac{8}{5}Butene \qquad (5.3)$$

$$\frac{1}{5}MgBu_2 + \frac{4}{5}MgH_2 \xrightarrow{\substack{1bar\_Ar,\\ 370^oC}} Mg + \frac{2}{5}Butene + H_2 \qquad (5.4)$$

Combining the DSC data of heat content of each peak with the MS data/XRD data detecting which are the products of the reaction and in what amount they have been produced (from the TGA data) it is possible to calculate the enthalpy for the process of decomposition of DBM and spontaneous formation of MgH_2. The DSC sample was 0.02067 g and the molecular weight (MW) for DBM is 134.95 g mol^{-1}. This makes 1.53 x 10^{-4} mol of initial product. From the MS experiment the DBM consumption ratio in the first peak is 0.815 then the moles of DBM consumes in first reaction (first peak) are 1.25 x 10^{-4} mol. Since the decomposition reaction generates two moles of butene and that the molecular weight of butene is 56.12 g mol^{-1} then the amount of butene produced is 1.4 x 10^{-2} g corresponding to a weight loss of 67.8 wt% in agreement with the experimental value of 68 wt% (figure 4.17). From the DSC experiment the heat content of first peak is 316.7 J g^{-1} which for that sample mass correspond to 6.54 x 10^{-3} kJ which divided by the number of moles of DBM consumed in first reaction makes an enthalpy of reaction of 52.4 kJ mol^{-1}.

For the second peak the moles of remaining DBM consumed are 2.83 x 10^{-5} moles or 3.17 x 10^{-3} g of butene produced, equivalent to a 15 wt% weight loss. Experimentally the weight loss measured was 14 wt%. Since the enthalpy for the reaction of DBM to MgH_2 is now calculated and now calculating the moles of DBM

consumed during the second peak we can extract the contribution of this decomposition to the overall heat content of the reactions occurring in correspondence of the second peak. The contribution of DBM decomposition in the second peak is 71.7 J g^{-1} and the second peak having a heat content of 240.8 J g^{-1} it leaves a contribution of 169.1 J g^{-1} for the dehydrogenation of MgH_2. Using the DSC sample weight and the enthalpy of dehydrogenation of MgH_2 being 75.9 kJ mol^{-1} [287] and the molecular weight of H_2 of 2.028 g mol^{-1} then the grams of hydrogen produced can be calculated to be 9.21 x 10^{-5} g and therefore a weight loss, or a capacity, of 0.44 wt%.

The enthalpy of formation of DBM from butane and magnesium is reported as -167.5 kJ mol^{-1} [288] but when having the intermediate formation of MgH_2 the process of decomposition to Mg and butene is the sum of the two steps which is 128.3 kJ mol^{-1} suggesting that using butene, rather than using butane, in the synthesis would require less energy.

When DBM is impregnated into carbon nanocones and then decomposed to form magnesium hydride then as such the hydride is present above the temperature of experimental dehydrogenation. This is due to the formation of isolated particles of magnesium on a large hydride particle. This formation follows a dynamics of heterogeneous nucleation with a large nucleation energetic barrier as demonstrated by Danaie [289]. The author states that since the phase transformation from MgH_2 to metallic Mg is accompanied by a significant reduction in volume (24.6 %) [289], generating a large strain energy in the process, it is unlikely that α-MgH_2 would easily yield during bulk nucleation of magnesium. The metal nucleation not being energetically easy, it will not lead to a multitude of magnesium nucleation sites and growth fronts per hydride particle as instead proposed by Zhdanov [290]. Leaving

some hydride particles fully hydrogenated while other particles are already dehydrogenated.

Such coexistence of hydrided and dehydrided particles due to the heterogeneous nucleation serves to explain the presence of two dehydrogenations peaks on at 320 °C and 370 °C. Depending on the size of the particle the heterogeneous nucleation might hinder, and hence delay, or facilitate the dehydrogenation. The TGA analysis at 250° C (figure 4.17) shows a rapid weight loss, in less than 10 minutes, of 68 wt% corresponding to ca. the weight loss needed for the 81.5% of total decomposition of DBM (68 wt%). For the sample of DBM impregnated into carbon nanocones the theoretical sample weight loss of formation of MgH_2, considering the decomposition stoichiometry of equation 5.3, would have been 25.8 % and the experimental weight loss was 28 % of the total weight of the sample. Considering only the DBM component of the sample, the only component that would have to lose weight, then the converted experimental weight loss is 73% comparing with the calculated weight loss of 68 wt%. The difference with the theoretical weight loss is probably due to error committed in dosing the DBM solution during the synthesis. Handling a small amount of solution, a small error committed in dosing the solution would lead to a larger error for the DBM to carbon ratio.

The TEM analysis exemplified by figure 4.23 showed a particle size of 29.9 ± 3.8 nm based on 261 particles counted. Using the full width half maximum (FWHM) measurement of the peaks corresponding to MgH_2 in the XRD patterns depicted in figure 4.22 and using the Scherrer equation [232] the average crystal size is 47 nm. Such difference between the direct and indirect measurements can be due to imperfections in the 3D order of the crystals, which is a requirement of Bragg's law. Those imperfections can be a basis for quantitative deviation from the Bragg

requirement for perfect 3D ordering which is infinite in all spatial directions. Deviations from the latter requirement have been explained by Simeonova *et al*. [291] in terms of 3D features: finite crystallite size random motions of atoms in a crystalline lattice (Debye thermal broadening) or disruption in the long-range order of the crystal. The author found a deviation of 50 %, from 48 nm to 70 nm, when measuring the crystal size of a magnesium oxide sample using a direct microscopy technique and an indirect x-ray analysis consistent with the observations here.

5.6. Mixture of hydride to combine with carbon nanostructures

In the attempt to decrease the temperature of decomposition (250°C) and dehydrogenation (375°C) of the newly formed magnesium hydride the precursor DBM was mixed with another hydride ($LiAlH_4$).

The XRD of the mixture $LiAlH_4$-DBM which has a Al:Mg ratio of 4:1 (figure 4.26) shows only XRD peaks corresponding to $LiAlH_4$ (middle pattern) due its abundance compared to DBM (top pattern). The DSC plot (figure 4.25) however, is very different from that belonging to pure $LiAlH_4$ (figure 4.24). Rafi-ud-din *et al*. [292] identified the DSC peaks of pure $LiAlH_4$ as follows: the first exothermic peak around at 160–163 °C is assigned to the interaction of $LiAlH_4$ with surface hydroxyl impurities, and the first endothermic peak at 166–172 °C corresponds to the melting of $LiAlH_4$. The second exothermic peak at 173–192 °C corresponds to the decomposition of liquid $LiAlH_4$ (first reaction stage) into Li_3AlH_6, and the second endothermic peak at 232–253 °C is assigned to the decomposition of Li_3AlH_6 (second reaction stage) into LiH. The third endothermic peak at 398–428 °C is ascribed to the decomposition of LiH forming the alloy $LiMgAl_2$.

The DSC plot of the mixture $LiAlH_4$-DBM (Al-Mg 4:1) has an endothermic peak at 170 °C, an exothermic peak at 195 °C, another endothermic peak at 220 °C and an endothermic peak at 348 °C. The combination of DSC, TGA and FTIR experiments made it possible to identify the reaction occurring at each peak of the DSC pattern (figure 4.25). The FTIR spectrum (figure 4.30) of the starting material has the peaks at 2955, 2922 and 2869 cm^{-1} and at 1461 and 1376 cm^{-1} that are characteristic of the DBM. and does not match with any peaks with the FTIR spectrum of pure $LiAlH_4$ with stretching modes at 1760 and 1610 cm^{-1} and bending modes at 900 and 803 cm^{-1} [293].

The peak at 170 °C corresponds to the endothermic melting of $LiAlH_4$ followed by its exothermic decomposition into Li_3AlH_6 at 194 °C. At 170 °C as can be observed from the XRD pattern of figure 4.26 (second pattern from the bottom) that beside the peaks corresponding to $LiAlH_4$ at 2θ of 26.61° and 27.20° there is already the formation of Li_3AlH_6 with the peaks at 2θ of 38.34° (d_{113} = 2.34 Å) and 2θ of 44.58° (d_{004} = 2.03 Å) . This result is confirmed also by the FTIR spectrum (figure 4.30) for the sample heated at 170 °C where there is a broad band starting around at 1450 cm^{-1} till 1100 cm^{-1} which is found also in the spectrum of the starting material having a maximum at 1374 cm^{-1}. Ares *et al*. [294] found that a peak corresponding to Li_3AlH_6 lies around 1400 cm^{-1} for the stretching mode v_3(F1). The presence of Li_3AlH_6 can be explained by considering the sequence of peaks at 170 °C and at 195 °C in DSC pattern where the first endothermic peak is the melting of $LiAlH_4$ and the following exothermic peaks the transformation of $LiAlH_4$ into Li_3AlH_6. Due to the rapid sequence of reaction the decomposition of $LiAlH_4$ might already have started at that temperature.

At 195 °C there was a complete decomposition of $LiAlH_4$ and the disappearance of the peak at 1374 cm^{-1} while the peaks at 1457 cm^{-1} and 1374 cm^{-1} were attributed to stretching mode ν_3(F1) and a peak at 1043 cm^{-1} was attributed to bending mode ν_4(F1) of Li_3AlH_6 in accordance with Ares *et al*.[294].

At 220 °C both the decomposition of DBM into MgH_2 and the endothermic decomposition of Li_3AlH_6 into LiH take place. Both of these reactions are destabilized to a lower temperature compared to the previous experiment where the pure DBM decomposition temperature is 250 °C and pure $LiAlH_4$ decomposed into Li_3AlH_6 the at 248 °C.

In fact the XRD pattern at 220 °C (figure 4.28) shows the appearance of peaks at 2θ of 27.91° (d_{110} = 3.19 Å), 35.73° (d_{101} = 2.51Å) attributed to MgH_2. In the FTIR spectrum at 220°C there is a peak at 1084 cm^{-1} that corresponds to MgH_2 (Wang *et al*. [295] found a characteristic peak for MgH_2 at 1160 cm^{-1}). The decomposition of Li_3AlH_6 into LiH was confirmed by the FTIR analysis at 300°C with a broad peak at 1250 cm^{-1}. Awbery *et al*. [296] and Mikheeva [297] showed that LiH has peaks at 1280 cm^{-1} and 1300 cm^{-1} respectively. The XRD analysis however, does not provide a clear confirmation of the presence of LiH. This is because of the similar lattice spacing of LiH and Li_3AlH_6 and also LiH is known to be a poor X-ray scatterer [298]. The TGA analysis revealed at 300°C a weight loss of 36% compared to the theoretical value of 41 % for the loss of two butene from the decomposition of DBM and 6 H_2 from the reactions:

$$4LiAlH_4 \xrightarrow{195°C} \frac{4}{3}Li_3AlH_6 + \frac{4}{3}Al + 4H_2 \quad (5.5)$$

$$Mg(C_4H_{10}) \xrightarrow{220°C} MgH_2 + 2C_4H_8 \quad (5.6)$$

$$\frac{4}{3}Li_3AlH_6 \xrightarrow{220°C} 4LiH + \frac{4}{3}Al + 2H_2 \quad (5.7)$$

Furthermore, the TGA at 400 °C revealed a weight loss of 41 % which is very close to the theoretical value of 42 % (decomposition of DBM, dehydrogenation of the following formed MgH_2 and total dehydrogenation of $LiAlH_4$).

The TGA experiment at 585 °C with a weight loss of 42 % confirms that all the dehydrogenation occurred below 400 °C. This means that the DSC peak at 348 °C corresponds to the dehydrogenation temperature of LiH which is significantly lowered compared to the temperature of 410 °C [292] found by Rafi-ud-din. This is confirmed by the FTIR spectrum at 400 °C and 585 °C that sees the disappearance of LiH peak at 1250 cm^{-1}. In addition, in the XRD patterns at 350 °C, 475 °C and 535 °C only the Al peak can be detected. It is observed that the Al peak is progressively shifting to higher d spacing with increasing temperature. Such a shift is not due to formation of alloys but to the thermal expansion. This is confirmed by analysing the d spacing trend at each temperature step (figure 5.3) where the lattice expansion has an evident linear trend. This linear trend is the same for a sample of pure Al used as a standard reference.

Once the Al is allowed to cool down it forms the $LiMgAl_2$ alloy as observed in the XRD pattern at 30 °C (figure 4.29 top pattern).

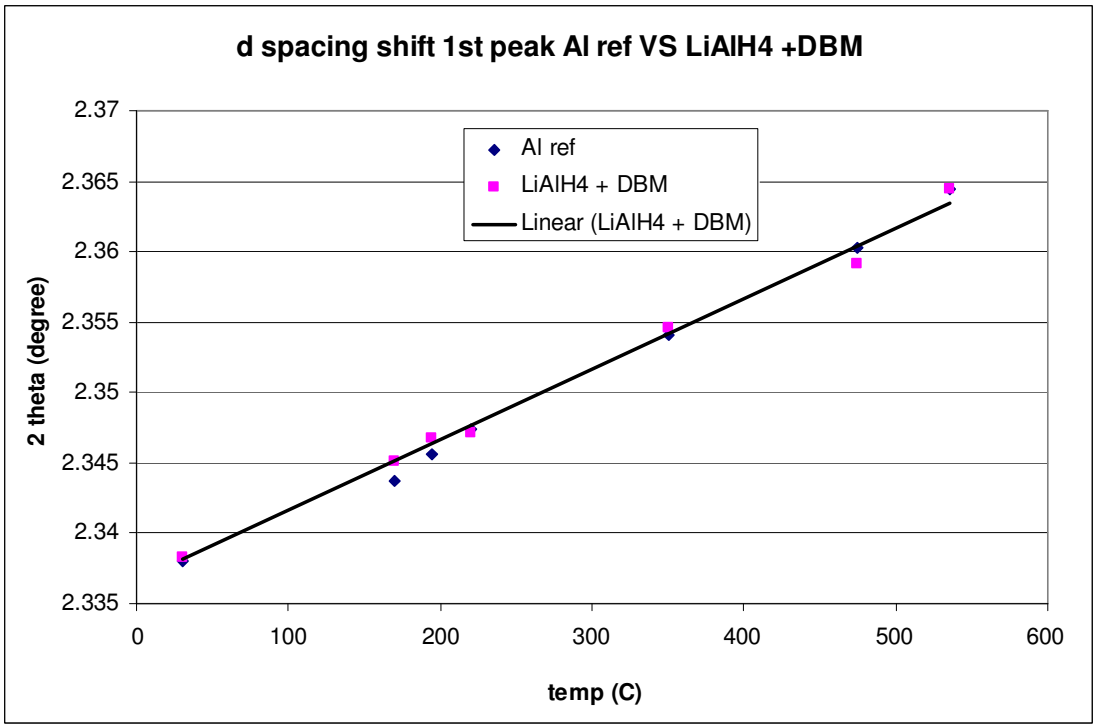

Figure 5.3 Variation of 2θ with temperature showing a linear trend for the d spacing of the Al peak at various temperatures in the $LiAlH_4$-DBM (Al-Mg 4:1) sample and pure Al sample used as standard reference

In the system examined by the Rafi-ud-din [292] $LiAlH_4$ is doped with 2 wt% of TiC resulting in a drop of 50°C of temperature for the decomposition of $LiAlH_4$ (equation 5.6) and a drop of 60°C for the decomposition of Li_3AlH_6 (equation 5.7). However, the TiC catalyst does not appear to decrease significantly the dehydrogenation of LiH with a modest decrease of 18 °C from 428 °C to 410 °C reported. In the work of this thesis the temperature for the decomposition of $LiAlH_4$ (equation 5.6) does not vary significantly between the reference $LiAlH_4$ sample (185 °C) and the mixture $LiAlH_4$-DBM (Al-Mg 4:1) (194 °C). The decomposition of Li_3AlH_6 (equation 5.7) drops by 28°C and the temperature for dehydrogenation of LiH decreases by 142 °C from 490 °C to 348 °C. This means that systems of $LiAlH_4$ doped with MX (M = Ti, Nb, Ni X=halide, oxide, carbide) [299-302] such that used

by Rafi-ud-din are not effective to destabilize LiH, and this is the reason why those studies focus on narrower the temperature ranges till 300 °C.

However, as reported by Zhang *et al* [303] Mg is a good destabilizing catalyst for LiH reporting a dehydrogenation temperature for LiH and MgH_2 of 334 °C. The MgH_2 - $LiAlH_4$ system achieving such temperature corresponded to a ratio of 1:1 with the desorption temperature increased with the increase of MgH_2 content. However, the MgH_2 - $LiAlH_4$ 1:1 intention was to use LiH to destabilize MgH_2 and not vice versa. In this work the MgH_2 - $LiAlH_4$ 1:4 system, being rich in $LiAlH_4$, confirms the catalytic effect between MgH_2 and LiH is mutual with a decrease in the decomposition temperature for the MgH_2 from.375 °C to 348 °C which was the purpose of this attempt of mixing However, the author noticed that increasing the content of $LiAlH_4$ the temperature for LiH dehydrogenation increases again, hence if the purpose was to decrease the dehydrogenation temperature for LiH the optimal ratio MgH_2 - $LiAlH_4$ is of 1:1.

The two stages of dehydrogenation of $LiAlH_4$ (reaction equation 5.4 and 5.6), are reported by Zhang to happen between 200°C and 250°C whether Mg is present or not, showing that a MgH_2 rich MgH_2 - $LiAlH_4$ system does not have destabilizing effect on first two stages of decomposition of $LiAlH_4$ and also in the work of this thesis remains unchanged. In the work of Shu-Shen *et al* [304] the MgH_2 – Li_3AlH_6 system in various ratios was studied including the MgH_2 deficient system with a 1:4 ratio. Results of Shu-Shen study show that also the MgH_2 deficient system does not decrease the temperature of transformation of Li_3AlH_6 into LiH while the work presented here shows a 28 °C decrease from 248 °C to 220 °C. This means that MgH_2 is capable to decrease the dehydrogenation temperature for LiH and in some extent also the temperature for earlier stages of $LiAlH_4$ decomposition however, not as

efficiently as compounds like NbF_5 or TiF_5 as studied in the work Ismail [299] where for a sample of $LiAlH_4$ + 1 mol% NbF_5 at 135 °C and at 217 °C occurs the decomposition of $LiAlH_4$ and the decomposition of Li_3AlH_6 respectively. The authors motivates that this is due to the interaction between F^- and Li^+ that may release binding energy between Li and H.

.

6. Conclusions

The utilization of carbon nanocones toward a viable material of hydrogen storage started with an initial oxidative pre-treatment with H_2O_2 which increased the surface area from 22 to 27 m^2g^{-1} and changed the morphology of the surface creating some etching defects. The subsequent Pd catalyst impregnation via incipient wetness produced a catalyst oxide dispersion that has been successfully reduced to metal catalyst by two methods: in hydrogen atmosphere at room temperature and in aqueous solution with $NaBH_4$. The resulting dispersion showed a very fine particle size of ~ 1 nm for the sample decorated with Pd 5 wt%. The particle size increased as the metal load increased and conversely the surface area decreased with the increase of metal load. In comparison the same route of treatment and impregnation has been done on graphite nanofibres (GNF) showing a much larger metal particle size which does not increase with the metal loading while the surface area had no correlation with the increase of metal load. Other metal catalysts were impregnated on the carbon surface such as: Ni, a mixture of Pd-Ni, Pd-Cu and Pd-Ag but none of those achieved such small particle size as with the sample with only Palladium.

An intelligent gravimetric analysis of the hydrogen uptake at 77 K has been carried out for the carbon nanocone sample loaded with Pd at 5 10 and 15 wt% as well as for the GNF with the same Pd metal loadings and the results have been compared. For the carbon nanocone sample there was a linear decrease of hydrogen uptake with an increase in metal content indicating that the hydrogen physisorption directly correlated with the surface area only and was not affected by the presence of a metal catalyst at 77 K. For the GNF material the hydrogen uptake has been found to correlate to the pore volume.

Results from the hydrogen uptake analysis at room temperature showed an increase of the hydrogen adsorption with an increase in the metal content for nanocones with Pd and the experimental values matched the cumulative sum of the carbon substrate plus the metal hydride contribution. The hydrogen adsorption for as synthesized GNF appeared to be comparable to that of carbon nanocones demonstrating that at room temperature the contribution of physisorption was minimal, due to the weak interaction between hydrogen molecules and the surface. On the other hand the GNF samples impregnated with Pd showed a higher hydrogen uptake than that of the cumulative sum of the two above mentioned contributions. This means that the catalyst has been able to dissociate the hydrogen molecules into hydrogen atoms that then will diffuse on the surface. Such a spillover contribution accounts for a maximum of 0.117 wt% for the GNF sample with Pd 15 wt%. An interesting future work direction in that sense would be to compare the contribution of different carbon nanostructure morphologies such as activated carbon, single wall carbon nanotubes (SWCNT), multi wall carbon nanotubes (MWCNT) and graphene.

The use of another metal catalyst Ni mounted on GNF resulted in a hydrogen adsorption of 0.072 wt% which is again attributable to small level of hydrogen spillover. Mixing Pd with other metal catalysts such as Ni, Cu and Ag resulted in an increase in hydrogen uptake for the carbon nanocones samples impregnated with Pd-Ni and Pd-Cu of 0.080 wt% and 0.097 wt%, respectively, in comparison with the carbon nanocones sample decorated with only Pd which was 0.076 wt% . This increase has been related to the fact that in such alloys there is a contraction of the lattice acting as a hydrogen trap. Confirming that mixing the Pd catalyst with cheaper metals, like Ni or Cu, would not only have economical advantages but also would

improve the hydrogen uptake. In the case of Pd-Ag there is an expansion of the lattice and this resulted in a decrease in the hydrogen uptake.

Carbon nanocones have also been mixed with the Mg organometallic precursor dibutyl magnesium (DBM). This organometallic precursor has been decomposed at 250°C in 1 bar Argon atmosphere forming successfully MgH_2. The novel formation of MgH_2 without the need of a hydrogen atmosphere was due to the two butyl groups being lost as butene leaving on the metal one hydrogen atom per butyl group. Through DSC and TGA analysis it was possible to establish that 81.5% of the DBM is decomposed at 250°C to MgH_2 and the remaining decomposed at 370°C forming MgH_2 which instantly desorbed hydrogen. Such decomposition reaction has an enthalpy of 52.4 kJ mol^{-1}.

The precursor DBM has been mixed with another metal hydride, $LiAlH_4$ and the sequence of decomposition reactions has been studied. Through a combination of DSC, TGA and FTIR analysis has been establish that the temperature of decomposition of DBM as well as Li_3AlH_6 is decreased from 248°C to 220°C and more importantly the temperature of decomposition of LiH decreased from 490°C to 348°C.

7. Future work

Since the GNFs have showed to have higher surface area and have revealed to be capable of hydrogen spillover then would be suitable as future work a thorough comparison of the hydrogen adsorption at room temperature for various types of carbon nanostructures. Focus of this comparison will be the correlation between the morphology and the hydrogen uptake. Through hydrogen uptake analysis, microscope image analysis of the pristine carbon nanostructures it will be established if the hydrogen spillover mechanism is mainly influenced by the curvature of there are other morphological aspects (such as defects in the graphene planes) rather than being the metal catalyst contributing to such mechanism.

On the other hand the metal catalyst contribution could be further characterized via cyclic voltammetry to measure the effectively active area of the metal particles dispersed on the surface. This measurement, in combination with hydrogen adsorption measurements, will help to understand the correlation between the particle size and the hydrogen uptake. Results of such investigation will not only be useful in the field of hydrogen storage but also in the reaction of oxygen reduction in the fuel cell membrane.

Furthermore has grown recently interests toward metal catalyst alloys for synthesis reactions such as Heck and Suzuki reactions hence will be of interests to continue the work of using metal alloys for hydrogen storage. The work will be focused on finding the metal catalyst alloys that would not only lower the costs but also present smallest average particle size, and the highest hydrogen uptake. In addition to that the metal catalyst alloys would offer the advantage of using an

alloying metal, such as Ru, that reduced the adsorption of carbon monoxide, considered poisonous for the metal catalyst in fuel cell applications.

As stated above cyclic voltammetry would be helpful to establish the correlation between particle size and hydrogen uptake and this can be repeated also for the samples impregnated with mixed metal catalyst alloys.

Another aspect of the hydrogen adsorption of metal assisted carbon nanostructures is the reproducibility of the results. Oftentimes scientific works omit to specify if the results achieved have been obtained with a certain interval of confidence. Establish the reliability of results through an error analysis would beneficial for the credibility of the publication, especially for controversial topics as the spillover effect treated in this thesis, and the instrument error assessment.

Carbon nanostructures besides being used to adsorb hydrogen have found interesting application in field of solid phase extraction. Within the different nanostructures, carbon nanocones have registered interesting results that would encourage their use in field of purification such as water pollutant removal.

Particularly good results in the decrease of the decomposition temperature for $LiAlH_4$ and Li_3AlH_6 has been discussed when has been added + 1 mol% NbF_5 to $LiAlH_4$. Hence would be of interest for further studies would be the system MgF_2 - $LiAlH_4$ and see if beside the contribution of the ion F^- tin lowering the early stages decomposition temperature of $LiAlH_4$ there is also the contribution of Mg in decreasing the decomposition temperature of late stages of $LiAlH_4$ decomposition. Furthermore, it would be of interest to analyse the cyclability of the system MgH_2 - $LiAlH_4$ obtained by decompositions of DBM, thanks to a fast kinetics correlated to the nanosized MgH_2 obtained also in the work of this thesis. In addition another interesting future development would be the exploitation of the combination of such

mix hydride with nanocones that in this thesis are found to have a beneficial effect in matter of decreasing the dehydrogenation temperature to 320°C, comparing to the temperature of 375°C of pure DBM sample to the catalytic role of carbon nanostructures on the dehydrogenation of $LiAlH_4$

8. Disseminations

The results contained in this thesis have been used to produce several scientific disseminations.

The work done on Pd particles dispersion over carbon nanocones has been presented at the oral session of the MRS 2009 fall meeting conference with the title "Supporting metal catalysts on modified carbon nanocones to optimize dispersion and particle size". Furthermore, a full paper has been published as proceeding of the above mentioned presentation and made available online in the Symposium proceeding volume 1216 [305].

Subsequently the work on metal dispersion over carbon nanostructure has been presented within the UK-SHEC consortium adding further findings on the metal dispersion characterization from the previous work published in the proceeding paper.

The work on hydrogen uptake performances for the carbon nanocones impregnated with Pd has been presented as oral presentation at 10th International Short Course and Advanced Research Workshop (ISCARW) "Progress in hydrogen safety" with the title "Hydrogen adsorption measurements on metal supported modified carbon nanocones" in Belfast in January 2011. Such presentation shed light on the limitations of hydrogen adsorption on metal assisted carbon nanocones reporting that such material adsorbs an amount of hydrogen corresponding to only the cumulative sum of the metal catalyst and carbon substrate contributions.

The findings showing the difference in hydrogen adsorption at room temperature between carbon nanocones and graphite nanofibres constitute a thorough characterization that is readily publishable. Such piece of work could be attempted to be published with the title "The influence of the carbon nanostructure morphology on

the spillover phenomenon and its quantification" within a selection of scientific journals such as "International Journal of Hydrogen Energy", "Applied Catalysis A: General" or "Materials Science and Engineering: B Advanced Functional Solid-State Materials" in order of decreasing impact factor.

The novel decomposition of DBM in milder condition along the quantification of its thermodynamics and the characterization of the products have scientific worth and is intended to be published very soon. The tentative of title would be "Characterization of the MgH_2 production from the decomposition of the precursor dibutyl magnesium in milder conditions" and could be submitted to the journals "Applied Physics A" or "Journal of Alloys and Compounds".

9. References

1. Bilgen E, *Domestic hydrogen production using renewable energy.* Solar Energy, 2004. **77**(1): p. 47-55.
2. Guo, X.M., et al., *Hydrogen production from agricultural waste by dark fermentation: A review.* International Journal of Hydrogen Energy, 2010. **35**(19): p. 10660-10673.
3. Antonopoulou, G., et al., *Biofuels generation from sweet sorghum: Fermentative hydrogen production and anaerobic digestion of the remaining biomass.* Bioresource Technology, 2008. **99**(1): p. 110-119.
4. Lipman, T.E., *What will power the hydrogen economy? Analysis and report prepared for the Natural Resources Defense Council.* 2004.
5. Escalante Soberanis, M.A. and A.M. Fernandez, *A review on the technical adaptations for internal combustion engines to operate with gas/hydrogen mixtures.* International Journal of Hydrogen Energy, 2009. **35**(21): p. 12134-12140.
6. Zhou, L., *Progress and problems in hydrogen storage methods.* Renewable and Sustainable Energy Reviews, 2005. **9**(4): p. 395-408.
7. Kapdan, I.K. and F. Kargi, *Bio-hydrogen production from waste materials.* Enzyme and Microbial Technology, 2006. **38**(5): p. 569-582.
8. Gustav P, D., *Hydrogen: The ultimate fuel and energy carrier.* International Journal of Hydrogen Energy, 1989. **14**(11): p. 777-784.
9. Offer, G.J., et al., *Techno-economic and behavioural analysis of battery electric, hydrogen fuel cell and hybrid vehicles in a future sustainable road transport system in the UK.* Energy Policy. **39**(4): p. 1939-1950.
10. Pearre, N.S., et al., *Electric vehicles: How much range is required for a day's driving?* Transportation Research Part C: Emerging Technologies, 2011. **19**(6): p. 1171-1184.
11. Pearre, N.S., et al., *Electric vehicles: How much range is required for a day's driving?* Transportation Research Part C: Emerging Technologies, 2011. **19**(6): p. 1171-1184.
12. Perry, R. and I.L. Gee, *Vehicle emissions in relation to fuel composition.* Science of The Total Environment, 1995. **169**(13): p. 149-156.
13. Yeh, S., et al., *An Integrated Assessment of the Impacts of Hydrogen Economy on Transportation, Energy Use, and Air Emissions.* Proceedings of the IEEE, 2006. **94**(10): p. 1838-1851.
14. Pearre, N.S., et al., *Electric vehicles: How much range is required for a day's driving?* Transportation Research Part C: Emerging Technologies. **19**(6): p. 1171-1184.
15. Sopian, K., et al., *Performance of a PV-wind hybrid system for hydrogen production.* Renewable Energy, 2009. **34**(8): p. 1973-1978.
16. Energy, U.S.D.o., *DOE Targets for Onboard Hydrogen Storage Systems for Light-Duty Vehicles*, U.S.D.o. Energy, Editor. 2011.
17. Guo, Z.X., C. Shang, and K.F. Aguey-Zinsou, *Materials challenges for hydrogen storage.* Journal of the European Ceramic Society, 2008. **28**(7): p. 1467-1473.
18. Storage, D.o.E.D.C.o.E.f.H., *2011 Interim Update Technical Plan — Storage*. 2010.

19. Tomioka, J.-i., et al., *Influence of temperature on the fatigue strength of compressed-hydrogen tanks for vehicles.* International Journal of Hydrogen Energy. **36**(3): p. 2513-2519.
20. Wolf, J., *Liquid-hydrogen technology for vehicles.* MRS Bulletin, 2002. **27**(9): p. 684-687.
21. Aceves, S.M., et al., *Vehicular storage of hydrogen in insulated pressure vessels.* International Journal of Hydrogen Energy, 2006. **31**(15): p. 2274-2283.
22. Ahluwalia, R.K. and J.K. Peng, *Dynamics of cryogenic hydrogen storage in insulated pressure vessels for automotive applications.* International Journal of Hydrogen Energy, 2008. **33**(17): p. 4622-4633.
23. Mori, D. and K. Hirose, *Recent challenges of hydrogen storage technologies for fuel cell vehicles.* International Journal of Hydrogen Energy, 2009. **34**(10): p. 4569-4574.
24. Ahluwalia, R.K., et al., *Technical assessment of cryo-compressed hydrogen storage tank systems for automotive applications.* International Journal of Hydrogen Energy. **35**(9): p. 4171-4184.
25. Aceves, S.M., et al., *High-density automotive hydrogen storage with cryogenic capable pressure vessels.* International Journal of Hydrogen Energy. **35**(3): p. 1219-1226.
26. International Energy Agency, O.f.E.C.-o.a.D., *Hydrogen and fuel cells*. 2006.
27. Sing, K.S.W., et al., 1985. **57**: p. 603.
28. Ho, S.T. and D.W. Hutmacher, *A comparison of micro CT with other techniques used in the characterization of scaffolds.* Biomaterials, 2006. **27**(8): p. 1362-1376.
29. Banard, P. and R. Chahine, *Storage of hydrogen by physisorption on carbon and nanostructured materials.* Scripta Materialia, 2007. **56**(10): p. 803-808.
30. Wang, H., et al., Carbon, 2009. **47**(9): p. 2259-2268.
31. Poirier, E., R. Chahine, and T.K. Bose, . International Journal of Hydrogen Energy, 2001. **26**(8): p. 831-835.
32. Han, S.S. and H.M. Lee, *Adsorption properties of hydrogen on (10,0) single-walled carbon nanotube through density functional theory.* Carbon, 2004. **42**(11): p. 2169-2177.
33. Sakintuna, B., F. Lamari-Darkrim, and M. Hirscher, *Metal hydride materials for solid hydrogen storage: A review.* International Journal of Hydrogen Energy, 2007. **32**(9): p. 1121-1140.
34. Bogdanovic, B., et al., *Thermodynamic investigation of the magnesium-hydrogen system.* Journal of Alloys and Compounds, 1999. **282**(1-2): p. 84-92.
35. Zaluska, A., L. Zaluski, and J.O. Strom-Olsen, *Nanocrystalline magnesium for hydrogen storage.* Journal of Alloys and Compounds, 1999. **288**(1-2): p. 217-225.
36. Friedlmeier, G. and M. Groll, *Experimental analysis and modelling of the hydriding kinetics of Ni-doped and pure Mg.* Journal of Alloys and Compounds, 1997. **253-254**: p. 550-555.
37. Andreasen, A., T. Vegge, and A.S. Pedersen, *Compensation Effect in the Hydrogenation/Dehydrogenation Kinetics of Metal Hydrides.* The Journal of Physical Chemistry B, 2005. **109**(8): p. 3340-3344.
38. Grochala, W. and P.P. Edwards, *Thermal decomposition of the non-interstitial hydrides for the storage and production of hydrogen.* Chemical Reviews, 2004. **104**(3): p. 1283-1315.

39. Jung, K.S., E.Y. Lee, and K.S. Lee, *Catalytic effects of metal oxide on hydrogen absorption of magnesium metal hydride.* Journal of Alloys and Compounds, 2006. **421**(1-2): p. 179-184.
40. Song, M., J.-L. Bobet, and B. Darriet, *Improvement in hydrogen sorption properties of Mg by reactive mechanical grinding with Cr2O3, Al2O3 and CeO2.* Journal of Alloys and Compounds, 2002. **340**(1-2): p. 256-262.
41. Zhu, M., et al., *Composite structure and hydrogen storage properties in Mg-base alloys.* International Journal of Hydrogen Energy, 2006. **31**(2): p. 251-257.
42. Wang, P., et al., *Hydriding properties of a mechanically milled Mg 50 wt.% ZrFe1.4Cr0.6 composite.* Journal of Alloys and Compounds, 2000. **297**(1-2): p. 240-245.
43. Dehouche, Z., et al., *Influence of cycling on the thermodynamic and structure properties of nanocrystalline magnesium based hydride.* Journal of Alloys and Compounds, 2000. **305**(1-2): p. 264-271.
44. Liang, G., et al., *Catalytic effect of transition metals on hydrogen sorption in nanocrystalline ball milled MgH2-Tm (Tm=Ti, V, Mn, Fe and Ni) systems.* Journal of Alloys and Compounds, 1999. **292**(1-2): p. 247-252.
45. Tien, H.-Y., et al., *Effect of hydride nucleation rate on the hydrogen capacity of Mg.* International Journal of Hydrogen Energy, 2009. **34**(15): p. 6343-6349.
46. Čermak, J. and L. Kral, *Hydrogen diffusion in Mg-H and Mg-Ni-H alloys.* Acta Materialia, 2008. **56**(12): p. 2677-2686.
47. Pedersen, A.S. and B. Larsen, *The storage of industrially pure hydrogen in magnesium.* International Journal of Hydrogen Energy, 1993. **18**(4): p. 297-300.
48. Bouaricha, S., et al., *Reactivity during cycling of nanocrystalline Mg-based hydrogen storage compounds.* International Journal of Hydrogen Energy, 2002. **27**(9): p. 909-913.
49. Jain, I.P., et al., *Hydrogen storage in thin film metal hydride: a review.* International Journal of Hydrogen Energy, 1988. **13**(1): p. 15-23.
50. Heiberg-Andersen, H., A.T. Skjeltorp, and K. Sattler, Journal of Non-Crystalline Solids, 2008. **354**(47-51): p. 5247-5249.
51. Kim, B.-J., Y.-S. Lee, and S.-J. Park, *Preparation of platinum-decorated porous graphite nanofibers, and their hydrogen storage behaviors.* Journal of Colloid and Interface Science, 2008. **318**(2): p. 530-533.
52. Contescu, C.I., et al., *Detection of Hydrogen Spillover in Palladium-Modified Activated Carbon Fibers during Hydrogen Adsorption.* The Journal of Physical Chemistry C, 2009. **113**(14): p. 5886-5890.
53. Zielinski, M., et al., *Hydrogen storage on nickel catalysts supported on amorphous activated carbon.* Catalysis Communications, 2005. **6**(12): p. 777-783.
54. Guczi, L., et al., *CO hydrogenation over cobalt and iron catalysts supported over multiwall carbon nanotubes: Effect of preparation.* Journal of Catalysis, 2006. **244**(1): p. 24-32.
55. Panella, B., M. Hirscher, and S. Roth, *Hydrogen adsorption in different carbon nanostructures.* Carbon, 2005. **43**(10): p. 2209-2214.
56. Zuo, S., et al., *Significance of the carbonization of volatile pyrolytic products on the properties of activated carbons from phosphoric acid activation of lignocellulosic material.* Fuel Processing Technology, 2009. **90**(7-8): p. 994-1001.

57. Conesa, J.A., M. Sakurai, and M.J. Antal Jr, *Synthesis of a high-yield activated carbon by oxygen gasification of macadamia nut shell charcoal in hot, liquid water.* Carbon, 2000. **38**(6): p. 839-848.
58. Tamai, H., et al., *Synthesis of Extremely Large Mesoporous Activated Carbon and Its Unique Adsorption for Giant Molecules.* Chemistry of Materials, 1996. **8**(2): p. 454-462.
59. Li, Y., et al., *A simple and highly effective process for the preparation of activated carbons with high surface area.* Materials Chemistry and Physics. **127**(3): p. 495-500.
60. Tseng, H.-H. and M.-Y. Wey, *Study of SO2 adsorption and thermal regeneration over activated carbon-supported copper oxide catalysts.* Carbon, 2004. **42**(11): p. 2269-2278.
61. Carabineiro, S.n.A., D.W. McKee, and I.F. Silva, *Uncatalysed and catalysed CO2 reaction using metal catalysts and binary vanadium mixtures supported on activated carbon.* Carbon, 2001. **39**(3): p. 451-463.
62. Calvo, L., et al., *Hydrodechlorination of diuron in aqueous solution with Pd, Cu and Ni on activated carbon catalysts.* Chemical Engineering Journal. **163**(3): p. 212-218.
63. Calvo, L., et al., *Treatment of chlorophenols-bearing wastewaters through hydrodechlorination using Pd/activated carbon catalysts.* Carbon, 2004. **42**(7): p. 1377-1381.
64. ZieliÅ„ski, M., et al., *Hydrogen storage in nickel catalysts supported on activated carbon.* International Journal of Hydrogen Energy, 2007. **32**(8): p. 1024-1032.
65. Huang, C.-C., H.-M. Chen, and C.-H. Chen, *Hydrogen adsorption on modified activated carbon.* International Journal of Hydrogen Energy. **35**(7): p. 2777-2780.
66. Liu, Y., et al., *Amorphous carbon nanotubes produced by a temperature controlled DC arc discharge.* Carbon, 2004. **42**(8-9): p. 1852-1855.
67. Huang, C.-W., H.-C. Wu, and Y.-Y. Li, *Hydrogen storage in platelet graphite nanofibers.* Separation and Purification Technology, 2007. **58**(1): p. 219-223.
68. Yang, Q.-H., et al., *Adsorption and capillarity of nitrogen in aggregated multi-walled carbon nanotubes.* Chemical Physics Letters, 2001. **345**(1-2): p. 18-24.
69. Hillert, M. and N. Lange, *The structure of graphite filaments.* Zeitschrift fur Kristallographie, 1959. **111**(1-6): p. 24-34.
70. Serp, P., M. Corrias, and P. Kalck, *Carbon nanotubes and nanofibers in catalysis.* Applied Catalysis A: General, 2003. **253**(2): p. 337-358.
71. Inoue, S., et al., *Capillary Condensation of N2 on Multiwall Carbon Nanotubes.* The Journal of Physical Chemistry B, 1998. **102**(24): p. 4689-4692.
72. Eswaramoorthy, M., R. Sen, and C.N.R. Rao, *A study of micropores in single-walled carbon nanotubes by the adsorption of gases and vapors.* Chemical Physics Letters, 1999. **304**(3-4): p. 207-210.
73. Bethune, D.S., et al., *Cobalt-catalysed growth of carbon nanotubes with single-atomic-layer walls.* Nature, 1993. **363**(6430): p. 605-607.
74. Dresselhaus, M.S., G. Dresselhaus, and P.C. Eklund, *Science of fullerenes and carbon nanotubes*. 1996, San Diego: Academic Press.

75. Mahdavian, L. and M. Monajjemi, *Alcohol sensors based on SWNT as chemical sensors: Monte Carlo and Langevin dynamics simulation.* Microelectronics Journal. **41**(2-3): p. 142-149.
76. Rao, C.N.R., et al., *Nanotubes.* ChemPhysChem, 2001. **2**(2): p. 78-105.
77. Charlier, J.C., *Defects in Carbon Nanotubes.* Accounts of Chemical Research, 2002. **35**(12): p. 1063-1069.
78. Menon, M., A.N. Andriotis, and G.E. Froudakis, *Curvature dependence of the metal catalyst atom interaction with carbon nanotubes walls.* Chemical Physics Letters, 2000. **320**(5-6): p. 425-434.
79. Chen, C.S., et al., *Modification of multi-walled carbon nanotubes with fatty acid and their tribological properties as lubricant additive.* Carbon, 2005. **43**(8): p. 1660-1666.
80. Lee, S., et al., *Chemical modification of carbon nanotube for improvement of field emission property.* Microelectronic Engineering, 2009. **86**(10): p. 2110-2113.
81. Zhang, D., et al., *Preparation and modification of carbon nanotubes.* Materials Letters, 2005. **59**(29-30): p. 4044-4047.
82. Garcia, J., et al., *Carbon nanotube supported ruthenium catalysts for the treatment of high strength wastewater with aniline using wet air oxidation.* Carbon, 2006. **44**(12): p. 2384-2391.
83. Li, L., G. Wu, and B.-Q. Xu, *Electro-catalytic oxidation of CO on Pt catalyst supported on carbon nanotubes pretreated with oxidative acids.* Carbon, 2006. **44**(14): p. 2973-2983.
84. Yao, Y.-l., et al., *Two-step pyrolysis process to synthesize highly dispersed Pt-Ru/carbon nanotube catalysts for methanol electrooxidation.* Carbon, 2006. **44**(1): p. 61-66.
85. Peng, F., et al., *Preparation of carbon nanotube-supported Fe2O3 catalysts and their catalytic activities for ethylbenzene dehydrogenation.* New Carbon Materials, 2007. **22**(3): p. 213-217.
86. Huang, Y., et al., *Accurately measuring the hydrogen generation rate for hydrolysis of sodium borohydride on multiwalled carbon nanotubes/Co-B catalysts.* International Journal of Hydrogen Energy, 2008. **33**(23): p. 7110-7115.
87. Murayama, H. and T. Maeda, *A novel form of filamentous graphite.* Nature, 1990. **345**(6278): p. 791-793.
88. Marella, M. and M. Tomaselli, *Synthesis of carbon nanofibers and measurements of hydrogen storage.* Carbon, 2006. **44**(8): p. 1404-1413.
89. JimÃ©nez, V., et al., *Synthesis and characterization of ruthenium supported on carbon nanofibers with different graphitic plane arrangements.* Chemical Engineering Journal. **168**(2): p. 947-954.
90. Bessel, C.A., et al., *Graphite Nanofibers as an Electrode for Fuel Cell Applications.* The Journal of Physical Chemistry B, 2001. **105**(6): p. 1115-1118.
91. Lueking, A.D., et al., Carbon, 2007. **45**(4): p. 751-759.
92. Endo, M., et al., *Structural characterization of cup-stacked-type nanofibers with an entirely hollow core.* Applied Physics Letters, 2002. **80**(7): p. 1267-1269.
93. Rodriguez, N.M., A. Chambers, and R.T.K. Baker, *Catalytic Engineering of Carbon Nanostructures.* Langmuir, 1995. **11**(10): p. 3862-3866.

94. Bououdina, M., D. Grant, and G. Walker, *Effect of processing conditions on unsupported Ni-based catalysts for graphitic-nanofibre formation.* Carbon, 2005. **43**(6): p. 1286-1292.
95. Babu, J.S.S. and C.G. Kang, *Nanoindentation behaviour of aluminium based hybrid composites with graphite nanofiber/alumina short fiber.* Materials & Design. **31**(10): p. 4881-4885.
96. Kim, B.J. and S.J. Park, *Preparation of nanoporous carbons from graphite nanofibres.* Nanotechnology, 2006. **17**(17): p. 4395-4398.
97. Seo, M.-K. and S.-J. Park, *Thermomechanical properties of graphite nanofibers/poly(methyl methacrylate) composites.* Materials Science and Engineering: A, 2009. **508**(1-2): p. 28-32.
98. Wu, Y., et al., *Electroanalytical application of graphite nanofibers paste electrode.* Sensors and Actuators B: Chemical. **145**(2): p. 749-755.
99. Krungleviciute, V., A.D. Migone, and M. Pepka, *Characterization of single-walled carbon nanohorns using neon adsorption isotherms.* Carbon, 2009. **47**(3): p. 769-774.
100. Iijima, S., et al., *Nano-aggregates of single-walled graphitic carbon nano-horns.* Chemical Physics Letters, 1999. **309**(3-4): p. 165-170.
101. Murata, K., et al., *Pore structure of single-wall carbon nanohorn aggregates.* Chemical Physics Letters, 2000. **331**(1): p. 14-20.
102. Yamaguchi, T., S. Bandow, and S. Iijima, *Synthesis of carbon nanohorn particles by simple pulsed arc discharge ignited between pre-heated carbon rods.* Chemical Physics Letters, 2004. **389**(1-3): p. 181-185.
103. Murata, K., et al., *Porosity Evaluation of Intrinsic Intraparticle Nanopores of Single Wall Carbon Nanohorn.* Nano Letters, 2001. **1**(4): p. 197-199.
104. Kasuya, D., et al., *Selective Production of Single-Wall Carbon Nanohorn Aggregates and Their Formation Mechanism.* The Journal of Physical Chemistry B, 2002. **106**(19): p. 4947-4951.
105. Yang, C.M., et al., *Highly Ultramicroporous Single-Walled Carbon Nanohorn Assemblies.* Advanced Materials, 2005. **17**(7): p. 866-870.
106. Murata, K., M. Yudasaka, and S. Iijima, *Hydrogen production from methane and water at low temperature using EuPt supported on single-wall carbon nanohorns.* Carbon, 2006. **44**(4): p. 818-820.
107. Lammert, P.E. and V.H. Crespi, *Graphene cones: Classification by fictitious flux and electronic properties.* Physical Review B, 2004. **69**(3): p. 035406.
108. Sattler, K., Carbon, 1995. **33**(7): p. 915-920.
109. Wang, W.H., Y.T. Lin, and C.T. Kuo, Diamond and Related Materials, 2005. **14**(3-7): p. 907-912.
110. Gotzias, A., et al., *A grand canonical Monte Carlo study of hydrogen adsorption in carbon nanohorns and nanocones at 77 K.* Carbon, 2011. **49**(8): p. 2715-2724.
111. Zhang, W., et al., Carbon, 2009. **47**(12): p. 2763-2775.
112. Sattler, K., *Scanning tunneling microscopy of carbon nanotubes and nanocones.* Carbon, 1995. **33**(7): p. 915-920.
113. Yu, X., et al., Applied Surface Science, 2008. **255**(5, Part 1): p. 1906-1910.
114. Strobel, R., et al., *Hydrogen storage by carbon materials.* Journal of Power Sources, 2006. **159**(2): p. 781-801.
115. Figueiredo, J.L., et al., *Modification of the surface chemistry of activated carbons.* Carbon, 1999. **37**(9): p. 1379-1389.

116. Yoo, J.-W., et al., *Adsorption and Desorption Characteristics of Maltooligosaccharide for the Surface Treated Activated Carbons.* Adsorption, 2005. **11**(0): p. 719-723.
117. Carrott, P.J.M., et al., *Preparation of activated carbon fibres from acrylic textile fibres.* Carbon, 2001. **39**(10): p. 1543-1555.
118. Kinoshita, K., *Carbon : electrochemical and physicochemical properties*. 1988, New York: Wiley.
119. Kitagawa, S., R. Kitaura, and S.-i. Noro, *Functional Porous Coordination Polymers.* Angewandte Chemie International Edition, 2004. **43**(18): p. 2334-2375.
120. Gomez-Serrano, V., et al., *Adsorption of mercury, cadmium and lead from aqueous solution on heat treated and suphurized activated carbon.* Water Research, 1998. **32**(1): p. 1-4.
121. Park, S.-J. and Y.-S. Jang, *Pore Structure and Surface Properties of Chemically Modified Activated Carbons for Adsorption Mechanism and Rate of Cr(VI).* Journal of Colloid and Interface Science, 2002. **249**(2): p. 458-463.
122. Strelko Jr, V. and D.J. Malik, *Characterization and Metal Sorptive Properties of Oxidized Active Carbon.* Journal of Colloid and Interface Science, 2002. **250**(1): p. 213-220.
123. Yantasee, W., et al., *Selective Removal of Copper(II) from Aqueous Solutions Using Fine-Grained Activated Carbon Functionalized with Amine.* Industrial & Engineering Chemistry Research, 2004. **43**(11): p. 2759-2764.
124. Yin, C.Y., M.K. Aroua, and W.M.A.W. Daud, *Review of modifications of activated carbon for enhancing contaminant uptakes from aqueous solutions.* Separation and Purification Technology, 2007. **52**(3): p. 403-415.
125. Benard, P. and R. Chahine, *Storage of hydrogen by physisorption on carbon and nanostructured materials.* Scripta Materialia, 2007. **56**(10): p. 803-808.
126. Benard, P. and R. Chahine, *Determination of the Adsorption Isotherms of Hydrogen on Activated Carbons above the Critical Temperature of the Adsorbate over Wide Temperature and Pressure Ranges.* Langmuir, 2001. **17**(6): p. 1950-1955.
127. Al-Hajjaj, A., et al., *On the application of standard isotherms to hydrogen adsorption in microporous materials.* International Journal of Hydrogen Energy. **36**(22): p. 14464-14476.
128. Hirscher, M., *Handbook of hydrogen storage : new materials for future energy storage*, Weinheim: Wiley-VCH.
129. Yan, Y., et al., *Exceptionally high H2 storage by a metal-organic polyhedral framework.* Chemical Communications, 2009 (9).
130. Texier-Mandoki, N., et al., *Hydrogen storage in activated carbon materials: Role of the nanoporous texture.* Carbon, 2004. **42**(12-13): p. 2744-2747.
131. Schimmel, H.G., et al., *Hydrogen adsorption in carbon nanostructures compared.* Materials Science and Engineering: B, 2004. **108**(1-2): p. 124-129.
132. Yurum, Y., A. Taralp, and T.N. Veziroglu, *Storage of hydrogen in nanostructured carbon materials.* International Journal of Hydrogen Energy, 2009. **34**(9): p. 3784-3798.
133. Harutyunyan, A., et al., *Large cryogenic storage of hydrogen in carbon nanotubes at low pressures.* MRS Proceedings. **706**(Z10.3.1).
134. Ye, Y., et al., *Hydrogen adsorption and cohesive energy of single-walled carbon nanotubes.* Applied Physics Letters, 1999. **74**(16): p. 2307-2309.

135. Dillon, A.C., et al., *Optimization of Single-Wall Nanotube Synthesis For Hydrogen Storage.* Proceedings of the 2000 U.S. DOE Hydrogen Program Review, 2000. **NREL/CP**(.): p. 507-28890.
136. Neville, A. and B.A.B. McDougall, *Erosion and cavitation corrosion of titanium and its alloys.* Wear, 2001. **250**(1-12): p. 726-735.
137. Hirscher, M., et al., Journal of Alloys and Compounds, 2003. **356-357**: p. 433-437.
138. Dillon, A.C., K.E.H. Gilbert, and P.A. Parilla, *Hydrogen storage in carbon single- wall nanotubes.* PProceeding of the 2002 US DOE hydrogen program review, 2002. **NREL/CP**(.): p. 610-32405.
139. Gupta, B.K. and O.N. Srivastava, . International Journal of Hydrogen Energy, 2000. **25**(9): p. 825-830.
140. Liu, C., et al., . Science, 1999. **286**(5442): p. 1127-1129.
141. Suttisawat, Y., et al., . International Journal of Hydrogen Energy, 2009. **34**(16): p. 6669-6675.
142. Ralph T, Y., *Hydrogen storage by alkali-doped carbon nanotubes- revisited.* Carbon, 2000. **38**(4): p. 623-626.
143. Chen, P., et al., *High H2 Uptake by Alkali-Doped Carbon Nanotubes Under Ambient Pressure and Moderate Temperatures.* Science, 1999. **285**(5424): p. 91-93.
144. Lueking, A.D. and R.T. Yang, Applied Catalysis A: General, 2004. **265**(2): p. 259-268.
145. Lachawiec, A.J., G. Qi, and R.T. Yang, *Hydrogen Storage in Nanostructured Carbons by Spillover: Bridge-Building Enhancement.* Langmuir, 2005. **21**(24): p. 11418-11424.
146. Li, Y. and R.T. Yang, *Hydrogen Storage on Platinum Nanoparticles Doped on Superactivated Carbon.* The Journal of Physical Chemistry C, 2007. **111**(29): p. 11086-11094.
147. Wang, L. and R.T. Yang, *New sorbents for hydrogen storage by hydrogen spillover - a review.* Energy & Environmental Science, 2008. **1**(2): p. 268-279.
148. Lachawiec, A.J. and R.T. Yang, *Isotope Tracer Study of Hydrogen Spillover on Carbon-Based Adsorbents for Hydrogen Storage.* Langmuir, 2008. **24**(12): p. 6159-6165.
149. Yang, R.T. and Y. Wang, Journal of the American Chemical Society, 2009. **131**(12): p. 4224-4226.
150. Hoang, T.K.A. and D.M. Antonelli, *Exploiting the Kubas Interaction in the Design of Hydrogen Storage Materials.* Advanced Materials, 2009. **21**(18): p. 1787-1800.
151. Kocabas, S., et al., *Effect of thermal treatments and palladium loading on hydrogen sorption characteristics of single-walled carbon nanotubes.* International Journal of Hydrogen Energy, 2008. **33**(6): p. 1693-1699.
152. Zacharia, R., et al., Chemical Physics Letters, 2005. **412**(4-6): p. 369-375.
153. Ansón, A., et al., Journal of Alloys and Compounds, 2007. **436**(1-2): p. 294-297.
154. Lupu, D., et al., International Journal of Hydrogen Energy, 2004. **29**(1): p. 97-102.
155. Rather, S.-u., et al., *Hydrogen uptake of palladium-embedded MWCNTs produced by impregnation and condensed phase reduction method.* Chemical Physics Letters, 2007. **441**(4-6): p. 261-267.
156. Zacharia, R., et al., Chemical Physics Letters, 2007. **434**(4-6): p. 286-291.

157. Park, S.-J. and S.-Y. Lee, *Hydrogen storage behaviors of platinum-supported multi-walled carbon nanotubes.* International Journal of Hydrogen Energy. **35**(23): p. 13048-13054.
158. Jain, P., et al., *Hydrogen Uptake of Platinum-Doped Graphite Nanofibers and Stochastic Analysis of Hydrogen Spillover.* The Journal of Physical Chemistry C, 2007. **111**(4): p. 1788-1800.
159. Campesi, R., et al., *Hydrogen storage properties of Pd nanoparticle/carbon template composites.* Carbon, 2008. **46**(2): p. 206-214.
160. Rather, S.-u., et al., Chemical Physics Letters, 2007. **441**(4-6): p. 261-267.
161. Kim, B.-J., Y.-S. Lee, and S.-J. Park, International Journal of Hydrogen Energy, 2008. **33**(15): p. 4112-4115.
162. Zielinski, M., et al., *Hydrogen storage in nickel catalysts supported on activated carbon.* International Journal of Hydrogen Energy, 2007. **32**(8): p. 1024-1032.
163. Zubizarreta, L., et al., *Improving hydrogen storage in Ni-doped carbon nanospheres.* International Journal of Hydrogen Energy, 2009. **34**(7): p. 3070-3076.
164. Park, S.-J., et al., *Influence of copper electroplating on high pressure hydrogen-storage behaviors of activated carbon fibers.* International Journal of Hydrogen Energy, 2008. **33**(6): p. 1706-1710.
165. Isobe, S., et al., *Catalytic effect of 3d transition metals on hydrogen storage properties in mechanically milled graphite.* Journal of Physics and Chemistry of Solids, 2004. **65**(2-3): p. 535-539.
166. Yildirim, T. and S. Ciraci, *Titanium-Decorated Carbon Nanotubes as a Potential High-Capacity Hydrogen Storage Medium.* Physical Review Letters, 2005. **94**(17): p. 175501.
167. Kim, H.-S., et al., *Hydrogen Storage in Ni Nanoparticle-Dispersed Multiwalled Carbon Nanotubes.* The Journal of Physical Chemistry B, 2005. **109**(18): p. 8983-8986.
168. Silva, L.M.S., J.J.M. Órfão, and J.L. Figueiredo, *Formation of two metal phases in the preparation of activated carbon-supported nickel catalysts.* Applied Catalysis A: General, 2001. **209**(1-2): p. 145-154.
169. Li, Y. and R.T. Yang, *Hydrogen Storage in Metalâ˜'Organic Frameworks by Bridged Hydrogen Spillover.* Journal of the American Chemical Society, 2006. **128**(25): p. 8136-8137.
170. Burch, R., S.E. Golunski, and M.S. Spencer, *The role of hydrogen in methanol synthesis over copper catalysts.* Catalysis Letters, 1990. **5**(1): p. 55-60.
171. Stoica, M., et al., *Some experimental evidences for hydrogen spillover on Pt/Al2O3 catalysts by electrical conductivity transient response.* Applied Catalysis A: General, 1999. **183**(2): p. 287-293.
172. Almasan, V., et al., *H/D isotopic exchange between oxide surface and spiitover hydrogen on nickel supported catalysts*, in *Studies in Surface Science and Catalysis*. 1999, Elsevier. p. 435-438.
173. Srinivas, S.T. and P.K. Rao, *Direct Observation of Hydrogen Spillover on Carbon-Supported Platinum and Its Influence on the Hydrogenation of Benzene.* Journal of Catalysis, 1994. **148**(2): p. 470-477.
174. Levy, R.B. and M. Boudart, *The kinetics and mechanism of spillover.* Journal of Catalysis, 1974. **32**(2): p. 304-314.
175. Kramer, R. and M. Andre, *Adsorption of atomic hydrogen on alumina by hydrogen spillover.* Journal of Catalysis, 1979. **58**(2): p. 287-295.

176. Bianchi, D., et al., *Hydrogenation of ethylene on alumina after hydrogen spillover.* Journal of Catalysis, 1975. **38**(1-3): p. 135-146.
177. Vannice, M.A., M. Boudart, and J.J. Fripiat, *Mobility of hydrogen in hydrogen tungsten bronze.* Journal of Catalysis, 1970. **17**(3): p. 359-365.
178. Agarwal, R.K., et al., *Effect of surface acidity of activated carbon on hydrogen storage.* Carbon, 1987. **25**(2): p. 219-226.
179. Benson, J.E. and M. Boudart, *Hydrogen-oxygen titration method for the measurement of supported platinum surface areas.* Journal of Catalysis, 1965. **4**(6): p. 704-710.
180. Ho, L., et al., *Hydrogen desorption properties of multiwall carbon nanotubes with closed and open structures.* Applied Physics Letters, 2002. **80**(4): p. 577-579.
181. Roland, U., T. Braunschweig, and F. Roessner, *On the nature of spilt-over hydrogen.* Journal of Molecular Catalysis A: Chemical, 1997. **127**(1-3): p. 61-84.
182. Zacharia, R., et al., *Spillover of physisorbed hydrogen from sputter-deposited arrays of platinum nanoparticles to multi-walled carbon nanotubes.* Chemical Physics Letters, 2007. **434**(4-6): p. 286-291.
183. Yildirim, T., et al., *Molecular and dissociative adsorption of multiple hydrogen molecules on transition metal decorated C_{60}.* Physical Review B, 2005. **72**(15): p. 153403.
184. Dag, S., et al., *Adsorption and dissociation of hydrogen molecules on bare and functionalized carbon nanotubes.* Physical Review B, 2005. **72**(15): p. 155404.
185. Lueking, A. and R.T. Yang, *Hydrogen Spillover from a Metal Oxide Catalyst onto Carbon Nanotubes--Implications for Hydrogen Storage.* Journal of Catalysis, 2002. **206**(1): p. 165-168.
186. Kubas, G.J., et al., *Characterization of the first examples of isolable molecular hydrogen complexes, M(CO)3(PR3)2(H2) (M = molybdenum or tungsten; R = Cy or isopropyl). Evidence for a side-on bonded dihydrogen ligand.* Journal of the American Chemical Society, 1984. **106**(2): p. 451-452.
187. Sachse, J.U., et al., *Hydrogen-atom number in platinum-hydrogen complexes in silicon.* Physical Review B, 1999. **60**(3): p. 1474.
188. Lueking, A. and R.T. Yang, Journal of Catalysis, 2002. **211**(2): p. 565-565.
189. Fukutani, K., et al., *Zero-Point Vibration of Hydrogen Adsorbed on Si and Pt Surfaces.* Physical Review Letters, 2002. **88**(11): p. 116101.
190. Cheng, H., A.C. Cooper, and G.P. Pez, *Comment on ``Theoretical evaluation of hydrogen storage capacity in pure carbon nanostructures''* The Journal of Chemical Physics, 2004. **120**(19): p. 9427-9429.
191. Li, J., et al., *Theoretical evaluation of hydrogen storage capacity in pure carbon nanostructures.* The Journal of Chemical Physics, 2003. **119**(4): p. 2376-2385.
192. Dillon, A.C., et al., *Storage of hydrogen in single-walled carbon nanotubes.* Nature, 1997. **386**(6623): p. 377-379.
193. Lachawiec, A.J. and R.T. Yang, Langmuir, 2008. **24**(12): p. 6159-6165.
194. Li, J. and S. Yip, *Response to ``Comment on `Theoretical evaluation of hydrogen storage capacity in pure carbon nanostructures' ''* The Journal of Chemical Physics, 2004. **120**(19): p. 9430-9432.
195. Chen, C.-H. and C.-C. Huang, International Journal of Hydrogen Energy, 2007. **32**(2): p. 237-246.

196. Chen, C.-H. and C.-C. Huang, *Enhancement of hydrogen spillover onto carbon nanotubes with defect feature.* Microporous and Mesoporous Materials, 2008. **109**(1-3): p. 549-559.
197. Wu, C.Z., et al., *Effect of carbon/noncarbon addition on hydrogen storage behaviors of magnesium hydride.* Journal of Alloys and Compounds, 2006. **414**(1-2): p. 259-264.
198. Lillo-Ródenas, M.A., et al., *Effects of different carbon materials on MgH2 decomposition.* Carbon, 2008. **46**(1): p. 126-137.
199. Hima Kumar, L., B. Viswanathan, and S. Srinivasa Murthy, *Dehydriding behaviour of LiAlH4--the catalytic role of carbon nanofibres.* International Journal of Hydrogen Energy, 2008. **33**(1): p. 366-373.
200. John J, V., *Influence of nano-confinement on the thermodynamics and dehydrogenation kinetics of metal hydrides.* Current Opinion in Solid State and Materials Science. **15**(2): p. 52-61.
201. Gross A F, et al., *Nanotechnology.* 2009. **20**(20): p. 204005.
202. Sun, D., et al., *New approach for synthesizing Mg-based alloys.* Journal of Alloys and Compounds, 1999. **285**(1-2): p. 279-283.
203. Li, L., T. Akiyama, and J.-i. Yagi, *Activity and capacity of hydrogen storage alloy Mg2NiH4 produced by hydriding combustion synthesis.* Journal of Alloys and Compounds, 2001. **316**(1-2): p. 118-123.
204. Zhao-Karger, Z., et al., *Altered thermodynamic and kinetic properties of MgH2 infiltrated in microporous scaffold.* Chemical Communications. **46**(44): p. 8353-8355.
205. S. Zhang, A.F.G., S. L. Van Atta, M. Lopez, P. Liu, C. C. Ahn, and J. J. Vajo and C. M. Jensen, Nanotechnology, 2009. **20**: p. 204027.
206. Nielsen, T.K., et al., *Confinement of MgH2 Nanoclusters within Nanoporous Aerogel Scaffold Materials.* ACS Nano, 2009. **3**(11): p. 3521-3528.
207. Fichtner, M., *Properties of nanoscale metal hydrides.* Nanotechnology, 2009. **20**(20): p. 204009.
208. Fichtner, M., *Nanoconfinement effects in energy storage materials.* Physical Chemistry Chemical Physics. **13**(48): p. 21186-21195.
209. Antolini, E., et al., Materials Chemistry and Physics, 2007. **101**(2-3): p. 395-403.
210. Zeng, J. and J.Y. Lee, Journal of Power Sources, 2005. **140**(2): p. 268-273.
211. Cullity, B.D., *Elements of X-ray diffraction*. 1956, Reading, Mass.: Addison-Wesley Pub. Co.
212. http://rsbweb.nih.gov/ij/docs/index.html, Date accessed 2012.
213. Kasap, S.C., Peter, *Springer handbook of electronic and photonic materials*, ed. Springer. 2007, USA.
214. De Graef, M., *Introduction to conventional transmission electron microscopy*. 2003, Cambridge, U.K.; New York, N.Y.: Cambridge University Press.
215. Williams, D.B., Carter, C. B., , *Transmission Electron Microscopy: A Textbook for Material Science*, ed. Springer. 1996, USA.
216. Banwell, C.N., McCash, E. M., , *Fundamentals of molecular spectroscopy*, ed. McGraw Hill. 1994, England.
217. Walker, G., *Solid state hydrogen storage*. 2008, Cambridge; Boca Raton (Fla.): Woodhead Pub. ; CRC Press.
218. Brunauer, S., P.H. Ehmmett, and E. Teller, *Adsorption of gases in multimolecular layers.* Journal of the American Chemical Society, 1938. **60**: p. 309-319.

219. Lowell, S. and J.E. Shields, *Characterization of porous solids and powders surface area, pore size, and density*. 2004, Dordrecht; Boston: Kluwer Academic Publishers.
220. Sing, K.S.W., et al., *Reporting Physisorption Data for Gas/Solid Systems*, in *Handbook of Heterogeneous Catalysis*. 2008, Wiley-VCH Verlag GmbH & Co. KGaA.
221. Iupac Symposium, C. and J. Rouquerol. *Characterization of porous solids III : proceedings of the IUPAC Symposium (COPS III), Marseille, France, May 9-12, 1993*. Amsterdam; New York: Elsevier.
222. Barrett, E.P., L.G. Joyner, and P.P. Halenda, *The Determination of Pore Volume and Area Distributions in Porous Substances. I. Computations from Nitrogen Isotherms.* Journal of the American Chemical Society, 1951. **73**(1): p. 373-380.
223. Schull, C.G., *The Determination of Pore Size Distribution from Gas Adsorption Data.* Journal of the American Chemical Society, 1948. **70**(4): p. 1405-1410.
224. Yeh, C.-S. *A study of nanostructure and properties of mixed nanotube buckypaper materials fabrication, process modeling characterization, and property modeling*. 2007; Available from: http://etd.lib.fsu.edu/theses/available/etd-11192007-121847.
225. Halsey, G., *Physical Adsorption on Non-Uniform Surfaces.* The Journal of Chemical Physics, 1948. **16**(10): p. 931-937.
226. Greer, A.L., *The use of DSC to determine the Curie temperature of metallic glasses.* Thermochimica Acta, 1980. **42**(2): p. 193-222.
227. Kornyushin, Y.V. and L.N. Larikov, *Principles of identification of the physical processes caused by variation of thermodynamic parameters in solids.* Journal of Materials Science, 1978. **13**(1): p. 1-20.
228. Netzsch, *TG 209 F1Libra® brochure*. http://www.netzsch-thermal-analysis.com/download/TG_209_F1_Libra_E_0711_en_555.pdf.
229. Pope, M.I. and M.D. Judd, *Differential thermal analysis : a guide to the technique and its applications*. 1977, London; Bellmawr, N.J.: Heyden.
230. Glish, G.L. and R.W. Vachet, *The basics of mass spectrometry in the twenty-first century.* Nat Rev Drug Discov, 2003. **2**(2): p. 140-150.
231. Darling, R.B., et al., *Micromachined Faraday cup array using deep reactive ion etching.* Sensors and Actuators A: Physical, 2002. **95**(2-3): p. 84-93.
232. Scherrer, P. and N.G.W. Gottingen, Math-Pys.Kl., 1918. **2**: p. 96–100.
233. Hernadi, K., et al., Solid State Ionics, 2001. **141-142**: p. 203-209.
234. Feng, Y., et al., Chemical Physics Letters, 2003. **375**(5-6): p. 645-648.
235. Chiang, Y.-C., W.-H. Lin, and Y.-C. Chang, *The influence of treatment duration on multi-walled carbon nanotubes functionalized by H2SO4/HNO3 oxidation.* Applied Surface Science. **257**(6): p. 2401-2410.
236. Dandekar, A., R.T.K. Baker, and M.A. Vannice, *Characterization of activated carbon, graphitized carbon fibers and synthetic diamond powder using TPD and DRIFTS.* Carbon, 1998. **36**(12): p. 1821-1831.
237. Bououdina, M., D. Grant, and G. Walker, *Synthesis and H2 adsorption on graphitic nanofibres.* Journal of Alloys and Compounds, 2005. **404-406**: p. 634-636.
238. Toebes, M.L., J.A. van Dillen, and K.P. de Jong, *Synthesis of supported palladium catalysts.* Journal of Molecular Catalysis A: Chemical, 2001. **173**(1-2): p. 75-98.

239. Della Negra, M., et al., *Study of the interactions between the overlayer and the substrate in the early stages of palladium growth on TiO2(1 1 0).* Surface Science, 2003. **540**(1): p. 117-128.
240. Beszeda, I., E.G. Gontier-Moya, and D.L. Beke, *Investigation of mass transfer surface self-diffusion on palladium.* Surface Science, 2003. **547**(1-2): p. 229-238.
241. Stockholm, D., et al., *The Origin of Phenotypic Heterogeneity in a Clonal Cell Population In Vitro.* PLoS ONE, 2007. **2**(4): p. e394.
242. Dannatt, C.W. and H.J.T. Ellingham, *Roasting and reduction processes. Roasting and reduction processes-a general survey.* Discussions of the Faraday Society, 1948. **4**: p. 126-139.
243. Yadav, G.D. and S.V. Lande, *Novelties of kinetics of chemoselective reduction of citronellal to citronellol by sodium borohydride under liquid-liquid phase transfer catalysis.* Journal of Molecular Catalysis A: Chemical, 2006. **247**(1-2): p. 253-259.
244. Kim, J., et al., *Reduction of aromatic and aliphatic keto esters using sodium borohydride/MeOH at room temperature: a thorough investigation.* Tetrahedron. **66**(23): p. 3995-4001.
245. Gómez-Lahoz, C., et al., *Cobalt(II) removal from water by chemical reduction with sodium borohydride.* Water Research, 1993. **27**(6): p. 985-992.
246. Yang, J.Q., B.H. Liu, and S. Wu, . Journal of Power Sources, 2009. **194**(2): p. 824-829.
247. Sun, Z.-P., et al., . Electrochemistry Communications, 2009. **11**(3): p. 557-561.
248. Calò, V., A. Nacci, and A. Monopoli, Journal of Molecular Catalysis A: Chemical, 2004. **214**(1): p. 45-56.
249. Schmid, G., *Clusters and Colloids*. 1994, Weinheim: VCH.
250. Zhu, J., et al., Applied Catalysis A: General, 2009. **352**(1-2): p. 243-250.
251. Beletskaya, I.P. and A.V. Cheprakov, Chemical Reviews, 2000. **100**(8): p. 3009-3066.
252. Krishnan, A., et al., Nature, 1997. **388**(6641): p. 451-454.
253. Amorim, C. and M.A. Keane, *Palladium supported on structured and nonstructured carbon: A consideration of Pd particle size and the nature of reactive hydrogen.* Journal of Colloid and Interface Science, 2008. **322**(1): p. 196-208.
254. Park, C. and M.A. Keane, *Catalyst support effects: gas-phase hydrogenation of phenol over palladium.* Journal of Colloid and Interface Science, 2003. **266**(1): p. 183-194.
255. Zhou, L., Y. Zhou, and Y. Sun, *Studies on the mechanism and capacity of hydrogen uptake by physisorption-based materials.* International Journal of Hydrogen Energy, 2006. **31**(2): p. 259-264.
256. Fierro, V., et al., *Experimental evidence of an upper limit for hydrogen storage at 77 K on activated carbons.* Carbon. **48**(7): p. 1902-1911.
257. Jordá-Beneyto, M., et al., *Hydrogen storage on chemically activated carbons and carbon nanomaterials at high pressures.* Carbon, 2007. **45**(2): p. 293-303.
258. Xu, W.C., et al., *Investigation of hydrogen storage capacity of various carbon materials.* International Journal of Hydrogen Energy, 2007. **32**(13): p. 2504-2512.

259. Kabbour, H., et al., *Toward New Candidates for Hydrogen Storage: High-Surface-Area Carbon Aerogels.* Chemistry of Materials, 2006. **18**(26): p. 6085-6087.
260. Zuttel, A., et al., *Model for the hydrogen adsorption on carbon nanostructures.* Applied Physics A: Materials Science and Processing, 2004. **78**(7): p. 941-946.
261. Browning, D.J., et al., *Studies into the Storage of Hydrogen in Carbon Nanofibers: Proposal of a Possible Reaction Mechanism.* Nano Letters, 2002. **2**(3): p. 201-205.
262. Lueking, A.D., et al., *Effect of Expanded Graphite Lattice in Exfoliated Graphite Nanofibers on Hydrogen Storage.* The Journal of Physical Chemistry B, 2005. **109**(26): p. 12710-12717.
263. Ströbel, R., et al., *Hydrogen adsorption on carbon materials.* Journal of Power Sources, 1999. **84**(2): p. 221-224.
264. T. B. Flanagan, W.A.O., Annual Review of Materials Science
1991. **21**: p. 269-304.
265. Kayanuma, M., et al., *Adsorption and diffusion of atomic hydrogen on a curved surface of microporous carbon: A theoretical study.* Chemical Physics Letters. **495**(4-6): p. 251-255.
266. Kostov, M.K., et al., *Influence of Carbon Curvature on Molecular Adsorptions in Carbon-Based Materials: A Force Field Approach.* Physical Review Letters, 2002. **89**(14): p. 146105.
267. Chen, L., et al., *Mechanistic Study on Hydrogen Spillover onto Graphitic Carbon Materials.* The Journal of Physical Chemistry C, 2007. **111**(51): p. 18995-19000.
268. Driessen, A., et al., *Metal hydride formation at pressures up to 1 Mbar.* Journal of physics: Condensed matter, 1990. **2**(49): p. 9797.
269. Baranowski, B. and S.M. Filipek, *45 Years of nickel hydride--History and perspectives.* Journal of Alloys and Compounds, 2005. **404-406**: p. 2-6.
270. McLellan, R.B. and W.A. Oates, *The solubility of hydrogen in rhodium, ruthenium, iridium and nickel.* Acta Metallurgica, 1973. **21**(3): p. 181-185.
271. Wayman, M. and G. Weatherly, *The H−Ni (Hydrogen-Nickel) system.* Journal of Phase Equilibria, 1989. **10**(5): p. 569-580.
272. Shizuku, Y., S. Yamamoto, and Y. Fukai, *Phase diagram of the Ni-H system at high hydrogen pressures.* Journal of Alloys and Compounds, 2002. **336**(1-2): p. 159-162.
273. Wang, L. and R.T. Yang, *Hydrogen Storage Properties of Carbons Doped with Ruthenium, Platinum, and Nickel Nanoparticles.* The Journal of Physical Chemistry C, 2008. **112**(32): p. 12486-12494.
274. Lin, K.-Y., W.-T. Tsai, and J.-K. Chang, *Decorating carbon nanotubes with Ni particles using an electroless deposition technique for hydrogen storage applications.* International Journal of Hydrogen Energy. **35**(14): p. 7555-7562.
275. Barlag, H., L. Opara, and H. Zuchner, *Hydrogen diffusion in palladium based f.c.c. alloys.* Journal of Alloys and Compounds, 2002. **330-332**: p. 434-437.
276. Howard, B.H., et al., *Hydrogen permeance of palladium-copper alloy membranes over a wide range of temperatures and pressures.* Journal of Membrane Science, 2004. **241**(2): p. 207-218.
277. Yoshihara, M. and R.B. McLellan, *The diffusivity of hydrogen in palladium-based solid solutions.* Acta Metallurgica, 1982. **30**(8): p. 1605-1611.

278. Kirchheim, R. and R.B. McLellan, *Diffusivity of hydrogen in dilute alloys of copper and niobium in palladium.* Acta Metallurgica, 1980. **28**(11): p. 1549-1554.
279. Opalka, S.M., et al., *Hydrogen interactions with the PdCu ordered B2 alloy.* Journal of Alloys and Compounds, 2007. **446-447**: p. 583-587.
280. Campesi, R., et al., Microporous and Mesoporous Materials, 2009. **117**(1-2): p. 511-514.
281. Chen, S., B.D. Adams, and A. Chen, *Synthesis and electrochemical study of nanoporous Pd-Ag alloys for hydrogen sorption.* Electrochimica Acta. **56**(1): p. 61-67.
282. Makrides, A.C., *Absorption of Hydrogen by Silver-Palladium Alloys.* The Journal of Physical Chemistry, 1964. **68**(8): p. 2160-2169.
283. Linstrom, E.P.J. and W.G. Mallard. *"Infrared Spectra" in NIST Chemistry WebBook, NIST Standard Reference Database*. retrieved August 5, 2010 [cited 2012 2012]; Available from: http://webbook.nist.gov/cgi/cbook.cgi?ID=C106978&Units=SI&Type=IR-SPEC#IR-SPEC.
284. NIST Mass Spec Data Center, S.E.S., director. *Mass spectrum (electron ionization) 1-butene*. 2012 [cited 2012 2012]; Available from: http://webbook.nist.gov/cgi/cbook.cgi?ID=C106989&Units=SI&Mask=1EFF#Mass-Spec.
285. NIST Mass Spec Data Center, S.E.S., director. *Mass spectrum (electron ionization) butane*. 2012 [cited 2012 2012]; Available from: http://webbook.nist.gov/cgi/cbook.cgi?ID=C106978&Mask=200#Mass-Spec.
286. NIST Mass Spec Data Center, S.E.S., director. *Mass spectrum (electron ionization) nitrogen gas*. 2012 [cited 2012 2012]; Available from: http://webbook.nist.gov/cgi/cbook.cgi?ID=C7727379&Mask=200#Mass-Spec.
287. Tanaka, K., *Hydride stability and hydrogen desorption characteristics in melt-spun and nanocrystallized Mg-Ni-La alloy.* Journal of Alloys and Compounds, 2008. **450**(1-2): p. 432-439.
288. Liebman, J.F., T. Holm, and S.W. Slayden, *The Thermochemistry of Organomagnesium Compounds*, in *PATAI'S Chemistry of Functional Groups*. 2009, John Wiley & Sons, Ltd.
289. Danaie, M., et al., *Analysis of deformation twins and the partially dehydrogenated microstructure in nanocrystalline magnesium hydride (MgH2) powder.* Acta Materialia. **58**(8): p. 3162-3172.
290. Zhdanov, V.P., A. Krozer, and B. Kasemo, *Kinetics of first-order phase transitions initiated by diffusion of particles from the surface into the bulk.* Physical Review B, 1993. **47**(17): p. 11044.
291. Simeonova, P., et al., *Evaluation of Mean Diameter values using Scherrer Equation Applied to Electron Diffraction Images*, in *Nanotechnology – Toxicological Issues and Environmental Safety and Environmental Safety*. 2007, Springer Netherlands. p. 231-237.
292. Rafi ud, d., et al., *Catalytic effects of nano-sized TiC additions on the hydrogen storage properties of LiAlH4.* Journal of Alloys and Compounds. **508**(1): p. 119-128.
293. Bureau, J.C., et al., *Comparative study of hydro- and deuteroaluminates of lithium LiaAlH4 and LiAlD4.* Etude comparative des hydro- et

deuteroaluminates de lithium LiAlH4 et LiAlD4 II - Spectres de diffusion raman des composes solides, 1985. **20**(10): p. 1147-1155.
294. Ares, J.R., et al., *Thermal and mechanically activated decomposition of LiAlH4.* Materials Research Bulletin, 2008. **43**(5): p. 1263-1275.
295. Wang, X. and L. Andrews, *Infrared Spectra of Magnesium Hydride Molecules, Complexes, and Solid Magnesium Dihydride.* The Journal of Physical Chemistry A, 2004. **108**(52): p. 11511-11520.
296. Awbery, R.P., D.A. Broughton, and S.C. Tsang, *In situ observation of lithium hydride hydrolysis by DRIFT spectroscopy.* Journal of Nuclear Materials, 2008. **373**(1-3): p. 94-102.
297. Mikheeva, V.I. and N.N. Mal'tseva, *Infrared absorption spectra of some simple hydrides.* Journal of Structural Chemistry, 1964. **4**(5): p. 643-646.
298. Leng, H.Y., et al., *Investigation of reaction between LiNH2 and H2.* Journal of Alloys and Compounds, 2008. **463**(1-2): p. 462-465.
299. Ismail, M., et al., *Effects of NbF5 addition on the hydrogen storage properties of LiAlH4.* International Journal of Hydrogen Energy. **35**(6): p. 2361-2367.
300. Ismail, M., et al., *Significantly improved dehydrogenation of LiAlH4 catalysed with TiO2 nanopowder.* International Journal of Hydrogen Energy. **36**(14): p. 8327-8334.
301. Xueping, Z., et al., *Effect of catalyst LaCl3 on hydrogen storage properties of lithium alanate (LiAlH4).* International Journal of Hydrogen Energy, 2007. **32**(18): p. 4957-4960.
302. Sun, T., et al., *The effect of doping NiCl2 on the dehydrogenation properties of LiAlH4.* International Journal of Hydrogen Energy, 2008. **33**(21): p. 6216-6221.
303. Zhang, Y., et al., *The destabilization mechanism and de/re-hydrogenation kinetics of MgH2-LiAlH4 hydrogen storage system.* Journal of Power Sources, 2008. **185**(2): p. 1514-1518.
304. Liu, S.-S., et al., *Hydrogen storage properties of destabilized MgH2-Li3AlH6 system.* International Journal of Hydrogen Energy. **35**(15): p. 8122-8129.
305. Matelloni, P., *Supporting metal catalysts on modified carbon nanocones to optimize dispersion and particle size*, in *MRS Fall Meeting 2009*, MRS, Editor. 2009, MRS (Warrendale, PA) manuscript ID: 1216-W02-02.R1.: Boston, MA.